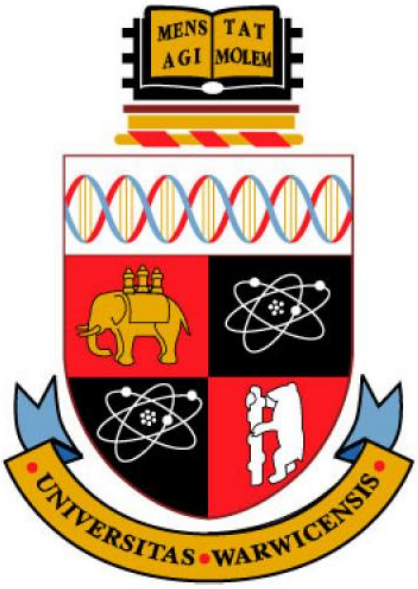

ULTRASONIC CHARACTERISATION OF ROLLED ALUMINIUM AND STEEL SHEET CORRELATED WITH ELECTRON BACKSCATTER DIFFRACTION MEASUREMENTS

By

Stephen Essex

THESIS

Submitted to the University of Warwick
for the degree of

DOCTOR OF PHILOSOPHY

Department of Physics
SEPTEMBER 2009

CONTENTS

For Deega, Wiggy, James,

Alex and Pebs

Not many days pass where you do not enter my thoughts.

I dedicate this to you all.

LIST OF FIGURES

LIST OF TABLES

ACKNOWLEGEMENTS

I would like to firstly acknowledge the funding provided by the UK Research Centre for Non-Destructive Evaluation (RCNDE) for the duration of my PhD.

There is also a list of people as big as the Chelsea trophy cabinet that I really want to thank. My supervisor Steve Dixon has been absolutely amazing; a great help academically throughout my PhD studies, yet it is his words of wisdom on the subject of 'life' (that I was subjected to incessantly) that I will probably best remember (and which I eventually acted upon). Rachel Edwards, Queen of Physics, has also offered great support throughout, and I thank you for that. Thank you also to Mark Potter for all his help and expertise with EMATs, and to Charley Fan for his unrivalled knowledge and subsequent help with FEM simulations. Fletch, Jim, Phyllis, Francisco, Timothy, Sue, Ben and Shimi, you all stay classy.

There are some other wonderful characters in the physics department I must thank. 'The grand old Stevie York, he has an SEM'. I've never tired of singing that, and thanks for everything. Your 'happy go lucky' nature and ever-present smile made endless hours of EBSD pretty fun. Richard Dobedoe also offered great insight into the world of microscopy, it is much appreciated. And as for Cheryl's cups of tea.....

My Warwick experience would have been severely dampened without my beloved Golf club. It's provided me with some of the best opportunities and I have been incredibly fortunate to have made so many great friends. Benji, Dr Giblin, Lidmaw, Wolfy, Val, J Mac III, Fenny, Pearso, Ali.... the list is endless; and there are many more from the pre-PhD days: I thank you all for making Wednesday golf day! Also, the Warwick Sport crew have been a major source of entertainment: you are all fantastic people and have been great friends. Can I have a bursary now?!

Last but not least I thank my family, and in particular my parents. My Mum and Dad are the major influences in my life, and have been an inspiration to me since day one. I hope you're as proud of me as I am of having you as parents, I love you both. By the way Dad, those trees on Lots Road are only going to get bigger....! And finally, a mention for the love of my life, Chelsea, I mean, my fiancée Sarah. Thank you for the love and wonderful support during my PhD. Roll on Friday 13th August 2010!

DECLARATION

This thesis presents the culmination of my original work that I have completed from October 2005 - June 2009 at the commencement of my PhD studies. Where the published work of others has been used, every attempt has been made to reference and acknowledge them suitably. Any help received has been acknowledged.

This PhD was completed under the supervision of Dr Steve Dixon at the Department of Physics, University of Warwick. None of this work has been submitted previously to any academic institution for the admission of a higher degree. Some of the work and figures have been published previously in publications, which are detailed in the publication list given.

PUBLICATION LIST

Conference proceedings

1. Dixon S, Essex S, *Texture measurement of aluminium sheet using electron back scattered diffraction and electromagnetic acoustic transducers*, BINDT 2006 Stratford, BINDT conference proceedings

2. Dixon S, Essex S, Potter MDG, *Ultrasonic measurement of crystallographic texture in metals*, WCEAM- CM 2007 conference proceedings, Harrogate

3. Essex S, Potter MDG, Dobedoe RDS, Dixon S, *Ultrasonic Characterization of texture validation using EBSD*, NDT 2007 Glasgow, BINDT Conference Proceedings.

4. Essex S, Potter MDG, Dixon S, *Calculation of Elastic Anisotropy Using EMATs Validated by EBSD in Rolled Aluminium Sheet*, NDT 2008 Shrigley Hall, Cheshire, BINDT Conference Proceedings.

ISI indexed published proceedings

5. Essex SD, Dixon S, and Potter MGD, *Ultrasonic Characterization of Texture in Rolled Aluminium in Collaboration with Electron Backscatter Diffraction Measurements*, Rev. Prog. in QNDE 2006, **26B**, pp. 1237-1244, 2007

6. Morrison J, Dixon S, Potter MGD, and Essex S, *The Correspondence Between Elastic and Plastic Anisotropy in Nominally Pure and AA3104 Aluminium Sheets*, Rev. Prog. in QNDE 2007

7. Essex S, Potter MGD, Dobedoe RS and Dixon S, *Ultrasonic characterization of effective elastic constants and texture in Aluminium correlated with EBSD*, Rev. Prog. in QNDE, 2007

8. Palmer S.B, Essex S, Potter M.D.G, and Dixon S, *Determination of crystallographic texture in metal sheets using ultrasound and EBSD*, Proc. SPIE 6934, 69340F, 2008

9. Essex S, Potter MGD, and Dixon S, *S_0 Lamb Wave Calculation of Texture Validated by EBSD in Rolled Aluminium and Steel Sheet*, Rev. Prog. in QNDE, 2008

10. Essex S, Potter MGD, and Dixon S, *Utilizing EBSD to Validate NDT techniques*, Rev. Prog. in QNDE 2008

SUMMARY

This thesis is based on the characterization of material properties of interest in rolled aluminium and steel sheet, both popular materials used across a wide-range of applications. The forming processes involved in producing rolled sheet metal depend on plastic deformation, inducing elastic anisotropy as a consequence. These changes result in a variation from the simple isotropic and cubic symmetry systems possessed by steel and aluminium prior to cold-working. The most significant changes include the introduction of crystallographic texture and the morphology of the crystallographic grains in size and shape to accommodate the plastic deformation.

It is desirable in industries that use rolled product for manufacturing components to quantify such changes. The literature has postulated links between plastic and elastic properties, and hence any quantification of the elasticity, crystallographic texture and grain morphology can aid in the prediction of future formability behaviour.

This thesis presents non-destructive, rapid ultrasonic measurements to characterize some of the changes that are evident in rolled aluminium and steel sheet. These ultrasonic results have then been correlated to crystallographic orientation measurements generated from using a microscopic technique called electron backscatter diffraction (EBSD). The level of agreement between the two contrasting methods has been analysed and is presented here.

The non-destructive ultrasonic measurements include quantifying crystallographic texture utilising theory linking the S_0 Lamb wave velocity and the direction of propagation in a rolled sheet with respect to the rolling direction. This leads to the determination of texture coefficients known as orientation distribution coefficients (ODC). Through-thickness linearly polarized SH waves have then been used to analyse grain morphology using attenuation data, and elasticity measurements from velocity data.

EBSD datasets have been manipulated to produce predictions of the effective elastic stiffness constants, which in turn can be used to generate comparable S_0 Lamb wave velocity predictions to be directly compared to the ultrasonic measurements. This process has required a novel method to generate such ultrasonic velocity predictions as a function of angle, together with predictions for the nine effective elastic stiffness constants inherent to rolled orthorhombic sheet. The facility to measure grain size and shape accurately from EBSD data has been utilized.

The thesis starts with a general introduction in non-destructive testing and microscopy, with focussed discussion on ultrasound, electromagnetic acoustic transducers (EMATs), EBSD and metallurgy in the subsequent chapters. Chapter 6 introduces the development of correlation methods between the ultrasound and EBSD results, with chapters 7 and 8 displaying the empirical ultrasound and EBSD data respectively. Chapter 9 compares the data from the two methods, with the final conclusions given in chapter 10.

CHAPTER 1

Introduction

1.1 – Requirement for non-destructive testing

Aluminium and steel are two of the most important and frequently used materials in the construction of a diverse array of components and structures, with wide-ranging applications [1, 2]. For example, both are used widely in the automotive, rail and aerospace industry [3-5]. Their versatility is evident; the two are essential in the construction of diverse structures, from nuclear power plant components [6] to drink cans [7]. It is this adaptability, the abundance, the cost and the favourable material properties characteristic of both that lends themselves to these potential applications with the selection of the most suitable alloy.

When considering transport applications, failures, be it in car engines, rail track or aerospace components, can lead to catastrophic consequences. Therefore, with increasing necessity there is a need for the development of techniques to aid in the detection, and preferably the prevention, of flaws within such structures, in addition to characterizing and optimising the elastic and plastic properties.

Suitable methods for characterising components would reduce the occurrence of material degradation leading to structural integrity failures, because repairs could be implemented before defects became significant or even detected. Such systems would require the ability to locate defects at the surface and within the bulk of a component. The financial implications of component failure are that, together with wastage or inefficient manufacture, such testing would reduce costs over a sustained period of time.

However, the focus of this report is to investigate the properties of the raw sheet material before it is manufactured into more complex components, as it is of benefit to ascertain the suitability of a material for a particular application before further manufacturing. For example, being able to predict the plastic behaviour of rolled aluminium or steel sheet and

predict whether it has the necessary physical properties to maintain the desired performance once formed, is very important [8]. In effect, this pre-determined knowledge of the micro and macroscopic properties would ensure a more efficient production line with improved performance from the final products. Wastage would be minimized, suggesting such testing has beneficial environmental effects too. This would improve quality and process control programs, and provide quantitative material property measurements beyond what is currently achieved.

1.2 – Non-destructive testing

Ideally, the detection of defects, analysis of the evolution in the material properties during manufacturing, and determining material suitability, should be completed in a non-destructive manner and be capable of performance in an online or in-service environment.

The development of such a non-destructive testing (NDT) method begins with lab-based measurements. NDT approaches are desirable for material characterization as they can provide faster and less expensive solutions to obtaining the material properties of interest than the traditional diffraction methods employed such as X-Ray diffraction (XRD). NDT processes on rolled sheet require little surface preparation in the majority of cases, and can also provide a macroscopic average over a large area which again is a major advantage compared to the diffraction methods. NDT methods developed in the lab can then be applied during manufacturing of rolled metal sheet and for in-service components. Therefore testing should be integrated into the production line, generating real-time quantitative information that rapidly determines the suitability of the sheet for specific applications [9]. If defects or undesirable physical characteristics are detected, then the sheet can be downgraded to another application or completely withdrawn before being used. For components already in operation, testing would be performed without requiring the shutdown of the component; again generating real-time information regarding the existence of significant defects or evolving material properties that may reduce performance or lead to failure.

NDT is an expanding area of research globally and an essential activity within large industrial companies. The last few decades have seen many advances in the development of techniques to detect and characterize flaws in a variety of environments for multifarious specimens. The techniques utilised include thermography [10,11], magnetic particle inspection, eddy current testing, alternating current field measurements (ACFM) and alternating current potential drop (ACPD) [12-14], along with the versatile ultrasonic measurement systems now available [15-17].

Rapid NDT processes are desirable, making the use of ultrasound of particular interest for aluminium and steel. Both allow the generation and the detection of ultrasound using Electromagnetic Acoustic Transducers (EMATs) [18]. The ability of EMATs to generate both surface and bulk waves, being able to control the frequency, polarisation and propagation directions, means that the elastic and structural information that can be measured is greatly enhanced in comparison to conventional contacting ultrasound techniques. However, EMATs do have some disadvantages, such as poor ultrasonic energy efficiency, and a strong dependence on standoff (distance between the transducer and the sample), the electrical conductivity and magnetostricton properties of the sample under investigation.

1.3 – Material properties of interest for rolled metallic sheet

The work in this thesis is focussed specifically on measuring the crystallographic texture and grain characteristics in rolled aluminium and steel sheet. Cold-rolling in particular imparts large stresses on the samples being processed to reduce components such as billets and plates to a required thickness within the range of 5 to 0.2 mm. As a result of this deformation, changes are induced in the elastic and plastic properties [19]. Often, these sheets are subjected to further formability e.g. Drink cans. However, the change in material properties or another subsequent forming process may be so severe during sheet production that the final product can be flawed. For example in deep drawing, the sheet may shear during the drawing process, or the final product be outside of the tolerance of the specification.

The following describes some of the measurable material properties that would either have changed or developed as a result of rolling. Determining these parameters would give a better understanding of the micro and macrostructural properties of the sheet, and hence its suitability for a particular application.

1.3.1 - Crystallographic texture

A rolling process to reduce aluminium and steel sheet thickness enforces a rolling direction in the sheet, which imparts preferential axes of symmetry for crystallographic alignment that influences the orientation of the crystals within the crystallite structure, both in the rolling direction and out of plane [20]. This can be seen as the introduction of elastic anisotropy, known as crystallographic texture [21]. This implies elasticity is directionally-dependent; this may or may not be beneficial. Crystallographic texture can be detected using ultrasonic velocity measurements. The anisotropic properties extend to the elastic moduli in different directions with respect to the rolling direction, hence changing the velocities.

1.3.2 - Crystallite elastic stiffness constants

Rolled aluminium and steel sheet has orthorhombic symmetry [22] as a direct consequence of the geometry of the working. For orthorhombic symmetry there are nine independent elastic constants, which can be determined with the correct combination of a number of ultrasonic waves [9, 23]. Knowledge of the density of the material and the single crystal elastic constants are required for this, and for aluminium in particular these parameters are well documented [24].

1.3.3 - Grain size

Grains are volumes within polycrystalline aggregates, constructed from a number of individual crystals that each has equivalent (or very similar) orientations. Extrapolating the average size of grains for polycrystalline materials leads to a better understanding about a

number of material properties, such as the strength [25, 26]. The grain boundaries act as sources of elastic scattering to ultrasound propagation. Therefore attenuation measurements can, in principle, be used to obtain a measurement of grain size [27].

1.3.4 - Grain aspect ratio

The stress and strain states of sheet products are greatly altered as a result of rolling. The grains, which when in an isotropic state are typically equiaxial, will change in shape. The grains become elongated and flattened when worked, changing the grain aspect ratio [19]. This grain aspect ratio is an indication of strain present in the sample. Ultrasonic attenuation measurements can be performed to determine this ratio.

1.4 - Correlating the NDT techniques

When developing new techniques and analysing the results obtained, it is preferable scientifically to compare the data to either previously calibrated results or to equivalent results obtained from another established method. This thesis utilises a diffraction technique called Electron Backscatter Diffraction (EBSD), to correlate the ultrasound methods deployed. EBSD is a microscopic technique which calculates individual crystallographic orientations in Eulerian angle form. This data can be manipulated to obtain values for texture, elastic constants and grain size and shape information. The texture measurements typically associated with diffraction methods are based upon stereographic projection pole figures [28]. This thesis goes further than this, attempting to develop innovative ways to directly predict the ultrasonic behaviour expected on the test sheets. The prediction of the elastic constants in anisotropic sheet is obtained from the mathematical manipulation of the EBSD data, whereas the typical inverse pole figure maps produced by EBSD give a unique description of the microstructure and hence information on the grain structure [29].

1.4.1 – Previous work linking NDT and EBSD

EBSD is a relatively new technique, only becoming an automated process in the late 1990's [30]. There have been some sporadic examples of research in the field of NDT that have used EBSD as a correlation tool [31, 32]. It appears that no work has so far been undertaken that is comparable to the scale and the scope of this body of work.

1.5 – Summary of thesis objectives

The thesis investigates some rapid ultrasonic measurement techniques designed to ultimately be suitable for online testing on rolled metallic sheet. The experimental body of work focuses specifically on the cases of aluminium and steel, though the techniques could be applied to other metals.

The results generated from the ultrasonic measurements are designed to help characterize and quantify the material properties quickly, allowing information to be generated confirming the sheet is suitable for its final intended purpose. Ultrasound methods do have limitations however, and hence the information that can be obtained often gives only a good approximation to the mechanical properties. The importance of the relevant information theoretically attainable is discussed throughout the body of this work. In contrast, EBSD gives a very accurate measure of the microstructure, but is a technique which is comparatively slow, expensive and unsuitable for online measurement.

The foremost objective of this work is to determine the accuracy and reliability of the rapid ultrasonic texture measurements deployed for predicting parameters linked to microstructural and macrostructural properties. To do this, a diffraction method has been utilised, the data of which has been manipulated to replicate, and hence correlate with, the ultrasound methods. EBSD was performed on the sample sheets after ultrasonic measurements were taken. EBSD was chosen as it presents the chance to fully understand the interaction and relationship between the microstructure and the wave as it propagates. It also

provides an opportunity to review NDT and diffraction methods, highlighting their respective strengths and limitations in determining material parameters.

This work sets out to correlate the ultrasound measurements with the EBSD measurements to confirm that the ultrasound technique is a valid method to be considered for quantifying crystallographic texture amongst other material properties. It will also develop new applications for utilising EBSD as a way to predict elastic behaviour, and in turn ultrasonic propagation characteristics

1.6 - Proceeding chapter overview

Chapter 2 describes some background theory of ultrasound. This develops the link between the stress and strain of a sample, defining elasticity, and describes the existence of various symmetry systems that are common to rolled metallic sheet.

Chapter 3 gives a critical review of methods used to (non-destructively) generate and detect ultrasound, culminating in the theory of transduction using Electromagnetic Acoustic Transducers (EMAT), and their applicability to characterizing sheet metal. The capabilities of what can be achieved using EMATs are given. Particular reference is made to Lamb waves and shear waves, both used extensively throughout the experimental work.

Chapter 4 deals with the theoretical background and development of microscopy; in particular the Scanning Electron Microscope (SEM) and specifically Electron Backscatter Diffraction (EBSD). How EBSD works, together with its capabilities is discussed. The typical methods by which the orientation data is used to characterize metal is summarised. The operations of the microscope and user parameters are detailed at the end of the chapter.

The final background chapter talks about metallurgy, starting by introducing the formation of the microstructure of a metal. The rolling process is summarised, and the plastic deformation linked to the working is discussed. The effect of cold-rolling on the elasticity is examined, together with the changes in the material parameters of interest. The use of aluminium and steel and their suitability for experimentation implementing EMATs and EBSD is analysed.

Chapter 6 develops the relationship between the two contrasting techniques provided by ultrasound and EBSD. It describes the mathematical framework behind the manipulation of the EBSD data to produce ultrasonic behaviour predictions. Algorithms are developed that are required to predict the elastic constants needed to characterize a rolled sheet with orthorhombic symmetry. The experimental methods required to determine crystallographic texture is defined. The process used to define grain size and aspect ratios from EBSD data is optimized, thus enabling the correlation of ultrasonic attenuation measurements with EBSD measurements to extrapolate microstructural information.

Chapter 7 displays the ultrasound results obtained for all the samples, for the crystallographic texture and attenuation measurements used to characterize the sheets. Firstly the ultrasound techniques employed are described, and experimental details are specified, together with the relevant error analysis. Analysis of the ultrasound results for the aluminium and steel sheets is completed, with calculations completed for the quantitative texture coefficients. Predicted grain sizes and aspect ratios are also determined from attenuation measurements, as described in the methods discussed in chapter 5.

The EBSD data collected from the aluminium and steel samples studied is presented in chapter 8. In this chapter, quantitative measurements of the orientation distribution coefficients, S_0 mode Lamb wave predictions, elastic constants and grain size and shape characterization are completed.

The penultimate chapter correlates the EBSD results taken from the sample sheets with ultrasonic measurements; this provides a direct comparison of microstructural data to bulk ultrasound results on the macroscopic scale. Firstly, the Eulerian angle data is manipulated to generate ultrasonic predictions which are directly compared to the ultrasound crystallographic texture results. These results show a good correlation across a number of aluminium and steel sheets, though in some cases the limitations of both techniques, flawed when texture inhomogeneity through-thickness occurs, is highlighted. To solve the issues, Finite Element Modelling (FEM) was performed to aid in providing explanations of the behaviour. Elastic stiffness constants, which can be inferred from ultrasonic velocity

measurements, are also generated from EBSD data and are compared to the ultrasonically determined values. Finally EBSD-measured grain sizes and aspect ratios are used to compare to the empirical ultrasonic attenuation measurements.

Finally, the thesis ends with a discussion and general conclusions drawn from the research, summarising the body of the experimental work, and putting it into context with previous research completed in the field of interest. The implications of the results are considered. Further work to investigate interesting areas that arise from the research are also postulated.

1.7 - References

1. *Honeycombe RWK, Steels – Microstructure and Properties, Arnold, 1981*
2. *Dwight JB, Aluminium design and construction, E & FN Spon, 1999*
3. *Kollgaard JR, LaRiviere SG, Rev. of Prog. in QNDE, 2007, Plenary lecture*
4. *Dasch CJ, Rev. of Prog. in QNDE, 2007, Plenary lecture*
5. *Fan Y, Dixon S, Edwards RS, Jian X, NDT&E International, **40**, 2007, pp. 471–477.*
6. *Ahmed S, Thompson RB, J. Acoust. Soc. Am., **99**, 1996 pp. 2086-2096*
7. *Morrison J, Dixon S, Potter MDG, Davis C, Rev. of Prog. in QNDE, 2008, pp.1192-1198.*
8. *Stickels CA, Mould PR, Met Trans, **1**, 1970, pp. 1303-1312*
9. *Alers G, Sinclair AN, Rev. of Prog. in QNDE, **18**, 1999, pp. 1695-1701*
10. *Avdelidis NP, Hawtin BC, Almond DP, NDT&E International, **36**, 2003, pp. 433-439*
11. *Inagaki T, Ishii T, Iwamoto T, NDT&E International, **32**, 1999, pp.247-257*
12. *Tian GY, Sophian A, NDT&E International, **38**, 2005, pp. 319-324*
13. *Papaelias MP, Lugg MC, Roberts C, Davis C, NDT&E International, **42**, 2009, pp.328-335*
14. *Bowler N, J. Phys. D: Appl. Phys, **39**, 2006, pp. 584-589*
15. *Palmer SB, Dixon S, Insight, **45**, 2003, pp. 211-217*
16. *Scruby CB, Drain LE, Laser Ultrasonics, techniques and applications, Bristol: Adam Hilger, 1990*
17. *Krautkrämer J, Krautkrämer H, Ultrasonic Testing of Materials, Springer-Verlag, 1990*
18. *Hirao M, Ogi H, EMATS for science and industry: non-contacting ultrasonic measurements, Kluwer Academic Publishers, 2003.*
19. *Wenk H-R, Van Houtte P, Rep. Prog. Phys., **67**, 2004, pp. 1367-1428*

20. *Kocks UF, Tome CN, Wenk H-R, Texture and Anisotropy, Cambridge University Press, 2000*

21. *Roe R-J, Krigbaum WR, Journal of Chemical Physics, **40**, 1964, pp. 2608-2615*

22. *Nye JF, Physical Properties of Crystals, Oxford Press, 1957*

23. *Sayers CM, J. Phys. D: Appl. Phys., **15**, 1982, pp. 2157-2167*

24. *Courtesy of the OIM helpfile.*

25. *Bunge HJ, Journal of Nondestructive Evaluation, **12**, 1993, pp. 3-10*

26. *Lasalmonie A, Strudel JL, J. Mat. Sci, **21**, 1986, pp. 1837-1852*

27. *Smith RL, Ultrasonics, 1982, pp. 211-214*

28. *Rajan K, Representations of texture in orientation space, a contribution to Electron Backscatter Diffraction in Materials Science, pp.31-38, Kluwer Academic Publishers, 2000*

29. *Essex S, Potter MDG, Dixon S, Rev. of Prog. in QNDE, 2009, pp.1727-1734*

30. *Adams BL, Wright SI, Kunze K, Metall Trans, **24A**, pp. 819-831*

31. *Panetta PD, Thompson RB, Margetan FJ, Rev. of Prog. in QNDE, **17A**, 1997, pp. 89-96*

32. *Scruby CB, Young RMK, Bull CE, Humphreys FJ, Mats. Science and Tech., **19**, 2003, pp. 163-172*

CHAPTER 2

Ultrasound

2.1 – Introduction

Ultrasonic testing is an invaluable method with which to measure some of the physical properties of metallic samples. Measuring velocity, frequency, phase change and amplitude of various wavemodes and how they change as the wave propagates can give rise to a variety of information regarding the material properties and the existence of defects.

One major advantage of ultrasonic techniques is the non-destructive nature of the method, which is a specifically desirable characteristic as outlined in the introductory chapter of this thesis.

This chapter introduces the mechanics involved in defining a propagating ultrasonic wave in anisotropic media (such as rolled sheet metal). A description and definition of Lamb, Rayleigh and bulk shear and compression waves is given for propagation in both isotropic and anisotropic media.

2.2 – Ultrasound: Introductory theory

2.2.1 – Relationship of stress and strain

An ultrasound wave propagates through an elastic media as a result of the small deformation of the crystal lattice (see chapter 5 for a description of the metallurgy). The elasticity property that governs this interaction is derived from the relationship between the stress state of the sheet and the strain, and is defined by Hooke's law (equation 2.1) [1]:

$$\sigma_{ij} = c_{ijkl}\varepsilon_{kl} \tag{2.1}$$

Here c_{ijkl} is the 4th rank elasticity tensor, with σ_{ij} the 2nd rank stress tensor and ε_{kl} is the 2nd rank strain tensor. The two 2nd rank tensors are *3*x*3* matrices and are defined by equation 2.2:

$$\sigma_{ij} = \begin{pmatrix} \sigma_{11} & \sigma_{12} & \sigma_{13} \\ \sigma_{21} & \sigma_{22} & \sigma_{23} \\ \sigma_{31} & \sigma_{32} & \sigma_{33} \end{pmatrix} \qquad \varepsilon_{ij} = \begin{pmatrix} \varepsilon_{11} & \varepsilon_{12} & \varepsilon_{13} \\ \varepsilon_{21} & \varepsilon_{22} & \varepsilon_{23} \\ \varepsilon_{31} & \varepsilon_{32} & \varepsilon_{33} \end{pmatrix} \tag{2.2}$$

The *ijkl* subscripts can each have a value of either 1, 2 or 3; these represent the three orthogonal directions of the Cartesian frame (*x,y,z*) [2].

For Hooke's law to be obeyed, the relative amplitude of the propagating waves must be small, so as not to exceed the elastic limit of the material. It is also a requirement that the ultrasonic wavelength λ, obeys the inequality $\lambda >>$ atomic scale (~Å) [3]. The range of ultrasonic frequencies used in this thesis covers the frequency range of 50 kHz –10 MHz which clearly satisfies the inequality $\lambda >>$ ~*nm*. The grain sizes in the sheet metal samples investigated are also $<< \lambda$, and so the samples will clearly act as a continuum displaying macroscopic properties, obeying Hooke's law.

The stress and strain tensors given by equation 2.2 are symmetric. For example, it can be shown that [2]:

$$\sigma_{12} = \sigma_{21} \tag{2.3}$$

Using this symmetry argument and applying it to the matrices defined in equation 2.2 reduces the corresponding tensors such that:

$$\sigma_{ij} = \begin{pmatrix} \sigma_{11} & \frac{1}{2}\sigma_{12} & \frac{1}{2}\sigma_{13} \\ \frac{1}{2}\sigma_{12} & \sigma_{22} & \frac{1}{2}\sigma_{23} \\ \frac{1}{2}\sigma_{13} & \frac{1}{2}\sigma_{23} & \sigma_{33} \end{pmatrix} \qquad \varepsilon_{ij} = \begin{pmatrix} \varepsilon_{11} & \frac{1}{2}\varepsilon_{12} & \frac{1}{2}\varepsilon_{13} \\ \frac{1}{2}\varepsilon_{12} & \varepsilon_{22} & \frac{1}{2}\varepsilon_{23} \\ \frac{1}{2}\varepsilon_{13} & \frac{1}{2}\varepsilon_{23} & \varepsilon_{33} \end{pmatrix} \tag{2.4}$$

Before detailing the governing equations of the ultrasonic wave, it is desirable to apply the matrix notation to these tensors. The six transformations are defined by the set of equations 2.5.1-5.6 [4]:

$$\sigma_{11} = \sigma_1 \tag{2.5.1}$$

$$\sigma_{22} = \sigma_2 \tag{2.5.2}$$

$$\sigma_{33} = \sigma_3 \tag{2.5.3}$$

$$\sigma_{23} = \sigma_{32} = \sigma_4 \tag{2.5.4}$$

$$\sigma_{13} = \sigma_{31} = \sigma_5 \tag{2.5.5}$$

$$\sigma_{12} = \sigma_{21} = \sigma_6 \tag{2.5.6}$$

These transformations are also applicable to the symmetric strain tensor. Reducing the coefficient notation for the stress and strain tensors is used to simplify Hooke's law, which now takes the form:

$$\sigma_i = c_{ij}\varepsilon_j \tag{2.6}$$

The stress and strain tensors simply become a 1x6 column matrix. The implication of this is that the elasticity tensor is reduced from the $3 \times 3 \times 3 \times 3$ c_{ijkl} tensor to a 6×6 c_{ij} square matrix, with 36 coefficients instead of 81. This new elasticity 2nd rank tensor is given in equation 2.7:

$$c_{ij} = \begin{pmatrix} c_{11} & c_{12} & c_{13} & c_{14} & c_{15} & c_{16} \\ c_{21} & c_{22} & c_{23} & c_{24} & c_{25} & c_{26} \\ c_{31} & c_{32} & c_{33} & c_{34} & c_{35} & c_{36} \\ c_{41} & c_{42} & c_{43} & c_{44} & c_{45} & c_{46} \\ c_{51} & c_{52} & c_{53} & c_{54} & c_{55} & c_{56} \\ c_{61} & c_{62} & c_{63} & c_{64} & c_{65} & c_{66} \end{pmatrix} \tag{2.7}$$

where c_{ij} are the elastic stiffness constants.

Again, tensor symmetry identities are valid, such that $\sigma_{ij} = \sigma_{ji}$, and therefore equation 2.7 can be simplified further to an upper triangular matrix. There are thus twenty one independent elastic stiffness coefficients that fully describe the elasticity of an anisotropic sample with a regular symmetry.

There are three symmetry cases of particular interest for aluminium and steel sheet metal samples, namely the isotropic symmetry case, cubic symmetry and sheets displaying orthorhombic (rolled) symmetry [5]. The individual aluminium and steel crystals are cubic; face-centred cubic for aluminium and austenitic steel and body-centred cubic for ferritic steel [6, 7]. Aggregates of cubic crystallites can exhibit a macroscopic symmetry that is isotropic, cubic or orthorhombic. Cubic can be thought of as a sub-set of orthorhombic. The particular macroscopic anisotropy (or isotropy) exhibited by an aggregate of grains is dependent on the crystallographic alignment of the grains, which can be influenced by working processes such as rolling (see chapter 5).

An isotropic sheet is defined by just two elastic stiffness constants. A sheet adhering to cubic symmetry can be described by three elastic stiffness constants, and orthorhombic symmetry is defined by nine elastic stiffness constants. Equation 2.8 shows the configuration of the isotropic and cubic elasticity tensor where $c_{44} = \frac{1}{2}(c_{11} - c_{12})$ for isotropic symmetry. For samples displaying cubic symmetry, the anisotropy is quantified by the anisotropy parameter *c*, which is defined by $c = c_{11} - c_{12} - 2c_{44}$ [8].

$$c_{ij} = \begin{pmatrix} c_{11} & c_{12} & c_{12} & 0 & 0 & 0 \\ c_{12} & c_{11} & c_{12} & 0 & 0 & 0 \\ c_{12} & c_{12} & c_{11} & 0 & 0 & 0 \\ 0 & 0 & 0 & c_{44} & 0 & 0 \\ 0 & 0 & 0 & 0 & c_{44} & 0 \\ 0 & 0 & 0 & 0 & 0 & c_{44} \end{pmatrix} \tag{2.8}$$

The elasticity tensor for rolled sheet, which has enforced orthorhombic symmetry, is given here by equation 2.9 [2, 5]:

$$c_{ij} = \begin{pmatrix} c_{11} & c_{12} & c_{13} & 0 & 0 & 0 \\ c_{12} & c_{22} & c_{23} & 0 & 0 & 0 \\ c_{13} & c_{23} & c_{33} & 0 & 0 & 0 \\ 0 & 0 & 0 & c_{44} & 0 & 0 \\ 0 & 0 & 0 & 0 & c_{55} & 0 \\ 0 & 0 & 0 & 0 & 0 & c_{66} \end{pmatrix} \quad (2.9)$$

The elastic stiffness coefficients c_{21}, c_{31} and c_{32} are equivalent to c_{12}, c_{13} and c_{32} respectively, and are only shown here for completeness.

Equations 2.8 and 2.9 have been displayed to show that although the numbers of independent coefficients increases with the changes in symmetry, the same spaces are occupied in the elasticity tensor for each of the isotropic, cubic and orthorhombic symmetry cases. For a weakly anisotropic sheet metal which possesses orthorhombic symmetry, the elastic stiffness constants could produce values that return an elastic stiffness tensor that approximately represents a sheet metal possessing cubic symmetry. This issue will be assessed in further detail in the results chapters.

2.2.2 – The Christoffel equation for anisotropic media

The ultrasonic response in rolled sheet metal is inherently elastically anisotropic due to the deformation and symmetry enforced by working. This is discussed in more detail in chapter 5. Therefore, it is important to express equations of motion for an ultrasonic wave in the anisotropic case.

In an infinite anisotropic sheet displaying homogeneity in the anisotropy, we can assume that Newton's law is the governing wave equation, and is given by [5]:

$$\frac{\partial \sigma_{ij}}{\partial x_j} = \rho \ddot{u}_i \quad (2.10)$$

Combining this with Hooke's law (equation 2.1) leads to:

$$\rho \ddot{u}_i = c_{ijkl}, \qquad \frac{\partial \varepsilon_{kl}}{\partial x_j} = c_{ijkl}\varepsilon_{kl,j} \tag{2.11}$$

With knowledge of the strain displacement and applying symmetry arguments $c_{ijkl} = c_{jikl}$, further manipulation can lead to an expression for the ultrasonic plane wave propagation. This is known as the Christoffel equation and is given by [5]:

$$(\rho\omega^2\delta_{il} - c_{ijkl}k_j k_k)u_l = 0 \tag{2.12}$$

Following from this, the Christoffel tensor Γ_{il} is defined by:

$$\Gamma_{il} = \lambda_{il} = c_{ijkl}n_j n_k \tag{2.13}$$

Here n_j and n_k are directional cosines normal to the wavefront. This implies that equation 2.12 can be simplified to:

$$k^2\Gamma_{il}u_l - \rho\omega^2 u_l = 0 \tag{2.14}$$

which in full tensor form becomes:

$$k^2\begin{bmatrix}\Gamma_{11} & \Gamma_{12} & \Gamma_{13}\\ \Gamma_{21} & \Gamma_{22} & \Gamma_{23}\\ \Gamma_{31} & \Gamma_{32} & \Gamma_{33}\end{bmatrix}\begin{bmatrix}u_x\\ u_y\\ u_z\end{bmatrix} - \rho\omega^2\begin{bmatrix}u_x\\ u_y\\ u_z\end{bmatrix} = 0 \tag{2.15}$$

In the cases when $i=l$, this leaves three equations which provides three real roots. In non-trivial cases, the determinant of equation 2.14 is set to 0 to solve the problem, as shown in equation 2.16:

$$\left|k^2\Gamma_{il} - \rho\omega^2\right| = 0 \tag{2.16}$$

2.2.3 – Group and phase velocity

There are two characteristic wave velocities that must be considered, namely the phase velocity c_p, and the group velocity c_g.

The *phase velocity* is recognisable from the common relationship given by equation 2.17 which links the velocity to the wavelength and frequency of the propagating wave [9].

$$c_p = f\lambda \tag{2.17}$$

where f is the frequency and λ is the wavelength. This velocity c_p can be understood as the velocity of an individual wave that maintains a constant phase. Equation 2.17 is derived from the application of Newton's 2nd law on considering the displacement of a small element of a propagating wave.

Another relationship integral to the understanding ultrasonics is given in equation 2.18;

$$k = \frac{2\pi}{\lambda} = \frac{\omega}{c_p} \tag{2.18}$$

where k is the wave number and ω is the angular frequency.

A harmonic wave can be defined as a function of position and time in the form shown in equation 2.19 [10];

$$u = A\cos(kx - \omega t) \tag{2.19}$$

where u is the displacement, A is the amplitude, x is the relative position along the propagation direction from the initial position x=0, and t is time.

The *group velocity* is particularly important to consider for wideband transmission of ultrasound, where numerous waves with similar velocities will propagate. The acoustic energy of a wideband wave packet and the resultant characteristic average velocity of this group of waves is defined as the group velocity.

Using the definition of *Rose* [5], it is convenient to consider two waves with characteristic frequencies and wave numbers close together, namely waves with the properties (ω_1,k_1) and (ω_2,k_2).

The group velocity c_g is determined from the ratio in the change in these frequencies and wave numbers, and is given by:

$$c_g = \frac{d\omega}{dk} \tag{2.20}$$

In contrast, the phase velocity is given by (see equation 2.18):

$$c_p = \frac{\bar{\omega}}{\bar{k}} \tag{2.21}$$

The broadband generation used in this experimental work in particular here will of course be more complex than just the considered two harmonic waves propagating simultaneously here, though equations 2.20 and 2.21 are valid.

Making $\bar{k}$ the subject in equation 2.21 and substituting into equation 2.20, means that the group velocity can be expressed in terms of the phase velocity by:

$$c_g = {c_p}^2 \left[c_p - \omega \frac{dc_p}{d\omega} \right]^{-1} \tag{2.22}$$

2.3 – Dispersion

Dispersion of a propagating ultrasonic wave pulse is essentially reflected in the discrepancy in the corresponding values of the group and phase velocity defined by equations 2.20 and 2.21 [11]. To simplify data analysis and to improve accuracy and reliability of results, it is often desirable to perform ultrasonic measurements in a frequency regime that minimises dispersion effects where possible. Of course, there are situations where one wishes to measure the dispersion of a wave in order to relate it to a physical measurement [12, 13].

Dispersion effects in the measurements described in this thesis have been considered and are described in chapter 7.

There are other factors that can affect the final waveform detected including attenuation due to geometric diffraction effects, absorption and scattering, which occurs predominately at grain boundaries in metals. Attenuation is addressed in chapter 6. Beam steering and beam spread are also issues that need to be addressed and minimised. These effects were considered when specifying the EMAT designs used in the experiments (EMAT designs have a major influence on beam spread), and are again discussed in chapter 7.

2.4 – Wave propagation in anisotropic media

Isotropic media can be described by just two constants, as shown previously in equation 2.8. In this instance the elasticity is fully defined by the single crystal elastic stiffness constants c_{11} and c_{12}. Alternatively the isotropic state can also be described by the Lamé constants λ and μ, which have been derived to be equivalent to:

$$\lambda = c_{12}^{x} \tag{2.23}$$

$$\mu = \frac{c_{11}^{x} - c_{12}^{x}}{2} \tag{2.24}$$

Here the *x* superscript denotes the values are the single crystal constants. Rolled metallic sheet is inherently anisotropic however, and therefore more coefficients are needed to describe the elastic anisotropy.

Elastic anisotropy is conveniently described by the Crystallite Orientation Distribution Function (ODF) $w(\xi,\psi,\varphi)$ [14]. The application of a probability distribution to this continuous function is a property of the ODF; this can identify the dominance of certain orientations within anisotropic samples.

The probability distribution, as a function of Roe-Euler angles, is given by:

$$\int_0^{2\pi}\int_0^{2\pi}\int_{-1}^{1} w(\xi,\psi,\varphi)d\xi d\psi d\varphi = 1 \tag{2.25}$$

Euler angles are three angles of rotation that define the orientation of an individual crystallite. These angles are discussed in chapter 4. Equation 2.25 is an integral of all crystallites within a sample volume, integrating over all possible orientations these crystallites could take.

For the isotropic case, each individual crystallite has an equally likely chance of possessing any given orientation defined by (θ,ψ,φ), with $\xi = \cos\theta$. In the existence of elastic anisotropy, a consequence of rolling, certain orientations will be more abundant, and some will be reduced due to the resulting plastic deformation (refer to chapter 5). Determining these orientations can be achieved via time-consuming diffraction techniques.

It is therefore convenient to expand equation 2.25 using a series of generalized spherical harmonics, hence $w(\xi,\psi,\varphi)$ can be expressed by:

$$w(\xi,\psi,\varphi) = \sum_{l=0}^{\infty}\sum_{m=-1}^{1}\sum_{n=-1}^{1} W_{lmn} Z_{lmn}(\xi)\exp(-im\psi)\exp(-in\varphi) \tag{2.26}$$

$Z_{lmn}(\xi)$ is the generalization of the associated Legendre function with the W_{lmn} term identified as the Orientation Distribution Coefficients (ODCs); these are of particular interest. The ODCs are quantitative texture coefficients. Previous work by *Roe* [14] and *Sayers* [15] amongst others, has shown that for cubic crystallites, the number of independent non-zero ODCs that exist reduces dramatically from symmetry arguments.

There are just three ODCs that contribute to the ODF for aluminium and steel samples [16, 17], and it has been shown they can be determined using ultrasound velocity measurements. These are W_{400}, W_{420} and W_{440}. Though this does not fully characterize the texture unlike diffraction methods, these three ODCs are of great importance for making formability predictions. Calculations have been completed by previous workers showing that only l = 4 terms contribute when considering ultrasonic measurements [14, 15]. For orthorhombic symmetry sheet, W_{lmn} = 0 when either m or n are odd (and also for l = 0). The

ODF cannot be imaginary, and hence this property further restricts the values that *m* and *n* can be.

The three ODCs that can be calculated from ultrasonic measurements each give different levels of information regarding the anisotropy present. The W_{400} term is a measure of resistance to deep drawing. The W_{420} coefficient gives information on the level of 2-fold symmetry present; effectively a measure of the existence of double earring within the sheet due to the texture. W_{440} is similar, describing the magnitude of the 4-fold symmetry present in the sheet [14, 15].

2.5 – Wave modes of interest

The experimental work completed for this thesis utilises two different waveforms: the shear wave and the Lamb wave. The following describes briefly the characteristics of these waves and some of the governing equations that define its propagation together with the theory described earlier in this chapter.

2.5.1 – Shear wave

The shear wave lattice deformation occurs in a direction orthogonal to the propagation direction of the wave [18]. The experimental work here looks at the specific case of the horizontal shear wave, commonly labelled SH.

The velocity of a shear wave, c_T, (equation 2.27) for homogeneous and isotropic media can be expressed in terms of the square root of the shear modulus (G) divided by the density (ρ) of the material it propagates in [19].

$$c_T = \sqrt{\frac{G}{\rho}} \tag{2.27}$$

Expressions for the velocity of shear waves with respect to a sheet with orthorhombic symmetry have been derived, and are stated by *Sayers* [15] amongst others. These are of

particular relevance given the experimental work completed is done exclusively with rolled sheet metals.

For an SH wave propagating in a rolled anisotropic sheet along the rolling and transverse directions (chapter 5) respectively, and polarised orthogonal to these propagation directions, the velocities can be calculated using equations 2.28 and 2.29, with c_{44}^{X} a single crystal elastic stiffness constant:

$$v_{SH_y} = \sqrt{\frac{\left(c_{44}^{X} + c\left[\frac{1}{5} - \frac{16}{35}\sqrt{2}\pi^2\left(W_{400} - \sqrt{\frac{5}{2}}W_{420}\right)\right]\right)}{\rho}} \tag{2.28}$$

$$v_{SH_z} = \sqrt{\frac{\left(c_{44}^{X} + c\left[\frac{1}{5} - \frac{16}{35}\sqrt{2}\pi^2\left(W_{400} + \sqrt{\frac{5}{2}}W_{420}\right)\right]\right)}{\rho}} \tag{2.29}$$

For a horizontal shear wave propagating through the thickness of an anisotropic sheet, the velocity for a wave polarised in the rolling and transverse directions are given by equations 2.30 and 2.31:

$$v_{SH_{rolling}} = \sqrt{\frac{\left(c_{44}^{X} + c\left[\frac{1}{5} - \frac{16}{35}\sqrt{2}\pi^2\left(W_{400} + \sqrt{\frac{5}{2}}W_{420}\right)\right]\right)}{\rho}} \tag{2.30}$$

$$v_{SH_{transverse}} = \sqrt{\frac{\left(c_{44}^{X} + c\left[\frac{1}{5} + \frac{4}{35}\sqrt{2}\pi^2\left(W_{400} - \sqrt{70}W_{420}\right)\right]\right)}{\rho}} \tag{2.31}$$

For equations 2.28 – 2.31, c is the anisotropy coefficient, ρ is the density of the sheet and W_{lmn} are the ODCs.

For an isotropic metal, W_{lmn} = 0, and the anisotropy factor c = 0, therefore the equations from 2.28 – 2.31 reduce to:

$$c_T = \sqrt{\frac{c_{44}^X}{\rho}} \tag{2.32}$$

Hence c_{44} is equivalent to the shear modulus G as stated by equation 2.24. Given the samples worked with in this investigation are all anisotropic, equations 2.28 – 2.31 will be considered as they give in essence a better and more complete description of the wave velocity.

2.5.2 – Lamb wave

The other waveform employed in this investigation is the zeroth order symmetric (S_0) Lamb wave mode. A Lamb wave is a plate wave and is unique in that it propagates with both longitudinal and transverse plane wave components [20]. It displays a symmetrical vertical particle displacement orthogonal to the central plane, which is referred to as a quasi-longitudinal wave. For the S_0 Lamb wave, the most desirable property is that the in-plane energy distribution for low frequencies is evenly distributed across the wavefront, which implies a through-thickness average of the material properties is measured.

The Lamb-Rayleigh wave equation is given by equations 2.33 and 2.34 which represent the symmetric and antisymmetric modes respectively; the derivation to which is given by *Rose* [5]:

$$\frac{\tan(qh)}{\tan(ph)} = -\frac{4k^2pq}{\left(q^2-k^2\right)^2} \tag{2.33}$$

$$\frac{\tan(qh)}{\tan(ph)} = -\frac{\left(q^2-k^2\right)^2}{4k^2pq} \tag{2.34}$$

where h is half of the sheet thickness d, and the coefficients p and q are given by:

$$p = \sqrt{\left(\frac{\omega}{c_L}\right)^2 - k^2} \tag{2.35}$$

$$q = \sqrt{\left(\frac{\omega}{c_T}\right)^2 - k^2} \tag{2.36}$$

with c_L the longitudinal velocity. The sheet thickness is a very important parameter to consider in Lamb wave propagation behaviour. The ratio of the sheet thickness d to the wavelength λ determines the velocity of the Lamb wave. It can also be concluded from equations 2.33 – 2.36 that the Lamb waves are dispersive (see section 2.3).

To calculate the dispersion for given frequencies and different sheet material and thicknesses, one can analyse dispersion curves, and phase and group velocity profiles for the relevant media [5]. These are typically represented by a plot of velocity against *f.d*, where *f.d* is the product of the frequency and sheet thickness. Figure 2.1 is a graph representing the phase and group velocities for an isotropic Aluminium sheet. As can be seen, in the low frequency limit $\left(f.d \to 0\right)$ there is negligible dispersion [5] (Figure 7.5 displays a close up of this area of interest).

Note in figure 2.1 that c_g and c_p converge for higher values of the *f.d* product. These are tending to the Rayleigh wave velocity c_R. Rayleigh waves are surface waves that can propagate in thicker plate where thickness >> λ.

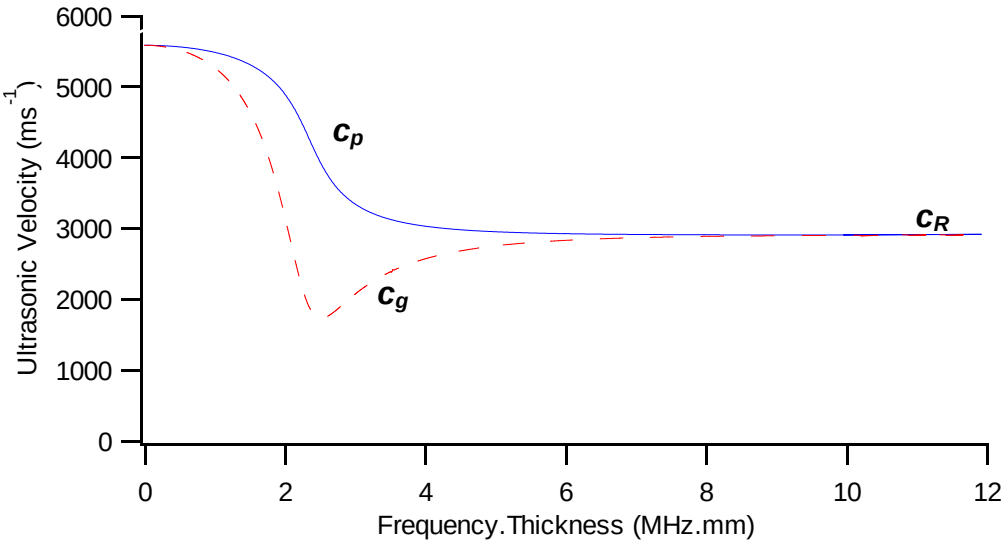

Figure 2.1: Graph showing phase and group velocity for the symmetric S_0 mode Lamb wave in an isotropic aluminium sheet. The blue line indicates the phase velocity c_p and the red line represents the corresponding group velocity c_g for different frequency-thickness products. It is evident at small products for thin sheet and/or in the low frequency limit, that dispersion is negligible.

The velocity of an S_0 Lamb wave in a sheet displaying elastic anisotropy has been derived by *Thompson et al* [16]. For a sheet metal, stress components in the normal direction out of the plane of the sheet, namely σ_{13}, σ_{23} and σ_{33}, are equal to zero at the surface of a sheet. With the initial application of the Christoffel equation (equation 2.16), the phase velocity of an S_0 mode Lamb wave as a function of angle subtended from the rolling direction can be derived, and can be given by (to first order approximation):

$$\rho v_{S_0}^2 = A + BW_{400} + CW_{420}\cos(2\theta) + DW_{440}\cos(4\theta) \tag{2.37}$$

where:

$$A = \left(1 - \frac{\lambda^2}{(\lambda+2\mu)^2}\right)(\lambda+2\mu) \tag{2.38}$$

$$B = \frac{4c\pi^2}{35}\sqrt{2}\left(3 + \frac{8\lambda}{(\lambda+2\mu)} + \frac{8\lambda^2}{(\lambda+2\mu)^2}\right) \tag{2.39}$$

$$C = -\frac{4c\pi^2}{35} 4\sqrt{5}\left(1 + \frac{2\lambda}{\lambda + 2\mu}\right) \tag{2.40}$$

$$D = \frac{4c\pi^2}{35} 2\sqrt{35} \tag{2.41}$$

2.6 – References

1. *Achenbach JD, Wave propagation in elastic solids, North-Holland Publishing, 1973*

2. *Nye JF, Physical Properties of Crystals, Oxford Press, 1957*

3. *Auld BA, Acoustic fields and waves in solids, 2nd edition, Krieger publishing, 1990*

4. *Wright SI, J. Appl. Cryst., **27**, 1994, pp. 794-801*

5. *Rose JL, Ultrasonic waves in solid media, Cambridge University Press, 1999*

6. *Honeycombe RWK, Steels – Microstructure and Properties, Arnold Publishing,1981*

7. King F, Aluminium and its Alloys, Ellis Horwood Publishing, 1987

8. *Davies GJ, Goodwill DJ, Kallend JS, Metallurgical Transactions, **3**, 1972, pp. 1627-1631*

9. *Mason WP, Physical Acoustics and the Properties of Solids, D. Van Nostrand Company Inc., 1958*

10. *Rayleigh JWS, The Theory of Sound - Volume 1 of 2, second edition, Dover Publications, 1945 (reprint)*

11. *Ye L, Lin Y, Su Z, Smart Mater. Struct., **15**, 2006, pp.839-849*

12. *Challis RE, Alper T, Cocker RP, Holmes AK, White JDH, Ultrasonics, **29(1)**, 1991, pp. 22-28*

13. *Challis RE, Cocker RP, Ultrasonics, **33(4)**, 1995, pp. 311-319*

14. *Roe R-J, Journal of Applied Physics, **36**, 1965, pp. 2024-2031*

15. *Sayers CM, J. Phys. D: Appl. Phys., **15**, 1982, pp. 2157-2167*

16. *Li Y, Thompson RB, J.Acoust. Soc. Am., **91**, 1992, pp. 1298-1309*

17. *Dixon S, Edwards C, Palmer SB, J. Phys. D: Appl. Phys., **35**, 2002, pp. 816-824*

18. *Krautkrämer H, Krautkrämer J, Ultrasonic Testing of Materials, 4th edition, Springer-Verlag, 1990*

19. *Filipczynski L, Ultrasonic Methods of Testing Materials, Butterworths, 1966*

20. *Viktorov IA, Rayleigh and Lamb waves: physical theory and applications, Plenum Press, 1967*

CHAPTER 3

Electromagnetic Acoustic Transducers

3.1 – Non-destructive transduction of ultrasound

There are a variety of ways to generate and detect ultrasonic waves in a metallic sample, the most common being the piezoelectric transducers (PET). Piezoelectric transducers are the most widely used ultrasonic transducer for NDT applications, for both generation and detection. Usually made with piezoelectric ceramics such as Barium Titanate and Lead Zirconium Titanate (PZT), they utilize the asymmetry in the crystal structure to create electrical charges by subjecting a piezoelectric material to a mechanical stress [1]. The inverse is also true; applying a voltage to a piezoelectric material will induce a mechanical stress, making generation and detection of ultrasonic waves possible. PETs can be manufactured on a very small scale (~ cm dimensions). They compare better financially to other ultrasonic sources. Ultrasound generation efficiency in particular is extremely good for PETs.

The major disadvantage of PETs is the requirement for a couplant to be used to minimise the difference in acoustic impedance between the test material and air [2]. Without the couplant, minimal energy will be transmitted to the specimen under investigation. Without going into great detail, it follows that with the requirement for a couplant, it creates difficulties in maintaining consistency when conducting similar experiments, leading to difficulties in obtaining comparative results. Any contact will load the sample under investigation, with the generated waves propagating through all the elements of the transducer and couplant; the numerous echoes from each interface will interfere with the waveform of interest, influencing time-of-flight and attenuation measurements in particular. The couplant will possess different ultrasonic propagation properties to the test material, which also makes data analysis more complex. Application of a couplant also restricts the speed of data

acquisition in an online or in-service environment. With such a variety of problems involved with this contact transducer, other alternatives should be looked at too.

Air-coupled transducers have been used for investigations on materials and components that are otherwise difficult to inspect by other NDT applications, such as aerospace composites and wood [3]. The major difficulty is transmitting the mechanical energy of the transducer to the sample and back again for detection due to the significant difference in acoustic impedance between air and the test piece, creating large reflection losses. Developments in impedance matching layers that encourage a better transmission to air, generation of high sound pressures and great advances in digital filtering and low-noise preamplifiers have made it possible to receive signals with acceptable SNR.

Lasers offer another source for generating and detecting ultrasound. Pulsed lasers can provide power of the order ~*MW*, supplied to the sample from a pulse over a few *ns* [4]. This high intensity energy will cause a rapid heating of an element of the surface, with the resulting mechanical stress and heat dissipation resulting in an ultrasonic wave. The laser spot size can be minimized or broadened with the appropriate focussing optics. Depending on the level of this focus, the energy density of the pulsed laser can be found above or below the ablative threshold. If the laser is fully focussed, the energy density will be large such that a plasma will form at the surface at impact. This is known as the ablative regime and will create surface defects; hence it is not desirable for truly NDT applications. Reducing the energy density so that a plasma does not form will maintain the microstructure of the test piece and is called thermoelastic generation. This provides a non-destructive method of producing ultrasound in a sample. Common pulsed lasers used for ultrasonic generation include the Nd:YAG and CO_2 lasers.

Lasers can be utilised in ultrasound detection too. Interferometry can be used to detect the interference and deflection of a laser beam caused by the elastic deformation of a sample supporting a propagating wave. Such interferometers include the Michelson and Fabry-Perot [5]. Amplitude variation detectors, such as knife-edge detectors, work on the principle that the reflection of a laser beam irradiating a sample will move as an ultrasound

wave moves in the area under investigation [6]. The change in the reflected beam will give information on the wave amplitude.

The laser techniques can work at large standoff distances, which is a major advantage. They can also work at elevated temperatures. Generally lasers are expensive and Class IV Nd:YAG lasers for example can be very dangerous. Other disadvantages include the difficulty in the optic alignment and the criticality of surface finish on results too.

Bearing all this in mind, another transducer which uses electromagnetic coupling, namely the Electromagnetic Acoustic Transducer (EMAT), offers a good alternative for NDT investigations on rolled metallic sheet, and it is these transducers which have been selected to be used.

3.2 – Electromagnetic Acoustic Transducers

The Electromagnetic Acoustic Transducer (EMAT) provides an excellent option for NDT applications on metallic samples. They are coupled to the sample by electromagnetic waves, and therefore provide a non-contact solution to generating ultrasound [7]. EMATs can work at lift offs of the order of several millimetres above a sample surface, though efficiency falls with increasing separation between the conductive sample and transducer. Experiments utilising EMATs can be completed at elevated temperatures and in hostile environments [8]. The main disadvantages include they are restricted to only samples with good electrical conductivity, or with high magnetostriction such as the magnetite oxide scale often found on high temperature boiler tubes [9]. The transduction efficiency of EMATs is usually orders of magnitude lower than PETs, meaning that there needs to be a clear justification for using EMATs.

The ultrasonic measurements described in this thesis were done exclusively using EMATs. Although there are other EMAT designs available, such as ferrite-enhanced EMATs [10] or using EMATs that employ electromagnets [11], the EMATs used in this study are all consistent with the following described configuration.

The EMAT comprises of two main components: a coil and a permanent magnet [12]. The inductive coil is placed adjacent to the sample surface and positioned below a permanent NdFeB magnet arrangement. The magnetic flux density at the surface of the NdFeB magnets is typically between 0.5 T to 1 T. Changes in the geometry and arrangement of the coil and also the magnet configuration, allows for the generation of different wave modes and polarisations, depending on the desired application. The magnets, the coil and the electronics need to be housed in a suitable case and brass is used often, because it is easily machinable, provides good electrical screening and is non-magnetic. Figure 3.1 shows a photograph of an EMAT typically used in the work for this thesis, with figure 3.2 giving a simple schematic diagram displaying the components of an EMAT.

Figure 3.1: Photograph of a typical EMAT used for this study. The brass casing houses the permanent magnet and coil. The brass casing is 50 mm tall with a diameter of 45 mm.

Generating ultrasound using an EMAT is dependent on coupling electromagnetically to the sample. This is achieved by the induction of eddy currents in the sample skin-depth as a consequence of a time-varying current passing through the generation coil, and also the introduction of the static and dynamic magnetic fields due to the permanent magnet and coil.

As a result of this electromagnetic coupling, two mechanisms contribute to the force that is required to generate the subsequent ultrasonic wave. These are the Lorentzian and magnetoelastic mechanisms. The magnetoelastic mechanism is made up of contributions due to a magnetization force and a magnetostriction force. In this work, the Lorentzian

mechanism is the dominant contributor in both the aluminium and steel samples studied. Both mechanisms are discussed in detail in sections 3.2.1.3 - 3.2.1.5 after the electromagnetic coupling is formally introduced.

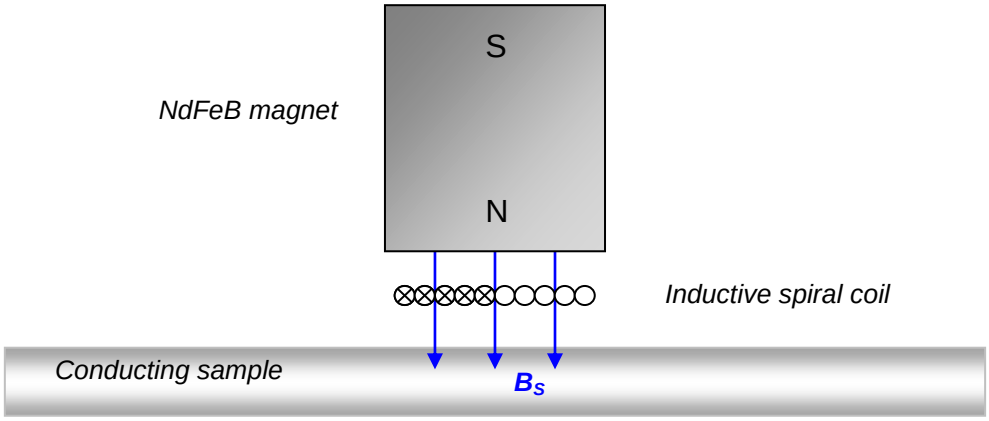

Figure 3.2: Schematic diagram of an EMAT and its typical components. B_S is the static magnetic field contribution from the permanent NdFeB magnet. There will also be a dynamic magnetic field contribution (B_D) from the coil, which is not shown here as this is dependent on the coil geometry.

Before describing the electrical coupling mechanism and ultrasound generation in more detail, the electromagnetic framework is needed to fully describe and understand the electromagnetic interactions.

3.2.1 – EMAT operation theory

3.2.1.1 - Maxwell's equations

In describing the electromagnetic interactions that produce the coupling mechanism between the EMAT and an electrically conductive metallic sample, the electromagnetic framework defined by Maxwell's equations is required [13], as listed in equations 3.1-3.6.

$$\nabla.\mathbf{D} = \rho \tag{3.1}$$

$$\nabla.\mathbf{B} = 0 \tag{3.2}$$

$$\nabla \times \mathbf{E} = -\frac{\partial \mathbf{B}}{\partial t} \tag{3.3}$$

$$\nabla \times \mathbf{H} = \mathbf{j} + \frac{\partial \mathbf{D}}{\partial t} \tag{3.4}$$

$$\mathbf{D} = \varepsilon_0 \varepsilon_r \mathbf{E} \tag{3.5}$$

$$\mathbf{B} = \mu_0 \mu_r \mathbf{H} \tag{3.6}$$

Here ***D*** is the electric displacement, ***B*** is the magnetic flux density, ***E*** is the electric field and ***H*** is the magnetic field intensity. The parameter ε is the electric permittivity and μ the magnetic permeability. The subscripts $_0$ and $_r$ refer to the free space and the relative values respectively. These equations link the electric and magnetic fields to the charge and current densities $\boldsymbol{\rho}$ and ***j*** respectively.

The following sections specifically detail the process of how an EMAT produces an ultrasonic response. To couple electromagnetically the sample to the EMAT, an image or eddy current needs to be generated in the sample.

3.2.1.2 – Eddy currents, *J* and *H*

When passing an alternating current through the inductive coil of an EMAT placed close to (within a few millimetres) a conducting surface, an image current, or eddy current, is induced within the sample [14]. Figure 3.3 shows a diagram of the induction of an eddy current. These currents are concentrated in the near-surface of the test sample, predominantly within the electromagnetic skin-depth δ. The magnitude and frequency of the eddy currents are dependent on the magnitude and rate of change in magnetic flux from the time-varying current in the generation coil. The induction of eddy currents is therefore insensitive to the presence of the static magnetic field produced by the permanent NdFeB magnet [15].

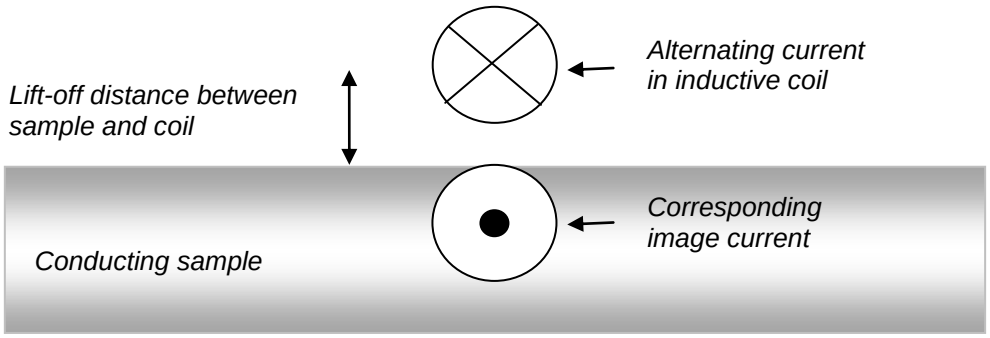

Figure 3.3: Diagram illustrating the generation of an image eddy current at the surface of a conducting sample when in the vicinity of an inductive time-varying current carrying wire.

The integration of the eddy current within the skin-depth effectively acts externally as though it is approximately a current out of phase with the current in the generation coil. In order to understand and fully classify the generation of the eddy currents and to quantify the corresponding current density, it is necessary to refer to Maxwell's equations, initially in particular equation 3.3, also known as Faraday's law. This states that with the introduction of an alternating current in the inductive coil that is in close proximity to a conducting sample, the associated time-varying magnetic field ***B*** that penetrates into a sample surface is related to the induced electric field ***E*** at the perimeter of this surface.

To visualise this more conveniently, Faraday's law can be manipulated and expressed in an integral form, the result of which is shown in equation 3.7:

$$-\int_{AREA} \frac{d\mathbf{B}}{dt}.dA = \int_{LINE} \mathbf{E}.dl \qquad (3.7)$$

Figure 3.4 illustrates the physical result of Faraday's Law in reference to just an EMAT coil and a conducting sample. The electromagnetic field from the coil does not instantaneously penetrate the sample surface unlike the transient dynamic ***B*** field. Via Faraday's law, one can calculate the ***E*** field at any moment in time from the ***B*** field present.

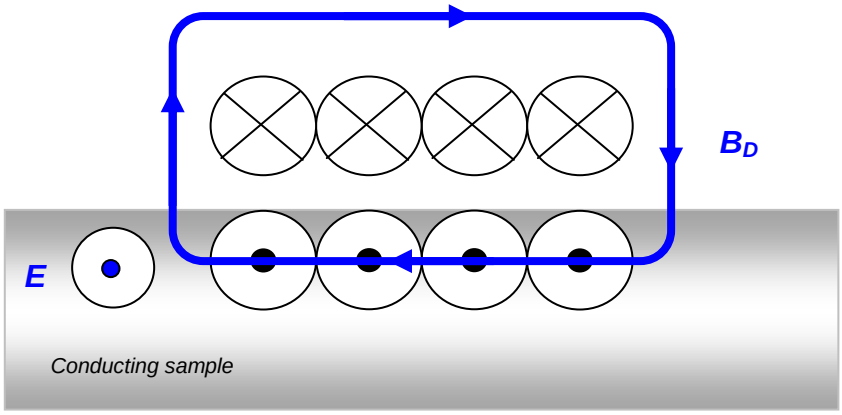

Figure 3.4: Diagram of a section from a spiral coil configuration EMAT. Highlighted is the image current, the resulting dynamic magnetic field B_D from the coil and also the induced E field at the surface of the conducting sample at this particular instant.

The delay in the electromagnetic field penetrating the surface of an electrical conductor can be rectified by making an assumption that the electromagnetic wave propagating from the EMAT coil to the sample surface can be approximated as a plane wave. The solution to this approximated plane wave for the ***E*** field is given by equation 3.8:

$$\mathbf{E} = \mathbf{E_0} \exp i(\omega t - kz + ikz) \tag{3.8}$$

where ***E*** is the electric field at a depth z below the surface, $\boldsymbol{E_0}$ is the electric field amplitude at the surface, t is the time with ω and k again the angular frequency and wave number respectively. For an infinite coil and sheet, it will follow that there would exist an infinite current plane in the coil, with the sheet being host to an infinite sheet current. It is under these assumptions, as used in the method of *Hirao* and *Ogi* [16] and the method that is followed here, that equation 3.8 will hold.

The "ikz" term in the exponential of equation 3.8 characterizes the attenuation of the electric field as it increases with penetration depth into the sample. From this equation the aforementioned skin depth δ, the depth where the amplitude of ***E*** reduces by *1/e*, can be determined. It can be shown that the skin depth is given by [14]:

$$\delta = \sqrt{\frac{2}{\mu_0 \mu_r \sigma \omega}} \tag{3.9}$$

σ is the electrical conductivity. The force exerted on the electrons within the sample is proportional to the induced ***E*** field and is given by:

$$\mathbf{F} = e\mathbf{E} \tag{3.10}$$

It intuitively follows then that the corresponding current density ***J*** within the conductor is also proportional to the ***E*** field. This relationship is defined by Ohm's law [17]:

$$\mathbf{J} = \sigma\mathbf{E} \tag{3.11}$$

Ohm's law provides a link between ***J*** and ***E***, and hence an equation analogous to equation 3.8, in terms of the current density, can be derived. This is given in equation 3.12:

$$\mathbf{J} = \mathbf{J_0} \exp i(\omega t' - kz - ikz) \tag{3.12}$$

Equation 3.12 gives the current density as a function of depth. It is important to note from this that not only does the amplitude of the current density decay with depth into the sample, but also the phase changes with depth too. The phase change has a linear dependence with depth in to the sample. The amplitude decays exponentially with depth.

For a sinusoidally varying current, the current density in the coil $\boldsymbol{J_{coil}}$, is related to the current density at the sample surface by:

$$\mathbf{J}_{coil} = \mathbf{J_0} \exp i\omega t \tag{3.13}$$

It then follows that the electric field at the surface of the sample is proportional to $\boldsymbol{J_0}$ by [14]:

$$\mathbf{E} \propto -\mathbf{J_0}(i\omega)\exp(i\omega t)$$

$$\Rightarrow \mathbf{E} \propto -\mathbf{J_0}\exp\left(i\left(\omega t - \frac{\pi}{2}\right)\right) \tag{3.14}$$

The electric field at the surface therefore lags the current density at the surface by $\frac{\pi}{2}$.

From here it can be deduced that the complete term for the current density apparent in a conducting sample due to an EMAT coil is given by:

$$\mathbf{J} = \mathbf{J_0}\exp\left(i\left(\omega t - \frac{\pi}{2}\right)\right)\exp\left(-\frac{z}{\delta}(1+i)\right) \tag{3.15}$$

The equations that define the relative change of phase and amplitude with the first two multiples of skin depth are therefore given by:

For $z = \delta$ $$\mathbf{J} = \mathbf{J_0}\exp(-(1+i)) \approx 0.37|\mathbf{J_0}| \tag{3.16}$$

For $z = 2\delta$ $$\mathbf{J} = \mathbf{J_0}\exp(-2(1+i)) \approx 0.14|\mathbf{J_0}| \tag{3.17}$$

The current density at a depth $\delta = z$ lags the current density at the surface by 1 radian (57.3˚), and at $2\delta = z$, the phase lag is equal to 2 radians (114.6˚).

With expressions for the electric field ***E*** (equation 3.8) and current density ***J*** (equation 3.15) generated by an inductive EMAT coil, an analysis of the dynamic magnetic field external to the sample can be completed.

Equation 3.4 links the external magnetic field intensity (***H***) to the current density (***J***) and electric field displacement (***D***). ***D*** = 0 for a current flowing through a conductor [14], hence reducing Maxwell' equation to:

$$\nabla \times \mathbf{H} = \mathbf{J} \tag{3.18}$$

This equation is equivalent to [14]:

$$\oint \mathbf{H}.dl = \oint \mathbf{J}.dA$$

$$\Rightarrow \mathbf{H} = \int_{z=0}^{z=\infty} \mathbf{J}.dz \tag{3.19}$$

The chosen integral path for equation 3.19 is depicted in figure 3.5.

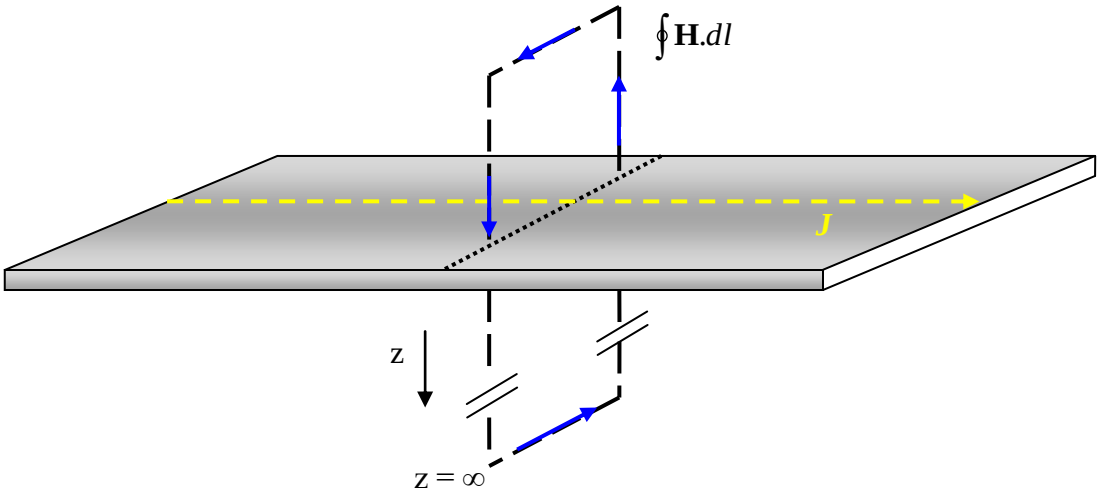

Figure 3.5: Diagram showing the preferred chosen path of the line integral in equation 3.19. The vertical lines cancel each other by symmetry arguments. Choosing a path where one of the horizontal integral lines is extended to a distance $z = \infty$ ***, the integral of the line an infinite distance away into the surface is zero.***

With the vertical lines when summed equalling zero by symmetry, choosing to complete the path with lines parallel to the sheet and extending one an infinite distance away such that the line integral there is also equal to zero, this allows us to determine the relationship between the external magnetic field ***H*** and the integral of the current density ***J*** within the surface enclosed by the path.

Substituting in the expression for ***J*** (equation 3.15) into equation 3.19 and performing the line integral of the described path yields an expression for ***H***:

$$\mathbf{H} = \mathbf{J_0} \exp\left(i\left(\omega t - \frac{\pi}{2} \right) \right) \delta \frac{\exp\left(-i\frac{\pi}{4} \right)}{\sqrt{2}} \tag{3.20}$$

Combining the exponential terms reduces the expression to:

$$\mathbf{H} = \mathbf{J_0} \exp(i\omega t) \delta \frac{\exp\left(-i\frac{3\pi}{4} \right)}{\sqrt{2}} \tag{3.21}$$

From this expression it can be deduced that the external dynamic magnetic field lags the current in the coil by $\frac{3\pi}{4}$ radians.

3.2.1.3 – Lorentz force mechanism

With an eddy current induced in the sample skin depth, generating an ultrasonic response is achieved via a Lorentz interaction between the eddy current and a magnetic field [18]. The Lorentz force is the major contributor to generating ultrasound in aluminium and steel samples for the transducers and samples used here, and is defined by:

$$\mathbf{F} = q.\mathbf{v} \times \mathbf{B} \tag{3.22}$$

When an $\boldsymbol{E}$ field is present in a conducting sample, each electron experiences a Coulomb force – e$\boldsymbol{E}$ (Equation 3.10). In the presence of the magnetic field $\boldsymbol{B_0}$ as is the case for an EMAT configuration, this means that equation 3.22 becomes:

$$\mathbf{F} = e.\mathbf{v_e} \times \mathbf{B}_0 \tag{3.23}$$

where $\boldsymbol{v_e}$ is the mean electron velocity. Figure 3.6 displays the Lorentz force due to the static magnetic field resulting from the permanent magnet, with figure 3.7 showing the Lorentz force as a result of the dynamic magnetic field due to the current-carrying inductive coil.

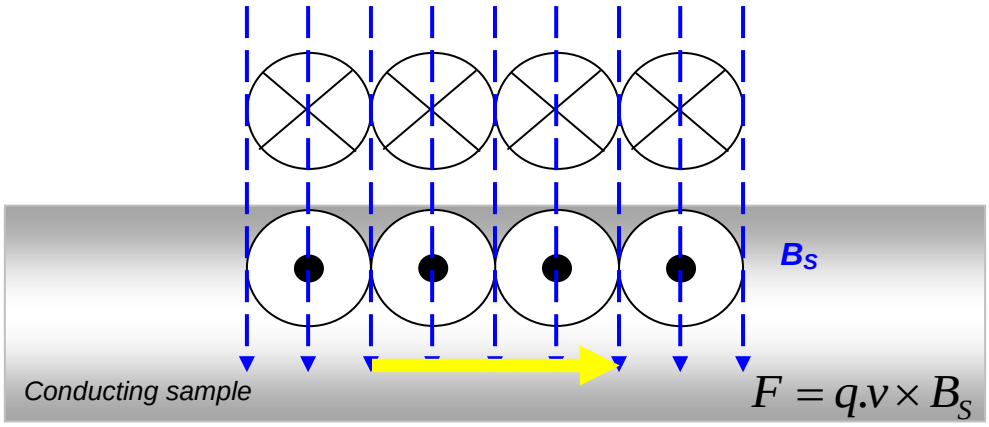

Figure 3.6: Diagram showing the Lorentz force contribution due to the static magnetic field and the eddy currents induced in the near-surface of the sample.

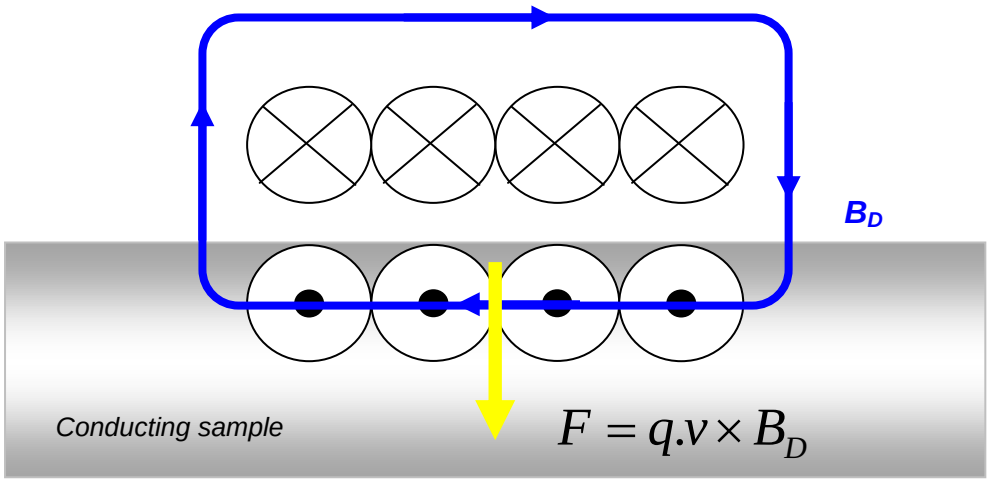

Figure 3.7: Diagram showing the Lorentz force contribution due to the dynamic magnetic field from the coil and the eddy currents induced in the near-surface of the sample.

The Lorentz contribution is usually dominated by the force generated from the static magnetic field, as the dynamic magnetic field is negligible in comparison for coil currents < 100 A. This self-field interaction is only seen in this case due to the very large currents used ~ approaching 600 A. It does however fall off rapidly with increasing stand-off.

Newton's second law states that the force on an electron is given by [16]:

$$\mathbf{F} = m\frac{d\mathbf{v}_e}{dt} \tag{3.24}$$

where m is the electron mass. It therefore follows from equations 3.23 and 3.24 that the equation of motion for an electron is given by:

$$m\frac{d\mathbf{v_e}}{dt} = -e(\mathbf{E} + \mathbf{v_e} \times \mathbf{B_0}) - \frac{m\mathbf{v_e}}{\tau} \tag{3.25}$$

τ is the average time between collisions for a given electron with the ions in the crystal lattice; hence the average impulse force from each electron scattering and exchanging momentum with the lattice ions is given by mv_e / τ. τ is usually of the order x10^{-14} s [16] and is much smaller than the time period of the current in the EMAT coil.

The implication of this is that the mean electron velocity is not changing and hence both sides of equation 3.25 are equal to zero. Equation 3.25 can then be rearranged such that:

$$-e(\mathbf{E} + \mathbf{v_e} \times \mathbf{B_0}) = \frac{m\mathbf{v_e}}{\tau} \tag{3.26}$$

When considering a volume of a metal, which has an electron density of n_e and ion density N_e, the transfer of momentum to the ions from the scattering of electrons imparts a force on the ions given by:

$$\mathbf{F} = N_e Z_e (\mathbf{E} + \mathbf{v_{ion}} \times \mathbf{B_0}) + n_e \frac{m\mathbf{v_e}}{\tau} \tag{3.27}$$

Z_e is the charge of the ion. $\boldsymbol{v_{ion}}$ is the average velocity of the ions. Given that the sample is charge neutral, such that $Z_e N_e = e n_e$ and also that the average velocity of electrons is significantly greater than the average velocity of the ions ($\boldsymbol{v_e} >> \boldsymbol{v_{ion}}$), equation 3.27 can be approximated to:

$$\mathbf{F} = n_e e(\mathbf{E}) + n_e \frac{m\mathbf{v_e}}{\tau} \tag{3.28}$$

Combining equations 3.26 and 3.28 reduces the term representing the force.

$$\mathbf{F} = -n_e e\left(\mathbf{v_e} \times \mathbf{B_0}\right) \tag{3.29}$$

$$= \mathbf{J_e} \times \mathbf{B_0} \tag{3.30}$$

where $\boldsymbol{J_e}$ is the eddy-current density.

Having already established and defined the existence of an eddy current in the near-surface of a sample, and in the presence of a ***B*** field, the force acting on it to produce an ultrasonic wave can be determined.

3.2.1.4 – Magnetostriction force

For ferromagnetic materials such as steel, acoustic waves can also be induced via a magnetostriction mechanism [19]. The introduction of a magnetic field to a ferromagnetic material will induce a dimensional change of the magnetic domains as the material minimizes the energy of the 3d orbits. This breaks the established long range magnetic order of the domains. The contribution made by the magnetostriction mechanism in generating ultrasound in steel is small compared to the Lorentz mechanism for the EMATs used in this study.

3.2.1.5 – Magnetization force

Magnetization, represented by ***M***, is inherent with ferromagnetic materials when exposed to a magnetic field of intensity ***H***. The force through the bulk of the sample and also at the surface due to magnetization effects is given by [20]:

$$\mathbf{F} = \int_{Volume} \nabla * \left(\mathbf{M} \cdot \mathbf{H}\right) dv + \frac{1}{2}\mu_0 \int_{Surface} \mathbf{n} M_n^2 dS \tag{3.31}$$

n is a unit vector in the normal direction, and M_n is the magnetization component also normal to the surface. The magnetization force is given by the first integral of equation 3.31.

3.2.2 - Detection EMATs

In the presence of a static magnetic field, an elastic deformation, such as that caused by an acoustic wave travelling in a metallic sheet, will induce eddy currents in the skin depth of the sheet as evident by equation 3.20. This propagating ultrasonic wave is comprised of the coherent oscillations of the ions moving together with the electrons. The static magnetic field will lead to a Lorentz force on both the ions and electrons, though the resultant acceleration of the ions due to the Lorentz force is insignificant when compared to that of the electrons, because the ions are much more massive and not as free to move. The electrons are relatively free to move and will form an eddy current, and for electrons within the order of magnitude of the electromagnetic skin depth will give rise to a time varying magnetic field above the surface o the sample. This time varying magnetic field will create an electromotive force in the detection EMAT coil, as is evident from equation 3.3.

In effect, there are three elements to consider for the detection mechanism; the eddy currents induced by the acoustic wave in the presence of the static magnetic field, the rate of deformation of the boundary at the surface where the fields pass through between the EMAT and sample, and the resulting time-varying magnetic field above the sample surface that can induce an EMF in a detection coil.

In the EMAT detection mechanism, the electric field ***E*** induced inside the sample by the acoustic wave is proportional to the cross product of the rate of change of the displacement of the ions and the static magnetic field ***B*** [16], which is shown in equation 3.32:

$$\mathbf{E} \propto \frac{du}{dt} \times \mathbf{B} \tag{3.32}$$

This of course is analogous to the term in the Lorentz force equation, a $\mathbf{v} \times \mathbf{B}$ term. As the eddy current induced in the sample is proportional to the electric field inside the sample then the resultant magnetic field generated outside the sample must also be proportional to the rate of change of the displacement of the ions. The EMF induced in the detector coil above the

sample surface is proportional to the time varying magnetic field and thus it is also proportional to the rate of change of the displacement of the ions.

A key observation that follows on from this is that EMATs are velocity sensors. A more detailed analysis of these phenomena considering the integration of the resulting external magnetic fields as the ultrasonic wave passes a detection coil produces the same result. This has been shown by *Kawashima* [21] and *Dixon* [22] amongst others.

3.3 – Sample suitability

The material characteristics that influence the EMAT transduction include the sample's electrical conductivity, magnetic properties, density and elastic stiffness. Details of their respective influence are discussed by *Dobbs* [23], though referring to the previous text in this chapter and also chapter 2, it is apparent the importance that these material properties all have in the generation, propagation and detection of ultrasound using EMATs.

3.3.1 – EMAT operation on aluminium

Aluminium is a weakly paramagnetic material. The implication of this is that the only significant contribution to the ultrasound generation mechanism is from the Lorentz interaction. In comparison to other industrial metals, such as steels and titanium, EMAT generation efficiency is also favourable for aluminium due to its comparatively low electrical resistivity, low density and relatively high stiffness [24]. The electrical resistivity ρ = 2.42x10^{8} Ωm at room temperature, with the electrical conductivity σ given by 1/ρ. This property is particularly important as the current density (equation 3.11) and the skin depth (equation 3.9) are dependent on it. It follows that aluminium is an ideal material to investigate for non-destructive testing when using EMATs.

3.3.2 – EMAT operation on steel

Steel samples can be ferromagnetic as well as paramagnetic. Typically, ferritic steels possess a bcc lattice structure and are ferromagnetic, whilst austenitic steels have an fcc crystal structure and are paramagnetic. There are exceptions where certain steel grades classed as austenitic can be ferromagnetic. In addition, steel samples will often contain more than one phase and the total magnetic response and behaviour of the steel is dependent on the influence on the microstructure by the various phases that may be present.

The samples investigated and described in this work are ferromagnetic, with EDX and EBSD (see chapter 4) results showing they can all be approximated to sheets of pure iron. It follows that the magnetization force (equation 3.31) will provide a contribution to the force generated by an EMAT on these steel samples, and magnetostriction effects will contribute to the EMAT transduction mechanism. Experiments have been successfully undertaken on austenitic sheets using the same equipment as used for the experimental work in this body of work [22, 24]. However, due to the strength of the field provided by the NdFeB magnet, together with the magnitude of the supplied current pulse (discussed in chapter 7), the Lorentz force mechanism is still the major contributor to generating the force experienced by the sample [25].

The value of the electrical resistivity of iron is $\rho = 8.57 \times 10^{-8}\,\Omega$m. In comparison to typical steel alloys, carbon steel has a value of $\rho = 17.0 \times 10^{-8}\,\Omega$m, with stainless steel having a resistivity of approximately $55.0 \times 10^{-8}\,\Omega$m [24]. There are of course many different grades of both carbon steel and stainless steel, with a wide range of corresponding resistivities and the values quoted are nominal. It can be concluded that the electrical conductivity of steel is significantly lower than that of aluminium and iron. The efficiency of acoustic transduction on steel is, as a consequence, relatively poor compared to EMAT transduction on aluminium. The operation efficiency on steel sheet is however usually sufficient to produce ultrasonic signals with a signal to noise ratio suitable for Lamb wave and shear wave measurements. The range of physical properties in various steel alloys relevant to EMAT transduction means

that the efficiency of operation on steel alloys is highly variable when compared to operation on different aluminium alloys.

3.4 – EMAT coil design

The coil design and geometry, together with the arrangement in the geometry of the permanent magnets, allows for the generation of a number of wave modes, some of which are unachievable with transducers such as PETs. Typical coil designs include the linear coil, the meander coil and the spiral coil [16]. Figure 3.8 shows plan views of these designs. Each coil design has different associated dynamic magnetic fields, and can hence influence the magnetic field experienced by the sample under investigation. For instance the pancake spiral coil has radial symmetry, and hence can generate Lamb waves that propagate in all directions.

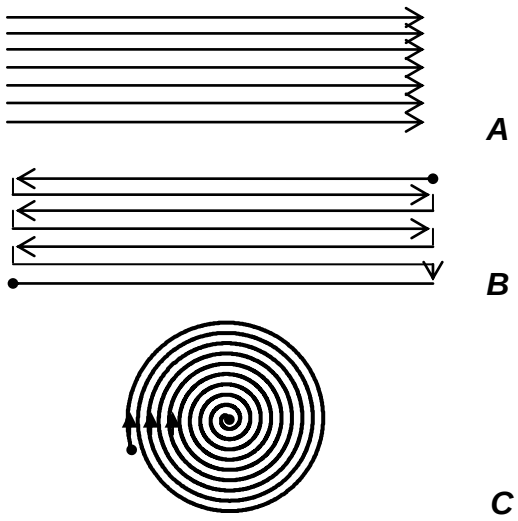

Figure 3.8: Schematic diagrams showing the plan views of some typical coil designs used for EMATs. The diagrams show the (A) unidirectional linear coil design, the (B) meander coil design and the (C) pancake spiral coil. Each instigates its own force response and can be used to generate different wave modes accordingly.

3.4.1 – Shear wave EMAT configuration

To generate a shear wave efficiently, intuitively a shear force needs to be applied within the sample skin depth. Previous workers such as *Bresse* and *Hutchins* [26] have shown

that a finite sized, purely piston like, out-of-plane force will generate some bulk shear wave components and vice-versa for a purely in-plane force.

In this case, linearly polarised shear or in-plane force is generated using a spiral coil EMAT, where the direction of the dynamic magnetic field is opposed in one half of the coil compared to the other. This is demonstrated in figure 3.9. The magnet configuration can also be changed to determine the polarisation and propagation directions of the shear wave.

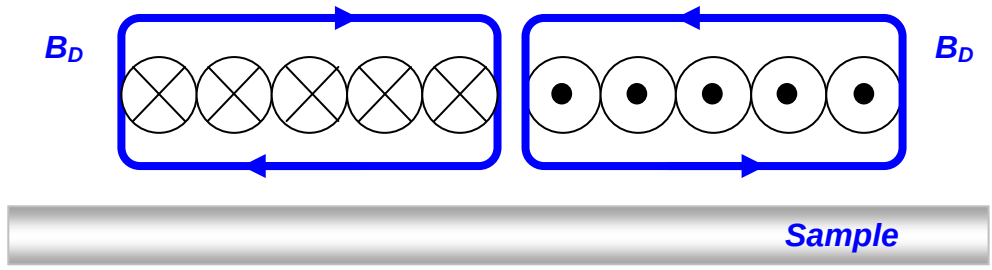

Figure 3.9: Diagram showing a spiral coil configuration. The dynamic magnetic fields, B_D, that result from each half of the coil oppose each other.

Figure 3.10 shows a diagram of a design configuration for a shear wave EMAT that generates a shear wave propagating in the normal direction. The polarisation of the shear wave can be controlled by the position of the magnet relative to the current in the coil [27].

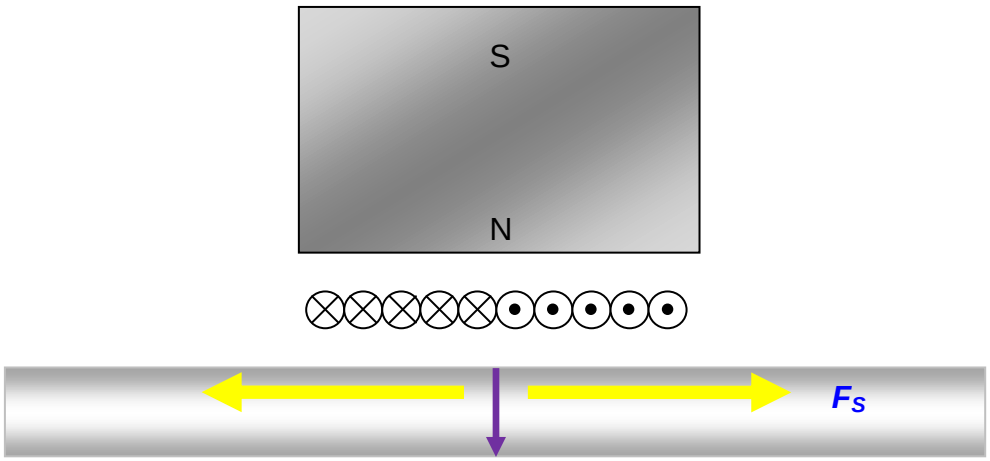

Figure 3.10: Diagram showing the design configuration for a linearly polarised SH wave EMAT. Note the split magnet design. The yellow arrows represent the direction of the force, F_S, generated in the skin depth of the sample. The purple arrow shows the corresponding direction of propagation of the wave

3.4.2 - Lamb wave EMAT configuration

For an EMAT to generate a non-dispersive S_0 Lamb wave within a thin metal, a large symmetric in-plane force is ideally required. Any EMAT coil design will create such an in-plane force. Figure 3.11 displays an EMAT with a linear coil, the basis of the design configuration used in this work [28].

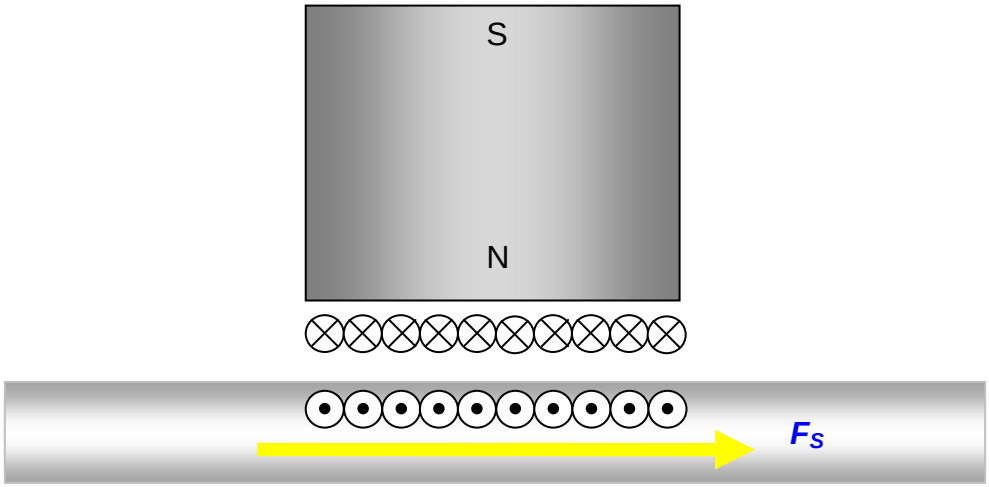

Figure 3.11: Diagram showing a typical linear coil design configuration for an EMAT that can produce a non-dispersive S_0 mode Lamb wave.

3.5 – References

1. *Blitz J, Simpson G, Ultrasonic Methods of Non-destructive Testing, Chapman & Hall, 1996*

2. *Krautkrämer H, Krautkrämer J, Ultrasonic Testing of Materials, 4th edition, Springer- Verlag, 1990*

3. *Lobkis OI, Chimenti DE, Zhang H, J. Acoust. Soc. Am.,* ***107(4)****, 2000, pp. 1852-1858*

4. *Scruby CB and Drain LE, Laser ultrasonics, techniques and applications. Bristol: Adam Hilger, 1990*

5. *Davis CC, Lasers and Electro-Optics, Cambridge University Press, 1996*

6. *Kumar R, Kaura SK, Sharma AK, Chhachhia DP, Aggarwal AK, Optics & Laser Technology,* ***39****, 2007, pp. 256-261*

7. *Palmer SB, Dixon S, Insight,* ***45(3)****, 2003, pp. 211–217*

8. *Jian X, Baillie I, Dixon S, J. Phys. D: Appl. Phys.,* ***40****, 2007, pp.1501-1506*

9. *Halaby HM, Corrosion, **62(10)**, 2006, pp. 930-941*

10. *Fan Y, Dixon S, Jian X, Rev. of Prog. in QNDE, **28A**, 2008, pp. 835-840*

11. *Hernandez-Valle F, Dixon S, Rev. of Prog. in QNDE, **28A**, 2008, pp. 936-941*

12. *Ogi H, J. Appl. Phys., **82**, 1997, pp. 3940-3949*

13. *Maxwell JC, A Treatise on Electricity and Magnetism, third edition, Dover Publications, 1954*

14. *Grant IS, Phillips WR, Electromagnetism 2nd edition, John Wiley & Sons, 1998*

15. *Dixon S, Jian X, Applied Physics Letters, **89**, 2006, 193503-(1-3)*

16. *Hirao M, Ogi H, EMATs for Science and Industry: Noncontact Ultrasonic Measurement, Kluwer Academic Publishers, 2003*

17. *Lerner LS, Physics for Scientists and Engineers, Jones & Bartlett, 1996*

18. *Hirao M, Ogi H, Ultrasonics, **35**, pp. 413-421, 1997*

19. *Thompson RB, J. Appl. Phys, **48(12)**, 1977, pp. 4942-4950*

20. *Moon FC, Magneto-Solid Mechanics, Wiley Publishing New York, 1984*

21. *Kawashima K, IEEE Trans. Sonics Ultrason. **SU-31(2)**, 1984, pp. 83-94*

22. *Dixon S, Edwards C, Palmer SB, Ultrasonics, **39**, 2001, pp. 445-453*

23. *Dobbs ER, Physical Acostics, Vol X, Edited by Mason WP, Thurston RP Academic Press New York, pp. 127-189, 1973*

24. *Kaye GWC, Laby TH, Tables of Physical and Chemical Constants, Fifteenth edition. Longman Scientific & Technical publishing, 1989*

25. *Potter MDG, Dixon S, Nondestructive Testing and Eval., **20(4)**, 2005, pp. 201-210*

26. *Mair HD, Bresse L, Hutchins DA, J. Acoust Soc. Am., **84(4)**, 1988, pp. 1517-1525*

27. *Jian X, Dixon S, Baillie I, Edwards RS, Morrison J, Fan Y, Appl. Phys. Lett., **89**, 2006, 244106*

28. *Potter MDG, Dixon S, Davis CL, Meas. Sci. Technol., **15**, 2004, pp 1303-1308*

CHAPTER 4

Electron Backscatter Diffraction

4.1 - Scanning electron microscopy

4.1.1 - Introduction

The scanning electron microscope (SEM) is an extremely important analysis tool, integral to aiding a variety of research as technologies and their components become orders of magnitude smaller. It is a technique adopted across wide-ranging research topics throughout the sciences [1-3]. Of particular interest here, its adaptability and functionality is advantageous for work involving materials characterization. SEM applications utilize the elastic and inelastic scattering phenomena between incident electrons and an interrogated material, being able to generate topographical images in addition to metallurgical information. Chemical composition and phase identification are standardized specifications within the new generation of SEM. At Warwick, the recently purchased *Zeiss Supra 55VP* SEM gives access to all these features, creating the opportunity to study samples at a highly detailed level on the microscopic scale [4].

The SEM possesses distinct advantages as a technique in comparison to the more traditional optical microscopy methods. For example, the wave-particle duality argument applied to visible light can also be applied to a beam of electrons, meaning the de Broglie wavelength for an electron beam with energy of 10 kV (a typical accelerating voltage) is approximately 10 pm [5]. In contrast the approximate wavelength of visible light is 0.5 μm. However, the apparent wavelength of the electrons is not the definitive limitation on the achievable resolution. Due to limitations imposed by the optics, the beam spot size, aperture sizes and the interaction volume (refer to section 4.1.3) the beam has with a sample; the actual resolution is usually of the order of a few nm. As listed in its specifications, the Zeiss Supra 55VP SEM has an optimised resolution of 1 nm at 15 kV, achieved with the aid of an in-lens

detector. This implies therefore that the resolution is at least 250 times higher using an SEM compared to the highest resolution optical methods. Further improvement in the resolution can be obtained using a Transmission Electron Microscope (TEM) [6]. The TEM technique was not used during this study, and so no further mention of it will be made.

The objective of microscopy is usually to generate an image of orders of magnitude larger than the object of interest. Modern SEM systems can achieve magnification levels in excess of $\times 10^6$, which again is a significant advancement over even the most advanced optical microscopy instruments.

4.1.2 – SEM theory

Figure 4.1 shows a schematic diagram of the SEM setup. The sample is mounted on a specimen holder which acts as an electrical ground, required to eliminate electrostatic charging issues [7]. Due to the restricted size of these holding stubs, the mechanical stage and the SEM chamber, sample sizes are limited. The quoted interior dimensions for the Zeiss SEM chamber are 330 mm × 330 mm × 270 mm, and with consideration of the mechanical stage and size of the specimen stubs, it follows that samples investigated can be no larger than a few centimetres in any one dimension.

An SEM requires an electron source, supplied usually by a cathode ray tube (CRT) or, as is the case for the Zeiss Supra 55VP, a Field Emission Gun (FEG) [4]. The generated beam is propagated and accelerated along the electron column, focussed by a series of magnetic condenser and objective optics, such that the spot size diameter incident on the sample can have a tolerance level of just a few nm. The technique requires a high vacuum because the electrons are charged and would have a strong interaction with gaseous atoms [8]. A typical vacuum level associated with SEM is 10^{-6}–10^{-7} mbar. The vacuum is essential in stabilizing the projected energy and trajectory of the beam. Depending on the application and material of interest, suitable surface preparation is required, not just to withstand the vacuum conditions, but also to present an accessible surface to the electron source [5].

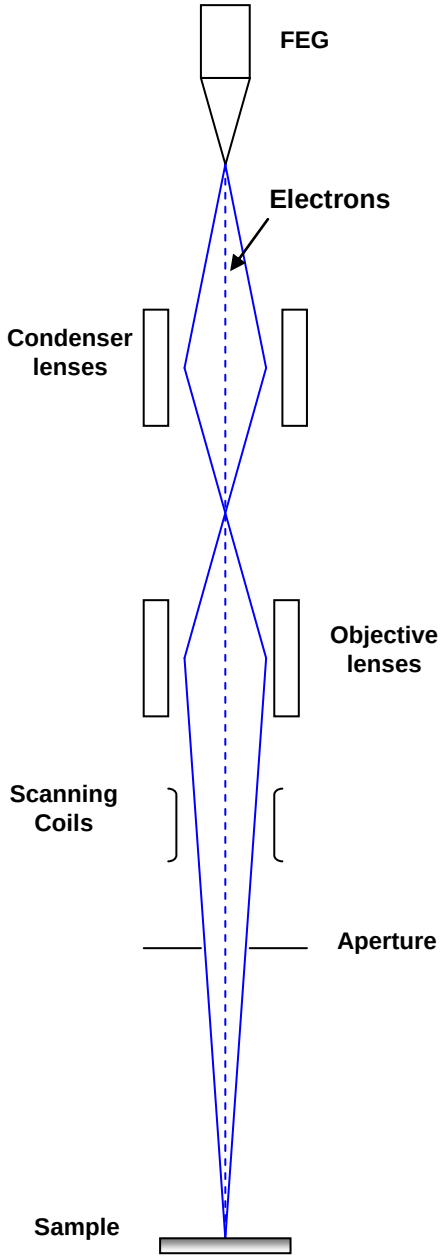

Figure 4.1: Schematic diagram of the principal of operation of the SEM, highlighting the systematic approach of using magneto-static and electromagnetic optics to focus the electron beam on the sample.

The analysis that can be completed using an SEM depends upon the products resulting from the interaction between the sample and the high energy electron beam. These products originate from what is known as the interaction volume.

4.1.3 – Interaction volume

The interaction volume is an important parameter and plays a considerable role in the limitations of the resolution achievable. It is the fundamental region from which electrons and x-rays are emitted after irradiation by a high energy electron beam [9]. A diagram of the interaction volume is shown in figure 4.2. As illustrated, the secondary electrons emitted are from the near-surface whereas the elastically backscattered electrons from the primary beam can be resolved from a greater depth. The characteristic x-rays are dependent on the elements present in the sample, and can be emitted from a region significantly deeper than the origin of the backscattered and secondary electrons. The depth of the volume, typically of the order ~μm, is dependent on the atomic number *Z* (depth decreases with increasing Z) and the accelerating voltage of the electron beam (depth increases with increasing energy). For a 20 kV electron beam for a metal with a relatively low atomic number such as aluminium, the secondary electrons typically arise from a depth of no more than 100 Å. The backscattered electrons arise from depths of up to hundreds of nm, and the x-rays up to 2 μm [9].

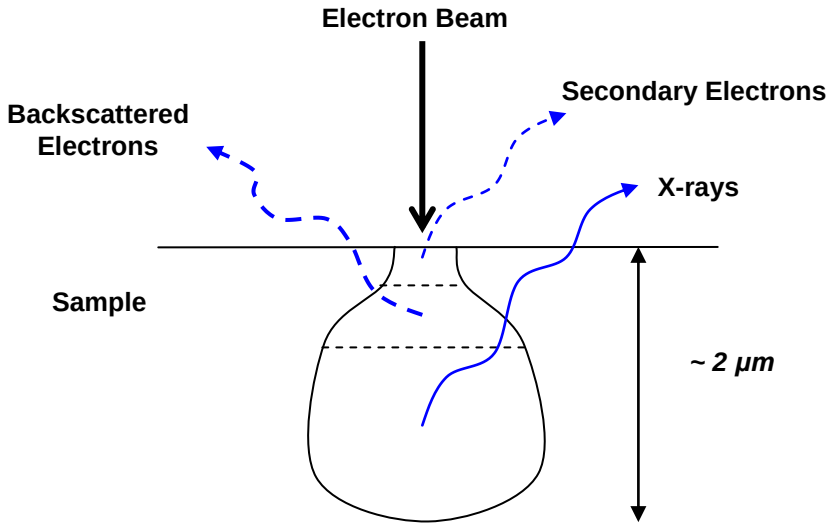

Figure 4.2: Diagram displaying the interaction volume, and the origin of the products emitted as the incident electron beam penetrates into the sample of interest. The secondary electrons are emitted

from the top few angstroms signifying they come from the near lattice crystals, with the backscattered electrons and x-rays coming from depths of the order ~ µm.

These three primary products resulting from the irradiation of the electron beam each contain varying amounts of information, and enables a comprehensive assessment of a material, where various properties can be extrapolated with the correct interpretation. The properties that can be characterized are discussed in section 4.2.

4.2 - SEM applications

The various products shown in figure 4.2 are emitted as a result of an electron beam irradiating an electrically conductive sample. The detection of these products emitted from the surface can be utilized to generate different information. These specific applications are discussed in more detail in sections 4.2.1-4.2.3.

4.2.1 - Secondary electron imaging

This function allows the detailed imaging at a microscopic scale of any electrically conductive sample. The process of generating an image requires the detection of the lower-energy secondary electrons, with energies around 5 eV, emitted from the orbits of the near-surface atoms from a sample subjected to the high energy primary electron beam. The low energy of the secondary electrons means only those within a few nm can escape from the surface to be detected.

A set of scanning coils deviate the electron beam, creating a rapid raster-scan formation [5, 7]. This allows the electrons to collide and interact with the sample across a desired region of interest. The secondary electrons emitted across this area are then collected by a detector, with the received signals amplified. The relative intensities of these amplified signals create a greyscale image associated with secondary electron imaging, an example of which is shown in figure 4.3; an image of an aluminium sample. The SNR level of an image can be improved significantly by increasing the scan time, and together with the

advancements in hardware and software, high resolution real-time images can be collected in just fractions of a second.

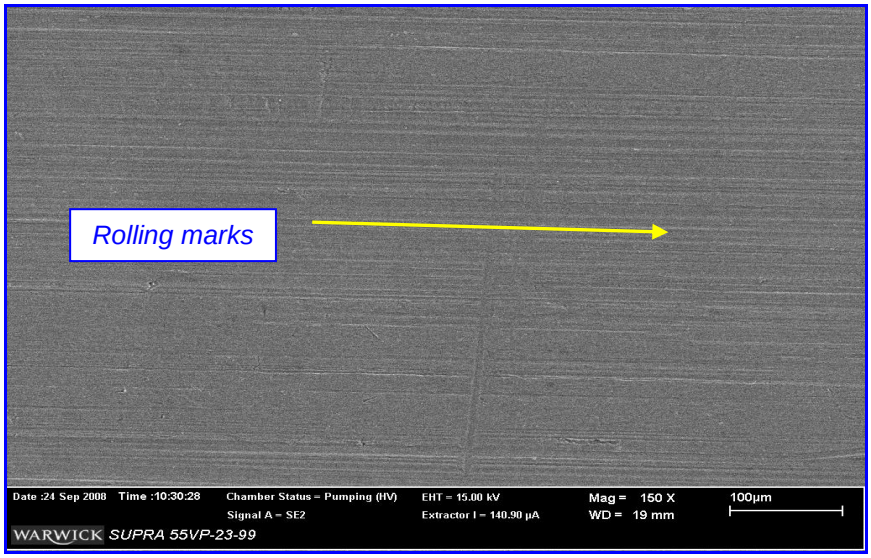

Figure 4.3: SEM micrograph of the surface of a rolled aluminium sample.

The technique is not limited to electrically conductive metallic samples. Given its unrivalled ability to image at high magnifications, its potential applicability within science is wide-ranging. Typical applications in Biology for instance include observing micro-organisms [10]. Such specimens are not ideally suited to SEM due to poor electrical conductivity, with electrostatic charging being a major issue to overcome. This can be resolved using sputter-coating to envelope such samples in a thin, electron-rich, metallic coating. Common metals used for sputtering include gold, platinum and palladium; the coating alleviates the conduction and grounding problems [7], and allows an image to be generated.

SEM imaging is important for this work as it offers a method to observe the quality of surface finishes, an essential factor in the success of electron backscatter diffraction. Figure 4.3 depicts an as-rolled aluminium sheet sample, illustrating the level of surface finish prior to any surface preparation. Subsequent polishing images can then be compared, ensuring the surface finish has improved.

4.2.2 - Chemical composition

Available with the Zeiss Supra 55VP is the EDAX software package, this analysis software is used to determine the composition of a sample by analysing the detected characteristic x-rays emitted from the near-surface [11]. This technique of analysing the x-rays is known as Energy-Dispersive X-Ray Spectroscopy (EDX), and is based on the principle that as each element has its own unique atomic structure, the emitted characteristic x-rays, and in particular the frequency, will be representative of the elements present in the sample. Determination of not just what elements exist, but their relative percentages within a sample, is therefore possible [12]. Figure 4.4 shows an EDX spectrum displaying the chemical composition for a rolled steel sheet.

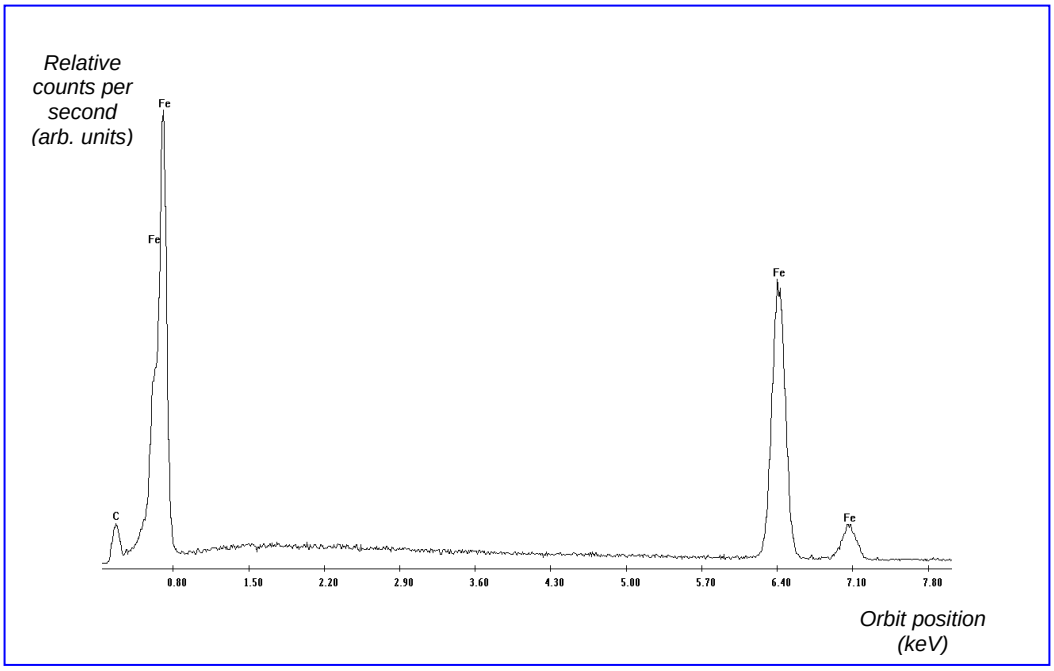

Figure 4.4: EDX chemical composition spectrum for the steel sheet DC05 supplied by Corus. As is shown here, it has picked out the L and K orbits for Fe. There is also a small L-peak for carbon: this offers validation of the alloy specification provided by Corus for the metal (listed in chapter 7 and 8).

EDX is a useful analysis tool, and is certainly a relevant method to use for this research, given the use of steel samples in the body of experimental work conducted. Having the facility to characterize accurately the chemical composition of the alloys studied, enables the correct identification of the iron-phases present, which is important when acquiring EBSD data. This fact is apparent in figure 4.4, which depicts an EDX scan result on a steel sample. The EDAX

program can be used to quantify the iron content, and pick out the other elements that feature in the composition.

4.2.3 – Phase identification

If incident at the correct Bragg angle on a near-surface lattice plane, primary electrons from the SEM electron beam will elastically backscatter. The modulation of the backscatter electron intensity that exits the sample form diffraction patterns that are dependent on the orientation, symmetry and the phase of the sample [13]. These patterns are therefore characteristic of the sample's crystallographic structure, and can be analysed to determine phase identification, in addition to generating microstructural information. A technique, based on the analysis of the backscattered electron diffraction patterns, is electron backscatter diffraction (EBSD), and is a facility available on the equipment used in this study.

4.3 – Electron Backscatter Diffraction

4.3.1 – Introduction

Electron backscatter diffraction (EBSD) is a relatively new technique, gaining popularity over the last decade as its functionality has increased since becoming fully automated [14, 15]. It is used extensively in materials science research due to the unique quantitative information it generates when determining crystallographic orientations of the near-surface crystals [16]. This simultaneously generates an insightful, qualitative picture of the microstructure.

EBSD is dependent on the angular distribution of the elastically backscattered electrons, and as discussed, is a surface-specific technique. The diffracted primary electrons produce diffraction patterns containing the symmetry and lattice planar spacing information needed to measure the orientations of the crystals acting as the diffracting source [17]. Typically EBSD is completed via a raster scan, the user defining an area on a sample and setting a step size between each discrete point that fits to a grid within the area.

At each point, the crystallographic orientation is determined, with the angle data saved. It is standard to display the results via a colour-coded inverse pole figure (IPF) map; such a map is shown in figure 4.5 [18]. Each colour represents a specific orientation and provides the user with a unique visualization of the microstructure. This 2-D representation demonstrates only part of the information that is available in the stored data.

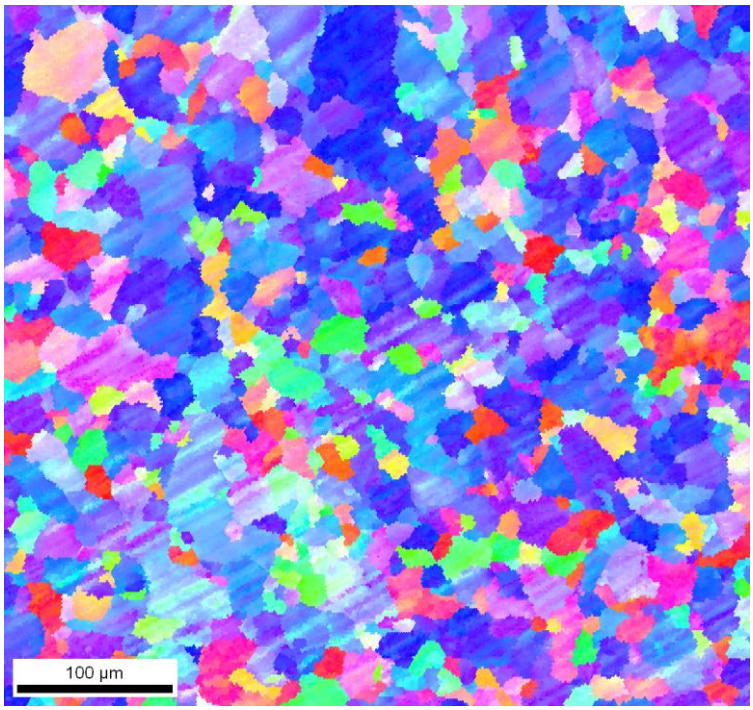

Figure 4.5: An Inverse Pole Figure EBSD map taken from a steel sheet. The colours represent a particular orientation. Areas of similar colour indicate a grain.

The scale bar in figure 4.5 (indicating 100 µm) is indicative of one of the limitations of EBSD. It is a technique that requires the sample to be tilted; maintaining focus over a large area is difficult because of the variation in working distance, which is the distance between the sample and the electron beam optics. An area of 1 mm^2 is considered large, and at that scale in conjunction with a small step size (~µm) EBSD scans can take several hours.

Nevertheless, it is still a method which can provide quantitative information about crystallographic microstructure, and can aid the understanding of ultrasound propagation behaviour, which as demonstrated throughout chapter 2 and 3, is dependent on the micro- and macroscopic properties of the material.

4.3.2 – EBSD theory

Recent advances in microscopes, computer hardware and software have enabled EBSD to become a fully automated technique, removing the need for expert users to solve individual diffraction patterns to determine the orientations [19]. The orientation data can produce IPF maps along with other important information. This includes identifying different phases in multi-phase materials, generating pole figure information comparable to x-ray diffraction measurements [20] and determining strain levels [21].

EBSD requires meticulous sample surface preparation; the surface needs to be relatively flat and free from defects, contaminants and inclusions, in order that the characteristics of the backscatter patterns detected will be truly indicative of the crystal under investigation [7]. The Zeiss SEM has a maximum accelerating voltage of 30 kV but even at this high energy level, the interaction volume is only of the order of a few microns. The specific sample preparation methods for rolled aluminium and steel sheet are discussed in section 4.5, with the methods employed stated in chapter 8. Figure 4.6 shows a schematic diagram of the EBSD technique.

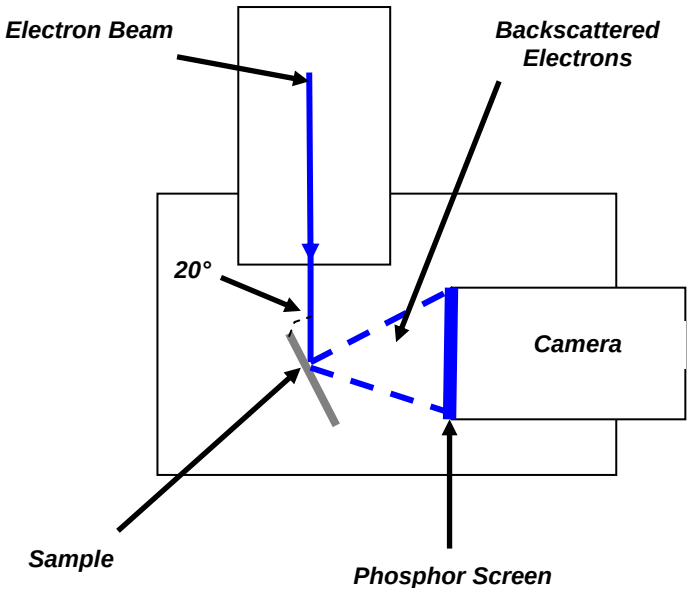

Figure 4.6: Schematic diagram showing the setup requirements for Electron backscatter Diffraction. The important parameters to consider in the setup are labelled accordingly.

The method is performed at a high vacuum. The polished sample is tilted at a small angle of 20° to the vertical. A specialized phosphor screen camera is used to detect the diffracted electrons.

The sample is tilted to maximise the backscatter yield of the primary electrons [22]. Not only will more electrons diffract, but at this angle, they can also escape more readily from the surface. The electrons scatter off the near-surface Bragg planes when incident at the corresponding Bragg angle for the material [23]. This scattering satisfies Bragg's Law (equation 4.1):

$$\lambda = 2d \sin \theta_B \tag{4.1}$$

Here λ is the de Broglie wavelength of the electrons, d is the interplanar spacing for the crystal under investigation and θ_B is the corresponding Bragg angle. This is the fundamental rule that drives EBSD, and is illustrated in figure 4.7. With a known wavelength source emitted from the FEG, lattice planar spacing's can be determined by equating the Bragg angles at which diffraction occurs. This function therefore enables the identification of different phases within a multi-phased material [24].

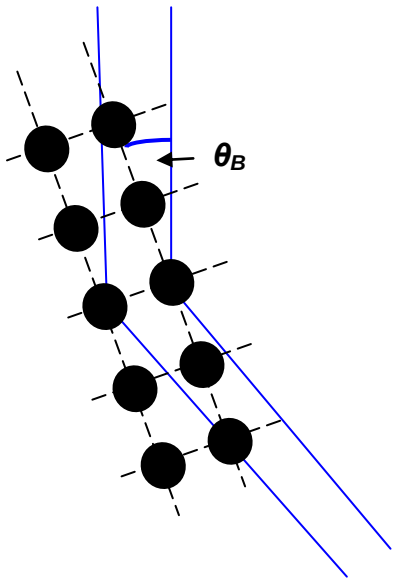

Figure 4.7: Elastically backscattered electrons incident on lattice planes rotated in the EBSD setup. Elastic backscattering is more frequent for rotated samples as the magnitude of θ_B is usually small.

4.3.3 – Generation of orientation information

When the primary electrons enter a polycrystalline sample, they will be inelastically scattered diffusely in all directions [24]. This guarantees that electrons will then arrive at nearby lattice planes, approaching at the Bragg angle θ_B. These electrons can then diffract elastically. This backscattering occurs in all directions, and as such, these high energy primary electrons project like a surface of a cone. Figure 4.8 shows a diagram of how these cones are formed, and how they coincide to form bands of high electron density.

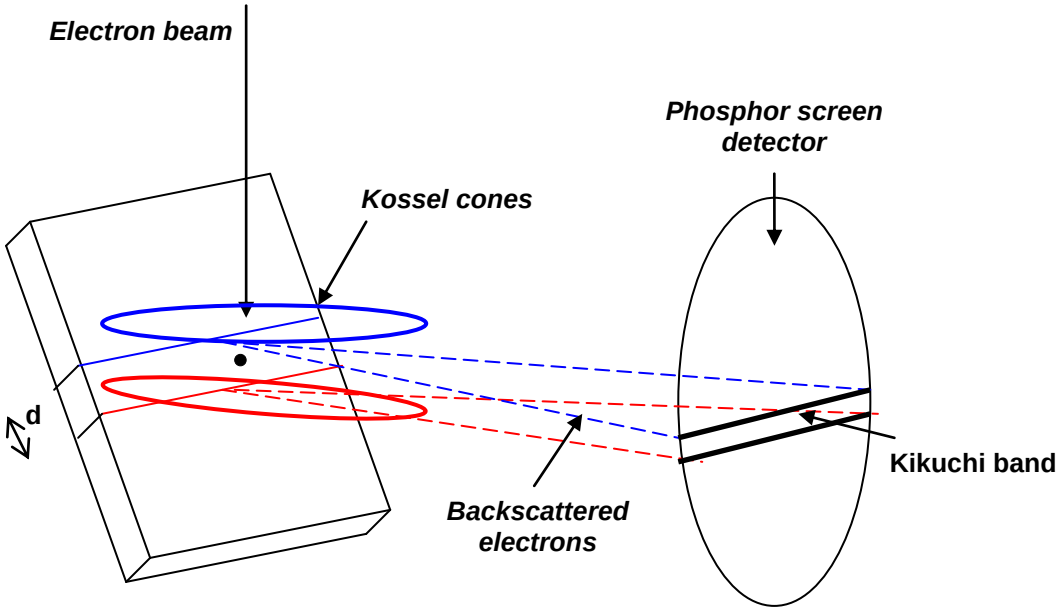

Figure 4.8: Formation of Kossel-cones from divergent backscattered electrons incident on neighbouring Bragg planes of a tilted sample. The black dot behaves as the scattering source, sandwiched between two lattice planes, of lattice planar spacing d. Each plane elastically scatters electrons in all directions, forming conic surfaces. These surfaces extend until they coincide with the detector and form bands of high electron density, called Kikuchi bands.

The conic surfaces appear flat, approximately circles, because the Bragg angle is small, typically around 0.5°, which implies a large apex angle of the cone [24]. This is illustrated in the schematic diagram shown in figure 4.9.

The high electron density lines detected at the camera are called Kikuchi lines [24]. The corresponding pair coincident at the camera makes up what are known as Kikuchi bands.

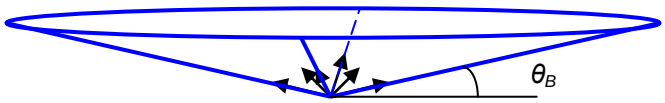

Figure 4.9: Diagram showing the Kossel cone in closer detail. A scattering source diffracts the electrons in all directions at an angle θ_B. This scattering source acts like the apex of a cone. The Kossel cones can be approximated as circles because θ_B approaches 0˚. Consequently, these backscattered electrons are detected as lines by the EBSD camera.

4.3.3.1 – Kikuchi patterns

Kikuchi bands are the building blocks of a backscatter diffraction pattern. Each band, detected as a contrast from a low-electron density collected background using a Hough transform (refer to section 4.4.1.2 for more details), has a distinct width that correlates to a particular crystallographic plane. Kikuchi patterns are made up of numerous Kikuchi bands; a typical pattern from an aluminium sample is shown in figure 4.10. A point where two Kikuchi bands coincide is known as a zone axis, with the intersection of numerous Kikuchi bands, such as those indicated on figure 4.10, being termed a major zone axis [25].

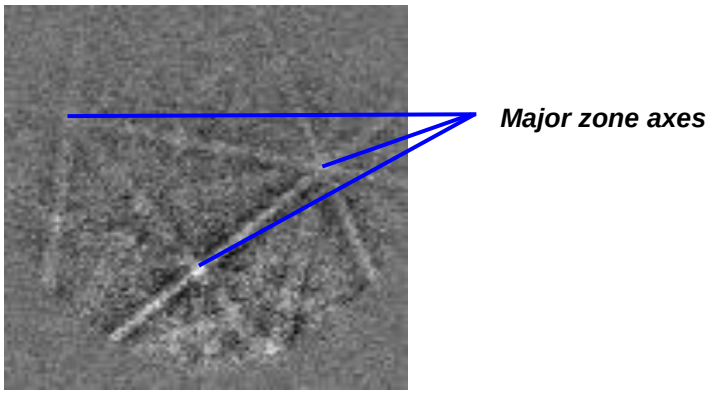

Figure 4.10: A real-time EBSD Kikuchi pattern generated from an aluminium sample. A number of Kikuchi lines are visible. The major zone axes are highlighted which have to be identified to calculate the orientation of this particular crystal.

By identifying the position of the zone axes, and calculating the planes represented by the Kikuchi bands present, means that these diffraction patterns can be interpolated to generate crystallographic orientation data.

4.3.4 – Representation of crystallographic orientation information in EBSD

Crystallographic orientations can be represented in a variety of ways. For crystals with cubic unit cells (see chapter 5) as in the case of steel and aluminium, crystal directions are usually represented using Miller indices <hkl> [26]. Miller indices can be derived from the EBSD data, and are utilised in the qualitative representation of the microstructure. The Miller index notation describes families of orientations and planes. For example, an <001> orientation is not unique in itself, as it can hold true in numerous ways due to symmetry. The rotation matrix required to define a Miller index constitutes nine coefficients, so for EBSD, three Euler angles are recorded to define the orientation which is more suitable for computing.

4.3.5 – Euler angles

Three Euler angles can be used to describe a crystallographic orientation. There are a number of ways to select and define these angles: this section describes the method utilised in the EBSD software. The Bunge-Euler angles ($\varphi_1, \Phi, \varphi_2$) definition requires the introduction of orthogonal Cartesian frames, choosing a rotation method that rotates the individual crystal Cartesian frame (x,y,z) into the Cartesian frame of the polycrystalline aggregate (X,Y,Z) [27]. The frame of reference for the aggregate is chosen conveniently such that the three axes align with the rolling, transverse and normal directions (see chapter 5).

The Bunge-Euler rotations are completed by successive rotations about the z, x and then z axes, which ultimately align (x,y,z) with (X,Y,Z). The first Bunge-Euler angle φ_1 is a

rotation about the z-axis of the crystal frame, transforming the axes of the crystal frame from positions (x, y, z) to (x′, y′, z′) where z = z′. The value of φ_1 is such that the x' axis will be in the XY plane. The second rotation ψ is about the newly formed x' axis. The new axes resulting from this are labelled (x'',y'',z''). As a consequence of this rotation the z'' and Z axes will be coincident. The final rotation, Φ, is about the z'' axis, aligning the axes (x''',y''',z''') with (X,Y,Z). and therefore the frame of reference of the crystal with the axes and frame of reference of the sample (see section 5.4.1). These rotations are illustrated in figure 4.11.

The conversion between the *Roe* [28] (as used in the ODF probability function) and *Bunge* [29] definitions of Euler angles is relatively trivial; table 4.1 shows how they compare accordingly, along with their respective relationship with another notation, the symmetric Euler angle system [30].

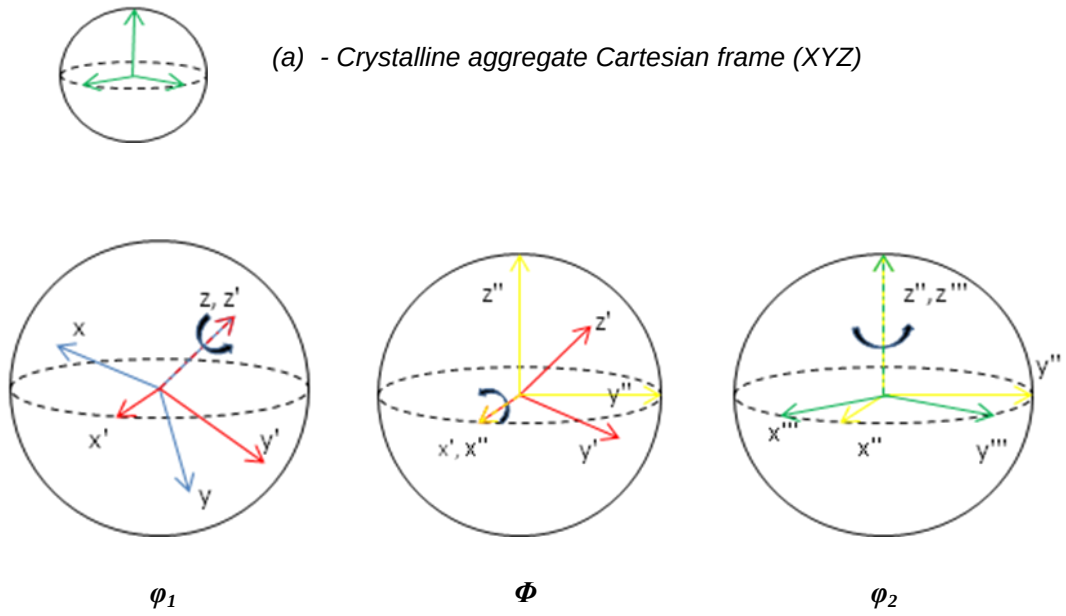

Figure 4.11: The Bunge-Euler angles mapping the Cartesian frame (xyz) of the crystal to the Cartesian frame of the crystallite (XYZ). φ_1 ***is the first rotation about z (blue frame to red), followed by*** Φ ***about x′ (red to yellow),with the final rotation*** φ_2 ***about z (yellow to green), which aligns with the XYZ crystalline frame shown in (a).***

Bunge	Roe	Symmetric
$\pi/2 - \varphi_1$	Ψ	Ψ
Φ	Θ	Θ

$\pi/2 - \varphi_2$	$\pi - \Phi$	Φ

Table 4.1: Relevant conversions required to change between different Eulerian angle notations.

4.4 – Orientation Imaging Microscopy

The automated process of EBSD is often referred to as Orientation Imaging Microscopy (OIM) [31]. This is the process that collects, and allows the respective analysis of, the Euler angle data.

Besides the surface preparation, the requirements of the user is in essence reduced to only focussing the beam on the area of interest, selecting the area to raster scan, and defining a step size for the required resolution. Other parameters, such as those used to optimise the diffraction pattern analysis, are stated at the end of this chapter (table 4.2), citing typical values used for these parameters during the experimental work conducted.

The software used for this thesis is the EDAX OIM software. This incorporates two programs: one is a specific data collection program, with the second a data analysis program.

4.4.1 – EDAX OIM Data Collection

4.4.1.1 – OIM setup conditions

When the sample has been tilted suitable focussing must then be achieved. Firstly, any aberration effects must be resolved; manual x-y stigmatism controls are available in conjunction with inbuilt correcting procedures. Once established, the specialised EBSD camera can be employed.

Initially a background measurement is collected using the camera; this is done to optimise the contrast levels of the Kikuchi diffraction patterns detected. This is achieved by optimising the Gain (dB) and greyscale level for the pre-specified aperture, in addition to setting the exposure time (time per point). The minimum time that can be chosen with the EDAX system is 0.02 s (50 patterns per second). Increasing the exposure time enhances the signal to noise ratio and thus the quality of the pattern, improving the accuracy in detecting

the Kikuchi bands and thus the orientations measured. All scans performed during this study were done with an exposure time = 0.25 s. This relates to a fair compromise between an advantageous SNR, the size of the scan area and the time to complete the scans.

The user must define which phases they wish to identify in their scan, and also optimise their Hough transform parameters (see section 4.4.1.2). The phases are stored in an archived database, with each containing the relevant pre-calculated simulated pattern data and d-spacing values required for resolving the diffraction patterns.

An SEM image of the sample is taken that contains the area of interest to be scanned; this area is then selected by the user. The step size, δ_{step}, is defined, which in effect is a control of the resolution of the EBSD IPF map that will be generated. There is again a trade-off to consider between enhancing the resolution and the time to complete the scan. A point to consider when choosing δ_{step} is the average grain size value if known. For example there is no advantage in selecting δ_{step} = 1 μm for a sample with an average grain size of 200 μm because the orientations obtained will be continuously repeated. In this case, a 20-50 μm step size would suffice, maintaining a good resolution, but improving the scan time or allowing an increased area to be scanned in a similar time.

4.4.1.2 – Hough transform

The automated indexing of the diffraction patterns in OIM is completed utilising a statistical voting system. The software locates the Kikuchi bands digitally, assigning a line coincident with the centre of each band. The number of bands to be detected and highlighted can be pre-defined by the user. These lines are mapped to points in Hough space, using the Hough transform. This is a mathematical transformation mapping a two-dimensional line in Cartesian space (x,y) to a point in Hough space (ρ_H, θ). Equation 4.2 gives the mathematical representation of the Hough transform [32]:

$$\rho_H = x\cos\theta + y\sin\theta \tag{4.2}$$

where (x,y) are a pair of coordinates which are found along a Kikuchi line represented in Cartesian space, with (ρ_H,θ) the Hough parameters. Figure 4.12 shows the relationship of ρ and θ to each pixel in the (x,y) plane.

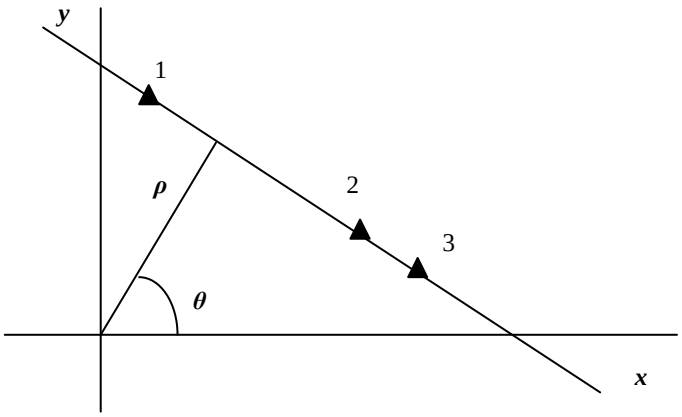

Figure 4.12: Graphical representation of the relationship between (x,y) and (ρ_H,θ). ρ_H is the distance of the perpendicular bisector to the Kikuchi line from (0,0), with θ the angle swept between x-axis and the Kikuchi band. 1, 2 and 3 are arbitrary points found along the Kikuchi line.

The Hough parameter ρ_H is the length of the perpendicular bisector between the Kikuchi line and the origin in Cartesian space, with θ the angle swept between the x-axis and the perpendicular bisector. As mentioned, the number of Kikuchi bands detected is pre-defined, with priority of detection given to the bands of highest electron density. The highest intensity Kikuchi bands transform to the highest and most significant peaks in Hough space. It is these peaks that are compared to the downloaded phase information provided from the OIM phase database. The most likely orientation for a given selection of peaks is then assigned via the 'best fit' digital voting system.

4.4.1.3 – Operator parameters

For optimal performance, there are a number of parameters that can be altered to enhance certain characteristics of the OIM software performance. The selection of the aperture size can be changed, which has a big effect on resolution and SNR. A change in aperture will also require calibration of the microscope.

With the favourable electrical conductivity properties of aluminium and steel electrostatic charging issues are negligible, this allows for higher beam energies to be employed. An accelerating voltage of 25 kV was used as the accelerating voltage in these experiments. For all scans performed, the working distance was set at 25 mm. This is the distance between the final aperture and the sample surface where the electron beam is incident. This value is considered an optimum due to the geometry of the Zeiss microscope and the position of the detector in relation to the tilted sample at this distance.

The maximum and minimum number of peaks identified and digitally indexed can also be chosen. It is important to identify enough bands to obtain the necessary data to extrapolate all the orientation information available. Masking or inhibiting the real orientation information is a potential problem, though this can be controlled by changing the ρ fraction. This is the percentage of the Kikuchi pattern that is used [33]. A fraction of 1 would mean the entire pattern area is considered, whereas a fraction of 0.5 would focus on a circular area half of the maximum area value, maintaining the equivalent centre in the process.

Table 4.2 gives a definitive list of the parameters that can be changed together with the values deployed throughout the body of experimental work.

Parameter	***Setup conditions***
Electron Beam energy (kV)	25
Working distance (mm)	25
Aperture size (µm)	30 (standard)
Hough Transform type	Classic
Binned Pattern Size	Medium (9x9)
θ step size	0.5°
ρ fraction (Hough parameter)	0.79
Max Peak Amplitude	12
Min Peak Distance	5
Exposure time (s)	0.25

Table 4.2: Table of EBSD parameters and the selected values used for the experimental work.

4.4.2 – OIM Data Analysis program

The OIM data analysis software allows an unprecedented amount of detail to be extrapolated from the Euler angle data collected from an EBSD scan. Numerous maps and graphs can be generated, providing quantitative information on a variety of detailed micro and macrostructural-dependent material properties.

The typical representation of the Euler angle data is presented as an Inverse Pole Figure (IPF) map, of which figure 4.5 was an example. These maps represent specific orientations by assigning a colour; the colours are determined from the colour-coded inverse pole figure shown in figure 4.13 [34].

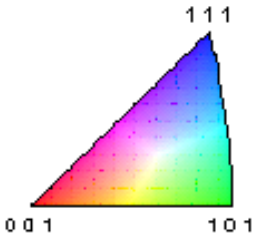

Figure 4.13: Inverse Pole Figure (IPF) used in OIM software for assigning a colour to a point with a given crystallographic orientation. <001> orientation is assigned a red tag. <101> assigned with green. <111> associated with blue.

The IPF is a unit triangle (see section 5.4.2.2), signifying that each point within the IPF represents a unique crystallographic orientation in <*hkl*> notation. The colours red, green and blue are associated with the principal directions <001> and its equivalents, <101> and its equivalents and <111> and its equivalents respectively.

Transforming between Miller index notation <*hkl*> and the Bunge-Euler angle ($\varphi_1, \Phi, \varphi_2$) orientation data is achieved via the following equations [35]:

$$h = n \sin \phi_2 \sin \Phi \tag{4.3}$$

$$k = n \cos \phi_2 \sin \Phi \tag{4.4}$$

$$l = n \cos \Phi \tag{4.5}$$

Here *n* is an integer-normalising factor. On analysis of these equations, the transformations to the Miller indices <hkl> from the Eulerian angle data are independent of the first Bunge-Euler angle φ_1; the two other angles Φ and φ_2 solely define the crystallographic direction. The angle φ_1 is a relative measurement defining the orientation of the crystal direction. After calculating the <hkl> values for each data point from the Eulerian angle data, the colour can be assigned by interpolating it from the colour-coded IPF.

From these IPF maps, regions of interest within the scans may become apparent. The OIM program allows datasets to be easily cropped. This is where a specific region of an EBSD plot can be selected and analysed exclusively. The enclosed data points within the region are extrapolated and mapped to a new grid.

There are different types of maps available besides the orientation IPF plots. These include grain identification and elastic stiffness. A number of graphs can be automatically generated, including the distribution of grain size and grain aspect ratios, which is of particular interest in this thesis.

Asides from the Eulerian angle data, a number of other coefficients are recorded for each data point. Figure 4.14 shows an example from an EBSD data set of one indexed point on a raster scan.

φ_1	Φ	Φ_2	*x*	*y*	*IQ*	*CI*	*Phase*	*A*	*B*
2.49037	1.66344	2.85083	18.000	0.000	151.8	0.259	0	18533	1.804

Figure 4.14: Example of the quantitative data saved for each data point by the OIM software.

The parameters measured aside from the Eulerian angles (in radians) include the Cartesian coordinates for the grid (*x* and *y*), the image quality (IQ) value, the confidence index (CI) and the calculated errors associated with these values in degrees. The image quality parameter is analogous to a measurement of the polished surface finish quality. The confidence index is a measure of the agreement of the voting scheme to the pre-selected phase

data. For multiphase materials it also indicates which pixel represents which phase, and there is also a measure of the signal amplitude detected.

The errors associated with EBSD, calculated from the IQ and CI values, are normally of the order of ± 0.2° for each of the three Euler angles [36]. This indicates the accuracy of the EBSD technique.

4.4.2.1 – Confidence index parameter

The confidence index (*CI*) parameter and image quality (*IQ*) value are two important coefficients that indicate the validity of the data collated. The voting system adopted to assign an orientation to a pixel does have inherent flaws, because in some circumstances incorrect indexing can occur. Scenarios explaining why points may be interpreted incorrectly are explained in section 4.4.2.2.

The confidence index in particular is an important statistical parameter, which indicates the statistical viability of a dataset and whether the data is truly representative of a sample. The *CI* can take values $\in [0,1]$, and is defined by equation 4.6 [37];

$$CI = \frac{V_1 - V_2}{V_{IDEAL}} \tag{4.6}$$

where *CI* is the confidence index for a data point, V_1 is the number of votes assigned to the orientation selected for a given data point, V_2 the number of votes given to the second most likely orientation, with V_{IDEAL} the total number of votes.

Therefore for a diffraction pattern that is conclusively resolved with a definite orientation, it will follow that it will have a high *CI* value (approaching 1), whereas a diffraction pattern that generates a variety of potential orientations will have very small *CI* values. It is therefore feasible that a pattern can be correctly indexed yet have a *CI* value = 0. It has been postulated that for data to be considered statistically viable, the average CI value is typically required to be > 0.1 [38].

4.4.2.2 – Digital data cleaning

With the OIM software using a voting scheme, comparing the Hough peaks to pre-calculated phase information to select the most likely crystallographic orientation, there can conceivably be problems with the data.

For example, occasionally the surface finish is inadequate, meaning an inclusion or a discontinuity in the near-surface crystalline structure will affect a generated Kikuchi diffraction pattern. A build up of plastic strain can also smear the Kikuchi bands making detection more difficult. There are many other types of discontinuities, the most frequent of which occur at grain boundaries [39]. At these points, the electron beam will inevitably produce backscattered electrons from two grains simultaneously, leaving the pattern irresolvable. When a pattern cannot be resolved and indexed, it is assigned a black colour on the IPF plot and given default Euler angle values of ($4\pi, 4\pi, 4\pi$) with a *CI* value of -1. There are also situations where the voting scheme will assign the incorrect orientation to a data point. If this occurrence is rare, this scenario will be easily visualised on an IPF map. Pixels within grains would probably be a different colour to the surrounding data points.

To optimise the quantitative data for further analysis, the OIM software has digital cleaning algorithms available to apply to the Euler angle data, which if applied correctly will enhance the data, and therefore the statistical reliability of the results [40]. Figure 4.15 shows a cropped section from an IPF map of an aluminium sample, displaying a grain with some erroneously indexed points, as circled. There are two images displayed; a pre- and post-application of a digital cleanup function.

Of the clean up algorithms built into the OIM software, the most effective ones are the grain dilation, the single average grain orientation and one that utilises a minimum confidence index parameter.

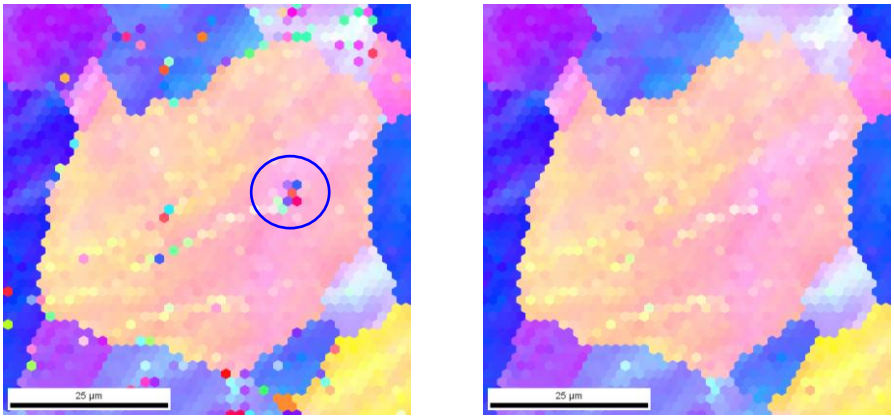

Figure 4.15: A cropped area, focussing specifically on a grain from an EBSD scan of a steel sample. On the left, erroneously indexed points are evident, as indicated by the circle, as they have been assigned different orientations in comparison to the surrounding grain orientation. Using suitable cleanup functions can resolve the problem, demonstrated by the grain on the right.

The grain dilation cleanup is a single iterative function that assesses each point and compares its angular difference in orientation with the neighbouring data points. For all scans produced in this thesis, each data point has 6 neighbouring points as the EBSD scans have been performed using a hexagonal grid. If a point does not satisfy the orientation agreement conditions defined by the operator, namely the point is not within the maximum acceptable misorientation angle and the minimum grain size, the point is assigned the average orientation of the 6 neighbours. This is an ideal technique to deploy for situations such as that demonstrated in figure 4.15, where isolated points within crystallographic grains can be easily converted to the average orientation of the 6 neighbouring points.

The single average grain orientation cleanup should be used when low-angle grain boundaries occur frequently. This is particularly prevalent in rolled steels where a high number of grains will align parallel to the <111> direction out of the plane of the sheet, as is the case for steel [30] (refer to section 5.4.4 for more detail). Selecting the minimum grain size and misorientation angle defines which grains to analyse. The cleanup function then takes the average orientation across the complete grain, and assigns each point within the grain the same average orientation.

The minimum confidence index (*CI*) value function requires the operator to choose a minimum *CI* value. Each point is checked, and for all those under the *CI* threshold, those points are assigned the orientation of the neighbouring point with the highest *CI* value above the threshold. It is typical to choose a min *CI* value close to the average *CI* of the overall dataset. This ensures that good data points are not unnecessarily changed.

4.5 – Surface preparation for EBSD

The optical microscope image displayed in figure 4.3 gave a good indication of the non-uniformity of a rolled metallic sample surface. With the primary electrons being diffracted by the near-surface lattice planes in EBSD, the existence of dislocations or artefacts can have significant effects on the intensity of the detected Kikuchi patterns.

4.5.1 – Polishing metallic samples for EBSD

Polishing a metallic sample for surface-specific microscopy can be compartmentalised into three discrete stages that are required to present a consistently homogeneous, flat and contaminant-free finish. These stages are grinding, fine mechanical polishing and electropolishing [41].

4.5.2 – Grinding

The initial grinding stage is only justified if the initial surface is extremely rough. This stage is done to enforce a consistent surface to perform the finer polishing on. Grinding uses Si-C paper, with the frictional heat created by the abrasive surface reduced with a wax coating and by applying water. The samples used in this study however were provided with a relatively uniform and flat surface, which meant this stage was not required.

4.5.3 – Mechanical polishing

The fine mechanical polishing stage utilises various diamond suspension solutions in conjunction with polishing cloths, selected dependent on the material. Aluminium and steel are recommended to be polished via a 1 μm diamond suspension, followed by a finer colloidal silica suspension polish.

4.5.4 – Electropolishing

Electropolishing is a technique which removes atoms from an anodic material and deposits it on a conductive cathode. The material being polished needs to be suitably electrically conductive for efficient results; aluminium and steel are ideal metals for electropolishing. This is all completed in an electrolyte specifically chosen for the material being polished. Electropolishing can work in two regimes; etching and polishing. The performance is dependent on the applied voltage. To calculate the polishing voltage, *voltage* vs. *current density* graph must be plotted and compared to the idealised *voltage* vs. *current density* curve (figure 4.16) where a plateau should exist for a discrete range of voltages. This defines the polishing voltage range for successful electropolishing [42].

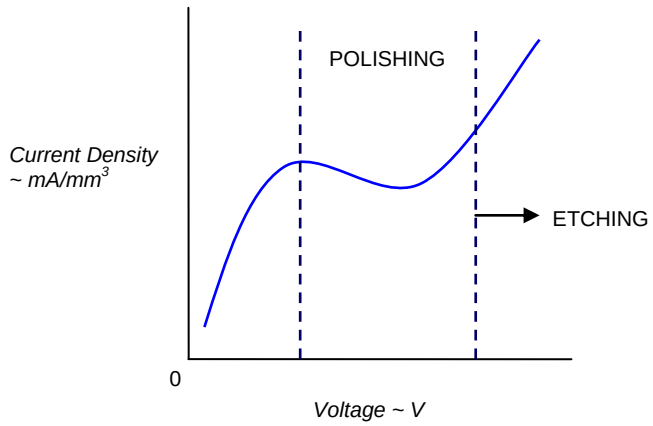

Figure 4.16: The theoretical Voltage (V) vs. Current density (j) curve for electropolishing

The specific operations, equipment used, timings and such like for each sample are detailed in chapter 8.

4.6 – Chapter summary

EBSD provides a suitable method to produce quantitative information on the microscopic scale by way of Eulerian angle data. This is in contrast to the bulk averaged ultrasonic data that can be collected using EMATs. EBSD provides a unique insight into the microstructure, and can provide a better understanding of the propagation and interaction of a wave with the microstructure.

4.7 – References

1. *Saunders M, Kong C, Shaw JA, Macey DJ, Clode PL, Journal of Structural Biology,* ***167(1)****, 2009, pp. 55-61*

2. *Zbik MS, Du J, Pushkarova RA, Smart R, Journal of Colloid and Interface Science,* ***336(2)****, 2009, pp. 616-623*

3. *Khedr MH, Farghali AA, Applied Catalysis B: Environmental,* ***61****, 2005, pp. 219-226*

4. *http://www.zeiss.com/C1256E4600305472/Contents-Frame/0689C92B86F9E5E9C1256E5A0049BA92*

5. *Goodhew PJ, Humphreys FJ, Electron Microscopy and Analysis, 2nd edition, Taylor & Francis, ISBN 0-85066-414-4*

6. *Thomas G, Goringe MJ, Transmission Electron Microscopy of Materials, Wiley- Interscience, 1979*

7. *Watt IM, The principles and practices of Electron Microscopy, 2nd edition, Cambridge University Press, 1997*

8. *Grant IS, Phillips WR, Electro-magnetism, 2nd edition, Wiley, 2001*

9. *Goldstein J, Newbury DE, Joy DC, Echlin P, Lyman CE, Lifshin E, Sawyer L, Scanning Electron Microscopy and X-Ray Microanalysis, 3rd edititon, Springer, 2003*

10. *Bozzola JJ, Methods Mol. Biol.,* ***369****, 2007, pp. 449-466*

11. *Michael JR, Electron Backscatter Diffraction in Materials Science edited by Schwartz AJ, Kumar M, Adams BL, Kluwer Academic, 2000, pp. 75-89*

12. *Janaky C, Visy C, Synthetic Metals,* ***128****, 2008, pp. 1009-1014*

13. *Michael JR, Goehner RP, MSA Bulletin,* ***23****, 1993, pp. 168-175*

14. *Kunze K, Wright SI, Adams BL, Dingley DJ, Textures Microstructures,* ***20****, 1993, pp. 41-54*

15. *Wright SI, Field DP, Proc. Microscopy and Analysis, 1997, Springer, pp. 561-562*

16. *Randle V, J. Mater. Sci., **44**, 2009, pp. 4211-4218*

17. *Dingley DJ, Wright SI, J Appl. Cryst., **42**, 2009, pp. 234-241*

18. *Essex SD, Potter MDG, Dixon S, Rev. Prog in QNDE, **28**, 2008, pp. 1727-1734*

19. *Wright SI, Electron Backscatter Diffraction in Materials Science edited by Schwartz AJ, Kumar M, Adams BL, Kluwer Academic, 2000, pp. 51-64*

20. *Davis CL, Strangwood M, Potter MDG, Dixon S, Morris PF, Metallurgical and Materials Transactions A, **39A(3)**, 2008, pp. 679-687*

21. *Wilkinson AJ, Electron Backscatter Diffraction in Materials Science edited by Schwartz AJ, Kumar M, Adams BL, Kluwer Academic, 2000, pp. 231-246*

22. *Humphreys FJ, Journal of Materials Science, **36**, 2001, pp. 3833-3854*

23. *Cohen JB, Diffraction Methods in Materials Science, Macmillan, 1966*

24. *Randle V, Electron Backscatter Diffraction in Materials Science edited by Schwartz AJ, Kumar M, Adams BL, Kluwer Academic, 2000, pp. 19-30*

25. *Schwarzer RA, Electron Backscatter Diffraction in Materials Science edited by Schwartz AJ, Kumar M, Adams BL, Kluwer Academic, 2000, pp. 105-122*

26. *Hook JR, Hall HE, Solid State Physics, 2nd edition, Wiley, 1991*

27. *Euler L, Formulae Generales, Nov. Comm Acad. Sci. Imp. Petrop., **20**, 1775, pp. 189-207*

28. *Roe R-J, Journal of Applied Physics, **36(6)**, 1965, pp. 2024-2031*

29. *Bunge H-J, Z. Metallk, **56**, 1965, pp. 872-874*

30. *Kocks UF, Tomé CN, Wenk H-R, Texture and Anisotropy, Cambridge University Press, 2000*

31. *Wright SI, J. Computer Assisted Microscopy, **5**, 1993, pp. 207-221*

32. *Russ JC, Bright DS, Hare TM, Journal of Computer-Assisted Microscopy, **1**, 1989, pp. 3-37*

33. *Sourced from OIM help file*

34. *Inokuti Y, Maeda C, Ito Y, Journal of the Japan Institute of Metals, **50**, 1986, pp. 874-878*

35. *Sourced from OIM help file*

36. *Demirel MC, El-Dasher BS, Adams BL, Electron Backscatter Diffraction in Materials Science edited by Schwartz AJ, Kumar M, Adams BL, Kluwer Academic, 2000, pp.65-74*

37. *Field DP, Ultramicroscopy, **67**, 1997, pp. 1-9*

38. *Petrov R, Kestens L, Wasilkowska A, Houbaert Y, Materials Science and Engineering A, **447**, 2007, pp. 285-297*

39. *Thompson RB, Margetan FJ, Haldipur P, Yu L, Li A, Panetta P, Wasan H, Wave Motion, **45**, 2008, pp. 655-674*

40. *Cao WQ, Godfrey A, Liu Q, Journal of Microscopy, **211(3)**, 2003, pp. 219-229*

41. *Tanem BS, Svenningsen G, Mårdalen J, Corrosion Science, **47(6)**, 2005, pp. 1506-1519*

42. *Bousfield B, Surface Preparation and Microscopy of Materials, John Wiley and Sons Inc, 1992*

CHAPTER 5

The Metallurgy of Rolled Sheet

Rolled aluminium and steel sheet are used in a range of manufacturing processes from beverage and food can production through to a wide range of white goods appliances and high technology and safety critical automotive and aerospace applications [1].

The manufacture of products from rolled sheet requires further forming, accomplished using processes such as extrusion and deep-drawing [2]. Before permanently and significantly deforming sheet metal, it is important to ensure that the mechanical properties of the as-rolled product are appropriate for the next production step.

The rolling process imparts elastic anisotropy to the polycrystalline structure, due to the large compressive forces applied to the metal by the rolls [3]. The morphology and alignment of the discrete grains is altered as their shape and dimensions are forcibly changed. Quantifying the crystallographic texture and the grain aspect ratio forms the foundation of the experimental work for this thesis. Previous workers have shown that quantifying ultrasonically such material properties enables one to make predictions of the formability behaviour and final mechanical properties of the plastically deformed sheet.

5.1 - Deformation effects at the microstructural level

5.1.1 – Crystal lattice structure of aluminium and steel

Before predicting the formability behaviour of sheet metal, it is imperative to develop an understanding of the initial atomic structure and its respective properties first. The resulting change from this initial frame of reference is determines the severity of the plastic deformation of the rolling process.

The atomic structure of metals is defined by the crystal lattice. The lattice is a regular, repetitive framework with the ions located at designated sites defined by the unit cell [4]. Aluminium and austenitic steel crystallise with a face centred cubic (fcc) unit cell, with the ferritic steel alloys typically crystallising with a body centred cubic (bcc) unit cell (shown in figures 5.1a and 5.1b).

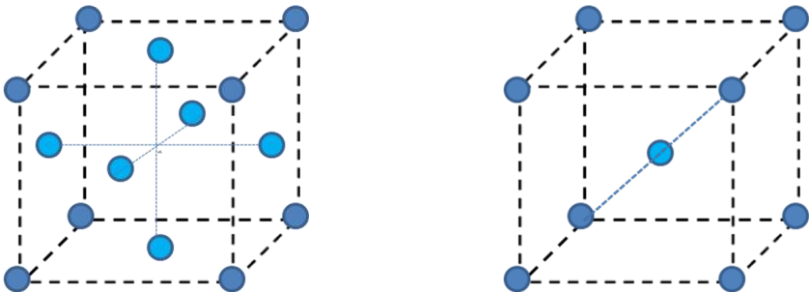

(a) fcc (b) bcc

Figure 5.1: Unit cells representing the lattice structure of metals that crystallise as a face-centred cubic (a) and body-centred cubic (b). For both, ions are positioned at the 8 corners of the cube. A bcc unit cell has a final ion positioned at the centre of the cube, with the fcc unit cell having an ion positioned in the geometric centre of the 6 faces of the cube.

Aluminium is the most abundant metal in the Earth's crust. However, it is found naturally as an alloy because of its high reactivity. Aluminium crystallises with an fcc lattice structure, and in comparison to steel is a simple material to work with and computationally model. It is resistant to corrosion, weakly paramagnetic, lightweight and malleable, making it an ideal material for a number of applications, as discussed in chapter 1.

In contrast, the unit cell structure of a steel alloy is more complex, and depends on the iron phase present. The phase can either be α-, γ- or δ-iron [1]. Nominally pure iron exists as the α-iron phase, typically known as ferrite, and crystallises with a bcc unit cell. This holds with the bcc staying structurally stable providing the ferrite material is not heated to a temperature above 910˚C. α-Ferrite can be considered pure iron, as in this circumstance only a very small weight % (~ 0.005%) of Carbon will exist in the alloy [1], and is ferromagnetic. At a temperature exceeding 910˚C, the iron is subjected to a phase transformation, switching

to an fcc unit cell, and is called γ-iron. This is known as austenite, which is non-magnetic. A further transformation reverting back to a bcc unit cell occurs at 1390˚C, known as δ-iron (δ-ferrite). This remains stable up to the melting point of iron which is 1536˚C [5]. With the ease in which carbon and nitrogen in particular can precipitate in iron and with the cooling rate of iron having a significant effect on the resultant microstructure, it is perhaps no surprise that there are other common iron phases.

Martensite is one such phase, and results when austenite is rapidly cooled [6]. It is a metastable iron phase which traps carbon atoms during cooling, preventing the diffusion of such atoms. Martensite has a body-centred tetragonal structure. If too much of this phase is present, steel would be brittle, though the existence of some improves hardness. Another phase, cementite (iron carbide Fe_3C), can form during the cooling of austenite, or from tempering methods (heat treatment) of martensite, mixing with ferrite components to produce a lamellar-type structure of pearlite and bainite [7]. With the presence of ferrite, cementite will make a contribution to the magnetic properties. Pearlite is constructed of α-iron and cementite, again existing as a lamellar structure it forms when austenite is cooled [1].

5.1.2 – Microstructure: grain formation

The composition of a polycrystalline aggregate's microstructure is determined by the orientation, morphology and size of the crystals and the constituent grains they belong to. A grain is a volume of crystals with similar crystallographic orientation. These crystallographic grains are of specific interest in this body of work, and are extremely important in characterizing the formability and mechanical properties of a metal [8].

Grain growth develops during solidification; the process when metal solidifies from a molten liquid state. This can be considered the extreme case of recrystallisation. Small nuclei above a critical size form in random locations, with each adhering to the lattice structure of the metal. Each of these nuclei grows independently, developing randomized lattice orientations relative to the other nuclei and also to the sample frame of reference [9]. A nucleation process is initiated, with each nucleus being a focal source of grain growth, which

spreads in all directions. The new adjoining atoms will (ideally) inherit the metal's lattice structure, maintaining the orientation of the initial nucleus. Eventually these discretely growing grains coincide, forming definitive grain boundaries.

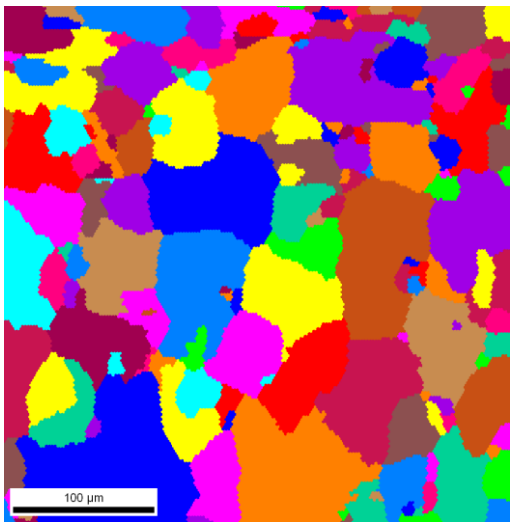

Figure 5.2: An EBSD Grain Identification Map (GIM) from a rolled aluminium sample. The colours of these grains highlighted by the GIM are arbitrary and independent of the crystallographic orientations of the grains themselves.

The aggregate of these grains constitutes the microstructure, which influences the physical properties that the metal exhibits. Using a microscopic technique such as EBSD with resolution on the *nm* scale means a good visualisation of the microstructure is possible, as demonstrated by the grain identification map in figure 5.2. Here each grain is assigned a random colour. Unlike the orientation IPF maps discussed in chapter 3, the colours are not indicative of any crystallographic orientation: the colours are assigned completely randomly to highlight the existence of a grain.

5.1.3 – Deformation of the microstructure

When under an applied load, a polycrystalline metal will deform. The deformation to the lattice will either occur *elastically* or *plastically* [9], dependent on the magnitude of the load relative to the yield strength of the metal.

5.1.3.1 – Elastic deformation

For applied loads below the yield stress, the crystal lattice will elastically deform in response to the applied force. Upon removing the load, the lattice returns to its initial state, maintaining the original interatomic planar spacing, shape and size. The elastic deformation can be quantified by such relationships as Hooke's law of elasticity and Poisson's ratio.

Chapter 2 introduced Hooke's law (equation 2.1) and the relationship between the 2nd rank tensor properties of stress, σ_{ij}, and strain, ε_{kl}, with the 4th rank elasticity tensor c_{ijkl}. c_{ijkl} is comprised of 81 elastic stiffness constants fully defining the elastic behaviour of a material. The isotropic state for metals was also introduced, with the tensor dependent on just the single crystal constants. For cubic symmetry materials such as aluminium and steel, these are c_{1111}, c_{1122} and c_{2323} (and its 3 equivalents).

5.1.3.2 – Plastic deformation

To reduce permanently the thickness of a billet, bloom or plate, plastic deformation is required. Plastic deformation can be visualised as the flow-like behaviour of a solid, with the resulting deformed metal often maintaining, and in certain cases enhancing, the initial material properties [10].

When the yield strength is exceeded, there are two conceivable options: the metal can either *fracture* or *slip*. A fracture is self-explanatory. Slip can be thought of as the movement of one atomic plane sliding over another. Using a 'least energy' argument, slip is typically a more desirable outcome compared to the catastrophic consequence of fracture. Slip induces a permanent and irreversible change in the shape and structure, though the polycrystalline volume is maintained.

5.1.4 – Slip: an introduction

The periodic nature of the crystal lattice can be observed on a macroscopic scale as many planes overlapping each other. These planes project in a number of different geometries. For example, for a primitive cubic lattice such as that shown in figure 5.3a, a plane such as that shown along A_1, can be seen in all three Cartesian directions x, y and z. The knowledge of the lattice structure for a given material can be extended to help understand further the formation and direction of prevalent slip planes. The most prevalent slip planes can therefore be predicted for different lattice structures [11].

For example, figure 5.3 depicts two lattice structures: Figure 5.3a depicts two planes, A_1 and A_2, with corresponding atoms directly aligned with each other. This is representative of a primitive cubic lattice system. In this instance, it has an interatomic planar spacing equal to the diameter of one atom. Each plane has a high atomic density both vertically and horizontally such as along A_1 and A_2. In figure 5.3b, the lattice structure defined by the planes B_1 and B_2 have a smaller atomic separation and lower atomic density. On consideration of the resistance to motion, slip is more likely to occur between planes A_1 and A_2.

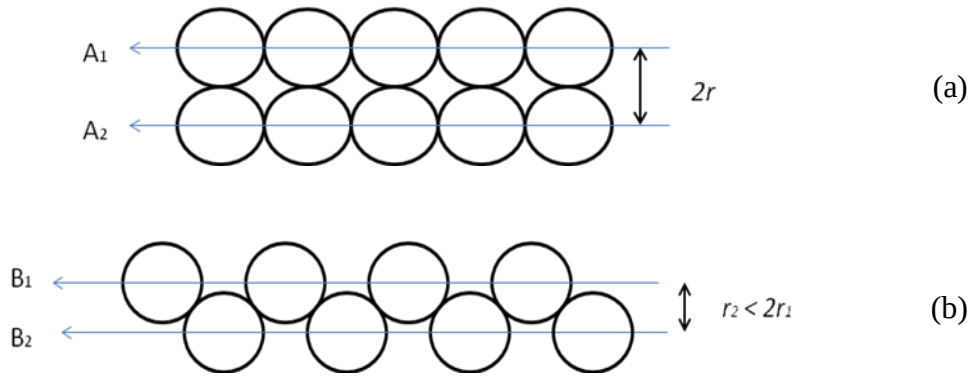

Figure 5.3: Schematic diagram showing atoms adhering to two different lattice structures. The first lattice (a) is representative of the primitive cubic lattice. The interplanar spacing is equivalent to the diameter of one atom, with the planes possessing maximum atomic density. In the second lattice (b), the planar spacing is smaller (assuming the atoms are the same size) with a smaller atomic density per plane.

5.1.5 – Slip planes in bcc and fcc polycrystalline metals

For a polycrystalline metal sheet, this simplified slip description is not valid, given it is constructed of discrete grains. The grains have different lattice orientations implying that the lattice structure is not homogenous throughout. The continuous propagation of one slip system throughout the bulk of the sheet is therefore not plausible [12]. Any resulting plastic deformation as the yield point is exceeded is consequently the averaged accumulation of the generated slip systems confined within each of the constituent grains.

Table 5.1 gives the characteristic primary and secondary slip systems for fcc and bcc metals [13]. Of note is the preference for bcc systems to slip aligning parallel to the <111> direction. This implies that for plastically deformed bcc ferritic steel, <111> crystallographic orientations will dominate perpendicular to the RD-TD plane (see figure 5.7).

Material	***Primary slip system***	***Secondary slip system***
fcc	$\{111\}\langle 1\bar{1}0\rangle$	-
bcc	$\{110\}\langle \bar{1}11\rangle$	$\{112\}\langle 11\bar{1}\rangle$ $\{123\}\langle 11\bar{1}\rangle$

Table 5.1: Shows the common slip planes {uvw} and directions <hkl> for fcc and bcc crystallising materials.

5.1.6 – Edge and screw dislocations

The initiation of slip systems in polycrystalline materials is due to the movement of line defects which are positioned along the slip planes. A defect is anything which interrupts the continuity of a crystal lattice, including point defects such as vacancies or extra interstitial atoms that manifest themselves within the crystal lattice.

The line defects are known as dislocations. There are two primary orientations of these dislocations; an edge dislocation, and a screw dislocation. A single edge dislocation is illustrated in figure 5.4; it is caused by the shearing of a crystal by one atomic distance about

a plane. The propagation of a dislocation completely through a crystal lattice eventually leads to an edge at the surface. This edge is small (~ Å) and hence is difficult to detect. However, an accumulation of a number of edge dislocations along the same slip plane can produce visible slip lines [14].

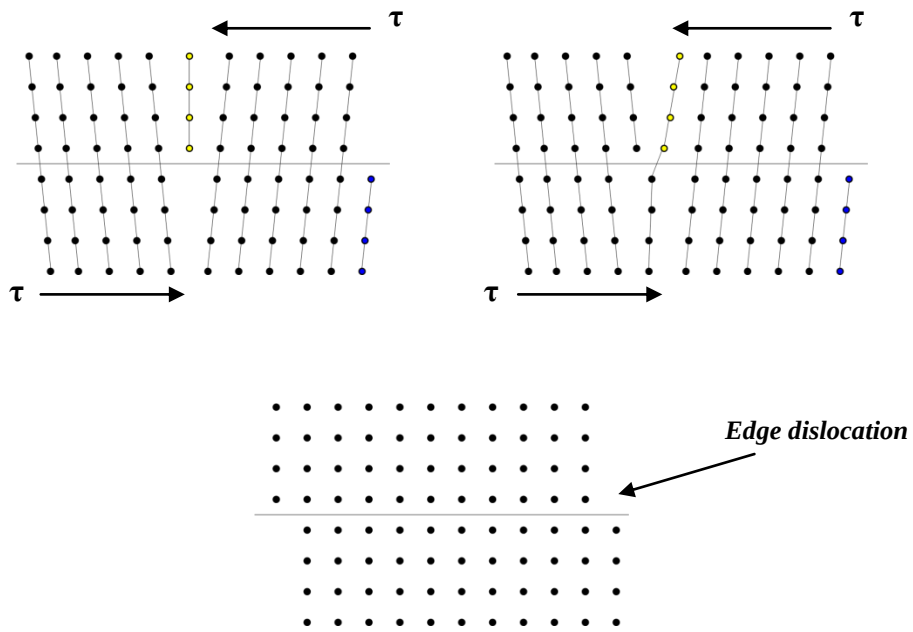

Figure 5.4: Schematic diagram showing the propagation of a single edge dislocation. A shear stress τ is applied such that the lattice is displaced by on atomic distance (blue atoms). The dislocation (yellow atoms) then propagates along the lattice as shown by the right hand diagram. If the dislocation propagates throughout the entire crystalline aggregate, a definitive edge dislocation is formed.

The other basic orientation, the screw dislocation, is difficult to visualise. The dislocation, which can be seen schematically in figure 5.5 [15], does not propagate right through the entire crystal like an edge dislocation. It is a helical-like defect, analogous to a spiral staircase, about the dislocation which involves crystals from the interatomic planes above or below the slip plane: which plane is involved determines the direction of the screw dislocation.

The magnitude and direction of a dislocation and corresponding lattice distortion is defined by a Burgers vector, **b**. For an edge dislocation, the Burgers vector is perpendicular to

the dislocation. The Burgers vector is parallel to the dislocation in the case of the screw orientation.

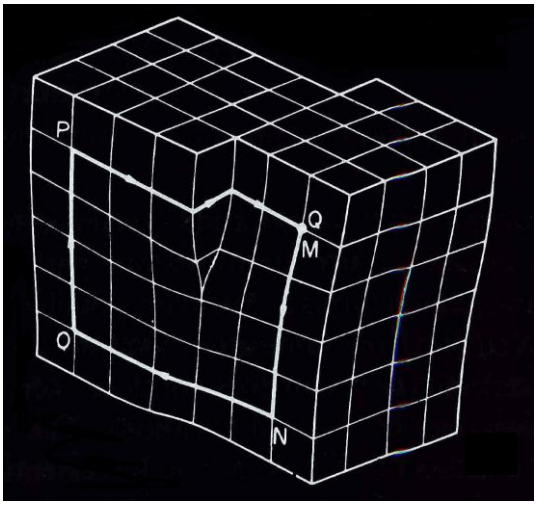

***Figure 5.5: Schematic diagram of a screw dislocation, taken from [15]. The highlighted path MNOPQ is a Burger's circuit which when placed in a perfect crystal would have to be altered to accommodate the lack of dislocation. This change in the circuit defines the Burgers vector* b.**

The dislocations stop propagating when they encounter a grain boundary. The increase in dislocation density at the grain boundaries is a major contributor to ultrasonic wave scattering, and is discussed in further detail later.

With the introduction of slip during rolling, a breakdown in isotropic / cubic symmetry will be enforced, implying the elastic behaviour in cubic-crystallising metals will change [9]. The lower symmetry order arises from a loss in isotropy of the ODF; despite the fact that each grain is cubic and elastically anisotropic (see section 5.4). The rolling process is inherently directional and as such means the material properties become directional too.

In conclusion, once anisotropy and the directionality dependence of material properties is evident, different types and levels of anisotropy, or texture, will have more desirable characteristics for particular applications. This is why characterizing rolled sheet metal is extremely important in maximising the reliability in and performance of the manufacturing process of the final product.

The remainder of this chapter describes the methods used to manufacture rolled aluminium and steel sheet, and then discusses the material properties of interest and how they are detected usually.

5.2 – Production of rolled sheet

Rolling is a formability process that reduces the thickness of a starting stock of metal, usually in billet, bloom or plate form [16]. This forming process can be completed in two temperature regimes; either above (hot rolling) or below (cold rolling) the recrystallisation temperature for the particular metal being rolled. As a guide typical recrystallisation temperatures for cold rolled aluminium are relatively low, with values as low as 150˚C. Iron (steel) in contrast has a minimum recrystallisation temperature of 450˚C [1].

The rolling process can be depicted on a simplified level as two rolls, rotating with opposite angular directions, which subject large pressures on the incoming bloom / billet / plate, with the purpose to reduce the thickness of the metal leaving the rolls (figure 5.6). The thickness of the resulting sheet is determined by the separation of the rolls (t_2). The rotational velocity of the rolls has to be greater than the speed of the metal as it enters; this is ensured by the large frictional forces that translate the compression component force of the rolls to produce the plastic deformation required to reduce the sheet thickness [17].

As metal is subjected to forming processes, the overall volume will be conserved; as thickness reduces a transverse displacement must therefore occur [18]. The ratio of reduction, r_{red}, is used to indicate the level of working a sheet has experienced and is given simply by:

$$r_{red} = \frac{t_2}{t_1} \tag{5.1}$$

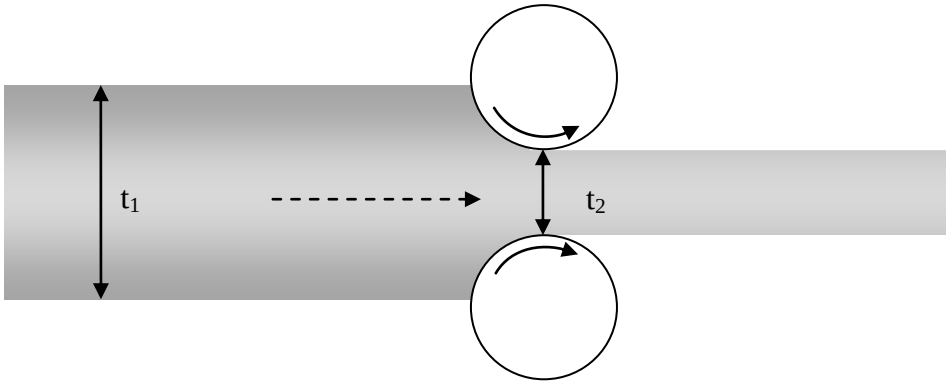

Figure 5.6: Schematic diagram showing the principal of rolling to manufacture sheet metal. This simplified configuration can be used in both the hot and cold temperature regimes. For hot rolling, the metal enters the rolls, with overall thickness being reduced. Recrystallisation then occurs as the metal is cooled.

with t_1 the original thickness and t_2 the final sheet thickness. Achieving high reduction levels where $t_1 >> t_2$, is usually achieved with a number of successive rolls, especially if working in the cold regime [16].

Aside from the simplified rolling setup displayed in figure 5.6, there are numerous arrays of complicated rolling arrangements available, used to produce a variety of rolled products [16]. Though rolling is commonly used to produce flat sheet, it is a versatile technique; it can be used to bend metal into desired shapes, completed by rolling configurations including the three-roll shoe-type and pyramid-type rolls.

5.2.1 - Hot rolling

Hot rolling is performed at temperatures above the recrystallisation temperature for a metal. In this instance both plastic deformation and recrystallisation mechanisms will occur simultaneously [19].

A major advantage of hot rolling is that the forces involved in reducing the thickness of a recrystallising metal stock is significantly lower in comparison to a metal when rolled at room temperature [16]. For a thicker starting stock, hot rolling is a more suitable and desirable method. There are disadvantages in using the hot rolling process; accurate control of

the temperature of the metal is crucial to maintain homogeneity of mechanical properties throughout the bulk of the sheet. A uniform distribution of temperature throughout the stock bulk of the hot metal is necessary to accomplish this, which is extremely difficult to achieve [16]. The major challenges lie in controlling the cooling rates, especially at the extremes in comparison to the bulk. With advancements in the understanding of such temperature-control uniformity, hot rolling processes have been improving continuously. Another disadvantage of the hot rolling process is that it can be difficult to produce very thin sheets, and it is near-impossible to make shaped products.

The resulting mechanical properties of hot rolled sheet are dependent on the cooling rates, which has a significant effect on the nucleation rate of grain growth. Microstructural anisotropy, such as grain elongation is however significantly reduced, with the grains tending to be equiaxed as they form. The severity of the anisotropy due to hot working is therefore not as significant in comparison to cold rolling.

5.2.2 - Cold rolling

Thin sheet is usually manufactured by cold rolling because it offers better accuracy dimensionally, as well as a substantially superior surface finish in comparison to hot rolling. The fundamental rolling principles are similar to hot rolling, with the preparation and control of the starting stock being much easier. However the machinery used requires more power due to the necessary increase in the compressive forces required to generate the friction between the rolling contact point and sample to reduce the thickness [20].

Not all cold-rolling processes require massive forces; they can be varied depending on the final product requirements. For example, skin-rolling is a technique that reduces the thickness by no more than 1% [16]. It is used to produce an optimum surface finish in conjunction with better malleability properties. This is ideal preparation before further cold-forming applications.

With sheet thickness reduction levels approaching 50% in some cases, the ductility is reduced in line with an increase in the yield strength [21]. With an increase in the reduction

ratio r_{red}, the condition of the resulting metal regarding its yield strength, ductility and anisotropy is indicated by its associated label such as half-hard and full-hard. For a half-hard material, the ductility properties are such that the sheet can be bent 90˚ before fracture. A full-hard material can bend 45˚ before fracture, and so on.

The continued deformation of a metal using cold-working will eventually result in fracture. Therefore when significant amounts of cold-working are planned, annealing stages are introduced to reduce the build up of strain. This is often the case in sheet production as thicknesses can be reduced down to as little as 0.2 mm. A specimen is considered to be a sheet when at a thickness of 5 mm or lower [22].

5.3 – Material properties of interest

The rolling process, and in particular cold-rolling, influences significantly the mechanical and elastic properties of the sheet. Grains elongate along the rolling direction, with the slip systems inducing preferential axes of alignment for the grains. The preferential alignment of crystallographic orientations, also known as crystallographic texture, is important in formability predictions, and can be linked to elastic anisotropy [23]. An indication of the magnitude of properties such as residual strain, yield strength and malleability can be determined from information on the average grain size and shape.

The following sections 5.4-5.7 details the material properties of interest that are to be measured using ultrasonic techniques and are correlated with data obtained from EBSD.

5.4 – Crystallographic texture

5.4.1 – What is crystallographic texture?

The consequence of slip leads to the constituent grains tending to align along preferential axes of alignment, with certain crystallographic orientations more abundant than others [24]. Texture is effectively a measure of the severity of this preferential alignment and

we measure its effect ultrasonically on the directionality of the elastic behaviour within the sheet.

It has been discussed that the directionality of rolling enforces orthorhombic symmetry [9] with a new orthogonal axis system created; the axes are coincident to the rolling direction, the transverse direction and the normal direction (figure 5.7). The elastic behaviour of a sheet with orthorhombic symmetry is defined by nine independent effective elastic constants (in matrix notation), in comparison to the three that define cubic symmetry.

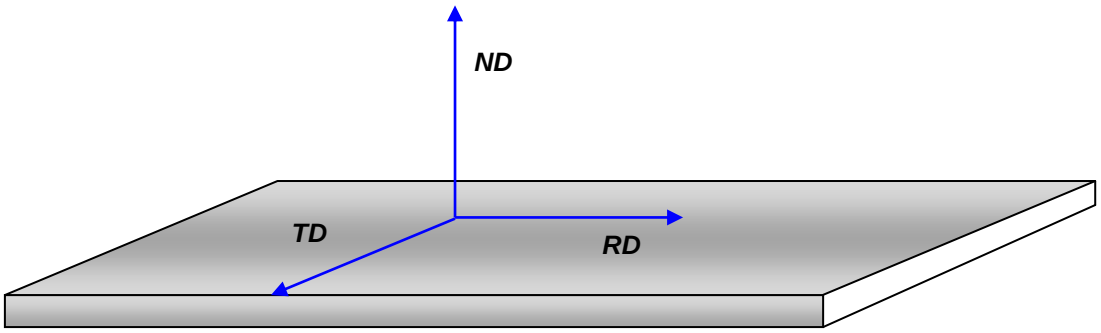

Figure 5.7: Geometry for the orthorhombic continuum associated with a rolled sheet. The three orthogonal axes are the rolling direction (RD), the transverse direction (TD) and the normal direction (ND).

In an isotropic, homogeneous situation, a crystal in an arbitrary position can take on any orientation with equal likeliness, and in the case of a polycrystalline sheet, this argument can be extended to grains. A probability distribution can be applied as a result of the properties possessed by the Crystallite Orientation Distribution Function (ODF) $w(\xi,\psi,\varphi)$ [25] (previously stated in equation 2.25):

$$\int_0^{2\pi}\int_0^{2\pi}\int_{-1}^{1} w(\xi,\psi,\varphi)\,d\xi\,d\psi\,d\varphi = 1 \qquad (5.2)$$

Here $\xi = \cos\theta$, with θ, ψ and φ the *Roe-Euler* angles that define a crystallographic orientation (section 4.3.3). The equation is an integration of all the crystals (or grains) over all

possible crystallographic orientations. In the isotropic case, each orientation would output an equal value, but in the orthorhombic case the probability for orientations will fluctuate.

The ODF has been shown to provide a potential and convenient way to measure texture quantitatively using ultrasound [26], discussed in detail in subsequent chapters 6 and 7. Given the ODF is a function dependent on Eulerian angle data, it has the scope to be solved quantitatively using EBSD data too.

5.4.2 – Usual representations of texture

There are numerous definitions of Eulerian angles; the OIM EBSD software works with Bunge-Euler angle notation, and from here on unless otherwise specified, any reference to Euler angles will be assuming Bunge notation ($\varphi_1, \Phi, \varphi_2$). The three angles ($\varphi_1, \Phi, \varphi_2$) are rotations used to map between the crystal system and the sample system [27]. This is mathematically represented by the orientation matrix g, which is dependent on the three Bunge Euler-angles, and has been modified from Roe's [25] orientation matrix definition:

$$g = \begin{pmatrix} \cos\phi_1 \cos\phi_2 - \sin\phi_1 \sin\phi_2 \cos\Phi & \sin\phi_1 \cos\phi_2 + \cos\phi_1 \sin\phi_2 \cos\Phi & \sin\phi_2 \sin\Phi \\ -\cos\phi_1 \sin\phi_2 - \sin\phi_1 \cos\phi_2 \cos\Phi & -\sin\phi_1 \sin\phi_2 + \cos\phi_1 \cos\phi_2 \cos\Phi & \cos\phi_2 \sin\Phi \\ \sin\phi_1 \sin\Phi & -\cos\phi_1 \sin\Phi & \cos\Phi \end{pmatrix} \quad (5.3)$$

Describing a crystallographic orientation with a 3 × 3 matrix such as that shown in equation 5.3 is not ideal because it has nine coefficients. Representing this data for a number of crystals, measured by techniques such as EBSD, in 2- or 3D plots is impossible without manipulation into another format.

An expedient way to represent crystallographic orientations is to use Miller indices. These give real, discrete values which can be plotted to solve the ODF and identify the existence of texture [4].

It should be noted that a <*hkl*> defined orientation can be obtained using a non-unique set of Euler angles. For example, and in reference to chapter 4 equations 4.3-4.5, the crystallographic orientation <001> is obtained for Φ and $\varphi_2 = 0^\circ$, though φ_1 can take on any

value $\in [0,2\pi]$. For less trivial directions such as <111>, there still exist a number of sets of values for Φ and φ_2, together with the independent φ_1 angle, which satisfy the equations.

Specific texture components are defined by Miller indices in a way analogous to slip systems, as they are specified by the two directions (see section 4.1.5) [28]. The first direction {*uvw*} represents a plane parallel to the rolling plane, with the second direction <*hkl*> parallel to the RD. The expected texture components in rolled sheet are discussed in the subsequent work, and are defined by {*uvw*}<*hkl*> notation.

There are three popular ways via diffraction methods to determine the existence of, and type of, texture within a given sample. All three require orientation information, presented in ($\varphi_1, \Phi, \varphi_2$) and <*hkl*> forms.

5.4.2.1 – Pole figure

The first method used in texture studies is the pole figure. A pole figure is a stereographic projection of three pre-defined primary axes for each crystal investigated onto the surface of a sphere: <001>, <010> and <100> are the axes typically chosen [29]. Producing such a plot requires crystallographic data, acquired from surface-specific diffraction techniques such as XRD, neutron diffraction or EBSD. A schematic diagram of the pole figure projection is shown in figure 5.8.

A primary axis pole [*hkl*] is required, and for experiments with rolled sheet, researchers use the [111] pole frequently, as for steel in particular, there is a preferential alignment of the crystals with the <111> direction out of the plane of the sheet. In the case where the [111] pole is selected, the <111> axis for each crystal, along with its geometric equivalents, are projected onto the surface of the sphere. Both hemispheres contain identical information, though inverted; it is convenient to extract just the pole data in the northern hemisphere, visualising the pole plots looking from above projected onto the southern hemisphere. Figure 5.9 illustrates the geometry of this, with figure 5.10 giving an example of a [111] EBSD pole figure plot taken from a rolled aluminium sample.

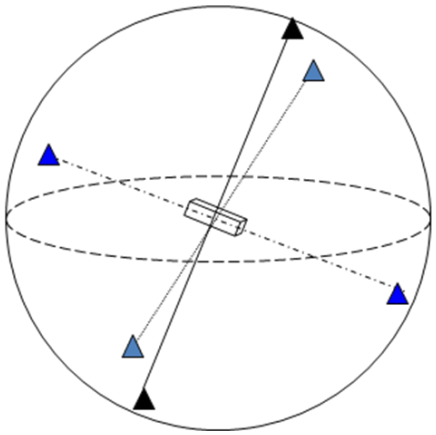

Figure 5.8: A stereographic pole figure projection. A pre-determined pole direction [hkl] is selected. For a crystal with cubic symmetry, the three axes that are equivalent to the defined pole are extended in both the positive and negative directions until they coincide with the unit sphere surface. This process is completed on all investigated crystals. The more abundant orientations will populate areas on the sphere surface with more intensity. Such data can be used to solve the ODF.

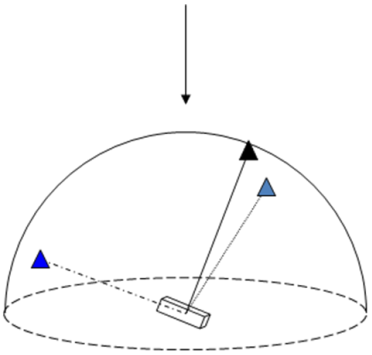

Figure 5.9: Geometry and chosen field of view of the northern hemisphere taken from the example depicted in figure 5.7. This is the data traditionally selected for stereographic pole figure analysis.

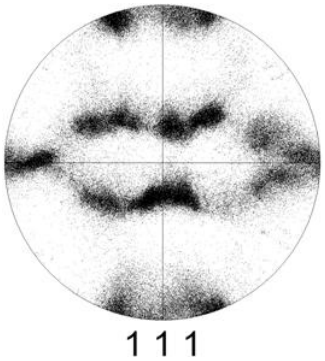

Figure 5.10: [111] Pole figure generated from Bunge-Euler angle data obtained from an EBSD scan on a rolled aluminium sample. This is the plot of the northern hemisphere poles looking from above the unit sphere.

The benefit of using pole figure projections is that it maps orientation data defined by the three Euler angles into two-dimensional plots. Referring to figure 5.10, sections that are densely populated are evident, and with expert knowledge make it possible to extrapolate instantaneous qualitative information regarding which orientations and texture components are dominant within the sample. Advances in analysis software, especially for XRD systems, has meant that quantitative data can be computed, relating the percentage and density of poles that correspond to specific crystallographic directions. This can therefore provide a method for solving the ODF [30].

5.4.2.2 – Inverse pole figure

The inverse pole figure (IPF), introduced in 4.4.2 when describing the colour code for Auto IPF plots generated using EBSD, is a specific subset of the surface of the unit sphere depicted in figure 5.8. IPFs are triangular in shape and are special divisions of the surface of the unit sphere used in full pole figure projections. There are numerous unit triangles on the surface; a unit triangle borders an area on the sphere surface where each point within it represents a unique crystallographic orientation (in <*hkl*> notation) [31]. All orientations are represented, and hence the IPF contains as much information as a full pole figure. It is this 'orientation uniqueness' property which is utilised in producing the colour-code for those EBSD plots.

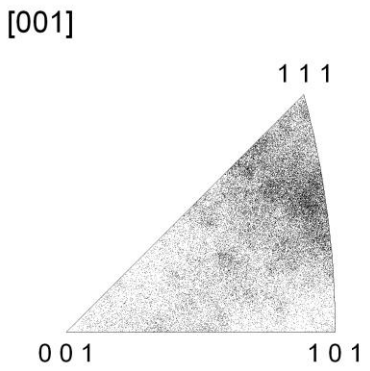

Figure 5.11: [001] IPF plot for a rolled steel sheet. The pole figure was generated from Bunge-Euler angle EBSD data taken.

Figure 5.11 is an example of a [001] IPF unit triangle plot generated from EBSD data for a rolled steel sample. As is observable, the orientations are labelled in an <*hkl*> format, with the three primary directions <001>, <101> and <111> assigned to the apexes of the triangle. In this instance there are more crystals with an orientation approaching <111> than either <101> or <001>, given by the denser population of poles in the <111> apex.

5.4.2.3 – Euler space ODF plot

Another way in which texture can be analysed is via 2D Euler space plots [32]. In contrast to pole figures and IPF's which map the crystallographic orientations onto the surface of the unit sphere, Euler space ODF plots plot two angles, usually φ_1 and Φ, fixing the third angle φ_2. A series of plots, such as in figure 5.12, is produced for varying values of φ_2 here increasing in 5˚ increments. This plot allows the user to ascertain the most prevalent orientations, designated by areas of high pole density, which can be used to solve the ODF. The use of Euler space plots is common in studies investigating texture evolution of a sample. It is convenient to compare the corresponding plots to observe the changes.

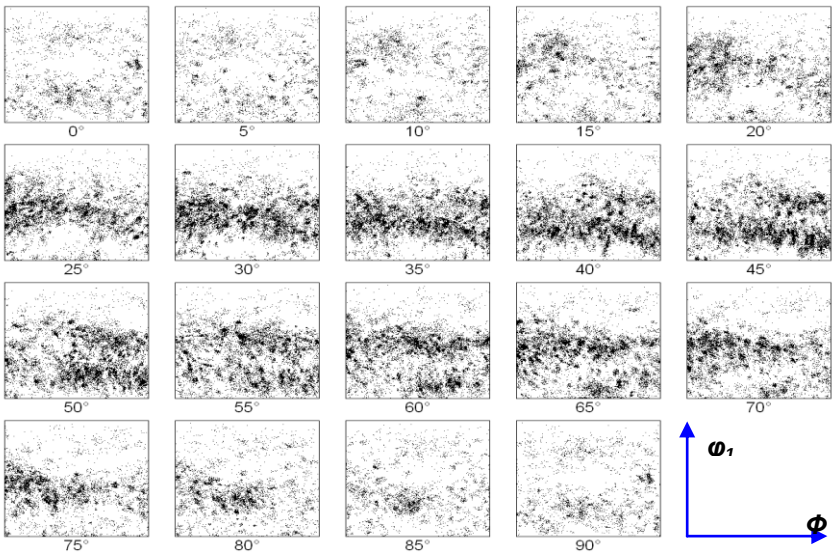

Figure 5.12: Euler Space ODF plot from a Steel sample, generated from EBSD data by the OIM analysis program. Each plot shows the orientations measured for a fixed φ_2 value, and plotting φ_1 (y-axis) versus Φ (x-axis). Areas that appear darker are indicative of the most abundant orientations.

Pole Figures, Inverse pole figures and Euler plots are achievable using diffraction techniques such as EBSD, X-ray Diffraction (XRD) and Neutron Diffraction. The data that would be produced from these three methods can be generated using both the OIM EBSD software and the *PANalytical X'Pert Pro Multi Purpose Diffractometer XG23* equipment and *X'pert Texture* software [33] (available at the University of Warwick).

Despite these diffraction techniques already being established, there is a need to measure texture using NDT methods. Orientation data acquisition by diffraction techniques is a time-consuming process, and the techniques are thus unsuitable for online testing. In addition, there are problems for online applications because of the required surface finish, the limited scan areas, the testing equipment and environment, and safety issues due to the radiation sources required. EBSD and XRD are also surface specific, and hence require assumptions on texture homogeneity in the bulk, for the results to be considered representative of the sample.

5.4.3 - Texture in rolled fcc metals (aluminium)

For fcc metals, the primary slip system is $\{111\}\langle 1\bar{1}0\rangle$ (table 5.1). Extensive research completed using pole figure data for rolled aluminium sheet has identified the most prevalent rolling textures. Table 5.2 lists these common texture components, defined by the indices {*uvw*}<*hkl*> along with their respective Euler angle values [34].

The indices representing the texture and slip systems must obey;

$$\{uvw\}.\langle hkl\rangle = 0 \tag{5.4}$$

$$\therefore uh + vk + wl = 0 \tag{5.5}$$

This arises from the orthogonal relationship between the {uvw} plane and the corresponding <hkl> direction.

Texture Type	*Indices*	*Bunge-Euler angles (φ_1,Φ,φ_2)*
Copper	$\{112\}\langle 11\bar{1}\rangle$	90°, 35°, 45°
Brass	$\{110\}\langle 21\bar{1}\rangle$	35°, 45°, 0°
Goss	$\{110\}\langle 001\rangle$	0°, 45°, 0°
S1	$\{124\}\langle 21\bar{1}\rangle$	59°, 29°, 63°
S2	$\{123\}\langle 41\bar{2}\rangle$	47°, 37°, 63°
S3 (often called S)	$\{123\}\langle 63\bar{4}\rangle$	59°, 37°, 63°

Table 5.2: List of common rolling texture components prevalent in fcc crystallising metals.

Figure 5.13 is a representative schematic diagram of a [111] pole figure showing the poles that would be densely populated in the existence of the Copper texture component [34]. Comparing this to the pole figure data shown in figure 5.10 for example, it would be a good approximation to state that the 'Copper' texture is a dominant component in that particular rolled sheet sample. Similar predictive pole figures can be made for each of the texture components listed in table 5.2.

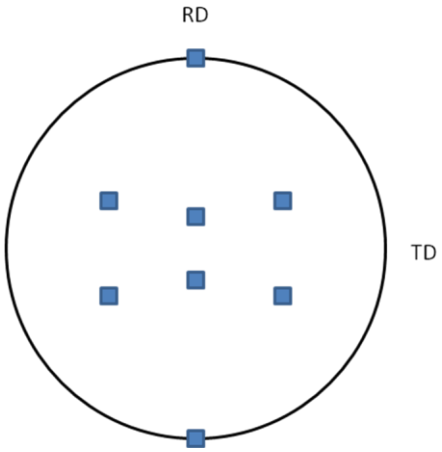

Figure 5.13: Schematic diagram of a [111] pole figure projection, showing the regions on the upper hemisphere of the unit sphere the poles would project onto in the existence of the rolling texture copper component $\{112\}\langle 11\bar{1}\rangle$.

The copper component is typically associated with metals that are nominally pure, whereas for alloys it is typically a lesser contributor. For anisotropic alloys, the Brass component is expected to be the most dominant [34].

Aside from these rolling components, there are also crystallographic texture components that result from recrystallisation. Depending on the deformation and temperature history for a sheet, such recrystallisation textures can also be evident. Table 5.3 gives the most common recrystallising textures [28].

Texture Type	*Indices*	*Bunge-Euler angles (φ_1,Φ,φ_2)*
Cube	$\{100\}\langle 001\rangle$	90°, 90°, 90°
Rotated Cube	$\{100\}\langle 0\bar{1}1\rangle$	45°, 90°, 90°

Table 5.3: List of the two most prevalent recrystallisation texture components for fcc metals.

It is a common misconception that reducing the thickness of a sheet further will have little effect on the texture components present, other than to increase their respective magnitudes. Previous research has shown that as r_{red} is increased over successive rolls, the orientation of the poles can move significantly, highlighted in particular by Euler space plot projections [28]. This implies a variation and evolution in texture with increasing strain. The relationship between the strain ε_{vM} and the reduction ratio r_{red} is best described with the *von Mises* equivalent strain equation, given by [35]:

$$\varepsilon_{vM} = \left| \frac{2}{3} \ln\left(1 - r_{red}\right) \right| \tag{5.6}$$

Using this strain relationship reiterates that small changes in r_{red} as it tends to 1, will result in bigger fluctuations in the value of ε_{vM}. This is representative of the actual strain imparted during the rolling process.

5.4.4 - Texture in rolled bcc metals (steel)

The first important and interesting point regarding bcc-metal deformation textures is that the primary slip system in bcc-crystallising metals is $\{110\}\langle\bar{1}11\rangle$ (Refer to Table 5.1).

On inspection this constitutes a transpose of the primary slip system for fcc metals, namely $\{111\}\langle 1\bar{1}0\rangle$ [13]. The secondary slip systems for bcc metals also have the <111> slip direction in common with each other. This transposition relationship means that much can be understood regarding bcc texture components from fcc texture behaviour.

For rolled steel, knowledge of texture components and the resulting anisotropic behaviour is well documented and studied, due mainly to the extensive use of steel in so many applications. Rolling textures in bcc metals are usually expressed as fibre textures.

A fibre texture can be initiated from a plane axis that displays isotropic symmetry radially, namely that the crystals are randomly oriented in the radial direction, but along the axis have very similar crystallographic orientation. When deformed along the direction of the axis, the radial symmetry will maintain its integrity, whilst along the fibre axis anisotropy of properties will be apparent [28]. Table 5.4 lists some of the expected texture fibres that develop in bcc metals.

Partial Fibre texture	***Defined Orientation of fibre***
α - <110> parallel to RD	$\{001\}\langle 110\rangle \rightarrow \{111\}\langle 1\bar{1}0\rangle$
γ - (111) parallel to ND	$\{111\}\langle 1\bar{1}0\rangle \rightarrow \{111\}\langle 112\rangle$
η - <110> parallel to RD	$\{001\}\langle 100\rangle \rightarrow \{011\}\langle 100\rangle$
ε	$\{001\}\langle 110\rangle \rightarrow \{111\}\langle 112\rangle$

Table 5.4: Definitions of some typical partial fibre textures found in bcc metals such as ferritic steel.

Figure 5.14 helps to visual these texture fibres, highlighting the orientation and direction of them. It has the three Bunge-Euler angles plotted in a Cartesian coordinate frame. As in the fcc case, these fibres can be identified by an experienced user assessing pole figure data.

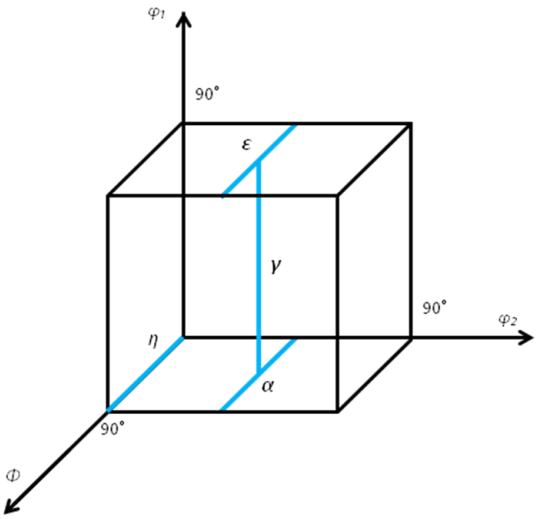

Figure 5.14: Plot showing four of the common idealised bcc texture partial fibres, here in Cartesian coordinates displayed in terms of Bunge-Euler angles.

5.5 – Elasticity

The concept of elasticity and its role in ultrasonic propagation has been introduced and discussed in chapter 2. The evolution of orthorhombic symmetry in the polycrystalline sheet due to cold-rolling is described by 9 elastic constants. This elasticity tensor is an important material characterisation measurement as it is a consequence of the introduction of crystallographic texture. The change in symmetry and magnitude of the elasticity tensor and its coefficients, by rolling, is governed by the variation in the stress and strain states. The nine elastic stiffness coefficients that define a sample with orthorhombic symmetry are discussed in depth in chapter 6, and have been introduced in matrix notation in chapter 2.

5.6 – Grain size

Determining the size of the constituent grains gives a physical measurement to represent the microstructure of a metallic sheet. It has been demonstrated that grain size can be easily measured using diffraction techniques such as EBSD. Grain boundaries act as ultrasound scatterers meaning grain size is a parameter theoretically calculable using ultrasound [36]. The grain size is a very important parameter due to its influence on the macroscopic behaviour.

For example, the yield strength, the minimum force required to plastically deform a material [37], is dependent on the average grain size. Determining the yield point is important in particular for predicting further cold-working formability behaviour. The yield point can be increased via a number of mechanisms. One such mechanism is work hardening, given by the following equation:

$$\Delta\sigma_y = G\mathbf{b}\sqrt{\rho_{dis}} \tag{5.7}$$

where $\Delta\sigma_y$ is the increase in yield stress required to plastically deform a material, G is the Shear modulus, $\boldsymbol{b}$ is the Burgers vector and ρ_{dis} is the dislocation density. The Burgers vector defines the magnitude and direction of a lattice distortion. With an increase in dislocation density the value for $\Delta\sigma_y$ must also increase.

Another mechanism that can increase the yield point is Hall-Petch strengthening [38]. This relies on the build up of dislocations at grain boundaries. When free dislocations move with applied stresses, they will propagate along the slip plane until inhibited by an obstruction such as a grain boundary. The boundaries then resist further propagation of dislocations into neighbouring grains. A pileup of dislocations will increase the strain linearly with number of dislocations present. With decreasing grain size, the ratio of the volume of the grain to its surface area has to decrease, which allows a higher percentage of dislocations to accumulate at the boundaries. This implies that the applied stress required to plastically deform the material will then be larger. The Hall-Petch relationship is given by:

$$\sigma_y = \sigma_0 + \frac{k}{\sqrt{\overline{D}}} \tag{5.8}$$

with σ_y the yield stress, σ_0 the stress needed to move a deformation, k is the Hall-Petch coefficient and $\overline{D}$ the average grain size.

Ductility properties will also change with grain size, which can have its advantages depending on the intended application of the sheet. A smaller grain size for example will imply a shorter slip length per grain. It follows that when a small grain is under load the small grain size will encourage a more homogeneous deformation. This is analogous to increasing the malleability of the sheet [16]. Knowledge of grain size would aid in predicting formability behaviour for subsequent working processes.

Magnetic properties of metals can also change with cold-working, with the increased strain at high reduction levels being shown to reduce the paramagnetic susceptibility of aluminium for example [28]. This is of interest given the dependence of the transduction efficiency of EMATs on the magnetic properties. In conjunction with the effects on magnetic properties, the electrical resistance, or piezoresistance, also changes with resulting strain [39]. Though these properties are not directly linked to the average grain size, strain information can be inferred from the elasticity measurements and EBSD diffraction patterns [40], and by measuring the severity of grain elongation.

5.7 – Grain aspect ratio

As the volume of rolled metal remains approximately constant during the rolling process, the grains in the sheet will change in size to accommodate the extension in the dimensions along the rolling direction and transverse direction with the thickness of the sheet along the normal direction being reduced. The two-dimensional average level of the dimensions of the grain is known as the grain aspect ratio, *R*, and is given by:

$$R = \frac{\overline{D}_{TD}}{\overline{D}_{RD}} \tag{5.9}$$

This ratio is the apparent average grain size in the transverse direction, $\overline{D}_{TD}$, divided by the apparent average grain size along the rolling direction, $\overline{D}_{RD}$. Rolling will induce a bigger

change in grain dimension along the RD than in the TD, and hence the grains when viewed in the RD-TD plane will appear elongated. The aspect ratio given in equation 5.9 is for the two-dimensional case, though of course there is the third dimension parallel to the normal direction, so strictly speaking this should also be considered. Currently at Warwick there is no facility to perform 3D EBSD scans, and as such means determining the aspect ratio difficult.

5.8 – References

1. *Honeycombe RWK, Steels Microstructure and Properties, Arnold Publishing, 1981*

2. *Hirao M, Fukuoka H, Fujisawa K, Muruyama R, Journal of Nondestructive Evaluation,* ***12(1)****, 1993, pp. 27-32*

3. *Potter MDG, Dixon S, Davis C, Meas. Sci. Technol.,* ***15****, 2004, pp. 1303-1308*

4. *Hook JR, Hall HE, Solid State Physics, Second Edition, Wiley Publishing, 1999*

5. *Kaye GWC, Laby TH, Tables of Physical and Chemical Constants, Fifteenth edition. Longman Scientific & Technical publishing, 1989*

6. *Higgins RA, Engineering Metallurgy, 6th edition, Arnold publishing, 1993*

7. *Pollack HW, Materials Science & Metallurgy, 4th edition, Prentice-Hall Inc., 1988*

8. *Reed-Hill RE, Physical Metallurgy Principles, D Van Nostrand Company, 1973*

9. *Nye JF, Physical Properties of Crystals, Oxford Press, 1957*

10. *Kurrein M, Plasticity of Metals, Griffin London, 1964*

11. *Barrett CS, Structure of Metals, McGraw-Hill, 1943*

12. *McLean D, Mechanical Properties of Metals, Wiley, 1962*

13. *Rollet AD, Wright SI, Texture and Anisotropy, Cambridge University Press, 2000, pp. 178-239*

14. *Reed-Hill RE, Physical Metallurgy Principles 3rd edition, PWS publishing, 1994*

15. *Hull D, Bacon DJ, Introduction to Dislocations 3rd edition, Pergamon Press, 1984*

16. *DeGarmo EP, Black JT, Kosher RA, Materials and Processes in Manufacturing, Prentice Hall, 1997*

17. *Kocks UF, Texture and Anisotropy, Cambridge University Press, 2000, pp. 11-43*

18. *Sezek S, Aksakal B, Can Y, Materials and Designs,* ***29****, 2008, pp. 584-596*

19. *Roberts WL, Hot rolling of Steel, Marcel Dekker, 1983*

20. *Larkiola J, Myllykoski P, Nylander J, Korhonen AS, Journal of Materials Processing Technology,* ***60****, 1996, pp. 381-386*

21. *Roberts WL, Cold Rolling of Steel, Marcel Dekker Inc., 1978*

22. *Sheet thicknesses available to purchase from Advent research materials. http://www.advent-rm.com/lines.asp?criteria=form&formid=13*

23. *Davies GJ, Goodwill DJ, Kallend JS, Metallurgical Transactions, **3**, 1972, pp. 1627-1631*

24. *Essex SD, Potter MDG, Dixon S, Rev. Prog in QNDE, **28**, 2008, pp. 1727-1734*

25. *Roe R-J, Journal of Applied Physics, **36(6)**, 1965, pp. 2024-2031*

26. *Li Y, Thompson RB, J.Acoust. Soc. Am., **91**, 1992, pp. 1298-1309*

27. *Euler L, Nov. Comm. Acad. Sci. Imp. Petrop., **20**, 1775, pp. 189-207*

28. *Rollet AD, Wright SI, Texture and Anisotropy, Cambridge University Press, 2000, pp. 178-239*

29. *Randle V, Engler O, Macrotexture, Microtexture and Orientation Mapping, Gordon & Breach, 2000*

30. *Roe R-J, Journal of Applied Physics, **37(5)**, 1966, pp. 2069-2072*

31. *Rajan K, Electron Backscatter Diffraction in Materials Science edited by Schwartz AJ, Kumar M, Adams BL, Kluwer Academic, 2000, pp. 31-38*

32. *Choi S-H, Choi J-K, Kim H-W, Kang S-B, Mat. Sci and Eng. A, **519**, pp. 77-87*

33. *Thanks to Dean Keeble for information and advice on XRD*

34. *Kocks UF, Texture and Anisotropy, Cambridge University Press, 2000, pp. 44-101*

35. *Mises Rv, Z. Agnew. Math & Meth., **8**, 1928, pp. 161-185*

36. *Rose JL, Ultrasonic waves in solid media, Cambridge University Press, 1999*

37. *Kocks UF, Texture and Anisotropy, Cambridge University Press, 2000, pp. 326-389*

38. *Kumar A, Jayakumar T, Palanichamy P, Raj B, Scripta Materialia, **40(3)**, 1999, pp. 333-340*

39. *Blazewicz S, Patalita B, Touzain P, Carbon, **35(10-11)**, 1997, pp. 1613-1618*

40. *Wilkinson A, Electron Backscatter Diffraction in Materials Science edited by Schwartz AJ, Kumar M, Adams BL, Kluwer Academic, 2000, pp. 231-246*

CHAPTER 6

Development of Correlating Procedures

The research objective is to develop non-destructive ultrasound measurements to characterise rolled metal sheet, and to correlate the data obtained with results from EBSD. The two contrasting techniques offer detail on the macro- and microscopic properties respectively, and if the results from each method concur then this will validate the data from the faster and more convenient ultrasound experiments.

Reference was made in the introductory chapter to some of the sporadic research correlating NDT processes with EBSD [1,2], but there is no precedent for research as far as we are aware that has investigated the direct prediction of ultrasonic propagation behaviour from EBSD data. This chapter describes the development of the correlation procedures to arrive at new solutions for predicting and understanding ultrasonic behaviour using EBSD, merging the topics of NDT and microscopy together in a way never achieved prior to the commencement of this PhD. This chapter generates the theoretical framework that allows the direct comparison of the two experimental techniques, both in the measurement of elasticity and crystallographic texture, along with some initial work in determining and analysing grain size and shape. The developed computer programs of these correlating procedures are given in appendix A.

6.1 – Crystallographic texture

6.1.1 – Ultrasound determination of crystallographic texture

As explained in chapters 2 and 5, a convenient way to describe the elastic anisotropy induced by rolling is via the crystallite Orientation Distribution Function (ODF). The probability distribution equation applicable to the ODF $w(\xi,\psi,\varphi)$ [3] is given by:

$$\int_0^{2\pi}\int_0^{2\pi}\int_{-1}^{1} w(\xi,\psi,\varphi)\,d\xi\,d\psi\,d\varphi = 1 \qquad (6.1)$$

where $\xi = \cos\theta$. Also previously explained, the ODF is a function dependent on the Euler angles *(θ,ψ,φ)*; these define the crystallographic orientation of a crystal / grain in a polycrystalline aggregate relative to the orthogonal axis system of the material it is within. The equation is a probability distribution, and will highlight orientations and texture components that are dominant in a rolled sheet, and which orientations are less common.

It has been shown that the ODF is solved typically using stereographic projection pole figures from diffraction data. However, it is difficult to conceive how these methods could be employed for 'online' measurements, where speed of measurement is essential. To measure ultrasonically the anisotropy utilising a rapid and quantitative system, the ODF equation needs to be manipulated to a more convenient format.

It has been shown that [3] by expanding equation 6.1 using a series of generalized spherical harmonics, $w(\xi,\psi,\varphi)$ can be expressed by the following (equation 6.2):

$$w(\xi,\psi,\varphi) = \sum_{l=0}^{\infty} \sum_{m=-1}^{1} \sum_{n=-1}^{1} W_{lmn} Z_{lmn}(\xi) \exp(-im\psi) \exp(-in\varphi) \qquad (6.2)$$

$Z_{lmn}(\xi)$ is the generalization of the associated Legendre function with the W_{lmn} terms identified as the Orientation Distribution Coefficients (ODCs); these are of particular interest as the ODCs are analogous too quantitative texture coefficients. Previous work by *Roe* [3] and *Sayers* [4] amongst others has shown that for cubic crystallites, the number of independent non-zero ODCs that exist reduces dramatically from symmetry arguments.

6.1.2 – Ultrasonically measurable ODCs

There are just three ODCs that contribute to the ODF for aluminium and steel [5], and they can be calculated using ultrasound velocity measurements. These are W_{400}, W_{420} and W_{440}. Though this does not fully characterize the texture, these three ODCs give rise to important information that can be utilised in predicting formability behaviour. The calculations have been completed by previous workers, showing for example that only l = 4

terms contribute when considering ultrasonic measurements [4]. For orthorhombic symmetry cases, $W_{lmn} = 0$ when either m or n are odd (and also for $l = 0$), and with the fact that the ODF cannot be complex, analysis of equation 6.2 shows further limitations on the values l, m and n can take.

The three ODCs each give different levels of information regarding the anisotropy present [6]. The W_{400} term is a measure of resistance to deep drawing. The W_{420} coefficient gives information on the level of 2-fold symmetry present; effectively a measure of the existence of double earring within the sheet due to the texture. W_{440} is similar, describing the magnitude of the 4-fold symmetry present in the sheet.

6.1.3 – Averaging schemes

Prior to any calculations, certain assumptions must be made regarding the stress and strain distribution before manipulating the elasticity tensor. Selecting an adequate averaging scheme is required. There are three typical averaging methods that have been adopted in similar work in this field.

6.1.3.1 - Voigt average scheme

The Voigt average [7] is based upon the assumption of assigning a uniform distribution of strain across the grain boundaries, such that any changes in the elasticity is detected by the change in the stress. Selection of this averaging scheme would imply that Hooke's law of elasticity would be equal to:

$$\sigma_{ij} = c_{ijkl}\varepsilon_{kl} \tag{6.3}$$

where σ_{ij} is the 2nd rank stress tensor, ε_{kl} the 2nd rank strain tensor and c_{ijkl} the 4th rank elasticity tensor made up of the elastic stiffness constants. This scheme typically gives an upper bound to the effective elastic constants.

6.1.3.2 - Reuss average scheme

The Reuss averaging scheme assumes a uniform stress across the grain boundaries [8]. Hooke's law now becomes:

$$\varepsilon_{ij} = s_{ijkl}\sigma_{kl} \tag{6.4}$$

with ε_{ij} and σ_{kl} representing strain and stress respectively, with s_{ijkl} the 4th rank elastic compliance tensor, constituted of the elastic compliance constants. This scheme generally gives lower bounds to the effective compliance constants.

6.1.3.3 - Hill average scheme

The Hill average is simply obtained from the mean value after applying both the Voigt and Reuss averaging schemes for the same sheet [9]. The elastic stiffness and compliance constants are therefore related by:

$$c = \frac{1}{s} \tag{6.5}$$

6.1.3.4 – Scheme selected

The mathematics used for the remainder of the chapter is based upon the application of Voigt averaging methods. This denotes that calculations of elasticity will be in terms of the elastic stiffness constants. This method has been chosen due to its convenience and popularity amongst other authors of work in the field.

6.1.4 – Obtaining the ODCs ultrasonically

The ultrasonic velocity of the S_0 mode Lamb wave, v_{S_0}, measured as a function of angle subtended from the rolling direction gives an indication of the elastic moduli variation induced by the texture. It has been shown previously that the elastic modulus, *E*, can be measured from the following relationship for a material composed of cubic crystallites [10]:

$$v_{S_0}{}^2 = 4\frac{\lambda+\mu}{\rho(3\lambda+2\mu)}E \tag{6.6}$$

λ and μ are the Lamé constants; these fully characterize the elastic properties of a homogeneous and isotropic material. ρ is the density, and along with the Lamé constants do not vary with direction. Therefore any variation in velocity v_{S_0} is due to a change in the elastic modulus, *E*.

When investigating thin metallic sheet it is convenient to use the symmetric S_0 Lamb wave. There are a number of modes that can be measured depending on frequency, but it is appropriate to measure the S_0 mode velocity in conjunction with using a low central frequency (kHz) where the corresponding wavelength $\lambda >> d$ (d = sheet thickness). This is necessary to ensure that the wave will be non-dispersive with a homogenous energy distribution through-thickness, negating the need for applying the excessive corrections during data analysis [11].

With reference to equation 6.6, note that the typical changes in the magnitude of *E* due to texture will be of the order of 1% (especially in aluminium). Therefore it is imperative the ultrasonic measurement system deployed is extremely accurate in order to get the necessary texture information.

Previous work, by *Thompson et al* in particular, and in reference to chapter 2 (equations 2.37 – 2.41), has derived the relationship linking the three ODCs of interest to the S_0 mode velocity of a Lamb wave and the angle subtended from the rolling direction [6]:

$$\rho v_{S_0}^2 = A + BW_{400} + CW_{420}\cos(2\theta) + DW_{440}\cos(4\theta) \tag{6.7}$$

where ρ is the density, v_{S_0} is the S_0 mode Lamb wave velocity, the W_{lmn} terms are the ODCs, θ is the angle subtended from the RD and the material parameters *A-D* are given by [12]:

$$A = \left(1 - \frac{P^2}{L^2}\right)L \tag{6.8}$$

$$B = \left(\frac{4c\pi^2}{35}\right)\sqrt{2}\left(3 + \frac{8P}{L} + \frac{8P^2}{L^2}\right) \tag{6.9}$$

$$C = -\left(\frac{4c\pi^2}{35}\right)4\sqrt{5}\left(1 + \frac{2P}{L}\right) \tag{6.10}$$

$$D = \left(\frac{4c\pi^2}{35}\right)2\sqrt{35} \tag{6.11}$$

With the constants in equations 6.8-6.11 given by:

$$P = \lambda \tag{6.12}$$

$$L = \lambda + 2\mu \tag{6.13}$$

$$c = c_{11}^x - c_{12}^x - 2c_{44}^x \tag{6.14}$$

c is the anisotropy parameter, dependent on the single crystal constants, c_{11}^x, c_{12}^x and c_{44}^x, of the material being investigated. Furthermore, the Lamé constants can be approximated by:

$$\lambda = c_{12}^x \tag{6.15}$$

$$\mu = \frac{c_{11}^x - c_{12}^x}{2} \tag{6.16}$$

μ is also equivalent to the shear modulus for an isotropic material [13].

In the isotropic situation the ODCs W_{lmn} = 0 (no texture). By combining and rearranging equations 6.6 and 6.7 in this case, the elastic modulus, *E*, can be expressed in terms of the Lamé constants:

$$\rho v_{S_0}^2 = \frac{4(\lambda+\mu)E}{(3\lambda+2\mu)} = \left(1 - \frac{\lambda^2}{(\lambda+2\mu)^2}\right)(\lambda+2\mu)$$

Which rearranges to:

$$\Rightarrow E = \frac{\mu(3\lambda+2\mu)}{(\lambda+2\mu)} \tag{6.17}$$

Therefore with prior knowledge of just the density and the single crystal constants for a cubic material, theoretical values for the elastic modulus can be determined if no texture is present, with the ODCs measurable once elastic anisotropy is induced in the sheet.

6.1.5 – Measuring *v* as a function of θ

There are two experimental approaches that can be used to obtain the ODCs expressed in equation 6.7. One approach is to take velocity measurements of the S_0 mode Lamb wave at three angles relative to the rolling direction, typically at 0˚ (parallel to RD), 45˚ and 90˚ (parallel to TD) [14]. Such experiments would reduce equation 6.7 into three solvable simultaneous equations where the ODCs can be calculated as functions of *v*, ρ, *c*, λ and μ.

Another approach is to record a number of S_0 Lamb wave velocity measurements for a range of angles, $\theta \in [0°, 360°]$ with 0˚ parallel to the RD, producing a *v* vs. θ plot and applying a mathematical fit to the data to obtain the ODCs. Measuring over a range of angles increases measurement accuracy and reduces the chance of large systematic errors in the calculated ODCs when compared to measuring the velocity at three discrete angles.

This second method is used for the experimental setup here, continuing on from the work of *Potter et al* and is explained in the experimental details specified in chapter 7.2 [15].

6.1.6 – Obtaining the ODCs utilising EBSD

It is desirable to obtain independently of the ultrasonic measurements the three ODCs W_{400}, W_{420} and W_{440} directly from EBSD data. Diffraction techniques are normally utilised in measuring texture via pole figure projections and Euler space plots, and methods to obtain the ODF from such discrete plots have been published [16]. Here though, a method is developed to quantify the texture coefficients directly from Bunge-Euler angle data, making it directly comparable to the non-destructive ultrasound results.

Assuming the implementation of the Voigt averaging scheme, the indices of the elasticity tensor c_{ijkl} can take values of 1, 2 or 3. These numbers correspond to the three principal axes inherited by the sheet after rolling, with 1 analogous to the RD, 2 representing the TD and with 3 equalling the ND. This implies that c_{ijkl} is a $3 \times 3 \times 3 \times 3$ tensor, and hence has 81 components.

It is convenient to use matrix notation to reduce the tensor to a 2 dimensional matrix with 36 elements. The reasons for this were explained in chapter 2, though effectively it is done to simplify the mathematics. Table 6.1 lists the transformations used in mapping from 81 to 36 components [17].

Tensor notation $c_{ij,kl}$	11	22	33	23, 32	31, 13	12, 21
Matrix notation $c_{i,j}$	1	2	3	4	5	6

Table 6.1: Matrix notation used to simplify from the 4th ranked elasticity tensor with 81 coefficients to a 2nd rank tensor with 36 coefficients.

The application of this therefore leads to the simplified 6×6 matrix representation of c_{ijkl} (as shown in equation 2.7).

$$c_{ij} = \begin{pmatrix} c_{11} & c_{12} & c_{13} & c_{14} & c_{15} & c_{16} \\ c_{21} & c_{22} & c_{23} & c_{24} & c_{25} & c_{26} \\ c_{31} & c_{32} & c_{33} & c_{34} & c_{35} & c_{36} \\ c_{41} & c_{42} & c_{43} & c_{44} & c_{45} & c_{46} \\ c_{51} & c_{52} & c_{53} & c_{54} & c_{55} & c_{56} \\ c_{61} & c_{62} & c_{63} & c_{64} & c_{65} & c_{66} \end{pmatrix} \tag{6.18}$$

Also, c_{ijkl} has been proven to be symmetric for cubic crystallites. For example:

$$c_{ijkl} = c_{ijlk} \tag{6.19}$$

Referring to work by *Nye* [17] on the independent elastic constants, together with the consideration of the symmetrical properties related to orthorhombic symmetry, the corresponding elasticity matrix is reduced to nine independent non-zero effective elastic constant components. These coefficients are:

$$c_{ii}, \text{ (with } i = 1 - 6), \; c_{12}, c_{13} \text{ and } c_{23}$$

The respective positions of the constants in the matrix, which have been shown previously, are shown in equation 6.20 for completeness.

Orthorhombic Symmetry:

$$c_{ij} = \begin{pmatrix} c_{11} & c_{12} & c_{13} & 0 & 0 & 0 \\ 0 & c_{22} & c_{23} & 0 & 0 & 0 \\ 0 & 0 & c_{33} & 0 & 0 & 0 \\ 0 & 0 & 0 & c_{44} & 0 & 0 \\ 0 & 0 & 0 & 0 & c_{55} & 0 \\ 0 & 0 & 0 & 0 & 0 & c_{66} \end{pmatrix} \tag{6.20}$$

These nine elastic constants govern the propagation of ultrasound in a polycrystalline aggregate with orthorhombic symmetry. If these are determined using EBSD, the angular-dependent ultrasonic S_0 Lamb wave velocity can be predicted, and hence ODCs can be evaluated that are comparable directly to those obtained through ultrasonic measurements.

The idealised determination of these nine elastic constants has been derived by numerous authors [4, 18]. Most are developed from the fundamentals of the ODF, which is dependent on the input of Euler angles. The described rotation from crystal to sample frame of reference is satisfied by the corresponding rotation matrix (equation 6.21), dependent solely on the three Roe-Euler angles *(θ,ψ,φ)* [3, 19]*:*

$$T(\psi,\theta,\varphi)=\begin{pmatrix} -\sin\psi\sin\varphi+\cos\psi\cos\varphi\cos\theta & \cos\psi\sin\varphi+\sin\psi\cos\varphi\cos\theta & -\sin\theta\cos\varphi \\ -\sin\psi\cos\varphi-\cos\psi\sin\varphi\cos\theta & \cos\psi\cos\varphi-\sin\psi\sin\varphi\cos\theta & \sin\theta\sin\varphi \\ \sin\theta\cos\psi & \sin\psi\sin\theta & \cos\theta \end{pmatrix} \quad (6.21)$$

Using the notation of *Sayers* [4], who expanded the work of *Roe* [3] and *Hearmon* [20] regarding the ODF, the nine elements from the matrix in equation 6.21 are defined as directional cosines, and labelled accordingly:

$$\begin{aligned} l_1 &= -\sin\psi\sin\varphi+\cos\psi\cos\varphi\cos\theta \\ l_2 &= -\sin\psi\cos\varphi-\cos\psi\sin\varphi\cos\theta \\ l_3 &= \sin\theta\cos\psi \\ m_1 &= \cos\psi\sin\varphi+\sin\psi\cos\varphi\cos\theta \\ m_2 &= \cos\psi\cos\varphi-\sin\psi\sin\varphi\cos\theta \\ m_3 &= \sin\psi\sin\theta \\ n_1 &= -\sin\theta\cos\varphi \\ n_2 &= \sin\theta\sin\varphi \\ n_3 &= \cos\theta \end{aligned} \quad (6.22)$$

These nine terms link the orthogonal axes 0-xyz (of the crystal) from 0-XYZ (of the crystallite) by:

$$\begin{aligned} x &= l_1X+l_2Y+l_3Z \\ y &= m_1X+m_2Y+m_3Z \\ z &= n_1X+n_2Y+n_3Z \end{aligned} \quad (6.23)$$

Knowledge of the single crystal constants, from which the anisotropy parameter c can also be calculated (equation 6.14), the nine effective elastic constants c_{ij} defining orthorhombic symmetry can then be determined by:

$$\begin{aligned}
c_{11}^{'} &= c_{11}^{x} - 2c\langle r_1 \rangle \\
c_{22}^{'} &= c_{11}^{x} - 2c\langle r_2 \rangle \\
c_{33}^{'} &= c_{11}^{x} - 2c\langle r_3 \rangle \\
c_{44}^{'} &= c_{44}^{x} + c\langle r_4 \rangle \\
c_{55}^{'} &= c_{44}^{x} + c\langle r_5 \rangle \\
c_{66}^{'} &= c_{44}^{x} + c\langle r_6 \rangle \\
c_{23}^{'} &= c_{12}^{x} + c\langle r_7 \rangle \\
c_{31}^{'} &= c_{12}^{x} + c\langle r_8 \rangle \\
c_{12}^{'} &= c_{12}^{x} + c\langle r_9 \rangle
\end{aligned} \tag{6.24}$$

where c_{11}^{x}, c_{12}^{x} and c_{44}^{x} are the single crystal constants, c is the anisotropy parameter, and the $\langle r_i \rangle$ terms are given by dividing the following set of equations (equation 6.25) by the number of data points investigated:

$$\begin{aligned}
r_1 &= l_1^2 l_2^2 + l_1^2 l_3^2 + l_2^2 l_3^2 \\
r_2 &= m_1^2 m_2^2 + m_1^2 m_3^2 + m_2^2 m_3^2 \\
r_3 &= n_1^2 n_2^2 + n_1^2 n_3^2 + n_2^2 n_3^2 \\
r_4 &= m_1^2 n_1^2 + m_2^2 n_2^2 + m_3^2 n_3^2 \\
r_5 &= l_1^2 n_1^2 + l_2^2 n_2^2 + l_3^2 n_3^2 \\
r_6 &= l_1^2 m_1^2 + l_2^2 m_2^2 + l_3^2 m_3^2 \\
r_7 &= m_1^2 n_1^2 + m_2^2 n_2^2 + m_3^2 n_3^2 \\
r_8 &= l_1^2 n_1^2 + l_2^2 n_2^2 + l_3^2 n_3^2
\end{aligned} \tag{6.25}$$

$$r_9 = l_1^2 m_1^2 + l_2^2 m_2^2 + l_3^2 m_3^2$$

with the *l*, *m* and *n* terms here the directional cosines defined in equation 6.21.

Equations 6.21 - 6.25 show that from using Eulerian angles alone, the nine effective elastic stiffness constants can be calculated from EBSD data. However, EBSD produces data with Bunge-Euler angles, meaning the directional cosines are in fact incorrect in the form given in equations 6.21 and 6.22. The correct matrix, *g*, for Bunge-Euler angles ($\varphi_1, \Phi, \varphi_2$), given in equation 6.26 is achieved through standard trigonometric relations:

$$g = \begin{pmatrix} \cos\phi_1 \cos\phi_2 - \sin\phi_1 \sin\phi_2 \cos\Phi & \sin\phi_1 \cos\phi_2 + \cos\phi_1 \sin\phi_2 \cos\Phi & \sin\phi_2 \sin\Phi \\ -\cos\phi_1 \sin\phi_2 - \sin\phi_1 \cos\phi_2 \cos\Phi & -\sin\phi_1 \sin\phi_2 + \cos\phi_1 \cos\phi_2 \cos\Phi & \cos\phi_2 \sin\Phi \\ \sin\phi_1 \sin\Phi & -\cos\phi_1 \sin\Phi & \cos\Phi \end{pmatrix} \quad (6.26)$$

From this, the steps described in equations 6.22 – 6.25 provide a valid method to obtain the elastic constants using relevant substitutions to accommodate the Bunge-Euler angles.

With the measurement of the elasticity tensor from EBSD now in place, the production of an angular dependent S_0 Lamb wave velocity is required to be able to compare directly to the ultrasonic measurement system. Once completed, the same curve fitting procedures applied to the experimental ultrasonic data can be applied to the simulated velocity data from EBSD, where the ODCs can be calculated.

A method to predict S_0 mode velocity directly from the elastic constants is required. Theory has been developed for the long wavelength limit of an S_0 mode (ratio of wavelength to sheet thickness) which is the case for the ultrasound experimental setup used in the determination of the ODCs [21]. As the stress

coefficients σ_{i3} (i = 1-3) vanish at the surface of a rolled sheet, with low frequency ultrasound, the strain terms ε_{13} and ε_{23} are also zero throughout the sheet.

As a result the S_0 mode Lamb wave velocity can be calculated from equation 6.27 (to a first order approximation). The mathematics to produce this relationship is described in detail by *Thompson* [21]:

$$v_{S_0} = \left(\frac{\hat{C}_L}{\rho}\right)^{\frac{1}{2}}\left[1+\frac{\hat{\alpha}}{4}\cos(2\theta)-\left(\frac{\hat{\beta}\hat{C}_T}{4\hat{C}_L}\right)(1-\cos(4\theta))\right] \tag{6.27}$$

with ρ the density, θ the angle subtended from the RD, and the undefined parameters within the equation calculated by:

$$\hat{C}_L = \left(\frac{c_{11}+c_{22}}{2}\right)-\left(\frac{c_{13}^2+c_{23}^2}{2c_{33}}\right) \tag{6.28}$$

$$\hat{C}_T = c_{66} \tag{6.29}$$

$$\hat{\alpha} = \frac{\left[(c_{11}-c_{22})-\frac{(c_{13}^2-c_{23}^2)}{c_{33}}\right]}{\hat{C}_L} \tag{6.30}$$

$$\hat{\beta} = \frac{\left[\left(\frac{c_{11}+c_{22}}{2}\right)-c_{12}-\frac{(c_{13}-c_{23})^2}{2c_{33}}\right]}{2c_{66}}-1 \tag{6.31}$$

Equations 6.28-6.31 are dependent on the nine elastic stiffness constants, calculable from EBSD measurements as shown previously. Equation 6.27 links the wave velocity and angle relative to the RD, and therefore a plot analogous to the ultrasound technique can be produced to compare the results from ultrasonic and EBSD measurements.

Summarizing, the theoretical framework for extrapolating quantitative texture coefficients using ultrasonic measurements has been described by fitting experimentally determined angular dependent velocities using equation 6.7. A new method utilizing Eulerian angle data from EBSD has been introduced; angle data is manipulated to generate the nine effective elastic stiffness constants inherent with orthorhombic symmetry, and further, be used to produce an angular dependent velocity prediction to again determine the ODCs using equation 6.27. The results of the calculated ODCs from each technique can then be compared and correlated.

6.2 – Determining grain size and aspect ratios

6.2.1 – Ultrasonic measurement of grain size

As an ultrasonic wave propagates through a metal sheet, the intensity or amplitude of the wave will attenuate with the distance travelled. There are a number of mechanisms that contribute to this reduction.

Naturally, diffraction of the wavefront as a consequence of the geometric effects of the sheet will inevitably result in beam spreading, diverging the energy from the initial direction of propagation. Intrinsic attenuation effects can be split into two contributing factors; absorption and scattering. Idealized theoretical relationships have been produced previously, linking the attenuation to the grain size of the material the wave propagates in. This grain size dependence in the attenuation equations is governed by the ratio between the ultrasound wavelength (λ) and the average grain size $\overline{D}$ [22].

Accurate, empirical attenuation measurements are extremely difficult to attain, because of all these contributing factors. Without a prior knowledge of the magnitude of the average grain size in a sample, it makes it difficult to know which attenuation regime to assume. Other issues that will make measuring successfully the attenuation more difficult include mode conversion of waves at back-wall reflections, and the small anisotropy in aluminium in particular, which is not conducive to large attenuation effects. The scattering

due to grain boundaries is much reduced compared to the more anisotropic metals such as lead and copper.

There are a couple of assumptions that can be made to aid subsequent data analysis. The contribution from absorption, which is the conversion of the wave energy to heat, is usually negligible in metals such as aluminium and steel, as they are weakly viscoelastic [23]. This means that scattering mechanisms will dominate the intrinsic attenuation component in such metallic sheets.

Scattering arises from the interaction between the wavefront and the discontinuities in the metal structure; the most frequent discontinuities in this instance are the crystalline grain boundaries themselves and the anisotropy of elastic properties between neighbouring grains which will have a value of misorientation between them. The boundaries deviate the direction of the ultrasonic wave, which will imply a reduction in the final intensity detected as the scattered energy is removed from the propagating wavefront [24]. This indicates that as the average grain size increases, the beam is deflected by a greater offset and hence scattering effects are more pronounced.

For a plane wave, the *total* attenuation coefficient, α, is related to the final amplitude A, initial amplitude A_0 and distance travelled x, by [22]:

$$A = A_0 \exp(-\alpha x) \tag{6.32}$$

α exponentially decays with distance travelled. From A-scans obtained in ultrasonic experiments, values for A at any point in time and the peak amplitude magnitude A_0 can be determined, and knowing the distance / thickness of propagation means that equation 6.32 can be solved. Alternatively, by rearranging equation 6.32, α can be made the subject and calculated via equation 6.33:

$$\alpha = -\frac{1}{x} \ln \left| \frac{A}{A_0} \right| \tag{6.33}$$

It was stated that the dependence of α on the average grain size is varying for different frequency ranges compared to the grain size. There are three scattering regimes, namely Rayleigh, Stochastic and Geometric [24].

Rayleigh scattering is prominent when the frequency $\lambda >> \overline{D}$, where $\overline{D}$ is the average grain size. It is documented that the minimum requirement for this regime to be the main contributor is [25]:

$$\frac{\lambda}{2\pi\overline{D}} > 1 \tag{6.34}$$

However, to be guaranteed that an experiment is adhering to the Rayleigh scattering regime, it would be preferable that λ is orders of magnitude greater than $\overline{D}$.

If equation 6.34 is satisfied, and assuming the real absorption attenuation coefficient is negligible, then the intrinsic attenuation has a cubed dependence on $\overline{D}$ and a 4th power dependence on frequency [24]:

$$\alpha = c_R \overline{D}^3 f^4 \tag{6.35}$$

where c_R is a constant of proportionality. The second scattering regime, the stochastic attenuation, will be valid when $\lambda \approx \overline{D}$, with the attenuation then determined by the relationship:

$$\alpha = c_S \overline{D} f^2 \tag{6.36}$$

with c_S a constant of proportionality. The geometric regime is applicable for the case when the inequality is reversed from equation 6.34, with the frequency much smaller than the grain size. The relationship between $\overline{D}$ and the attenuation coefficient is given in this instance by:

$$\alpha = c_G \frac{1}{\overline{D}} \tag{6.37}$$

with c_G a constant of proportionality.

Measurement of grain size using ultrasonics is theoretically calculable, with the importance of the correct scattering regime highlighted here. Knowledge of sheet thickness together with the production of A-scans from the empirical data will generate values for *A* and A_0, which will allow for a value of the total attenuation α to be determined from pulse-echo techniques. FFT analysis of the A-scan will allow for frequency analysis. From here, predictions for grain size may be made. The confidence in this measurement will be questionable, given the effects of diffraction, and perhaps the ambiguity in which scattering regime the attenuation will function in. There is certainly an argument that there will be contributions from more than one scattering regime, and this will be duly considered in data analysis procedures.

It is of note that the attenuation measurements will be completed using through-thickness propagating SH waves, with the experimental methods discussed in chapter 7.

6.2.2 – Ultrasonic measurement of grain aspect ratio

The two-dimensional aspect ratio, *R*, of a grain is given by equation 6.38:

$$R = \frac{\overline{D}_{TD}}{\overline{D}_{RD}} \tag{6.38}$$

For equiaxial grains, the apparent grain size would be the same in all directions meaning $R \approx 1$. For rolled sheet, as described throughout this thesis, the grains elongate to preserve the volume of the sheet during plastic deformation. The maximum average value of $\overline{D}$ will coincide with the rolling direction, though slight variation from this is possible depending on the level of grain rotation enforced by the existence of complex slip systems [19]. In essence, the aspect ratio should be approached as a three-dimensional property, with an apparent grain

size $\overline{D}_{ND}$ in the normal direction also requiring consideration. However, in the case of polarised shear waves propagating in the normal direction, the variation in attenuation will be due to the relative difference in the average grain size along the rolling and transverse directions.

A propagating ultrasound SH wave polarised in the rolling direction will attenuate at a different rate to a SH wave polarised in the transverse direction, due to the dependence on grain size of the scattering contribution to attenuation regardless of the regime. Therefore, using a polarised shear wave propagating through-thickness, polarised parallel to firstly the rolling direction, then the transverse direction, the relative α ratios can be determined.

The benefit of this approach to measuring *R* is that, regardless of the attenuation regime, be it Rayleigh, stochastic or geometric, such an aspect ratio measurement is a relative measurement. The proportionality constants would cancel, as will the frequency, controlled accordingly for EMAT measurements; this would leave relationships linking the aspect ratio solely to a ratio of the attenuation coefficients along the RD and the TD. For example, in the case of working in the Rayleigh scattering regime, performing attenuation measurements along the RD and the TD means that the corresponding attenuation coefficients are given by:

$$\alpha_{RD} = c_R \overline{D}_{RD}^3 f^4 \tag{6.39}$$

$$\alpha_{TD} = c_R \overline{D}_{TD}^3 f^4 \tag{6.40}$$

Dividing equation 6.40 with 6.39, and rearranging to make the aspect ratio, as given by equation 6.38, the subject leaves:

$$R = \frac{\overline{D}_{TD}}{\overline{D}_{RD}} = \sqrt[3]{\frac{\alpha_{TD}}{\alpha_{RD}}} \tag{6.41}$$

6.2.3 – EBSD measurement of grain size

EBSD has been shown in the introductory chapters to give a unique visualisation of a sample's microstructure, which the grain plays an integral part. It is an ideal technique therefore to measure the grain characteristics of a metallic sheet, enabling comparison and validation of the ultrasound measurements. EBSD automatically deciphers grains from the Auto IPF plots produced via misorientation calculations, and hence can automatically calculate the distribution and average grain size for a scan. There are three common methods to determine average grain size from EBSD datasets and these are described in sections 6.2.3.1-6.2.3.3 [26].

6.2.3.1 - Linear Intercept Method

The linear intercept method (LIM) is an iterative technique, scrutinising lines of data in the x and y direction on a two dimensional EBSD IPF map. It is demonstrated in figure 6.1.

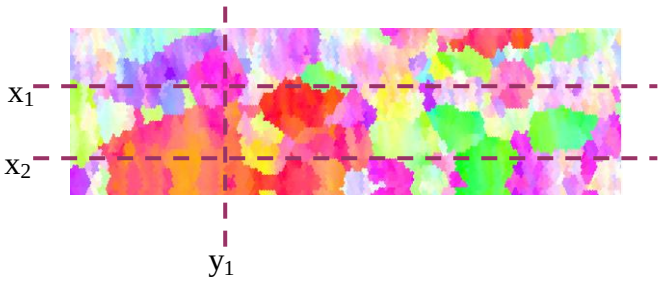

Figure 6.1: Cropped area from an EBSD scan of an aluminium sample. In the linear intercept method, lines in the x and y directions are used to obtain the average grain size by averaging the distance between line and grain boundary interactions.

Moving along a line, the number of high angle grain boundaries (HAGB) encountered is recorded. A high angle grain boundary is defined as a change in orientation > 15° between neighbouring pixels. This value can be changed manually however. The lines examined in the *x* direction must be sufficiently far apart, so as not to incorporate the same grain twice, with the same being true for the *y* direction.

Equation 6.42 calculates the mean linear intercept grain size, L_x:

$$L_x = \frac{R_x P_x \delta}{N_x} \tag{6.42}$$

where R_x is the number of x rows scanned, P_x the number of pixels in one row, δ is the scan step size and N_x is sum of HAGB intercepted. L_y can be determined by replacing x with y in equation 6.42, with the direction independent average $\overline{L} = (L_x, L_y)$. It is recommended that at least 200 grains are sampled to give a statistically viable average for the grain size

6.2.3.2 - Grain Reconstruction Method

The EBSD system software can generate grain maps automatically from the Auto IPF maps and can determine grain size using different grain definitions defined by the user. When selecting the grain size chart function (diameter) in OIM, the software applies the Grain Reconstruction Method (GRM).

The grain sizes are calculated from the step size δ and the number of pixels within each grain. Each pixel has an area dependent on δ, with each grain area determined by:

$$Area = n\frac{\sqrt{3}}{2}\delta^2 \tag{6.43}$$

where n is the number of points in the grain, and the $\sqrt{3/2}$ term is due to the hexagonal raster scan grid. If done on a square grid, the area would simply be equivalent to $n\delta^2$. Using this area, an equivalent circle diameter (ECD) can then be calculated by simply solving πr^2 and doubling r. The diameter calculated is considered the grain size. The ECD = 0.816 x the true grain size. Also the ECD = 1.224 x the mean linear intercept.

There are disadvantages to this method regarding the accuracy when applied to rolled sheet and the resulting elongated grains. A simple example; assuming a square EBSD grid, with $\delta = 3\mu m$, each pixel would represent an area of $9\mu m^2$. For a grain containing 30 pixels, the ECD = $18.5\mu m$. This method is applied irrespective of the relative strength of any stress

and the major axis / minor axis grain size ratio. Hence a long line of 30 pixels in one direction would be stipulated to have the same grain size as an equiaxial grain.

6.2.3.3 - Intelligent Data Acquisition

Intelligent Data Acquisition (IDA) is a technique under development for automated systems. The above two methods require a large data set for accuracy though the majority of data is surplus; the linear intercept method in particular. IDA involves placing a coarse grid upon an EBSD scan. Taking one square from the grid, the 4 corners are analysed. If each point has the same orientation, then the square is considered to be part of one grain, so the grid is made coarser. If at least 2 corners have different orientations, this implies that more than one grain component exists within the area. This iteration is continued on numerous areas of a scan until an average grain size is found.

6.2.3.4 – Method applied

Though the LIM and IDA are both promising methods, they are not available as an automated process with the OIM software. Grain size charts can be produced automatically, an example of which is shown in figure 6.2, using the GRM algorithm. It produces data in a binned data % fraction format, displaying the fraction of the grains to have a diameter within defined ranges. The number of bins, and hence the resolution of the graph can be changed accordingly.

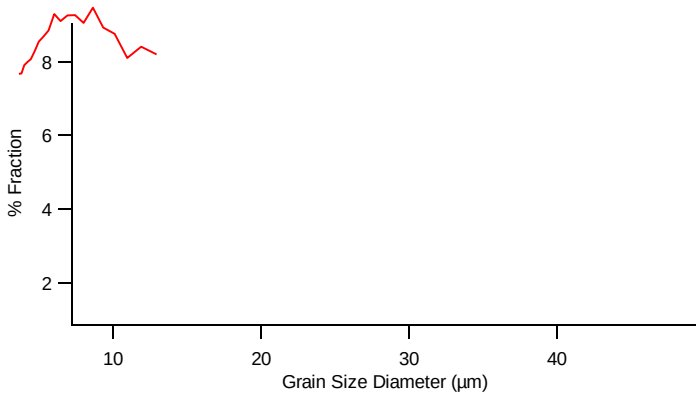

Figure 6.2: OIM grain size diameter data for a DC05 steel sheet provided by Corus. The data is represented in a % fraction form, calculating the number of grains that fall within limits defined by the user. The diameter is calculated using the Grain Reconstruction Method.

The OIM software also states the average value calculated from all the grains detected. For the steel sample scanned here in figure 6.2, the average grain size calculated from this EBSD map is 24.29 ± 0.01 μm.

6.2.4 – EBSD measurement of aspect ratio

With the EBSD grain size measurement algorithm assuming equiaxed grains, a direct measurement of aspect ratio from that data application is impractical. There is also a grain shape analysis system available, which is suitable to compare with the aspect ratio measurements taken using ultrasound. This system applies best fit algorithms to ellipses that are assigned to each detected grain. Once the ellipse geometry is established, the lengths of the major and minor axes are measured. The aspect ratio can then be simply calculated by dividing the magnitude of the minor axis with the major axis. Figure 6.3 displays an Auto IPF map along with a highlighted grain which on the right hand side is encapsulated by an ellipse. The program fits the ellipse in a way that minimises the distance between it and each of the boundary points.

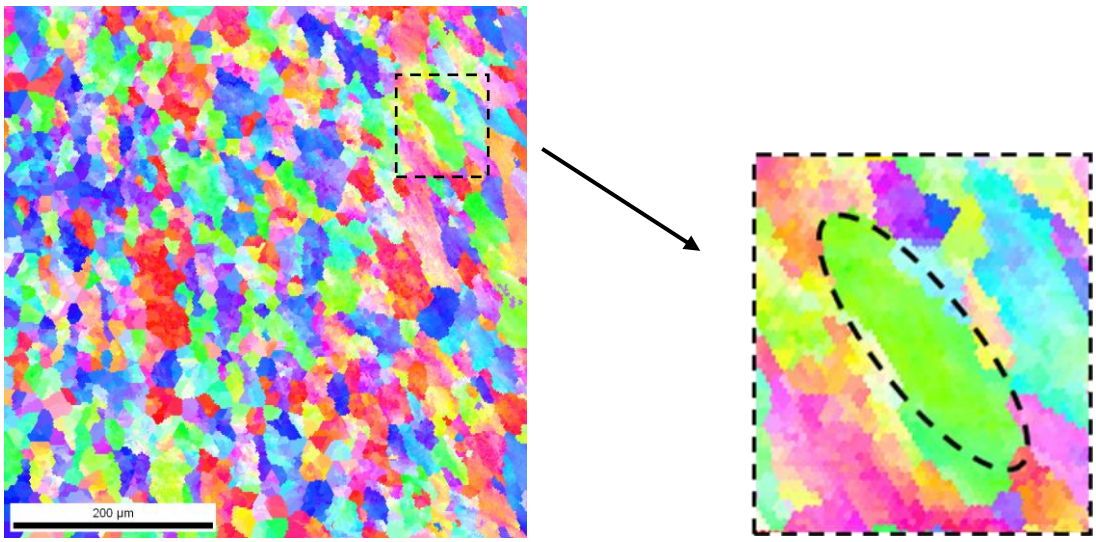

Figure 6.3: Auto IPF EBSD map of a rolled aluminium sample with one grain with a particularly severe aspect ratio R highlighted. Each grain detected is subjected to an iterative calculation to fit an ellipse to generate an accurate perception of the average aspect ratio for the sample.

The most convenient aspect ratio method used to fit an ellipse is by a least squares method, an approach developed by *Dingley* [27], which iteratively minimises the distance between all the coordinates of the EBSD data points that lie along a grain boundary to the corresponding ellipse. Data from this method is displayed similarly to the grain size calculation, presenting the % fraction of aspect ratios within a defined range. Figure 6.4 shows an example of an aspect ratio plot derived from EBSD data.

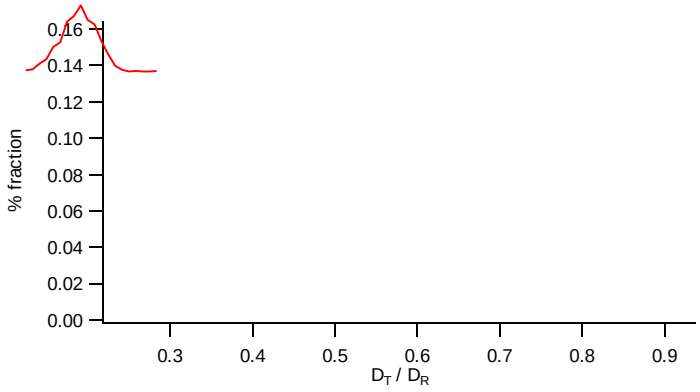

Figure 6.4: OIM Aspect Ratio data from an EBSD scan performed on a DC05 Steel Sheet sample provided by Corus. The data is represented in a % fraction form similar to the grain size measurement graph in figure 5, with the aspect ratio calculated for each complete grain on the scan area. Here, the mean aspect ratio is approximately 0.53.

6.3 – Elasticity measurements

As described by equations 6.22 to 6.25, the nine effective elastic stiffness constants can be predicted from EBSD data for all of the samples investigated here. A method to determine the elastic stiffness constants ultrasonically, using longitudinal and shear waves propagated and polarised in the necessary directions, has been derived previously by *Sayers* [4] and *Alers* [18], amongst others.

The attenuation measurements described above utilise shear waves propagating in the normal direction and polarised along the rolling and transverse directions respectively in

order to measure the aspect ratio. It has also been explained how the Lamb wave texture measurements described can quantify the three determinable ODCs. With this information and by measuring the shear wave velocity from the attenuation experiment A-scans, ultrasonic predictions for the elastic stiffness constants c'_{44} and c'_{55} can be calculated, and compared to the predicted EBSD values.

The equation linking c'_{44} and c'_{55} to the ultrasonic SH velocity is simply given by:

$$v = \sqrt{\frac{c'_{xx}}{\rho}} \tag{6.44}$$

Therefore only knowledge of the density and SH velocity is all that is required to make a prediction of these constants.

Of course, the rolled sheets to be studied are elastically anisotropic and for completeness this needs to be considered. The Lamb wave predictions of the ODCs can also give a prediction on the values of c'_{44} and c'_{55}. Solving equations 6.45 and 6.46 will give predicted values of the velocity v_{SH}, which can be then used in equation 6.44.

$$v_{SH_{rolling}} = \sqrt{\frac{\left(c_{44} + c\left[\frac{1}{5} - \frac{16}{35}\sqrt{2}\pi^2\left(W_{400} + \sqrt{\frac{5}{2}}W_{420}\right)\right]\right)}{\rho}} \tag{6.45}$$

$$v_{SH_{transverse}} = \sqrt{\frac{\left(c_{44} + c\left[\frac{1}{5} + \frac{4}{35}\sqrt{2}\pi^2\left(W_{400} - \sqrt{70}W_{420}\right)\right]\right)}{\rho}} \tag{6.46}$$

This will give a correlation of the ODC theory to the empirical shear wave velocity data, which again will add evidence to the legitimacy of this technique to measure texture.

6.4 – References

1. *Panetta PD, Thompson RB, Margetan FJ, Rev. of Prog. in QNDE,* ***17A****, 1997, pp.89-96*

2. *Scruby CB, Young RMK, Bull CE, Humphreys FJ, Mats. Science and Tech.,* ***19****, 2003, pp. 163-172*

3. *Roe R-J, Journal of Applied Physics,* ***36(6),*** *1965, pp. 2024-2031*

4. *Sayers CM, J. Phys. D: Appl Phys.,* ***15****, 1982, pp. 2157-2167*

5. *Roe R-J, J. Appl. Phys.,* ***37(5)****, 1966, pp. 2069-2072*

6. *Li Y, Thompson RB, J. Acoust. Soc. Am.,* ***91(3)****, 1992, pp. 1298-1309*

7. *Voigt W, Abh. Kgl. Ges. Wiss. Göttingen Math. Kl.,* ***34****, pp. 3-51, 1928*

8. *Reuss A, Z Agnew. Math. Mech.,* ***9****, 1924, pp. 49-58*

9. *Hill R, Journal of Mechanics and Physics of Solids,* ***5****, 1957, pp. 229-241*

10. *Davis CL, Strangwood M, Potter MDG, Dixon S, Morris PF, Mat Trans, in press*

11. *Rose JL, Ultrasonic waves in solid media, Cambridge University Press, 1999*

12. *Dixon S, Edwards C, Palmer SB, J. Phys. D: Appl. Phys.,* ***35****, 2002, pp. 816-824*

13. *Thurston RN, Physical Acoustics, Vol I, Edited by Mason WP, Academic Press 1964*

14. *Papadakis EP, Materials Evaluation,* ***51****, 1993, pp. 77-85*

15. *Potter MDG, Dixon S, Davis C, Meas. Sci. Technol.,* ***15****, 2004, pp. 1303-1308*

16. *Wright SI, Nowell MM, Bingert JF, Metallurgical and Materials Transactions A,* ***38A****, 2007, pp.1845-1854*

17. *Nye JF, Physical Properties of Crystals, Oxford Press, 1957*

18. *Alers GA, Sinclair AN, Rev. Prog. In QNDE,* ***18****, 1999, pp. 1695-1701*

19. *Kocks UF, Tome CN, Wenk H-R, Texture and Anisotropy, Cambridge University Press, 2000*

20. *Hearmon RFS, Acta. Cryst.,* ***10****, 1957, pp. 121-124*

21. *Thompson RB, Lee SS, Smith JF, Ultrasonics,* ***25****, 1987, pp. 133-137*

22. *Krautkrämer J, Krautkrämer H, Ultrasonic Testing of Materials, Springer-Verlag, 1990*

23. *Lakes RS, Viscoelastic Solids, CRC Press, 1999*

24. *Smith RL, Ultrasonics, 1982, pp. 211-214*

25. *Kesler HA, Shraifeld LI, Sov. J. NDT,* ***11****, 1975, pp. 76*

26. *Sourced from OIM helpfile*

27. *Biggin S, Dingley DJ, Journal of Applied Crystallography,* ***10****, 1975, pp. 376-385*

CHAPTER 7

Ultrasonic texture and grain characterization measurements

This chapter describes the experimental methods and apparatus involved in all of the ultrasonic measurements taken for this thesis. Ultrasonic data for a number of rolled aluminium and steel sheets, together with the relevant analysis, is also presented.

7.1 – Ultrasonic measurement of crystallographic texture

7.1.1 – Experimental detail

The generation of the quantitative ultrasonic measurements of the measurable ODCs can be acquired by velocity measurements of the S_0 mode Lamb wave as a function of angle to the RD. The measurements were obtained using a commercially available, non-destructive, EMAT-to-EMAT texture measurement system. The theoretical development of this argument has been discussed previously in chapter 6.

A photograph of the apparatus is shown in figure 7.1, with the photograph in figure 7.2 giving a closer view of the EMAT configuration. The texture measurement system used was provided by *Sonemat Ltd*. The method deployed in measuring the crystallographic texture is in line with the published work of *Potter et al* [1].

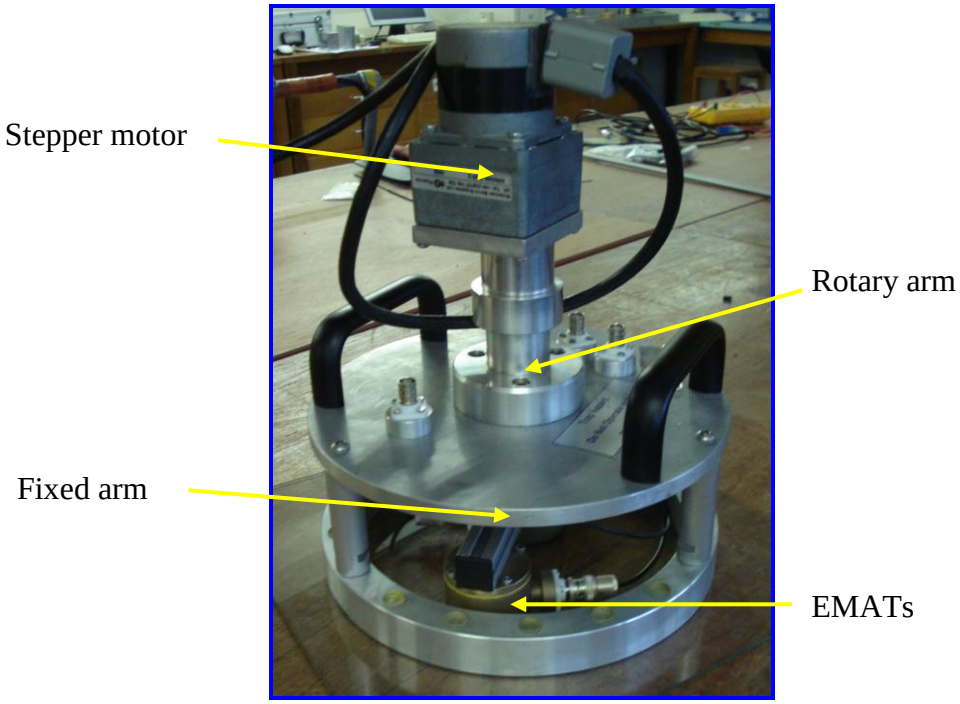

Figure 7.1: Photograph of the Sonemat Ltd. non-destructive texture measurement system utilising EMATs used in this study.

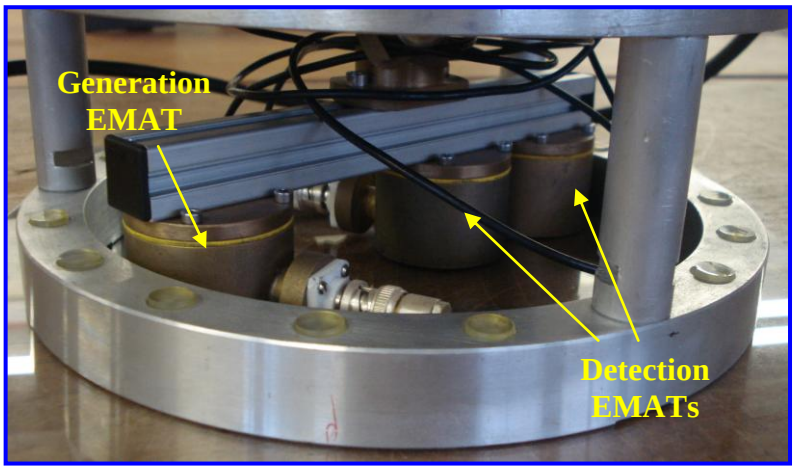

Figure 7.2: Close up photo showing the arrangement of the three EMATs that are incorporated in the online texture measurement system, as shown in figure 7.2.

The apparatus consists of one generation and two detection EMATs; the centres of the two detection EMATs set a fixed distance of 95.4 mm and 147.3 mm from the generating EMAT centre respectively. The use of two detection EMATs improves the accuracy of the

measurement, which yields improved accuracy in determining the absolute velocity of the generated S_0 Lamb wave mode. Using only one receive-EMAT would still be suitable for measuring the relative change in velocity with angle, but a calibration would be required to correct for the time lag in the received signal due to the EMAT-to-sample standoff distance. Using two EMATs calibrates the absolute velocity measurement and more importantly determining which part of the S_0 wave corresponds to the arrival time.

The generation EMAT is constructed with an NdFeB permanent magnet, and utilises a directional linear coil design. The coil has 10 turns, and is made with 0.315 mm diameter enamelled copper wire. The receive EMATs again have NdFeB permanent magnets, and also use linear coil designs to detect the Lamb wave. These coils are made with 0.08 mm diameter copper wire, and have 30 turns. Extensive work [1] has been completed to determine the optimal coil configuration to enhance the accuracy and efficiency of the generation and detection mechanisms for the texture measurement system.

The fixed arm supporting the EMATs is fully rotatable; the EMATs are securely suspended, maintaining a small lift-off above the sheet of approximately 1 mm. The arm rotation is driven by a stepper motor which in turn is controlled by a PC which also controls the pulse generator, data acquisition and signal processing.

When conducting experiments, the rolled sheet sample is positioned so that the rolling direction is aligned parallel to the bisector of the three EMATs. This is defined as $\theta = 0°$. The S_0 mode velocity of the generated Lamb wave is measured, and in this case was recorded as an average over 100 readings. The rotary arm is rotated 3.6° by the stepper motor, and the average velocity is again calculated. This process repeats for a complete 360° rotation to produce an average v vs. θ curve.

It should be noted that this method is non-destructive, relatively inexpensive, and gives the elastic anisotropy as a result of the average throughout the thickness of the sheet. Though in this instance, each measurement is averaged over 100 readings, in the requirement of a rapid texture measurement, the total scan speed can be increased considerably. Even at the sampling and average rates chosen here, a scan is completed in a few minutes.

To remind the reader, the velocity against angle data is subjected to graphical fitting procedures, using a least squared argument to extrapolate the best prediction for the ODCs from the data to quantify the texture by solving for equation 7.1 [2]:

$$\rho v^2 = A + BW_{400} + CW_{420}\cos(2\theta) + DW_{440}\cos(4\theta) \qquad (7.1)$$

Prior to data analysis, the Labview code requires the input of the single crystal constant parameters and the thickness of the sheet being used. Table 7.1 lists the singe crystal constants used throughout this study [3].

	C^x_{11} (GPa)	C^x_{12} (GPa)	C^x_{44} (GPa)	c – anisotropy parameter (GPa)
Aluminium	108.2	61.3	28.5	-10.1
Steel (DC)	230	135	117	-139

Table 7.1: Single crystal constants and anisotropy parameter values for aluminium and the steel samples used in the ultrasound and EBSD ODC determination measurements.

7.1.2 – Samples studied

The aluminium sheets investigated were purchased from *Advent Research Materials*. The sheets are nominally pure, characterised with > 99.5 % purity levels, which was confirmed with EDX measurements performed in the SEM. The sheets studied have thicknesses of 0.2 mm, 0.5 mm, 1 mm and 1.5 mm within the tolerance levels set by *Advent RM*. The sheet dimensions were all 300 mm × 300 mm × *d* (thickness = d), and all classified as tempered and half-hard, cold-rolled sheet.

The steel sheets tested were supplied by *Corus*, both of them from the *Corus* DC range of sheet steel. The sheets were labelled DC01 and DC05. The size of the sheets varied slightly, though all were within 5 % tolerance of a 300 mm × 230 mm surface area. The sheets were 1.48 mm and 1.3 mm thick respectively (± 0.01 mm). The composition of these sheets (data published by *Corus* [4]) is shown in table 7.2. The high iron content of these

alloys, > 99 %, was confirmed by completing EDX measurements again within the SEM. An example of such an EDX scan was shown in figure 4.5. The iron phase present was one that supported ferromagnetic properties, and from phase identification and Kikuchi diffraction pattern analysis, it was evident that the iron phase was δ-iron.

Steel	***C (max) %***	***Mn (max) %***	***P (max) %***	***S (max) %***
DC01	0.12	0.6	0.045	0.045
DC05	0.06	0.35	0.025	0.025

Table 7.2: The chemical composition, as detailed by Corus, of the DC series cold-rolled steel products supplied by them for this study. The values represent the maximum weight percentages of each element. Fe provides the remainder of the chemical composition.

7.1.3 – Dispersion considerations

The central frequency of the broadband pulse of the generated Lamb wave was consistently centred around 200 kHz, confirmed from frequency analysis of a typical S_0 Lamb wave mode A-scan. The corresponding wavelength is therefore large compared to the sheet thickness, and of particular importance is that the frequency-thickness product (MHz.mm) is small. This implies dispersion effects are negligible, and on inspection of the dispersion curve for the S_0 mode, specifically at the low frequency-thickness products (figure 7.3), this is confirmed. Following a method of *Thompson* [5], a correction to the first order to c_g was inbuilt into the data acquisition software to accommodate this small difference.

The resulting energy characteristic of the Lamb wave is such that the energy distribution will be homogeneous throughout the thickness [6]. There is also negligible out-of-plane displacement. This ensures that any detected variation in velocity with angle will be due to an average change of the effective elastic modulus through the bulk in that direction. This is desirable for this particular work and will improve the reliability of results obtained.

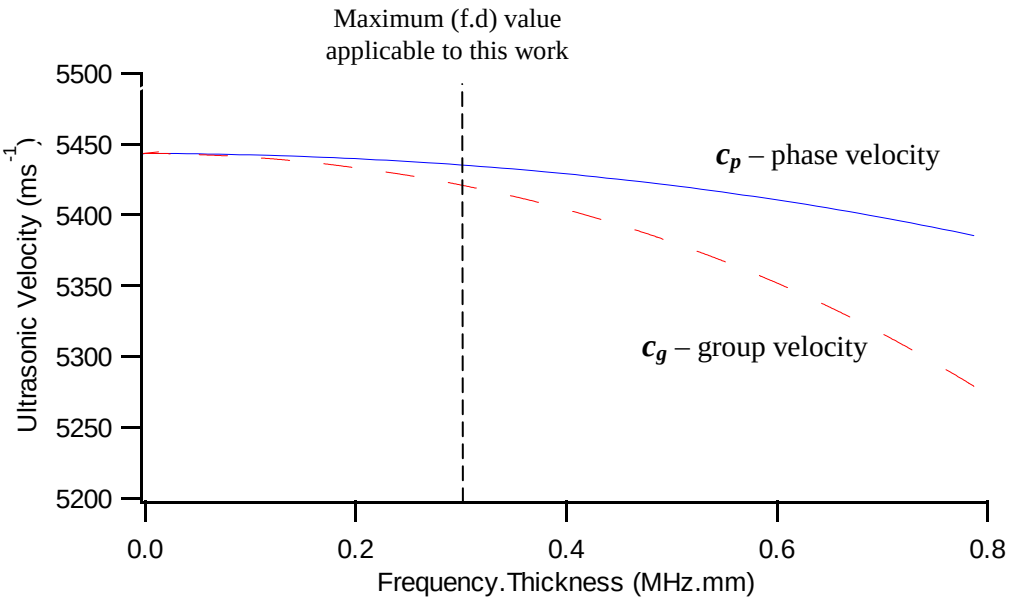

Figure 7.3: Dispersion curve for the S_0 mode Lamb wave, showing that at low frequency-thickness products approaching zero, the phase and group velocities c_p and c_g tend to the same value.

7.1.4 – Ultrasound texture measurement data

7.1.4.1 - Aluminium

The four aluminium sheets were not subjected to any further deformation or annealing procedures before being investigated, so in essence have been studied 'as-rolled'. The codes assigned to the respective samples are the product reference line numbers assigned by the distributors *Advent RM*.

For the texture measurements below, in each case the red line displayed on each graph represents the measured velocity data determined by the EMATs, and the blue line is the corresponding applied mathematical fit, which is used to obtain the ODCs. This data is displayed in figures 7.4-7.7.

Errors have been incorporated into the determined ODCs, and are discussed in section 7.1.5.

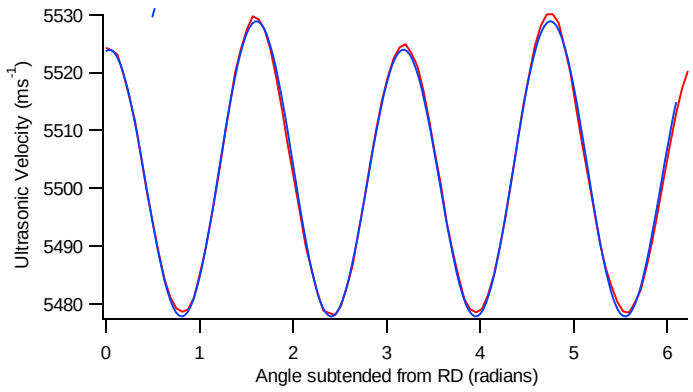

Figure 7.4: Ultrasonic velocity profile for 0.2 mm thick aluminium sheet AL101325. The red line is the measured velocity data, the blue line is the corresponding applied fit.

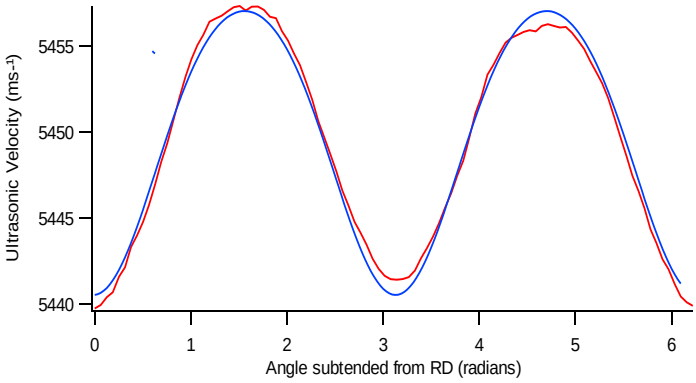

Figure 7.5: Ultrasonic velocity profile for 0.5 mm thick aluminium sheet AL104232. The red line is the measured velocity data, the blue line is the corresponding applied fit.

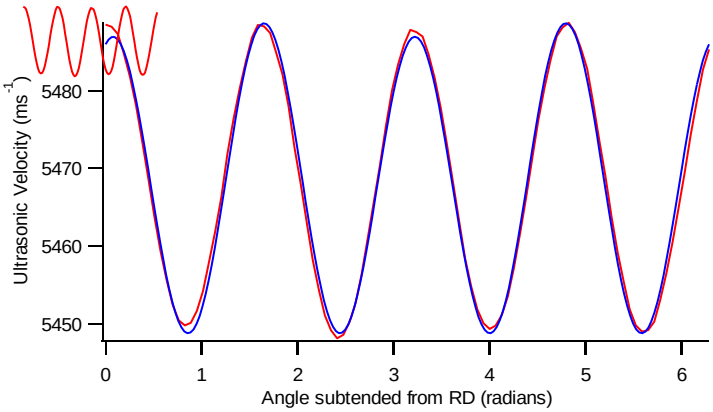

Figure 7.6: Ultrasonic velocity profile for 1 mm thick aluminium sheet AL104325. The red line is the measured velocity data, the blue line is the corresponding applied fit.

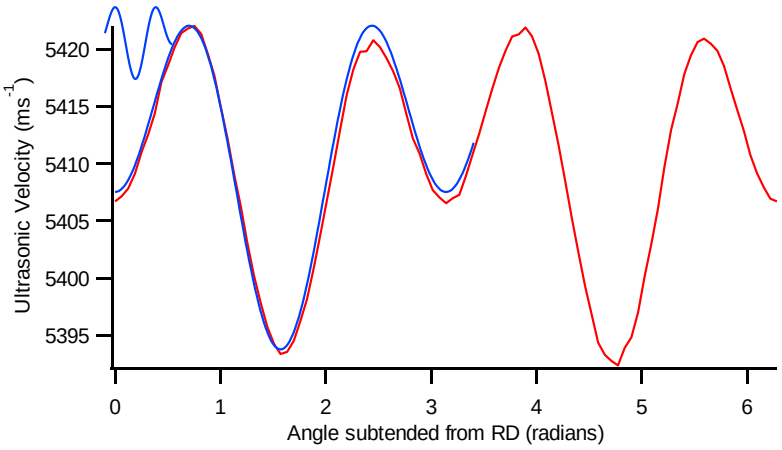

Figure 7.7: Ultrasonic velocity profile for 1.5 mm thick aluminium sheet AL104532. The red line is the measured velocity data, the blue line is the corresponding applied fit.

7.1.4.2 – DC steel series

As for the aluminium samples studied, the DC series steel sheets were not subjected to any further working and were tested as received.

Again, for the texture measurements below the red line displayed on each graph represents the measured velocity data and the blue line is the result of the applied fit to determine the ODCs from equation 7.1. This data is displayed in figures 7.8 and 7.9. Error analysis is incorporated into the determined ODCs, and is discussed in due course.

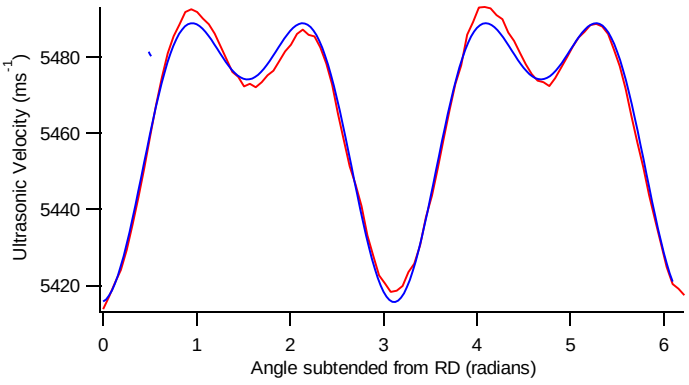

Figure 7.8: Ultrasonic velocity profile for steel sheet DC01. The red line is the measured velocity data, the blue line is the corresponding applied fit.

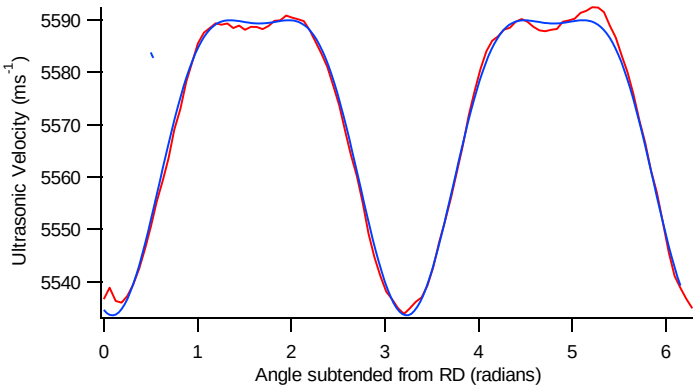

Figure 7.9: Ultrasonic velocity profile for steel sheet DC05. The red line is the measured velocity data, the blue line is the corresponding applied fit.

7.1.5 – Calculated ODCs

The mathematical fit was applied to the velocity data to calculate the necessary coefficients that can estimate the ODCs with the best accuracy. The results displaying the measured ODCs for the aluminium and steel sheet samples tested are given below in tables 7.3 and 7.4.

Thickness (mm)	W_{400}	W_{420}	W_{440}
0.2	-1.07×10^{-2}	-3.27×10^{-4}	-5.02×10^{-3}
0.5	-1.22×10^{-3}	-1.08×10^{-3}	1.34×10^{-4}
1	-4.61×10^{-3}	1.15×10^{-4}	-4.01×10^{-3}
1.5	-2.21×10^{-3}	1.19×10^{-3}	2.67×10^{-3}

Table 7.3: ODC values extrapolated from the ultrasonic velocity trace for the respective aluminium sheets. The largest calculated error magnitude for the ODCs was ± 3.5 ×10^{-5}.

Steel	W_{400}	W_{420}	W_{440}
DC01	-7.75×10^{-3}	-1.05×10^{-3}	9.54×10^{-4}
DC05	-1.36×10^{-3}	-1.02×10^{-3}	-4.36×10^{-4}

Table 7.4: ODC values extrapolated from the ultrasonic velocity traces for the DC steel sheets. The largest calculated error magnitude for the ODCs was ± 1.6 ×10^{-5}.

7.1.6 – Discussion of errors in texture measurements

There are two sources of errors that need to be considered carefully in this experiment. Firstly, the errors associated with measuring the absolute velocity of the Lamb waves. Secondly, further errors arise in the accuracy of the graphical fit of equation 7.1; these errors manifest in the accuracy of the determined texture coefficients.

Random errors affecting the accuracy of the absolute velocity measurements include EMAT lift-off variation which intuitively affects the signal received. The increase in stand-off would smear the waveform. Every effort was made to minimise this effect. The design of the apparatus afforded a consistent stand-off distance, particularly for aluminium which had no discernible magnetic interaction with the NeFeB permanent magnets.

100 velocity measurements were taken for each angle to further improve accuracy to reduce the random errors. For example, the texture measurement system has a 'fast' scan capability, taking 1 velocity measurement at each angle whilst the EMATs are continuously rotated. The data is collected in just a few seconds, though the speed of data acquisition comes at a cost in accuracy. The movement of the EMATs as the Lamb waves are being generated and detected gives larger random errors, with alignment and signal quality being compromised. Continuous movement of the stepper motor increases the presence of electrical noise also. Figure 7.10 illustrates the effect of the noise associated with the 'fast' experimental setup, here displaying fast data for the 0.2 mm thick aluminium scan (red trace). The mean velocity determined from 100 readings per point is also displayed on the graph (in blue) for comparison.

The main source of systematic error exist in the measured distance between the generation and the two detection EMATs. The Labview program requires the input of the distance between the EMATs to determine the velocity. Values of 95.4 mm and 147.3 mm were used in the program and were checked manually; both were agreeable within ± 0.05 mm, equating to absolute errors in the distances of 0.053% and 0.034% respectively. The texture measurement system had been calibrated previously using samples of known

velocity to confirm the distance accuracy. The effect of the size and design of the coils used was also researched extensively [1].

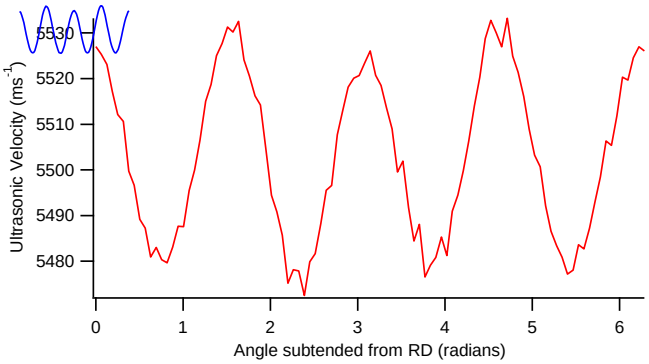

Figure 7.10: Ultrasonic velocity profiles for 0.2 mm thick aluminium sheet AL101325. The red trace is the velocity data taken with just one measurement per point, with the blue trace giving the mean velocity at each point from 100 measurements per point.

Any systematic errors that manifest in the velocity measurement are inherent in all the velocities at each angle of propagation. Therefore the velocity variation will always be detected, indicating that the magnitude of the angular dependent ODCs W_{420} and W_{440} will be unaffected. However, with a 0.034% uncertainty in distance, the absolute variation in velocity detected will have an uncertainty of approximately ± 0.02 ms^{-1} (figure 7.10 shows a velocity variation of ~ 50 ms^{-1} for example). This uncertainty is less than the noise in the signal, especially in the case for the 'fast' data.

Visually comparing the two corresponding sets of data from figure 7.10, the averaged curve is smoother, possessing less noise than the fast scan. This is to be expected as the signal to noise ratio is improved by a factor of 10. Taking the mean will eradicate errors caused by the directionality of the beam, electrical noise and stand-off fluctuations which are more significant with the rotating EMATs.

Applying the mathematical fit to both scans in figure 7.10 to extrapolate the ODCs gave the results displayed in table 7.5.

	W_{400}	W_{420}	W_{440}
Slow	$-0.0107 \pm 3.39 \times 10^{-7}$	$-0.000327 \pm 1.63 \times 10^{-5}$	$-0.00502 \pm 2.55 \times 10^{-5}$
Fast	$-0.0109 \pm 1.22 \times 10^{-6}$	$-0.00029 \pm 5.79 \times 10^{-5}$	$-0.00511 \pm 9.04 \times 10^{-5}$

Table 7.5: ODCs and errors associated with fast and slow texture scans for 0.2 mm thick aluminium sheet.

The errors indicated in table 7.5 are at least × 3.5 greater for the fast scan. The ODCs are similar, within 10% with correct orders of magnitude and sign; this suggests a fast scan is a viable option for the estimation of crystallographic texture.

The level of agreement between the mathematical fit and the velocity data needs to be considered however. The graphical fit applied to the ultrasound data was programmed in a proprietary data analysis program (*Igor*, *Wavemetrics)*, which was incorporated into the Labview data collection program provided by *Sonemat Ltd*. The fit utilises a least squares algorithm, iteratively determining the optimum solution to equation 7.1, by minimising the sum of the difference between each data point and the line of best fit (root mean squared errors). Error analysis was included in the analysis software, the errors given with the ODCs. Figure 7.11 shows the residual velocity between the measured velocity and the corresponding fit velocity (data given in figure 7.4).

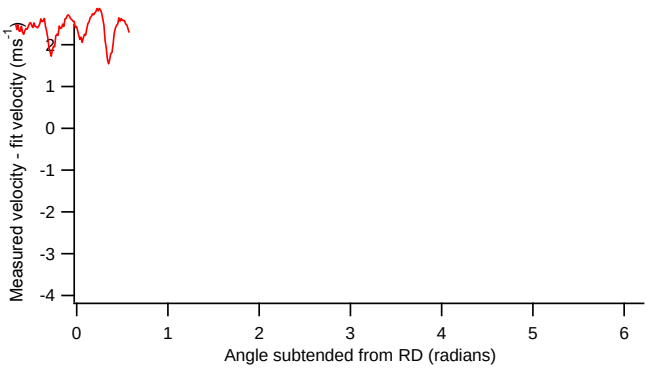

Figure 7.11: Residual velocity between EMAT measured and applied fit for 0.2 mm thick aluminium sheet.

Plotting the residuals in a histogram and taking 95% confidence intervals, the

standard deviation can be calculated to be ~ 0.76 ms^{-1}. Combining this with the 0.02 ms^{-1} absolute distance uncertainty leaves a total error in the fit of 0.79 ms^{-1}; this equates to ~ 0.014% error in the velocity for the 0.2 mm thick sheet, as shown in figure 7.12.

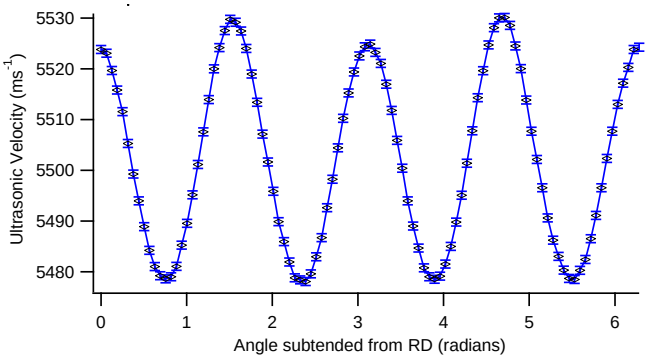

Figure 7.12: 0.2 mm thick aluminium sheet data including error bars.

The maximum errors for the measured ODCs in both steel and aluminium are given in tables 7.3-7.4. The largest calculated error in the ODCs was ± 3.5 $\times 10^{-5}$. The orders of magnitude of the ODCs are between $\times 10^{-2}$ and $\times 10^{-4}$; the smallest ODC value recorded is the W_{420} coefficient for the 1 mm thick aluminium sheet (table 7.6)

Sample	***W_{400} % error***	***W_{420} % error***	***W_{440} % error***
Al – 0.2mm thick	-0.0032	-4.99	-5.08
Al – 0.5mm thick	-0.0022	1.03	1.3
Al – 1.0mm thick	0.0045	2.05	**5.79**
Al – 1.5mm thick	-0.0036	1.53	1.07
DC01	-8.40E-03	-1.18	**8.18**
DC05	-4.97E-03	-1.11	1.69

Table 7.6: ODC % errors. The largest aluminium and steel errors are highlighted in bold.

The largest percentage error for an ODC in an aluminium sample was 5.79% and for steel it was 8.18%: both were for the W_{440} ODC. The calculated W_{440} ODC will in general have larger errors than the other two ODCs as it depends on W_{400} [7] also. Any errors from W_{400} (though usually small) will manifest within the error of W_{440}.

7.2 – EMAT SH measurements

7.2.1 – Experimental details

In contrast to the texture measurements, results for this experiment were collated using one linearly polarised SH wave EMAT in a pulse-echo setup. This allows for the measurement of the attenuation of amplitude over a number of successive echoes.

The EMAT had a pancake coil with 30 turns. It has a split magnet design, the magnet split in two with polarity switched, which allows the horizontal displacement associated to an SH wave. This is shown diagrammatically in figure 7.13 A comprehensive design plan of this particular EMAT is available in the literature [8].

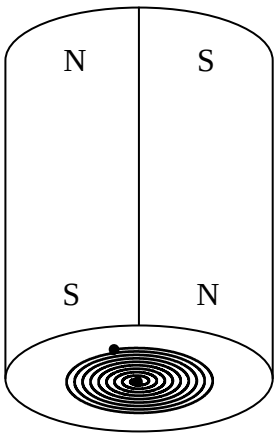

Figure 7.13: Schematic diagram of the magnet and coil setup of the linearly polarised SH wave EMAT used in this study.

The shear wave therefore propagated through-thickness, polarised in the plane of the sheet. Results were taken with the polarisation set along the RD and then repeated along the TD. The two respective measurements were taken in the same position on the sheet; the EMAT was rotated 90˚ to align the polarisation as appropriate.

Potential problems have been flagged in previous work using a pulse-echo EMAT setup. Used as a thickness gauge on thin rolled sheet, it has been shown that this experimental setup using a through-thickness shear wave is more suitable for aluminium samples than steel [8], so this is to be expected here. Problems with mode conversion of the shear wave at

reflections has been reported [9], causing interference of the echoes, and if present will impede on accurate results and analysis. This is more significant in thin sheet, and hence will affect the 0.2 mm and 0.5 mm thick aluminium sheet results in particular.

Figure 7.14 shows A-scans of consecutive SH waves detected in a pulse echo setup, on the left (a) for a 0.2 mm thick sample, and on the right (b) for a 1.5 mm thick sample.

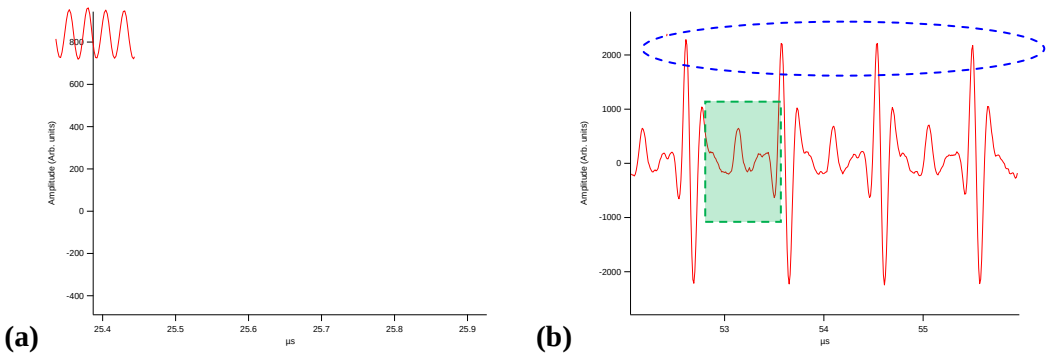

Figure 7.14: Successive SH echoes detected using a pulse-echo EMAT system in a (a) 0.2 mm thick aluminium sheet and a (b) 1.5 mm thick aluminium sheet.

With reference to figure 7.14b, it is noticeable there are smaller peaks detected, such as those highlighted within the green area, between each successive SH wave echo (the peaks of which are within the blue area). This is not the case for figure 7.14a because the thinner sheet means the SH peaks are detected so quickly (approximately 0.13 μs) the EMAT cannot differentiate between the mode conversion signals and the main SH wave. Hence they interfere and produce an A-scan which is sinusoidal in appearance. The mode conversions occur at each reflection: at each reflection at an interface normal to the sheet surface, a shear and a longitudinal component will result from an incident shear wave, as displayed schematically in figure 7.15. A similar mode conversion with an incident longitudinal wave generating shear and longitudinal components will also exist. The small peaks between the SH echoes are a consequence of LL, SL and LLLS (or similar) mode conversions. As a consequence of these mode conversions, velocity and attenuation measurements are harder to quantify for thin sheet. Velocities can however be obtained from FFT analysis.

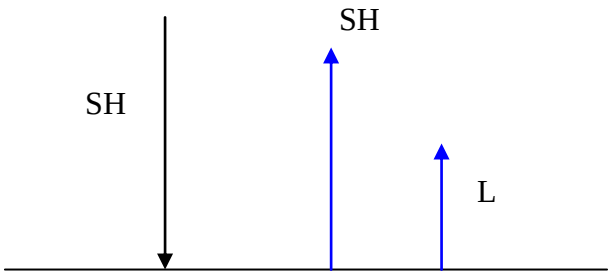

Figure 7.15: Schematic diagram detailing an example of mode conversion which can lead to interference in the amplitude of the shear wave. The mode conversions are relatively small

For the experiments the SH wave amplitude was recorded over 8160 data points, with each point taken at time intervals of 1×10^{-8} s. The total time is large compared to the time lost initially on the A-scans, where significant fluctuations in the amplitude of the SH wave is seen due to front end paralysis and the dead time of the EMAT. There is ample time for a number of shear wave back wall echoes to be recorded. This therefore gives the intrinsic attenuation an opportunity to have a significant and detectable effect on the subsequent amplitude of the corresponding peaks.

Data collection and analysis was completed using Labview; on completion of each A-scan, frequency analysis was carried out using a Fast-Fourier Transform (FFT). Each experiment was conducted seven times in each orientation, firstly to determine the repeatability, for averaging purposes to obtaining $\overline{\alpha}$, and finally to assess the frequency content at different windowed times in the scan. Data windows with a width of 1000 data points ($1x10^{-5}$ s) were selected, and positioned at initial data points starting from 1000, 2000, 3000, 4000, 5000, 6000 and 7000 sequentially. This would ensure an accurate measure of the shear wave frequencies present, and the latter FFT results would not be influenced by the initial large power pulse associated with the pulse generation, as this contains no useful ultrasound signal. There is also a time lag to consider when using one EMAT in a dual generation-receive system which also encourages Fourier analysis of an A-scan to be completed once the repeating peaks representing continuous echoes are apparent.

7.2.2 – Samples studied

The same aluminium and steel samples used previously were tested in their as-found condition.

7.2.3 – Ultrasonic attenuation measurements

The graph shown in figure 7.16 presents one of the shear wave A-scans taken for the 1.5 mm thickness aluminium sample. The red trace gives the amplitude as a function of time when the shear wave is polarised along the RD, the blue trace being the A-scan for the wave polarised in the TD.

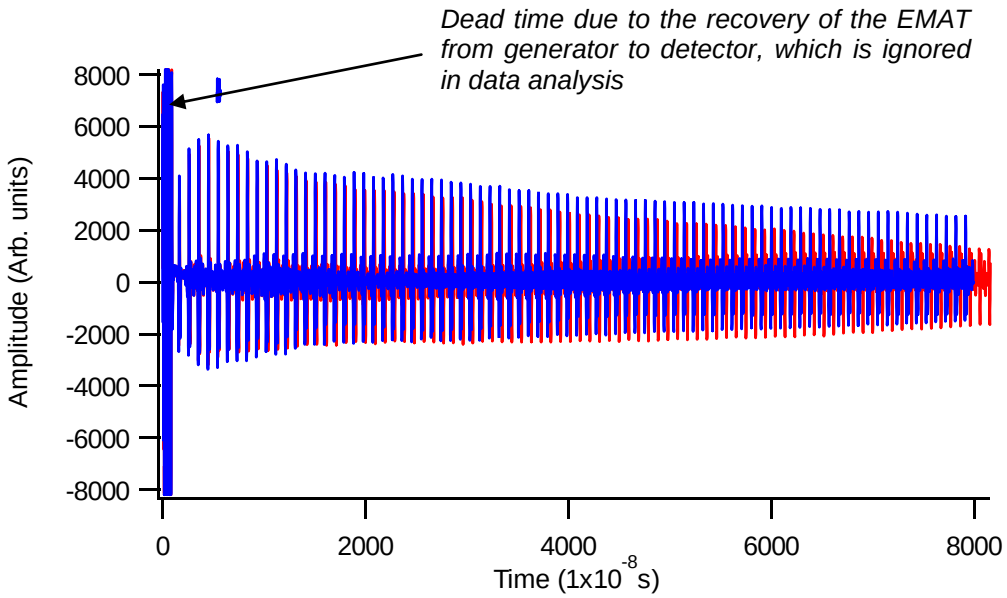

Figure 7.16: Ultrasonic through thickness shear wave response for waves polarised in the rolling (red) and transverse (blue) directions for the 1.5mm thick aluminium sheet.

It is noticeable in figure 7.16 that differentiating between the data is difficult. The detection time between peaks for the 0.2 mm thick sheet for example is over seven times shorter than the 1.5 mm sheet and hence these A-scans have not been printed. The following sections display a decay envelope from one A-scan of each sample taken.

7.2.3.1 - Aluminium

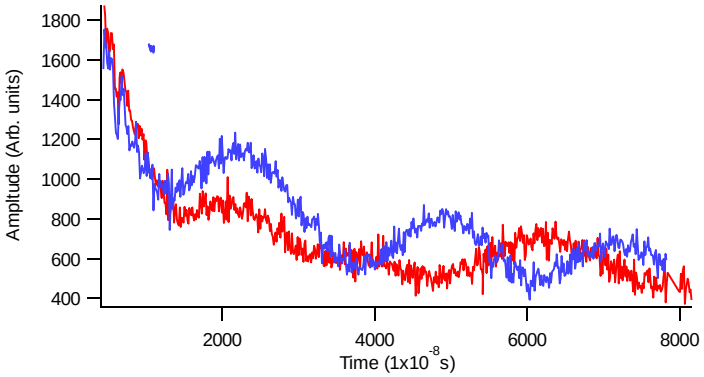

Figure 7.17: Decay envelopes for the shear wave response for the wave polarised in the rolling (red) and transverse (blue) directions for the 0.2 mm thick aluminium sheet.

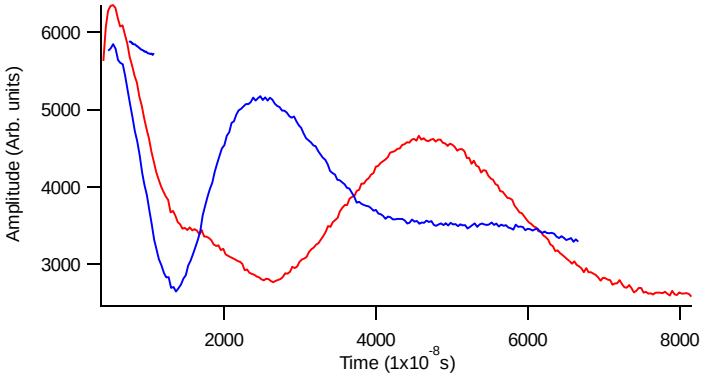

Figure 7.18: Decay envelopes for the shear wave response for the wave polarised in the rolling (red) and transverse (blue) directions for the 0.5 mm thick aluminium sheet.

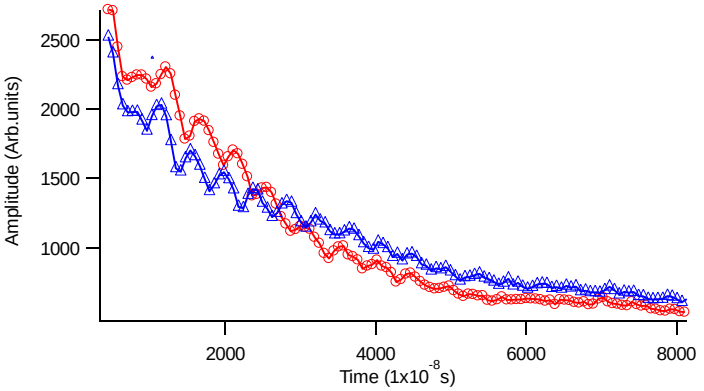

Figure 7.19: Decay envelopes for the shear wave response for the wave polarised in the rolling (red) and transverse (blue) directions for the 1 mm thick aluminium sheet.

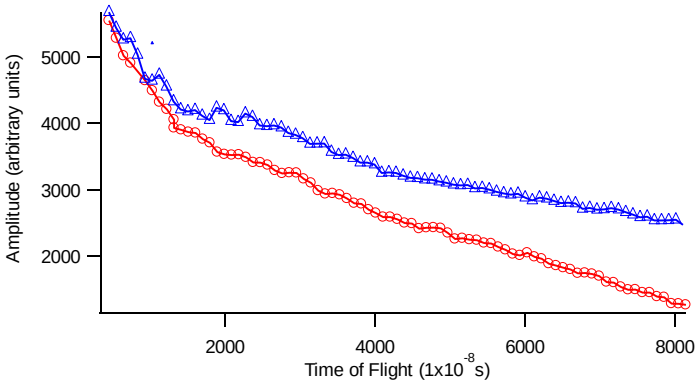

Figure 7.20: Decay envelopes for the shear wave response for the wave polarised in the rolling (red) and transverse (blue) directions for the 1.5 mm thick aluminium sheet.

7.2.3.2 – DC Steel series

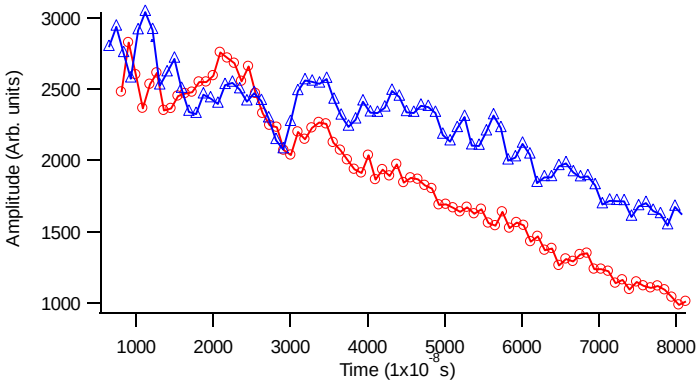

Figure 7.21: Decay envelopes for the shear wave response for the wave polarised in the rolling (red) and transverse (blue) directions for the DC01 steel sheet.

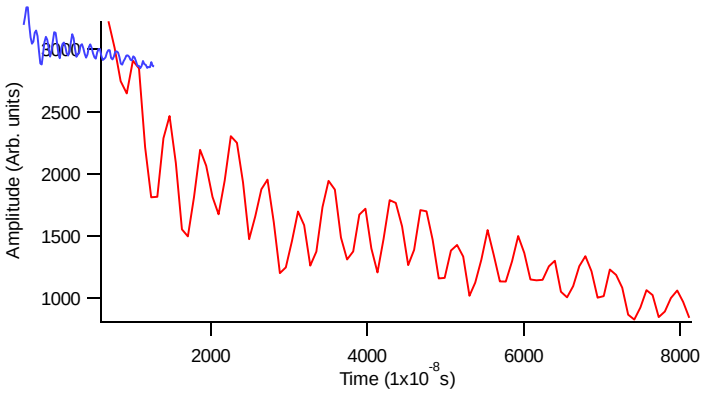

Figure 7.22: Decay envelopes for the shear wave response for the wave polarised in the rolling (red) and transverse (blue) directions for the DC05 steel sheet.

7.2.4 – Attenuation coefficients

Presented here are the results for the measured total attenuation coefficient α from each experiment, established from fitting an exponential decay curve to the decay envelopes to solve for equation 6.32. These values for α were checked for accuracy by solving α for each peak with reference to the first peak (from equation 6.32). Determining the amplitude of the initial peak, and defining that as A_0, and with the amplitude of each corresponding peak known too, an average value of α was determined from the seven A-scans taken per sample.

The results of this analysis are shown in tables 7.7 and 7.8. The errors are discussed in section 7.4, with the validity and extra analysis of these results completed in chapter 9.

Thickness (mm)	α_{RD}	α_{TD}
0.2	7.10	5.01
0.5	3.92	3.42
1	8.2	6.92
1.5	5.3	2.91

Table 7.7: Calculated total attenuation coefficients α_{RD} and α_{TD} for the aluminium sheet samples studied.

Steel	α_{RD}	α_{TD}
DC01	3.94	2.36
DC05	6.06	4.08

Table 7.8: Calculated total attenuation coefficients α_{RD} and α_{TD} for the steel sheet samples studied.

7.3 – Elasticity measurements

The measurement of the respective velocities of the shear waves polarised along the RD and TD for each sheet can be determined from the average peak-to-peak time difference from the generated A-scans.

The average velocity for the 1 mm and 1.5 mm thick aluminium sheet, and the steel samples, was calculated over the complete scan using all available peaks resulting from the back wall echoes. From this, the elastic stiffness constants c'_{44} and c'_{55} can be theoretically determined, as explained in section 6.3. Error analysis is calculated in section 7.4.

The velocities of the thinner aluminium sheets, where interference from mode conversions affects the A-scans produced were determined from magnitude FFT analysis. The peak frequency gives a more accurate representation of the time period between successive echoes, leading to a better interpretation of the SH wave velocity

7.3.1 – Aluminium velocity measurements

Thickness (mm)	v_{RD} (ms^{-1})	v_{TD} (ms^{-1})
0.2	3166.2	3167.7
0.5	3182.8	3168.4
1	3131.1	3125.0
1.5	3125.0	3134.8

Table 7.9: Calculated velocity measurements of the through-thickness shear waves propagated in the aluminium samples.

7.3.2 – Steel velocity measurements

Steel	v_{RD} (ms^{-1})	v_{TD} (ms^{-1})
DC01	3235.0	3152.3
DC05	3291.1	3241.0

Table 7.10: Calculated velocity measurements of the through-thickness shear waves propagated in the steel samples.

7.3.3 – Elasticity predictions

7.3.3.1 – From the shear wave equation

Tables 7.11 and 7.12 display the predicted values for c'_{44} and c'_{55} using the shear wave equation linking the velocity to the elastic constant and density. The values of ρ used are 2700 kgm^3 and 8000 kgm^3 for aluminium and steel respectively.

Thickness (mm)	***c'_{44} (GPa)***	***c'_{55} (GPa)***
0.2	27.07	27.09
0.5	27.35	27.10
1	26.37	26.47
1.5	26.53	26.37

Table 7.11: Prediction of the elastic stiffness constants c'_{44} and c'_{55} using the shear wave velocities for the waves polarised in the RD and TD for the aluminium samples.

Steel	***c'_{44} (GPa)***	***c'_{55} (GPa)***
DC01	79.50	83.72
DC05	84.03	86.65

Table 7.12: Prediction of the elastic stiffness constants c'_{44} and c'_{55} using the shear wave velocities for the waves polarised in the RD and TD for the aluminium samples.

7.3.3.2 – From the ODCs

Tables 7.13 and 7.14 give the predictions of the elasticity stiffness constants c'_{44} and c'_{55}, calculating them by predicting a shear wave velocity from the calculated ODCs given in table 7.4.

Thickness (mm)	c'_{44} *(GPa)*	c'_{55} *(GPa)*
0.2	26.32	25.76
0.5	26.49	26.29
1	26.50	26.78
1.5	26.41	26.46

Table 7.13: Prediction of the elastic stiffness constants c'_{44} and c'_{55} for the aluminium samples, using the ODCs measured in section 7.2.

Steel	c'_{44} *(GPa)*	c'_{55} *(GPa)*
DC01	87.85	80.85
DC05	89.26	86.56

Table 7.14: Prediction of the elastic stiffness constants c'_{44} and c'_{55} for the steel samples, using the ODCs measured in section 7.2.

7.4 – Error analysis of shear wave experiments

There are random errors, such as those that result in the fluctuating measurement of amplitude and velocity, as well as systematic errors that are incorporated in the accuracy of measuring the velocity (sheet thickness assumptions) and the directionality of the displacement of crystals (alignment of SH wave with respect to the RD and TD) that need to be addressed.

Amplitude is a relative measurement and therefore any error in amplitude will manifest within a complete A-scan. In measuring the velocity for the elasticity measurements, the amplitude is not so important as long as the peaks that are coincident with the SH wave arrival time are detectable. For the attenuation data however, it is imperative that the amplitude decays correctly. The EMAT remains stationary and in contact with the sheet the entire time, and as such, the amplitude should decay in conjunction with the attenuation coefficient of the sheet.

Errors in polarisation direction were reduced by pre-determining it prior to use of the EMAT in the experiment; the identified polarisation direction was marked on the EMATs brass casing for reference. Guide lines were then drawn on each sheet sample parallel to the RD and TD to improve the alignment further. When set up for the RD study, the position of the EMAT was also recorded to maximise the accuracy of the 90˚ rotation.

With a temporal accuracy of ± 0.5 $\times 10^{-8}$ s and a sheet thickness accuracy of within ± 5% for the 0.2 mm thick aluminium foil and tighter tolerances for the other sheet ~ ± 1%, absolute velocity measurement errors can be determined for the thicker sheets. Take for example a 1mm ± 0.01 mm thick aluminium sheet with an absolute SH velocity of 3125 ms^{-1} polarised along the TD. The largest magnitude error in the velocity measurement would occur for a sheet of 1.01 mm thick, measured from successive peaks, with the time interval between the successive echoes actually being 63.5 $\times 10^{-8}$ s instead of 64 $\times 10^{-8}$ s. This equates to a 1.8 % error, which relates to a calculated velocity of 3181 ms^{-1}. Though the % error seems small, when calculating elastic stiffness constants, this value will be squared. Calculating a value for c'_{xx} using the shear wave equation and values for velocity of 3125 ms^{-1} and 3181 ms^{-1} will give corresponding values for the elastic constant of 26.37 GPa and 27.32 GPa respectively. This gives a 3.6% error. Therefore velocity measurements in the thicker sheet (≥ 1 mm thickness) were calculated by identifying a number of successive peaks to increase the signal accuracy by reducing the temporal tolerance. The thicker the sheet thickness, the more confident a user can be in its results.

For thinner sheet, namely the 0.2 mm and 0.5 mm thick aluminium samples, the shear wave velocities were determined from magnitude FFT analysis. The peak frequency was converted to determine a period between echoes, and with knowledge of distance (twice the sheet thickness), a velocity was determined that way.

7.5 – References

1. *Potter MDG, Dixon S, Davis C, Meas. Sci. Technol., **15**, 2004, pp. 1303-1308*

2. *Li Y, Thompson RB, J. Acoust. Soc. Am., **91**, 1992, pp. 1298-1309*

3. *Kaye GWC, Laby TH, Tables of Physical and Chemical Constants, Fifteenth edition. Longman Scientific & Technical publishing, 1989*

4. From Corus website, products section. 'Cold-rolled strip steel'. Web address: www.corusgroup.com/file_source/StaticFiles/Business%20Units/CSPUK/Cold%20Rolled%20Steel.pdf

5. *Thompson RB, Smith JF, Lee SS, Johnson GC, Met. Trans. A, **20A**, 1989, pp. 2431-2447*

6. *Rose JL, Ultrasonic waves in solid media, Cambridge University Press, 1999*

7. *Alers G, Sinclair AN, Rev. of Prog. in QNDE, **18**, 1999, pp. 1695-1701*

8. *Fletcher M, MSc Dissertation, University of Warwick, April 2007*

9. *Dixon S, Edwards C, Palmer SB, Ultrasonics, **39**, 2001, pp. 445-453*

CHAPTER 8

EBSD data acquisition and results

This chapter firstly details the experimental methods applied for surface preparation of the aluminium and steel samples used. Calibration of the computer code, given in appendix A, is then presented. Data manipulation processes required to allow a direct comparison of the results is introduced. Experimental methods used to collate the texture and grain size data from EBSD are detailed. The quantitative results are presented accordingly, and are correlated to the ultrasonic data (presented in chapter 7) in chapter 9.

8.1 – Surface preparation

8.1.1 - Aluminium

Aluminium is a relatively soft metal; it is prone to scratching, which infers that mechanical polishing in particular is a difficult task. It is found naturally in abundance in an Al_2O_3 composition, as aluminium oxidises readily; maintaining a high quality polished finish for a sustained period in air is difficult. Sample polishing was therefore done immediately before EBSD.

Surface preparation of the aluminium was done by firstly mounting the samples taken from the sheet, approximately 15 mm × 15 mm in surface area, onto bakelite stubs. The stubs were compressed into the required shape to fit into the rotating sample holder of the *Buehler Phoenix 4000 SPS* system used for the mechanical polish. The samples were cold-mounted to minimise heat exposure to the samples which could affect the microstructure.

The *Struers* MD-Chem polishing cloth was selected to complete the mechanical polish with the lubricant provided by the *Struers* OP-S Colloidal Silica Suspension (non-crystalline), with a 0.04 μm grain size and a pH of 9.8. During mechanical polishing, the suspension was applied every 30 seconds via a spray to maintain suitable lubrication. The rpm

selected was 60, allowing a compromise between minimising heat energy to be transferred to the sample, and the polishing time. The mechanical polishing head was set to rotate in a clockwise direction in contrast to the anti-clockwise rotary direction of the pad. The downward normal force applied by the equipment to the samples was negligible, as the potential frictional effects can increase the temperature induced in the sample.

The SEM image (figure 8.1) shows an aluminium sample following a 20 minute Colloidal Silica polish. The length of time of the mechanical polish varied intermittently between each sample; progress was readily visualised just by the improvements in the reflectivity, achieved by checking the sample every few minutes. There is no evidence of severe rolling deformation here.

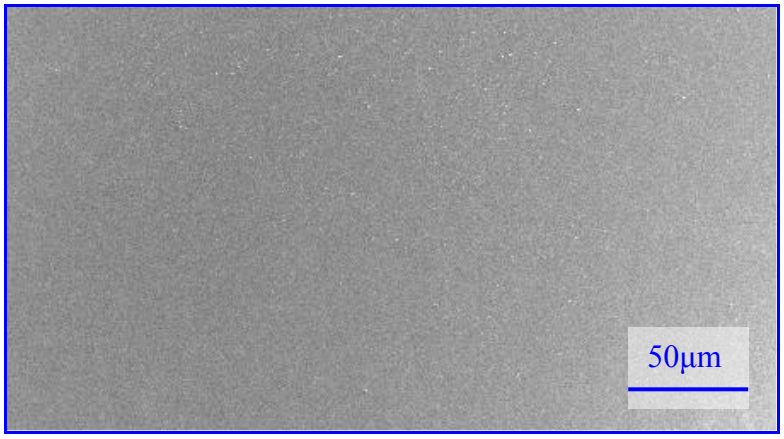

Figure 8.1: SEM image of the AL104232 sample surface after a 20 minute Colloidal Silica mechanical polish. The image is void of anything of interest, suggesting a flat, contaminant-free surface.

The surface scratches and pitting has been alleviated. It was evident that sometimes after polishing, OP-S suspension crystals adhered to the surface, leaving a residue. Polished samples were placed in an ultrasonic bath for 2 minutes within an isopropanol solution, removing any such residue.

The electrolyte used for the final electropolish of aluminium was 70% CH_3OH / 30% HNO_3 at a temperature $\leq$ -30ºC [1]. Creating the required temperature was achieved using dryice (frozen CO_2) as its surface temperature is -78.5ºC. The process of electropolishing is

typically exothermic, and with the prescribed electrolyte for aluminium there is the risk of explosion if too hot. A thermometer, scaled from 50ºC to -100ºC was used to measure the temperature of the electrolyte before and during electropolishing to maintain a safe operating temperature.

Figure 8.2 shows a schematic diagram of the laboratory setup. The samples were held from stainless steel tweezers connected to the circuit via crocodile clips. A copper cathode was held in position, with a sufficient volume submerged (submerged area > 1 cm^2) in the electrolyte to minimise resistance to current flow. The electrolyte was contained in a lab dish embedded in a cylindrical container packed with the dryice. Electropolishing was conducted in a fume cupboard for increased safety.

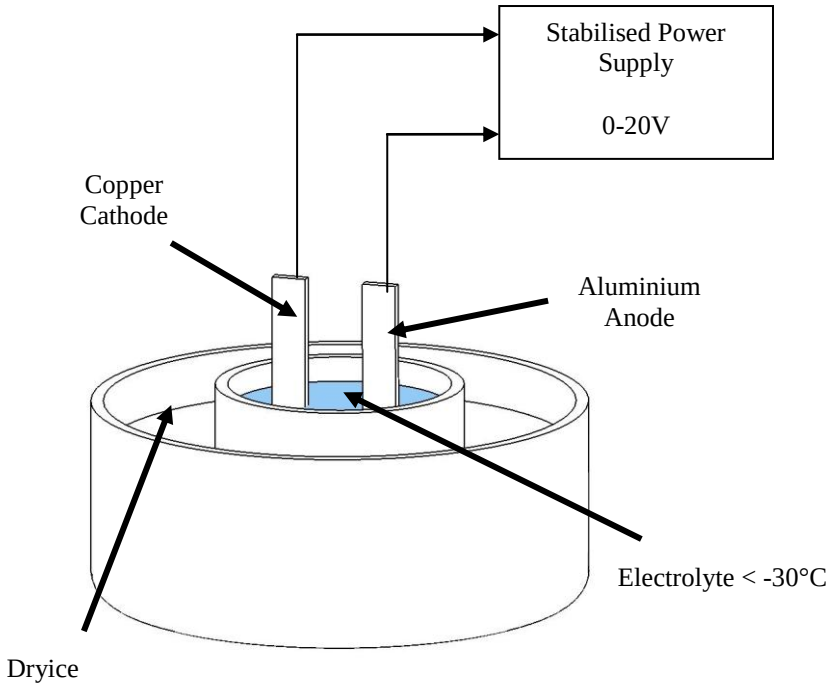

Figure 8.2: Schematic diagram of aluminium sample electropolishing experimental setup. For Steel, the electrolyte is different and dryice is not required and the anode would be the steel sample.

Voltage against current density curves were produced for all samples to obtain the polishing voltage range. Figure 8.3 shows the electropolish curve for the 0.5 mm thick aluminium sheet studied. The graph indicates the polishing voltage range for the sample is

approximately in the range 6-10 V. Further testing on samples concluded that a 75 s electropolish time on standard samples sufficed.

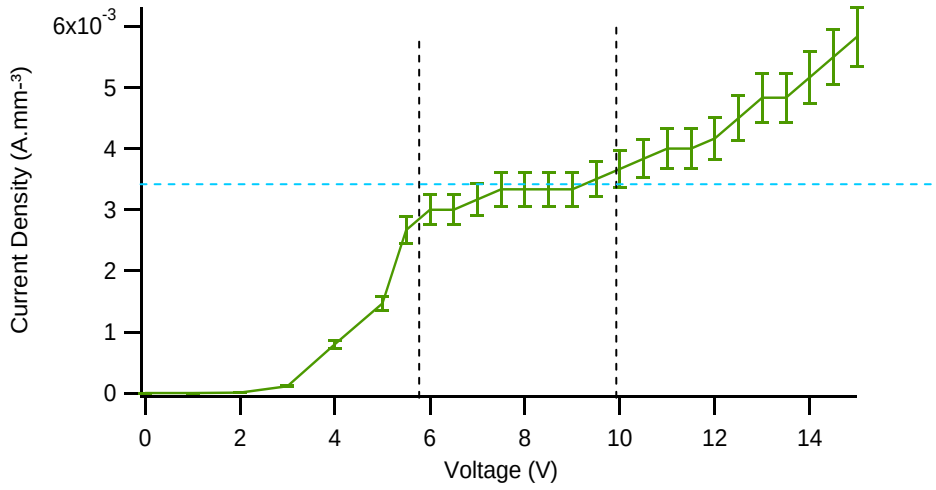

Figure 8.3: Electropolishing curve for a sample from the AL104232 sheet, the sample used here had volumetric dimensions of 10 ± 0.25 mm x 10 ± 0.25 mm x 0.5 mm (thickness)

8.1.2 – Steel

The mechanical polishing stage for the DC series steel samples also used colloidal silica as the polishing lubricant, followed by an electropolish with an electrolyte composed of 45% H_3PO_4, 35% H_2SO_4 and 20% H_20 (distilled) [2]. This electrolyte is less volatile and requires no temperature, hence dryice was not required. The timings for the polishing stages were maintained with surface finish results achieved comparable to the aluminium samples produced.

8.2 – Crystallographic texture predictions from EBSD data

8.2.1 – EBSD ODC algorithm configuration

Before formulating any predictions of the ODCs directly from EBSD data, the computer code required calibrating and tested using dummy datasets to confirm some benchmark results. The code is given in appendix A.

An initial test, here using the aluminium code, was to input a dataset of <111> orientations, with each point in the dataset having a random value for the φ_1 angle. The dummy dataset generated contained 10215 points, aligned to a hexagonal 339 μm × 231.29 μm grid. The auto IPF map is shown in figure 8.4, which is entirely blue (as expected) for all <111> orientations.

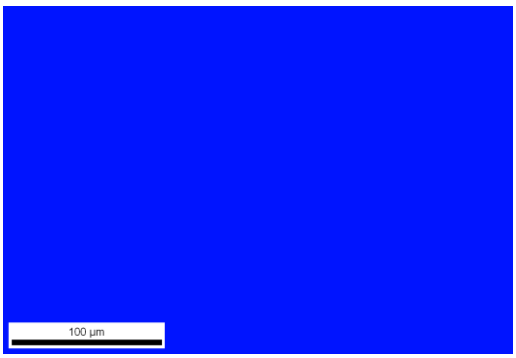

Figure 8.4: Auto IPF EBSD map for a dummy <111> dataset.

For a <111> orientation aligned parallel to the ND, the ultrasonic velocity propagating through the crystal in the perpendicular RD-TD plane is equivalent in any direction. This is because orthogonal to the <111> direction in a cubic crystal is elastically isotropic. The implication of this is that if the code works, the ultrasonic velocity prediction of the S_0 mode Lamb wave as a function of angle would stay constant. Figure 8.5 confirms that the velocity remains very close to constant over a 2π rotation.

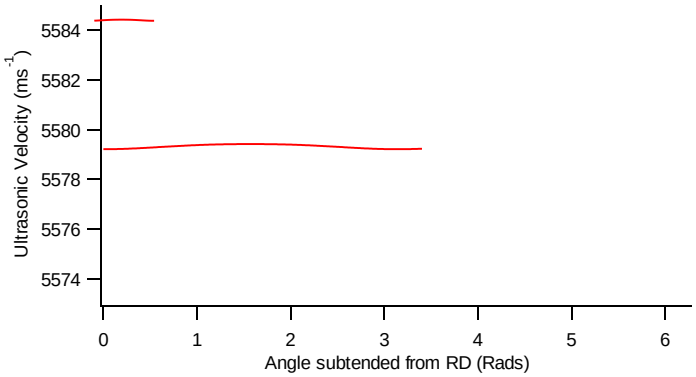

Figure 8.5: EBSD prediction of ultrasonic velocity for <111> dataset. It is evident that the velocity does not fluctuate as a function of angle, as is expected.

A second test was used to confirm the code functionality. This test was based on the orientation rotation matrix that maps the crystal axis system to align with that of the sheet system. On inspection of the rotation matrix used in the code (given by equation 8.1), it follows that for a [001] orientation defined by the set of Bunge-Euler angles (0˚,0˚,0˚) equation 1 will become an identity matrix.

$$g = \begin{pmatrix} \cos\phi_1\cos\phi_2 - \sin\phi_1\sin\phi_2\cos\Phi & \sin\phi_1\cos\phi_2 + \cos\phi_1\sin\phi_2\cos\Phi & \sin\phi_2\sin\Phi \\ -\cos\phi_1\sin\phi_2 - \sin\phi_1\cos\phi_2\cos\Phi & -\sin\phi_1\sin\phi_2 + \cos\phi_1\cos\phi_2\cos\Phi & \cos\phi_2\sin\Phi \\ \sin\phi_1\sin\Phi & -\cos\phi_1\sin\Phi & \cos\Phi \end{pmatrix} \quad (8.1)$$

The computer code does return the identity matrix for an input [001] dataset, which is confirmed by the output of the nine calculated effective elastic constants from the aluminium code. These are shown here:

c_{11}	=	108.2 GPa
c_{22}	=	108.2 GPa
c_{33}	=	108.2 GPa
c_{12}	=	61.3 GPa
c_{13}	=	61.3 GPa
c_{23}	=	61.3 GPa
c_{44}	=	28.5 GPa
c_{55}	=	28.5 GPa
c_{66}	=	28.5 GPa

The predicted moduli values for c_{11}, c_{22} and c_{33} are equivalent to c^x_{11}. It also holds that $c^x_{12}=c_{12}=c_{13}=c_{23}$ and $c^x_{44}=c_{44}=c_{55}=c_{66}$. This again is the expected result and confirms the code is performing correctly.

8.2.2 – Euler angle data manipulation

Each EBSD scan must be considered on its own merits with regard to applying digital cleaning algorithms. As stated in chapter 4, the average confidence index (*CI*) value for a scan is recommended to be greater than 0.1 [3] for the data to be considered a representative and accurate account of the sample under investigation. A reduction in the *CI* may be due to a minority of sporadic un-indexed points, or points which obviously have incorrect orientations assigned to them. The work completed here has adhered to a rule that if after one application of a *Minimum CI* cleaning filter the average *CI* value is not above the suggested 0.1 threshold, the data would not be considered for analysis. In the overwhelming majority of cases it was seen that the initial average *CI* value was above 0.1 before any data cleaning was implemented.

It is difficult to position each sample equivalently for every EBSD scan in the SEM. This means the rolling direction of the sample will not be aligned with the preset RD-TD plane defined by the OIM data collection software, used for generating pole figures. Such a misalignment means that the Euler angle data inputted into the computer algorithms would lead to effective elastic constant predictions not being generated with respect to the sample's orthogonal axes (RD-TD-ND).

A solution to resolve this issue was obtained by rotating the data about the ND, which is maintained as a common direction between the sample orientation in the SEM and also the OIM analysis software system. By producing a [111] pole figure for each scan together with the knowledge of what a pole figure for an orthorhombic sample looks like, the required data rotation is easily identifiable.

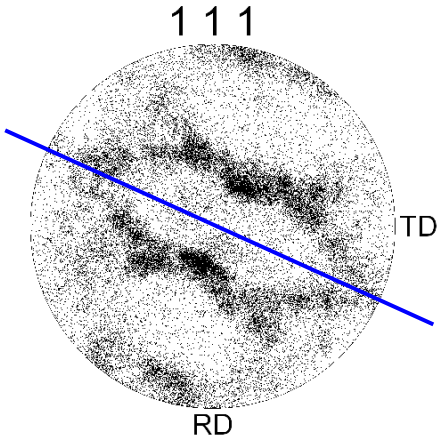

Figure 8.6: [111] Pole figure projection from sample 1 of the AL104232 sheet. The well defined rolling texture characteristics are evident in this pole figure. The blue line indicates the rotation in the sample: this should be parallel to the TD.

Figure 8.6 shows a 'raw' pole figure from a scan taken from the 0.5 mm thick aluminium sheet. Figure 8.7 displays the correct rotated pole figure.

Once the data is cleaned and rotated, ensuring alignment with the correct orthogonal frame, the correctly aligned data can be used and the code compiled to quantify the elastic stiffness and texture coefficients from the scan.

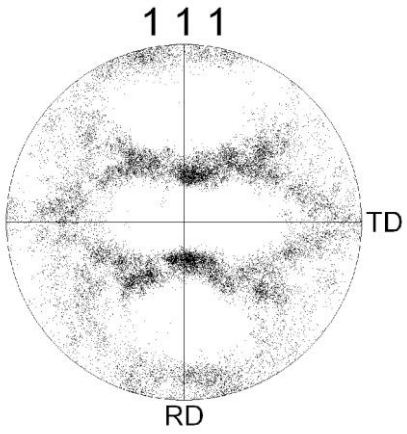

Figure 8.7: Rotated [111] Pole figure projection for sample 1 of the AL104232 sheet. This sample required a +31˚ rotation about the ND to align the pole figure with the OIM reference axes RD and TD.

8.2.3 – Sample size required

The ultrasonic texture measurement generates the ODCs from an average over all grains within a volume of 176.71 cm^2 x sheet thickness (cm). For grains of the order ~ μm in diameter, this equates to averaging over tens of thousands of grains. The relatively small size of an EBSD scan means that it is not statistically viable to use just one scan and expect it to be representative of the bulk sample. Twelve EBSD surface scans were taken per sample where possible, sampling as many grains as possible with each. Analysis of the minimum requirement of scans and grains needed to obtain statistically viable results are discussed and detailed in appendix B, where it is shown that 1400 grains are needed to minimize the effects of microtexture.

8.2.4 – S_0 Lamb wave velocity predictions

The following figures 8.8-8.13 show the predicted S_0 mode Lamb wave velocity as a function of angle for each sample, derived from average crystallographic data accumulated from the aggregation of six EBSD scans (three for the steel samples). The average effective elastic stiffness constants were calculated, and used to solve the velocity for each angle, ranging from 0 to 2π radians.

8.2.4.1 – Aluminium samples

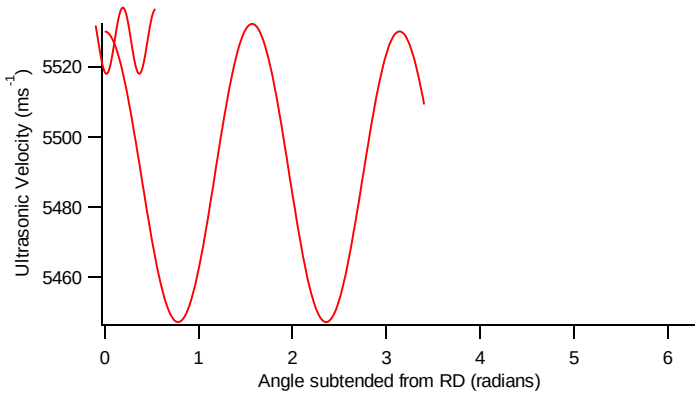

Figure 8.8: Ultrasonic velocity profile prediction for aluminium sheet AL101325 from the average EBSD data.

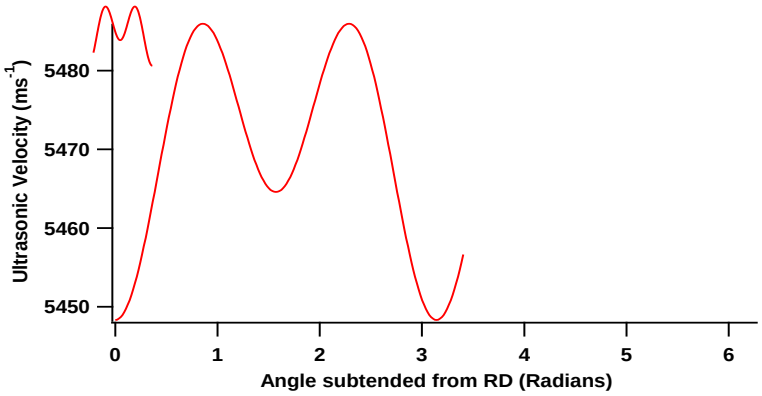

Figure 8.9: Ultrasonic velocity profile prediction for aluminium sheet AL104232 from the average EBSD data.

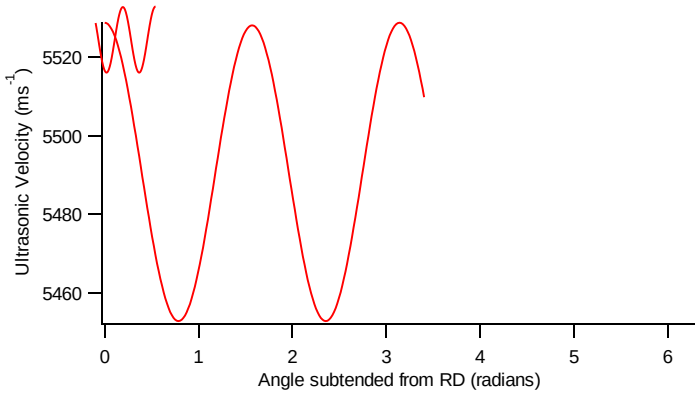

Figure 8.10: Ultrasonic velocity profile prediction for aluminium sheet AL104325 from the average EBSD data.

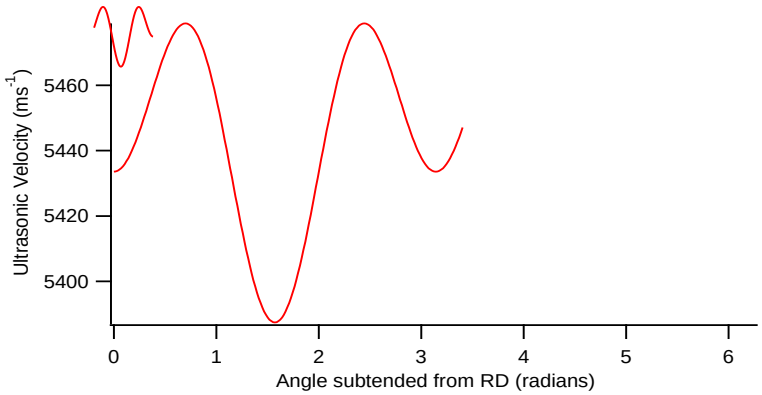

Figure 8.11: Ultrasonic velocity profile prediction for aluminium sheet AL104532 from the average EBSD data.

8.2.4.2 – DC steel series

Figure 8.12: Ultrasonic velocity profile prediction for steel sheet DC01 from the averaged EBSD data.

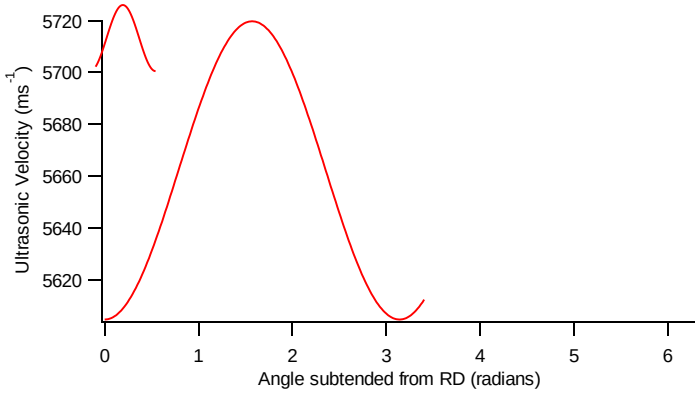

Figure 8.13: Ultrasonic velocity profile prediction for steel sheet DC05 from the averaged EBSD data.

8.2.5 – ODC predictions from EBSD data

The mathematical fit coded in Igor that was applied to the ultrasound velocity data was also applied to the predicted velocity data. The extrapolated ODCs are displayed for the aluminium and steel sheet samples in tables 8.1 and 8.2. The errors for the ODCs were all zero as the EBSD velocity datasets are idealised containing no experimental fluctuations. Therefore the graphical fit was coincident with the predicted velocity data.

Thickness (mm)	$\mathbf{W_{400}}$	$\mathbf{W_{420}}$	$\mathbf{W_{440}}$
0.2	-8.36×10^{-3}	-1.42×10^{-4}	-8.66×10^{-3}

0.5	-5.08×10^{-3}	-1.07×10^{-3}	2.97×10^{-3}
1	-8.63×10^{-3}	4.44×10^{-5}	-7.78×10^{-3}
1.5	-2.11×10^{-4}	3.00×10^{-3}	6.78×10^{-3}

Table 8.1: ODC values extrapolated from the ultrasonic velocity prediction data produced from the EBSD scans, for the respective aluminium sheets.

Steel	W_{400}	W_{420}	W_{440}
DC01	-1.23×10^{-2}	-5.81×10^{-4}	2.93×10^{-4}
DC05	-1.87×10^{-2}	-2.14×10^{-3}	-9.51×10^{-6}

Table 8.2: ODC values extrapolated from the ultrasonic velocity prediction data produced from the EBSD scans, for the respective steel sheets.

8.2.6 – Elastic stiffness predictions from EBSD

The Fortran code (appendix A) used to determine the Lamb wave velocity predictions generate the nine elastic stiffness constants that define the elasticity of a rolled sheet were determined. The elastic shear moduli values for c'_{44} and c'_{55} from the EBSD data are given in tables 8.3 and 8.4.

Thickness (mm)	C'_{44} (GPa)	C'_{55} (GPa)
0.2	26.288	26.319
0.5	26.480	26.640
1	26.289	26.279
1.5	27.193	26.542

Table 8.3: Predicted values for the elastic stiffness constants c_{44} and c_{55} from the EBSD data from the aluminium samples investigated.

Steel	C'_{44} (GPa)	C'_{55} (GPa)
DC01	87.970	89.589
DC05	79.601	85.829

Table 8.4: Predicted values for the elastic stiffness constants c_{44} and c_{55} from the EBSD data from scans the steel samples investigated.

8.3 – EBSD Grain Characterization Analysis

EBSD OIM analysis software charts were used to determine the grain size and grain aspect ratio of the rolled sheet samples.

Sections 8.3.1 and 8.3.2 present examples of results obtained from an aluminium and a steel sample, in each case showing an EBSD grain identification map, and the corresponding grain size / aspect ratio chart.

8.3.1 – Aluminium sample grain analysis data

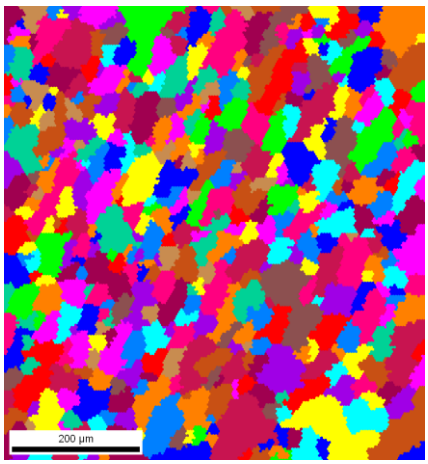

Figure 8.14: EBSD grain identification map for the 0.5 mm thick aluminium sheet AL104232.

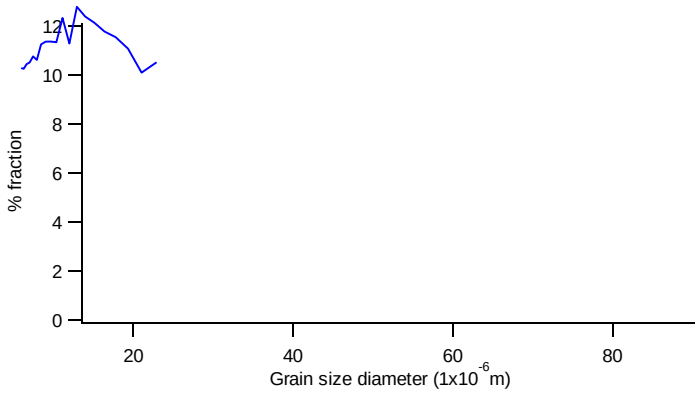

Figure 8.15: Graph representing the % fraction of grains with a grain size diameter within defined limits determined from EBSD data collected for the 0.5 mm thick aluminium sheet AL104232.

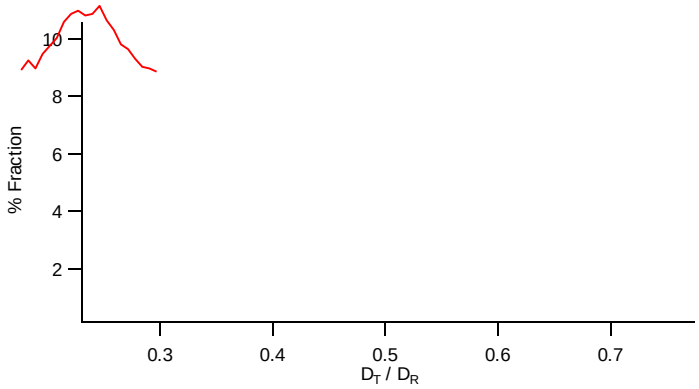

Figure 8.16: Graph representing the % fraction of grains with a grain size aspect ratio D_T/D_R determined from EBSD data for the 0.5mm thick aluminium sheet AL104232.

8.3.2 – Steel sample grain analysis data

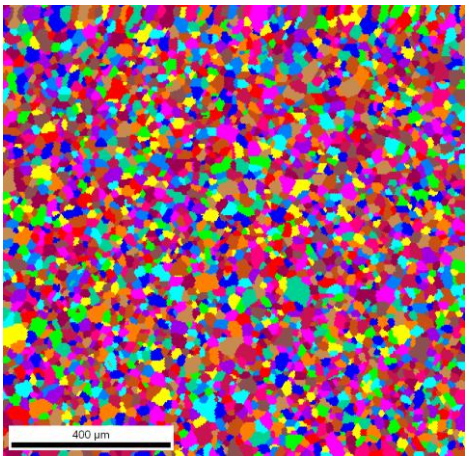

Figure 8.17: EBSD grain identification map for the DC01 steel sheet.

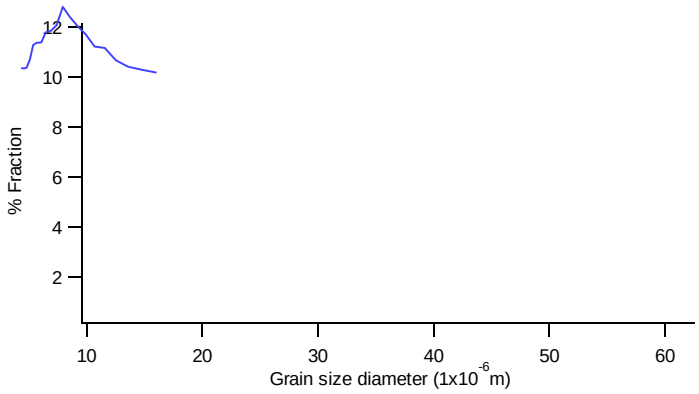

Figure 8.18: Graph representing the % fraction of grains with a grain size diameter within defined limits determined from EBSD data collected for DC01 steel sheet.

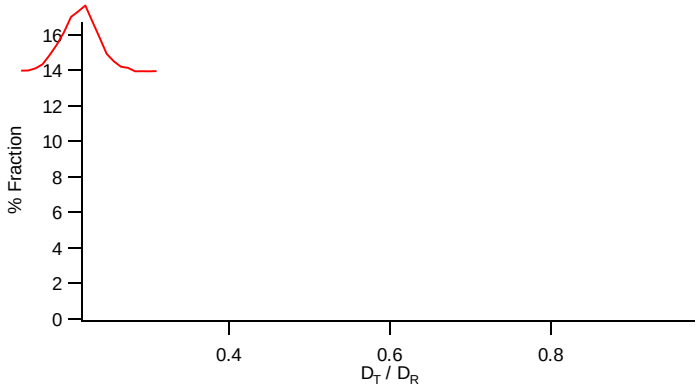

Figure 8.19: Graph representing the % fraction of grains with a grain size aspect ratio D_T/D_R determined from EBSD data for the DC01 steel sheet.

8.3.3 –Grain size and aspect ratio results

The average grain size and average aspect ratio measured for the aluminium samples are given in table 8.5 below. Similarly, the average grain size and average aspect ratio measured for the steel samples are given in table 8.6.

Thickness (mm)	$\overline{D}$ ***(μm)***	***Average*** $\frac{D_T}{D_R}$
0.2	12.6	0.48
0.5	31.7	0.50
1	39.49	0.47

1.5	26.44	0.50

Table 8.5: Average grain size, maximum grain size and the average aspect ratio values recorded from the EBSD scans taken for the respective aluminium sheets studied.

Steel	$\overline{D}$ **(*μm*)**	***Average*** $\frac{D_T}{D_R}$
DC01	20.14	0.55
DC05	16.25	0.51

Table 8.6: Average grain size, maximum grain size and the average aspect ratio values recorded from the EBSD scans taken for the respective DC steel sheets studied.

8.4 – EBSD error analysis

It has been discussed in previous chapters the errors intrinsic to EBSD. The three Eulerian angle calculations have minimal errors (± 0.2˚) which manifest as a smaller error still in the calculations of the elastic stiffness constants. The major errors are concerned with poor surface finish which would in essence result in incorrect diffraction of the primary electrons. The effects of this can again be checked via the image quality and confidence index parameters.

Digital cleaning and filtering functions allow for further screening and minimization of errors. In effect, the results generated by EBSD are extremely accurate and any quantitative information measured from the data can be considered statistically viable. Rotating the angular datasets to effectively align the orientation of the ultrasound experiments with the EBSD results again makes the comparisons made in chapter 9 statistically correct.

Errors due to localized changes in the microstructure and crystallographic texture have been minimized by averaging the results per sheet over six EBSD scans for the aluminium (twelve were infact taken). The explanation for this is given in

appendix B. The steel samples were averaged over three scans each due to the limitations in usage.

8.5 – References

1. *Robson JD, Materials Science and Engineering A, **382**, 2004. p112*

2. *Lin CC, Hu CC, Electrochemica Acta, **53**, 2008, pp.3356-3363*

3. *Petrov R, Kestens L, Wasilkowska A, Houbaert Y, Materials Science and Engineering A, **447**, 2007, pp.285-297*.

CHAPTER 9

Correlation of the ultrasonic and EBSD data

9.1 – Correlation of crystallographic texture

The major focus of this work has been centred on correlating the non-destructive, ultrasonic measurement of elastic anisotropy with EBSD derived predictions, by generating comparative quantitative information for crystallographic texture exhibited by rolled sheet.

9.1.1 – Comparison of velocity traces

The velocity versus angle plots from the EMAT-EMAT apparatus helps visualise the changing ultrasonic velocity with direction for a rolled sheet. Such qualitative analysis provides a good basis for evaluating the effectiveness of using EBSD to reproduce acceptable predictions of the S_0 mode velocity.

The six sheets studied have all been tested ultrasonically, and a number of EBSD surface scans have been completed on each for the correlating analysis. These stand-alone results are found in chapters 7 and 8 respectively, with the raw ultrasonic data, together with

the corresponding mathematical fits displayed in figures 7.4-7.9. The EBSD predictions are shown in figures 8.8-8.13.

Figures 9.1-9.6 give side-by-side views of the data for the six samples. The graphs with black curves on the left are the ultrasound measurements, with the red curved graphs on the right showing the predicted velocity behaviour from the EBSD datasets. The mathematical fitting curves have been removed to avoid confusion.

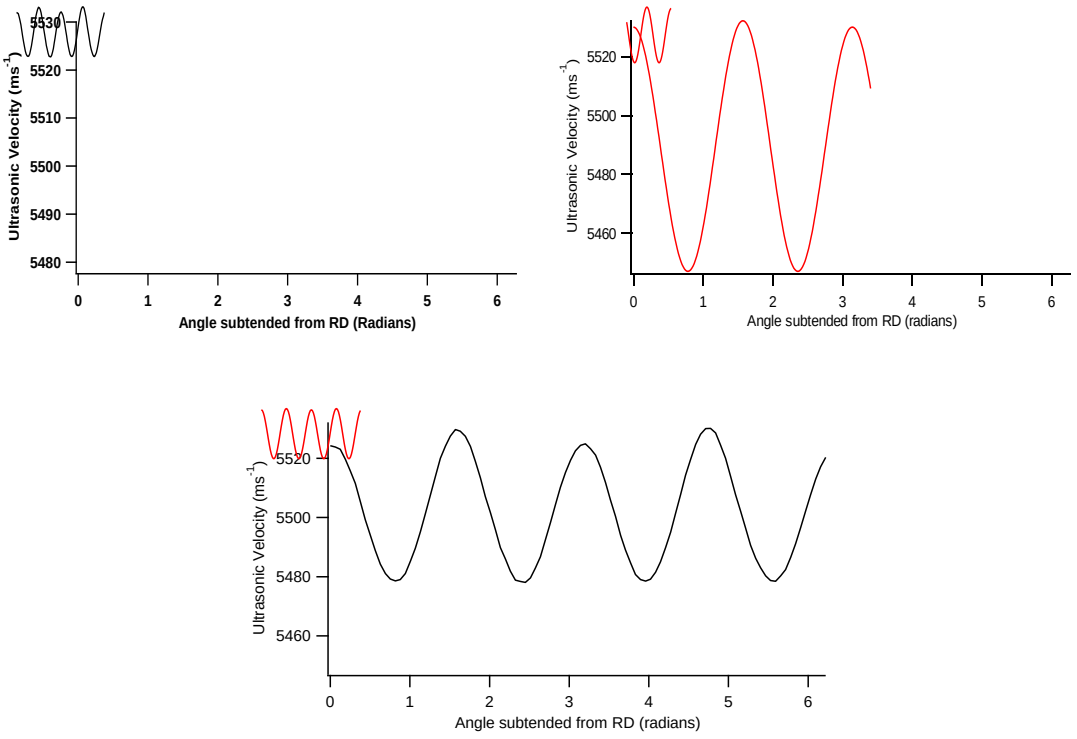

Figure 9.1: Ultrasound results (left) and prediction from EBSD data (right) for 0.2 mm thickness AL101332 sheet. Velocity absolution comparison is highlighted in the bottom graph.

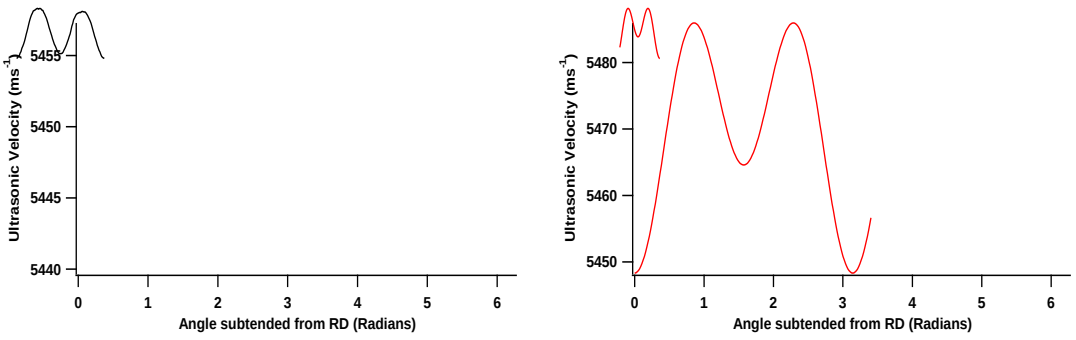

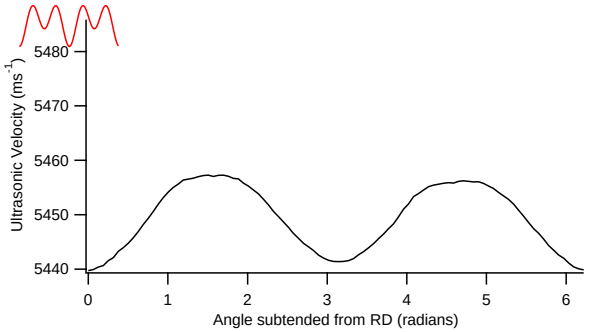

Figure 9.2: Ultrasound results (left) and prediction from EBSD data (right) for 0.5 mm thickness AL104232 sheet. Velocity absolution comparison is highlighted in the bottom graph.

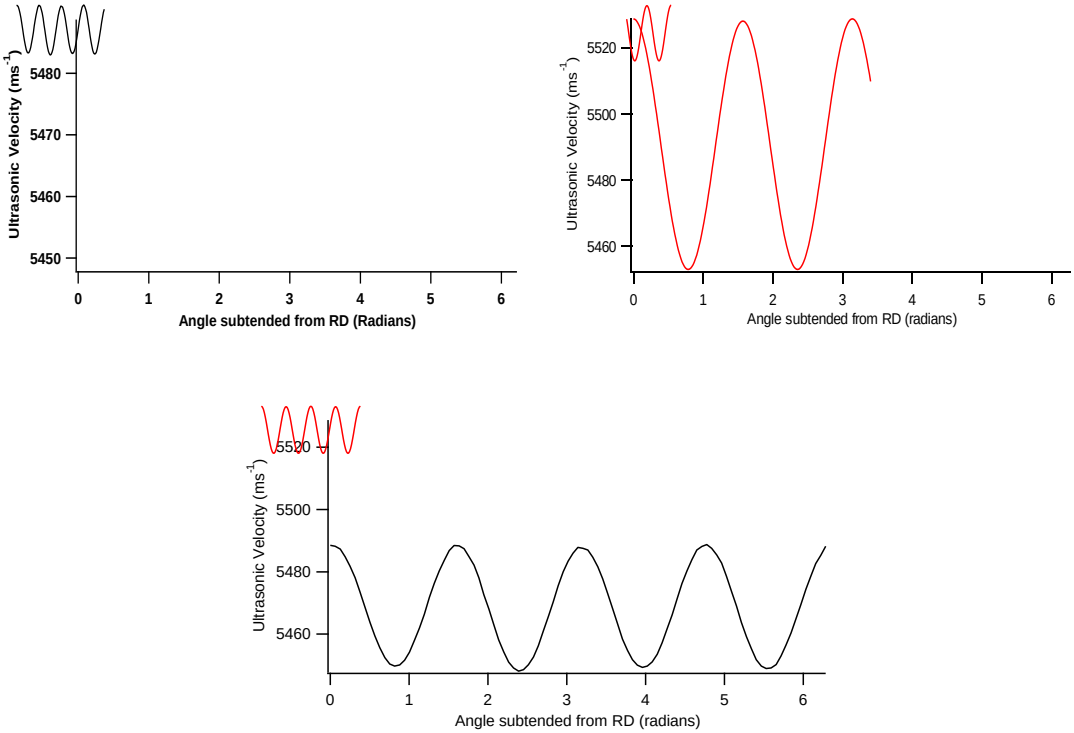

Figure 9.3: Ultrasound results (left) and prediction from EBSD data (right) for 1 mm thickness AL104332 sheet. Velocity absolution comparison is highlighted in the bottom graph.

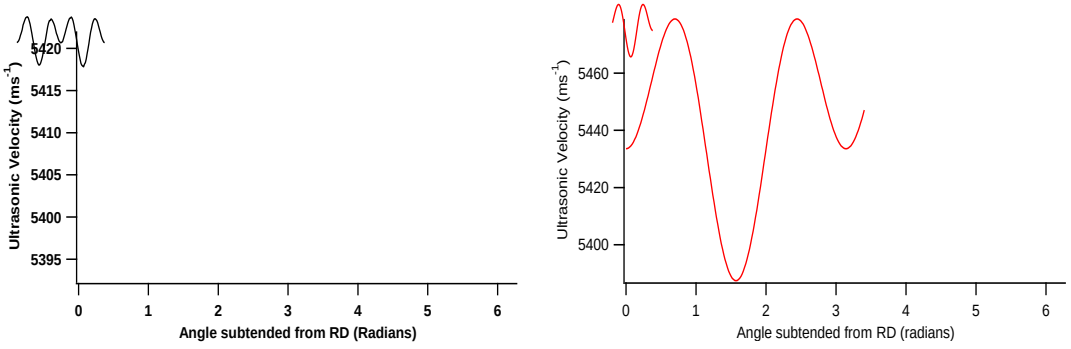

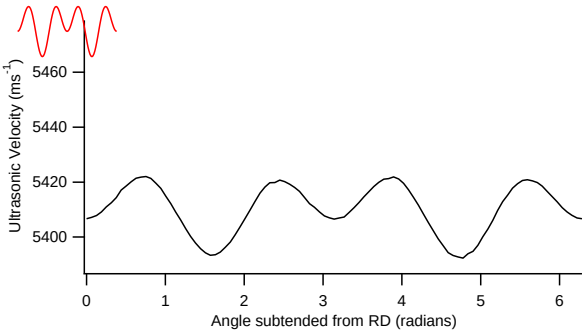

Figure 9.4: Ultrasound results (left) and prediction from EBSD data (right) for 1.5 mm thickness AL104532 sheet. Velocity absolution comparison is highlighted in the bottom graph.

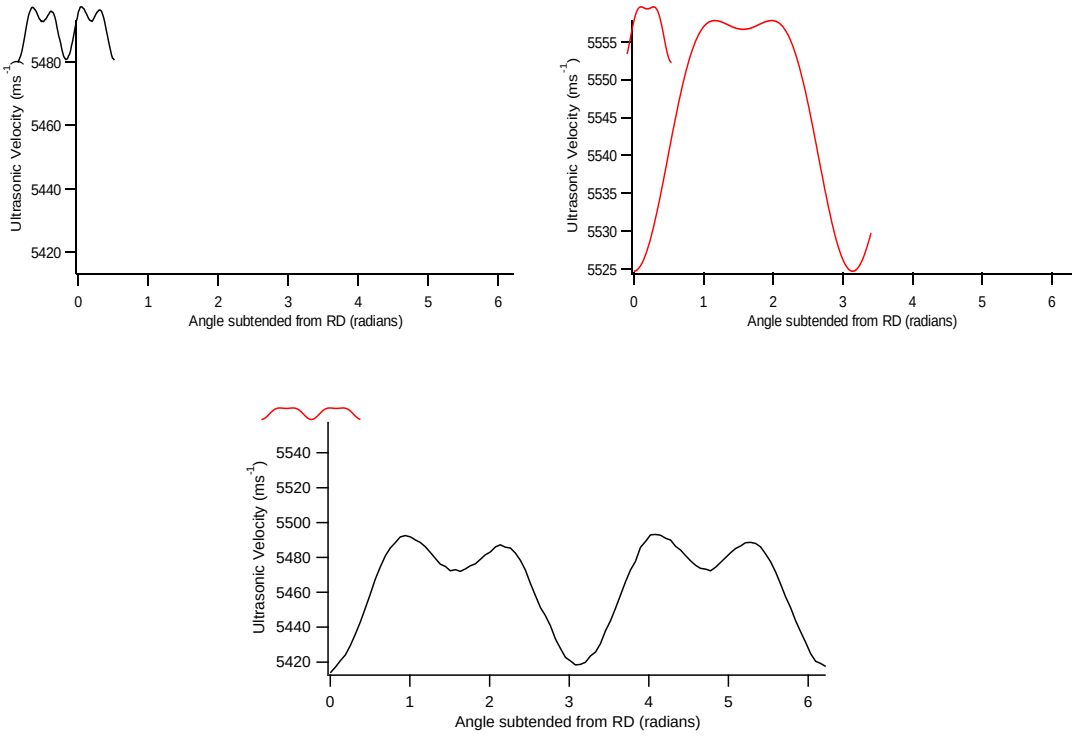

Figure 9.5: Ultrasound results (left) and prediction from EBSD data (right) for the steel sheet DC01. Velocity absolution comparison is highlighted in the bottom graph.

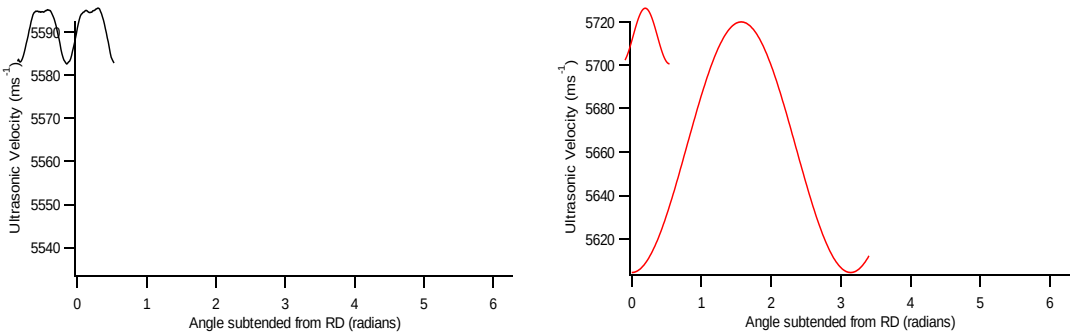

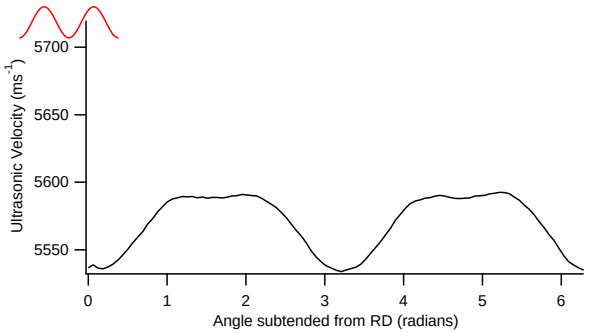

Figure 9.6: Ultrasound results (left) and prediction from EBSD data (right) for the steel sheet DC05. Velocity absolution comparison is highlighted in the bottom graph.

Observing the shapes of the corresponding curves, there is an extremely good correlation for five of the samples; the 0.2 mm, 1 mm and 1.5 mm thick aluminium sheets, and both steel samples DC01 and DC05. The averaged EBSD predictions have identified the slow and fast directions, in addition to the correct proportion of two and four-fold symmetry. In contrast, the 0.5 mm thick sheet AL104232 (figure 9.2) has produced a poor correlation in shape. With reference to figure 9.2, it is noteworthy that the EBSD data did determine that along the RD is the slowest direction, which was confirmed by the ultrasonic measurement. The data though suggests a component of four-fold symmetry (represented by the W_{440} ODC) of similar magnitude to the two fold symmetry.

The mean and absolute velocity comparisons do indicate significant differences. In 5 of the 6 samples, the variation in velocity predicted by EBSD is larger than the ultrasound measurements. Firstly, the issue regarding the average velocity measured ultrasonically needs to be discussed. It is important to note that the energy of the in-plane component of the S_0 Lamb wave wavefront is evenly distributed throughout the bulk of the sheet at small frequency-thickness products [1]. The literature states that for frequency-thickness products such as those applied here (max. value of 0.3 MHz.mm), the phase velocity of an S_0 Lamb wave remains constant in isotropic media with 1.5 mm thickness and less. The average ultrasonic velocity measured for these samples increased as sheet thickness decreased, ranging in the aluminium samples from 5410 ms^{-1} in the 1.5 mm thick sheet up to 5502 ms^{-1}

in the 0.2 mm thick sheet. Dispersion curve analysis for the S_0 Lamb wave does not concur with this apparent large change in the absolute velocity over this range of thickness variation.

The reason for such a variation in average velocity with thickness is due to the magnitude of the induced textures. The extra cold-working required to reduce an aluminium sheet down to a thickness such as 0.2 mm will encourage more <111> orientations to align in the plane of the sheet; the fastest ultrasonic wave direction.

The W_{420} and W_{440} coefficients are a measure of the relative variation in velocities with angle. The W_{420} magnitude differences (tables 9.3 and 9.6) show the smallest differences of the three ODCs, and the W_{440} predictions show very good agreement in the steel samples in particular. The important aspect in quantifying the texture and Lamb wave velocity variation from EBSD data is that the relative ratios and signs of the coefficients are predicted correctly, which in general they were. These ratios and the signs of the ODCs govern the shape of the velocity profile.

The other concern regards the differences in velocity variation; this is large in the majority of EBSD prediction cases. This could be due to a number of factors. Firstly, the EBSD technique is surface specific, and as a result, the thickness of the sample is not considered when making elastic stiffness constant predictions. The thickness is important with respect to how the Lamb wave interacts with the metal as it propagates, and how various types of texture aggregated together effect the velocity difference with direction. The elasticity the Lamb wave encounters across the bulk of the sheet could be less anisotropic in comparison to the EBSD predictions.

The EBSD prediction technique is reliant on the input of the single crystal elastic stiffness constants. If the values used, although they are approximately close given the magnitude of the velocities predicted are indeed sensible, are not entirely accurate, then this can have a major impact on the results. For example, if the single crystal constants are incorrect, this will inherently change the anisotropy parameter, which in turn influences how the velocity will vary. This issue is more of a problem in steel samples, due to the variety of grades and alloys available, the single crystal constants quoted in the literature can only be

considered an approximation. For the aluminium samples, the sheets studied were nominally pure, allowing for more certainty in the accuracy of the data obtained.

9.1.2 – Texture quantification

The ODCs calculated from the above data are given again as a reminder. Table 9.1 lists the ODCs determined from the graphical fit for the aluminium samples by both the ultrasound and EBSD experiments respectively.

Thickness (mm)	$\mathbf{W_{400}}$	$\mathbf{W_{420}}$	$\mathbf{W_{440}}$
0.2	-1.07×10^{-2} / ***-8.36×10^{-3}***	-3.27×10^{-4} / ***-1.42×10^{-4}***	-5.02×10^{-3} / ***-8.66×10^{-3}***
0.5	-1.22×10^{-3} / ***-5.08×10^{-3}***	-1.08×10^{-3} / ***-1.07×10^{-3}***	1.34×10^{-4} / ***2.97×10^{-3}***
1	-4.61×10^{-3} / ***-8.63×10^{-3}***	1.15×10^{-4} / ***4.44×10^{-5}***	-4.01×10^{-3} / ***-7.78×10^{-3}***
1.5	-2.21×10^{-3} / ***-2.11×10^{-4}***	1.19×10^{-3} / ***3.00×10^{-3}***	2.67×10^{-3} / ***6.78×10^{-3}***

Table 9.1: ODC values determined from non-destructive Lamb wave velocity (left) and the corresponding EBSD measurements (right, italics, bold) for the aluminium sheets investigated.

Table 9.2 gives the magnitude difference between the ODCs determined from the EBSD and ultrasound techniques, stated in table 9.1. It is of note that all of the signs of the corresponding ODCs are the same, indicating the validity of using EBSD to correlate these non-destructive ultrasound measurements.

Thickness (mm)	$\mathbf{W_{400}}$	$\mathbf{W_{420}}$	$\mathbf{W_{440}}$
0.2	2.34×10^{-3}	1.85×10^{-4}	3.64×10^{-3}
0.5	3.86×10^{-3}	1.00×10^{-5}	2.84×10^{-3}
1	4.02×10^{-3}	7.06×10^{-5}	3.77×10^{-3}
1.5	2.00×10^{-3}	1.81×10^{-3}	4.11×10^{-3}

Table 9.2: Table giving the magnitude difference between the ultrasonic and EBSD generated ODCs.

Tables 9.3-9.4 give the analogous data for the steel samples.

Steel	W_{400}	W_{420}	W_{440}
DC01	-7.75×10^{-3} / ***-1.23 ×10^{-2}***	-1.05×10^{-3} / ***-5.81 ×10^{-4}***	9.54×10^{-4} / ***2.93 ×10^{-4}***
DC05	-1.36×10^{-3} / ***-1.87 ×10^{-2}***	-1.02×10^{-3} / ***-2.14 ×10^{-3}***	-4.36×10^{-4} / ***-9.51 ×10^{-6}***

Table 9.3: ODC values determined from non-destructive Lamb wave velocity (left) and the corresponding EBSD measurements (right, italics, bold) for the steel sheets investigated.

Steel	W_{400}	W_{420}	W_{440}
DC01	4.55×10^{-3}	4.69×10^{-4}	6.61×10^{-4}
DC05	1.73×10^{-2}	1.12×10^{-3}	4.26×10^{-4}

Table 9.4: Table giving the magnitude difference between the ultrasonic and EBSD generated ODCs for the steel samples.

Firstly, it is noticeable that the largest differences in magnitudes observable are typically the W_{400} coefficient. The W_{400} coefficient depends on the mean velocity of the S_0 Lamb wave. The larger variation in velocity from the EBSD data also contributes to the error in W_{400}. The better agreement shown in the W_{420} and W_{440} coefficients is systematic of the good correlation in shape from the EBSD predictions.

It can be concluded that the EBSD prediction of velocity show promise in quantifying texture, solving the ODF in a novel way. It provides evidence that collating data at the microstructural level validates the ultrasonic texture measurement in the majority of cases.

9.1.3 – Texture inhomogeneity through-thickness

A question remains as to why the 0.5 mm thick aluminium sample did not exhibit a good correlation in shape like the other samples. This discrepancy is more concerning as none

of the twelve EBSD surface scans taken from across the sheet generated a good prediction to the empirical ultrasound data.

As discussed, one limitation of EBSD is its surface specificity. The premise of using surface scans to measure the crystallographic texture and predict the elastic stiffness constants is dependent on the homogeneity of these properties throughout the bulk of the sample.

A more in-depth analysis of the sheet was completed. Figure 9.7 is an auto IPF plot of a section of the 0.5 mm thick aluminium sheet. The aluminium sheets are nominally pure (> 99.5% Al); the sheets should predominately consist of the Copper rolling texture component $\{112\}\langle 11\bar{1}\rangle$ (see chapter 5.4.3). The notation of the Copper rolling texture suggests that grains align parallel to the RD with a <111> orientation, and are oriented orthogonal to that with a <112> orientation. Figure 9.7b shows the results from a partition function applied to figure 9.7a in the ND, highlighting only crystals possessing an orientation tolerance within 15˚ of the <112> orientation.

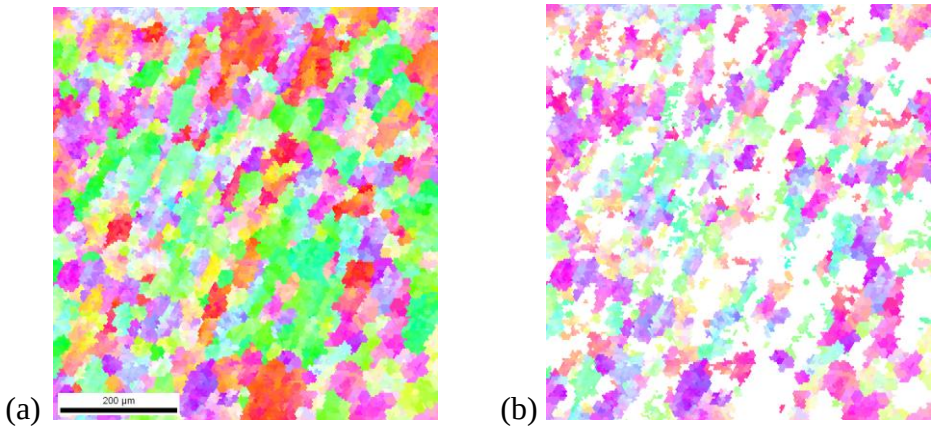

Figure 9.7: (a) Auto IPF plot from a surface scan taken from a sample of the AL104232 aluminium sheet. (b) EBSD Auto IPF partition, showing only points within a 15˚ misorientation of the crystal orientation <112>. 64% of the data points studied here satisfied the partition rule.

The high partition percentage of <112> orientations along with [111] pole figure data confirms the dominance of the Copper rolling texture.

A method to perform EBSD through-thickness was therefore developed to investigate if there was evidence of the microstructure or texture exhibiting inhomogeneity in the bulk.

There are a limited number of publications that report on through-thickness EBSD on metal sheet [2-5]; this has been achieved in a variety of ways. Suitable polishing conditions were established that enabled through-thickness scans from surface-to-surface to be completed. A set of steel coils were designed to attach to the sample to present a flat edge for polishing enabling through-thickness scans to be completed.

The orientation of the sample in the SEM was important: it would be expected that scanning an edge parallel to the RD will be dominated by <111> orientations, so this would act as a reference. Figure 9.8 shows the through-thickness sample orientation.

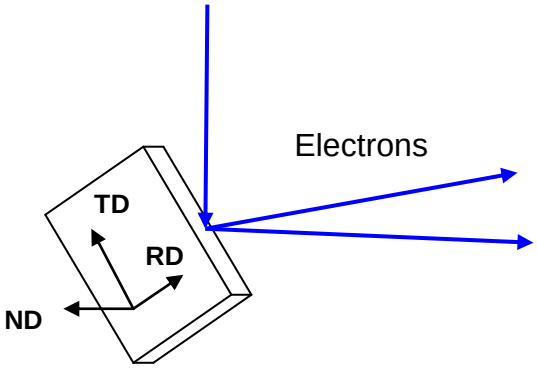

Figure 9.8: Schematic diagram displaying the orientation of the through-thickness EBSD samples made. The scan is taken looking 'into' the RD in the TD-ND plane.

Figure 9.9 is an example of one through-thickness scan taken from the aluminium sheet.

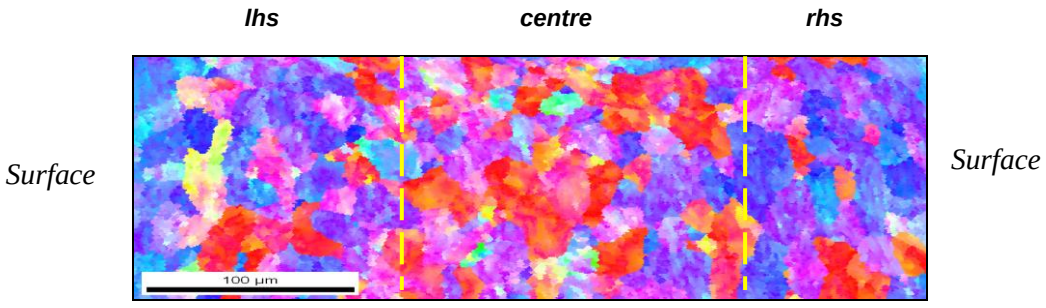

Figure 9.9: EBSD Auto IPF plot of through thickness EBSD scan of 0.5mm thick aluminium sheet.

Further scans were taken on this and numerous other samples from the 0.5 mm thick sheet; all other results were consistent with that shown in figure 9.9 [6], namely that there was a layering of texture, with <111> orientations being dominant sub-surface, with a more random distribution in the central region.

Through-thickness data was then compiled for the other samples investigated in this body of work, to clarify that the level of inhomogeneity apparent in the 0.5 mm thick aluminium sheet is more significant than the other sheets studied that gave a better correlation between ultrasound and EBSD. Figure 9.10 is an example of a through-thickness scan taken from the 1.5 mm thick aluminium sheet.

Figure 9.10: Auto IPF plot of through thickness EBSD scan of 1.5 mm thick aluminium sheet.

It is noticeable in figure 9.10 that there is no discernible banding of texture as reported in the 0.5 mm thick aluminium sheet; a full spectrum of colour is visible in the plot. This suggests an isotropic and homogeneous distribution of orientation, texture and material properties through the bulk with no significant changes in the grain size through-thickness. This result indicates an EBSD surface scan would be representative of the bulk texture. Similar data was determined for the 1 mm thick aluminium sample, as well as the steel samples. Each produced results suggesting homogeneity of texture through the bulk. A through-thickness scan could not be made on the 0.2 mm aluminium sheet as the polishing techniques deployed caused the sample to deform as it was too thin.

So the evident ‘layering’ of texture in the 0.5 mm sheet was not detected in the other samples investigated. This ties in well with the results collected, and the assumption made regarding the texture seen by EBSD surface scans being representative regardless of where it is taken throughout the bulk. Namely, that regardless of how much of the sample is polished away in reducing the thickness; the subsequent averaged angle data will give rise to representative texture information.

In the inhomogeneous sheet, sub-surface layers of between 80-140 μm thick existed with predominately <111> crystallographic orientation (figure 9.9). The central bulk region of the scans features a more random distribution of crystallographic orientations. To quantify this distribution of <111> orientations, data partitioning was applied to all of the through-thickness scans taken; three examples of which are given in figure 9.11.

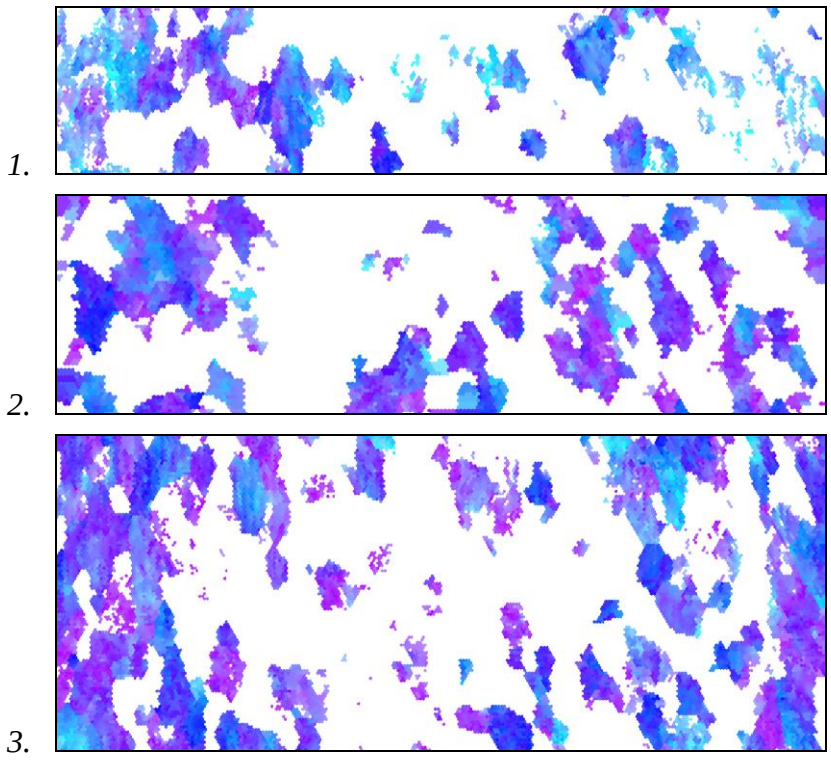

Figure 9.11: EBSD Auto IPF partitions of three through-thickness scans displaying points within 15˚ tolerance of <111>. Scan 1 has a total of 36.1% of data points in the partition. Scan 2 has 36.7% and scan 3 has 41.1%.

The through-thickness datasets were rotated into the ND frame of reference; the same as a surface scan. This way the effective elastic anisotropy and a prediction of the velocity variation can be made. Rotating the data 90˚ about the RD (figure 9.8) axis of the EBSD setup, will display the data in the surface frame of reference. Figure 9.12 shows the result of

the through-thickness scan (scan 3 from figure 9.11) when rotated into the surface frame of reference.

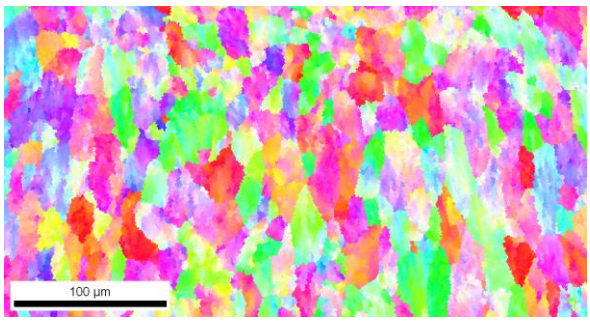

Figure 9.12: EBSD Auto IPF plot of scan 3 rotated 90˚ about the OIM RD axis to transform scan to the virtual RD-TD plane of the sheet.

Taking the angular data from this new rotated dataset, a prediction for the S_0 mode velocity was made. This is shown in figure 9.13. This prediction shows a good correlation with the prediction made by the EBSD surface scans (figure 9.2).

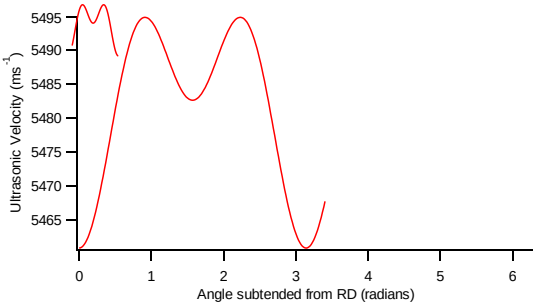

Figure 9.13: Ultrasonic velocity variation prediction from the rotated EBSD data taken from a through-thickness scan of the 0.5mm thickness aluminium sheet.

The through-thickness data was cropped into approximately the three apparent regions of texture (figure 9.9); the outer regions being the areas with a high density of <111> orientations and the central region having a more random distribution of orientations. These sections were labelled *lhs*, *centre* and *rhs* respectively. The three datasets were rotated into the surface plane, with velocity predictions made. Figure 9.14 gives the velocity prediction from the central region (example from scan 3 in figure 9.11).

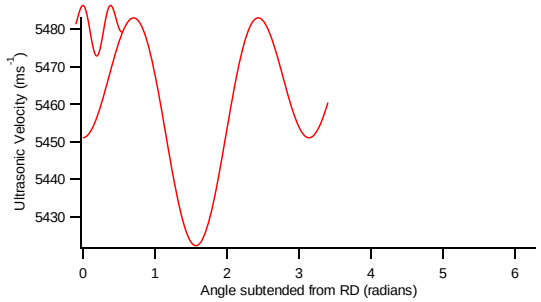

Figure 9.14: Ultrasonic velocity variation prediction from the central region of the rotated EBSD dataset taken from a through-thickness scan of the 0.5 mm thickness aluminium sheet.

Figures 9.15 and 9.16 show the velocity profile predictions for the sub-surface cropped sections, *lhs* and *rhs*, respectively (from scan 3 in figure 9.11).

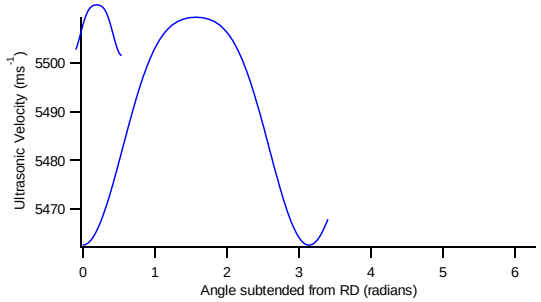

Figure 9.15: Ultrasonic velocity variation prediction of lhs of the rotated EBSD dataset taken from a through-thickness scan of the 0.5 mm thickness aluminium sheet.

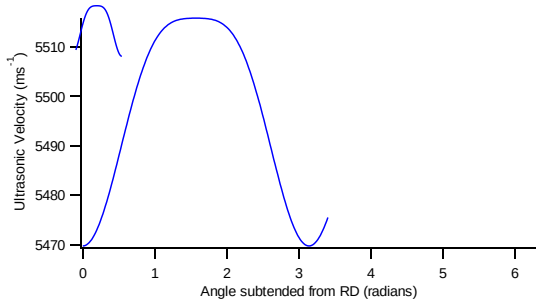

Figure 9.16: Ultrasonic velocity variation prediction of rhs of the rotated EBSD dataset taken from a through-thickness scan of the 0.5 mm thickness aluminium sheet.

Figures 9.15 and 9.16 illustrate a good agreement in shape to the ultrasonic measurement, though the absolute velocities and variations are greater, with an approximately 25 ms^{-1} larger variation between maximum and minimum velocity. In contrast the centre section, figure 9.14, has produced a poor correlation.

Analysis on other through-thickness scans produced the same behaviour, indicating 2-fold symmetry in the sub-surface sections that correlate well to the ultrasonic data.

9.1.4 – Simulation of inhomogeneous sample

The ultrasonic experiment for the 0.5 mm thick sheet has a frequency-thickness product of approximately 0.1 MHz.mm. Figures 9.14-9.16 suggest that the ultrasonic velocity profile could be due to the Lamb wave being quicker sub-surface in comparison to the bulk, which is inconsistent with the theory of the energy distribution for a non-dispersive S_0 mode wave in an isotropic sheet.

To investigate the plausibility of this hypothesis, finite element modelling (FEM) utilizing PZ Flex software was used [7]. In a 2D FE simulation, an aluminium sheet was simulated, constructed of 720 x 15 elements square elements with dimension of 33.3 μm. The sheet was constructed of three discrete layers, the top and bottom layers being 3 elements wide (100 μm), with a central layer of 9 elements.

The ends of the sheet were absorbing, minimizing possible interfering reflections. A generation EMAT, with a coil width of 2 mm, was placed at 45 mm from one side of the sheet, with a detector EMAT 150 mm away from the generation EMAT and 45 mm from the other end of the sheet. This separation simulated the experimental setup. The Lamb wave generation was stimulated by applying a piston force at the position of the generation coil. Figure 9.17 gives a schematic diagram of the FEM setup.

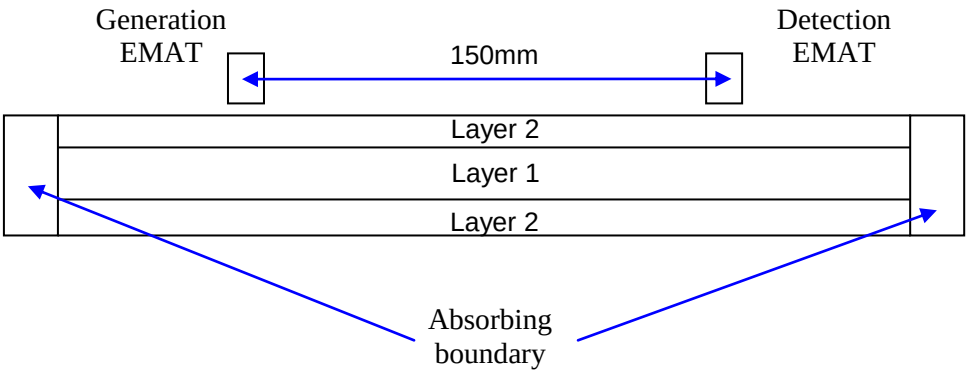

Figure 9.17: Schematic diagram of the FE simulation setup of the aluminium layered sheet. The central layer will have different material characteristics compared to the outer layers which will be given the same material properties.

The effective stiffness constants were determined for the three sections from the EBSD data, with the outer *lhs* and *rhs* layers being averaged to produce a two layer sandwich. Various simulation experiments were conducted, measuring the absolute velocity in the *x* and *y* directions at the surface and at the centre of the sheet. This was why a width of 15 elements was chosen, so the central velocity could be measured at the centre of the element and not on the edge between two elements.

Four different experiments were conducted: the first with the layers containing the different measured elastic constants; the second with the average elastic constants from the outer layers were applied to the entire sheet; thirdly an average of the centre layer elasticity was given to all the layers; finally the average from across the whole sheet was given to all the layers. The data sets were rotated to obtain the elastic stiffness constants in different directions ranging from parallel to orthogonal with the RD to allow for velocity against angle analysis to be completed if required. Figure 9.18 shows an A-scan of the particle displacement in the x-direction produced by the simulation.

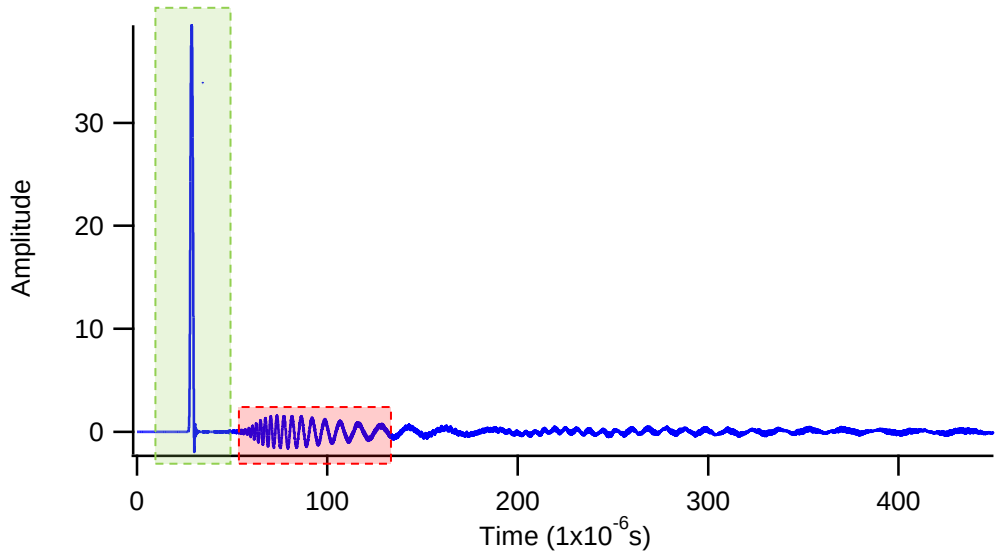

Figure 9.18: A-scan generated by FEM of layered aluminium sheet along the RD. This shows a typical Lamb wave trace. Highlighted is the S_0 (green) and A_0 (red) modes

Figure 9.19 shows a velocity at the surface (red) and the velocity at the centre of the sheet (blue) aligned parallel to the RD of the S_0 mode Lamb wave.

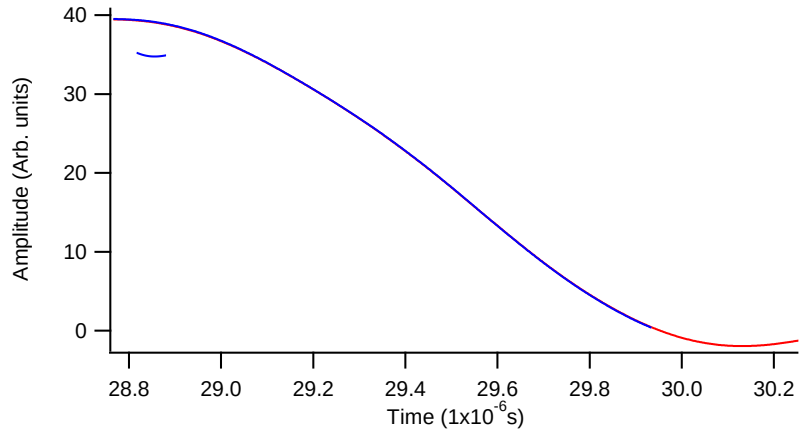

Figure 9.19: A-scan generated by FEM of layered aluminium sheet along the RD. The red line plot represents the in-plane velocity component at the surface, with the blue line representing the in-plane velocity component at the centre of the sheet. As can be seen, there is no discernable difference between the two.

As is evident, there is no discernible difference between the velocities, and any variance this small would not be detected by an EMAT within experimental error. Figure 9.20 gives a broader view of the S_0 mode generation, indicating further the identical velocities measured at the surface and bulk.

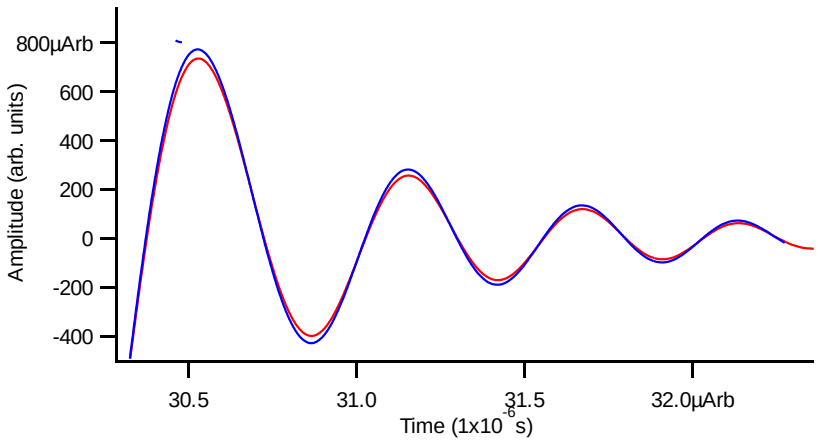

Figure 9.20: A-scans generated by FEM of layered aluminium sheet along the RD, displaying the S_0 mode generated. The red line plot represents the in-plane velocity component at the surface, with the blue line representing the in-plane velocity component at the centre of the sheet. The time of arrival at each change in peak is identical within ± 0.002 μs.

Similar analysis was conducted in each direction recorded. Figure 9.21 shows the simulation velocity results for the data rotated in line with the TD.

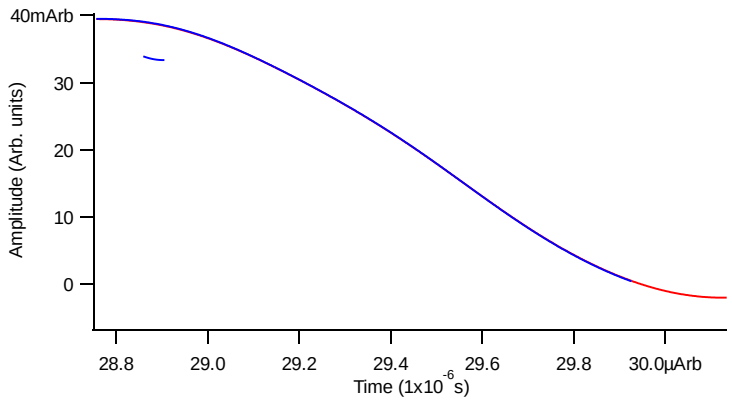

Figure 9.21: A-scan generated by FEM of layered aluminium sheet along the TD. The red line plot represents the in-plane velocity component at the surface, with the blue line representing the in-plane velocity component at the centre of the sheet.

The arrival time of the Lamb wave in the transverse direction is slightly quicker as expected from the ultrasound results. The simulation provides strong evidence suggesting that the theory regarding the energy distribution holds true for non-dispersive S_0 mode Lamb waves on these anisotropic, inhomogeneous sheets.

9.1.5 – Summary

There still is no conclusive explanation to the discrepancy in correlation between the layered through-thickness EBSD scans and the ultrasound measurement of the elastic anisotropy. It is interesting to note that EBSD measurements have highlighted that sheets,

even as thin as 0.5 mm, can exhibit inhomogeneity of texture through-thickness, which is an important result in its own right.

In the cases where texture homogeneity was maintained through the thickness of the sheet, such as that shown in figure 9.10, the correlation in shape between the ultrasonic velocity measurements and the EBSD predictions are very good. The ODC magnitudes do show discrepancies, in particular the W_{400} coefficient, but the EBSD data has identified the relative velocity patterns successfully in the majority of cases.

9.2 – Grain characterization

The ultrasonic characterization of grain size is extremely difficult. Many have reported encouraging results [8, 9] though it has never been shown definitively to work consistently. The difficulty, as explained in chapters 6 and 7, results from the inability to differentiate between the numerous contributing effects of ultrasonic attenuation on the amplitude of subsequent detected echoes.

Initial experiments were conducted observing the attenuation of the S_0 mode Lamb wave, incorporating a measurement of the amplitude of the S_0 wave built-in to the texture Labview software. However, these results were evidently influenced by the anisotropy in the elasticity and could not be considered to be viable for analysis. The method adopted when using the texture system is one of the two popular ways of measuring attenuation effects, where measurement of the amplitude of a propagating wave at two different positions of known separation relative to a generation source can lead to the determination of α.

It was decided to utilise the second option, which is to use a through-thickness wave, measuring consecutive back-wall echoes.

9.2.1 – Wavelength and scattering regime determination

With absorption minimal in aluminium and steel sheet, attenuation of the amplitude will be due to scattering and diffraction effects. To determine the scattering regime of the

attenuation for each sheet, the peak wavelength for each experiment is required to compare to the grain size. Taking the velocity results in tables 7.10 and 7.11, and then solving to get λ from $\lambda = \frac{v}{f}$ by taking the values for f determined from FFT analysis (table 7.6-7.7), the corresponding wavelengths are given in tables 9.5 and 9.6. The frequency selected was the peak resonant frequency. In some sheets, this peak value was different depending on the polarization.

Thickness (mm)	λ_{RD} (μm)	λ_{TD} (μm)
0.2	400	399.9
0.5	1000	999.9
1	998.7	667.9
1.5	600.9	428.7

Table 9.5: Wavelength of the shear wave propagating through-thickness in the aluminium sheets.

Steel	λ_{RD} (μm)	λ_{TD} (μm)
DC01	986.6	988.4
DC05	858.3	863.6

Table 9.6: Wavelength of the shear wave propagating through-thickness in the steel sheets studied.

Dividing these values with the respective average grain sizes determined from EBSD measurements, shows that the smallest ratio of $\frac{\lambda}{\overline{D}}$ in these experiments was approximately 17 (1.5 mm thick aluminium sheet) up to the largest ratio of approximately 53 (DC05 steel sheet). These values are both > 10 and 2π, two of the lower limits given in the literature for Rayleigh scattering [10, 11]. This indicates that Rayleigh scattering should be the major influence on the scattering component of the intrinsic attenuation. There is a realistic possibility that there will be a stochastic element of dependence influencing the scattering.

9.2.2 – Experimental problems

Other effects that influence the attenuation include absorption, which is negligible in metals such as aluminium and steel for reasons previously given, and reflection losses. A major experimental issue encountered, one which is prevalent in thin sheet, were the effects of mode conversions. Mode conversions were discussed in chapter 7 and occur when the SH wave reflects at each surface.

The existence of mode conversions and their effects on the wave amplitude measured was indicated in figures 7.11 and 7.12. The decay envelopes (figures 7.14 and 7.15) do not exponentially decay with time for the 0.2 and 0.5 mm thick aluminium sheet. The fluctuations seen appear to have a periodic increase and decrease, behaving like a beat. Suggestions for this behaviour could be explained from the analysis of two similar frequency sine waves.

Figure 9.22 shows a magnitude-FFT of the complete wave for the 0.2 mm sheet (polarised in the RD). It was noticeable that the main peak located at 7.916 MHz had an adjacent peak, though less significant, at 7.955 MHz.

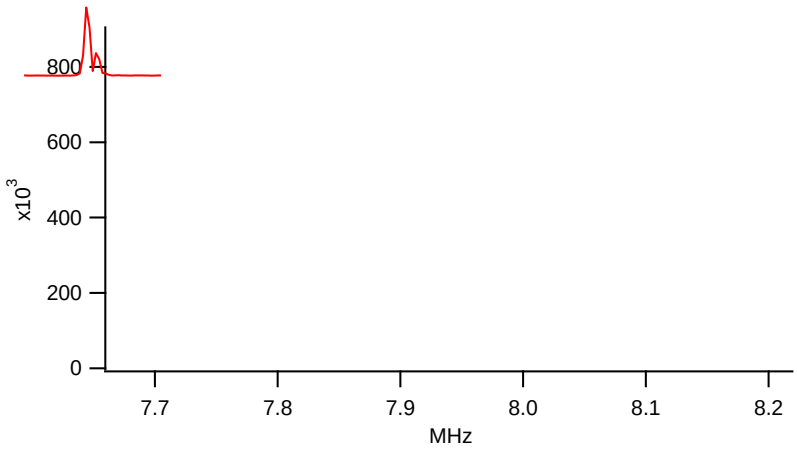

Figure 9.22: Magnitude-FFT of the 0.2 mm thick aluminium sheet, applying a Hanning window across the entire part of the wave containing useful data. The data was padded out taking advantage of the 2^n relationship to improve the resolution. As can be seen, two frequencies close together are detected.

The addition of two sine waves with frequencies in close proximity to each other, will result in a 'beating', generating periodic peaks and troughs as the two sine waves move in and

out of phase. Figure 9.23 displays this result, produced from a simple simulation of the addition of two sine waves with similar frequencies interfering.

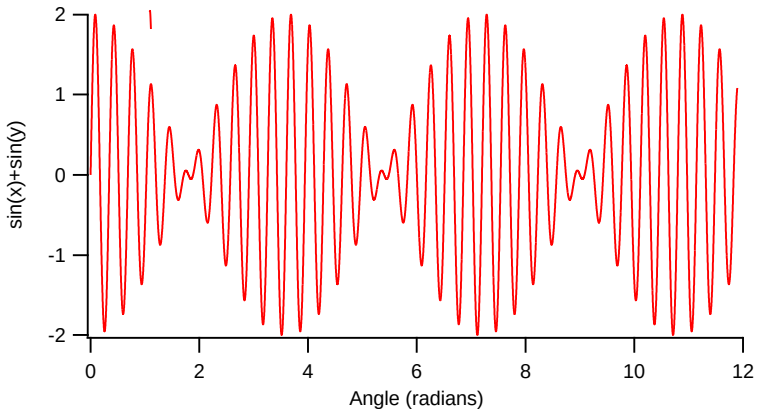

Figure 9.23: Graph showing the addition of two sine waves of similar frequency. The constructive and destructive interference is apparent as the waves periodically go in and out of phase.

With reference to figure 7.14, which displayed the decay envelopes along the RD and the TD for the 0.2 mm thick sheet, the decay also appears to increase and decrease periodically with time, much in the same way demonstrated in figure 9.23. There is the reduction in amplitude due to geometric effects and attenuation overall, though this is not a gradual progression. It is therefore more appropriate to fit an exponential curve not to the decay data as a whole, but to discrete points at a corresponding periodicity. Completing such analysis gives total attenuation coefficients for the 0.2 mm thick sheet along the RD of 6.05 and for the TD of 4.42. The relative ratios of these (0.73) is however similar to the initial attenuation measurements (0.71).

Attempts were made to minimise the modulation present in the decay envelopes. Glass and Perspex sheets were placed between the EMAT, the sample and the steel block to minimise any bend in the surface. The angle of reflection has a significant impact on the amplitude of successive echoes due to beam spreading. These changes to the experimental setup had no discernable impact on the measured results. Changing the frequency of the generation pulse again had no influence other than to change the signal intensity detected.

9.2.3 – Correlation of results – grain size

Any relative changes in attenuation from the wave polarised parallel to the RD and to the TD will be due to the change in the scattering component as a result of the change in the apparent grain size. Using equation 6.35 (for Rayleigh attenuation), applying the values for $\overline{D}$ from EBSD and the frequency *f* established from magnitude FFT analysis, values for the level of dependence of the scattering component can be determined and subtracted from the measured total attenuation coefficients α. However, there is the added issue regarding the constant of proportionality C_R that exists. Without knowledge of the magnitude of this proportionality constant, it is impractical to make any estimations of the average grain size from the attenuation measurement.

Having measured the grain size using EBSD, the grain sizes are all small, and this is having a discernible effect on the attenuation results. Much larger grain sizes would have produced more significant scattering, resulting in a more severe decay, though this in turn can limit the received signal.

9.2.4 – Aspect ratio correlation

There were some positive results to take from the attenuation data collated. It can be seen in tables 7.8 and 7.9 that the calculated value for α for the shear wave polarised in the RD is larger each time than the wave polarised in the TD. This is an expected result. This indicates that such an experimental setup can be used to identify the rolling direction for a sheet, which is certainly not obvious for steel sheets from visual inspection alone. Of course for the thinner sheets studied where mode conversion was an issue, this analysis cannot be considered completely reliable due to subsequent errors in the exponential fit.

9.2.4.1 – Thicker sheet analysis

The mode conversion effects on successive peak echo amplitudes were negligible in the thicker sheets tested, with the 1.5 mm decay envelope in particular (figure 7.17), showing

a consistent exponential decay in the amplitude with time. The 1 mm thick aluminium sheet (figure 7.16), as well as the thickest steel sample DC01 with a thickness of 1.48 mm (figure 7.18) also exhibit these similar and expected trends in amplitude decay. The total attenuation coefficients determined from exponential decay fitting for these thicker sheets are given in table 9.7. The effects of diffraction and beam spreading are cancelled in this relative measurement, with each set of data propagating the same distance. Therefore scattering produces the differences seen in the attenuation between the RD and the TD.

By dividing α_{TD} by α_{RD} one can establish a relative ratio of the total attenuation in the different directions. These results in comparison to the grain aspect ratio values obtained by EBSD measurements are within 10% tolerance levels for the 1.5 mm thick aluminium sheet and the steel sheet DC01. In each case, the ultrasonic ratio is higher than the EBSD ratio, but this is due to the presence of other attenuation effects that are inherent within both α_{TD} and α_{RD}.

Thickness (mm)	$\boldsymbol{\alpha_{RD}}$	$\boldsymbol{\alpha_{TD}}$	$\frac{\alpha_{TD}}{\alpha_{RD}}$	Aspect Ratio (EBSD)
Aluminium (1)	8.2	6.92	**0.844**	**0.47**
Aluminium (1.5)	5.3	2.91	**0.549**	**0.5**
DC01 steel (1.48)	3.94	2.36	**0.599**	**0.55**

Table 9.7: Attenuation coefficients, ultrasonically determined aspect ratio, and EBSD measured aspect ratio.

9.2.5 – Summary

The ultrasonic determination of grain size is an extremely difficult task, and with too many variables present and unknown, is difficult to quantify ultrasonically in the pulse-echo setup described here. Microscopic techniques therefore, such as EBSD, are more suitable for such a one-off measurement. Relative measurements of attenuation in different directions can give an indication of which direction the grains are elongated in (biggest attenuation = rolling direction). Measuring the grain aspect ratio from ultrasonic attenuation data minimises the

unknown parameters because they cancel within the ratio itself. There is scope to be able predict the severity of elongation in grains using attenuation data; in the experimental setup used here this was evident in sheet metal with a thickness over 1 mm. Below this thickness, interference due to mode conversions inhibited the accurate measurement of attenuation.

9.3 – Elasticity measurements

The EBSD data used to quantify the texture coefficients were finally compared to predicted elastic constants determined from ultrasonic data. With good agreement established in the Lamb wave velocity predictions it will be assumed here that the elastic stiffness constants measureable using the two shear waves used in the attenuation measurements will be considered predictable from the EBSD generated elastic stiffness constants.

Two methods have been previously described that can determine the elastic stiffness constants c'_{44} and c'_{55} from ultrasonic data. The simplest approximation can be made from the appropriate velocity squared multiplied by the density. The second was utilizing the previously determined ODCs from the Lamb wave data. Tables 9.8-9.9 give the determined values from each method.

	c'_{44} (GPa)	c'_{55} (GPa)	c'_{44} (GPa)	c'_{55} (GPa)	c'_{44} (GPa)	c'_{55} (GPa)
0.2	27.07	27.09	26.32	25.76	26.29	26.32
0.5	27.35	27.1	26.49	26.29	26.48	26.64
1	26.37	26.47	26.5	26.78	26.29	26.28
1.5	26.53	26.37	26.41	26.46	27.19	26.54

Table 9.8: Prediction of the elastic stiffness constants c'_{44} and c'_{55} using the shear wave velocities (red), the ODC velocity equations (blue) and the predicted values from EBSD (green) for the aluminium samples.

	c'_{44} (GPa)	c'_{55} (GPa)	c'_{44} (GPa)	c'_{55} (GPa)	c'_{44} (GPa)	c'_{55} (GPa)
DC01	79.5	83.72	87.85	80.85	87.97	89.59
DC05	84.03	86.65	89.26	86.56	79.60	85.83

Table 9.9: Prediction of the elastic stiffness constants c'_{44} and c'_{55} using the shear wave velocities (red), the ODC velocity equations (blue) and the predicted values from EBSD (green) for the steel samples.

The aluminium results are expectedly quite close. Aluminium has a comparably small anisotropy factor ($c = -10.1\ GPa$) and hence the maximum and minimum values that the effective elastic constants can physically have will be restricted.

Of the four values measured for c'_{44} by EBSD, two of the ODC-equation predictions were closer, and two from the shear wave equation were closer. The average errors from each method were calculated and shown in table 9.10.

Thickness (mm)	c_{44} ***% shear errors***	c_{55} ***% shear errors***	c_{44} ***% ODC errors***	c_{55} ***% ODC errors***
0.2	2.88	2.84	0.11	2.14
0.5	3.18	1.7	0.03	1.31
1	0.30	0.73	0.80	1.91
1.5	2.43	0.66	2.86	0.31
Average	***2.2***	***1.48***	***0.95***	***1.42***

Table 9.10: Calculated errors associated with the predicted measurement of the elastic stiffness constants c'_{44} and c'_{55} from ultrasonic data in comparison to the EBSD prediction of the same constants for the aluminium samples studied.

It is apparent from this error analysis that the agreement between the EBSD elasticity predictions and the elasticity predictions resulting from the ODC velocity equations (equations 6.45 and 6.46) is better than when made with the shear wave equation. This confirms the significance of crystallographic texture on the validity of the standard wave equation.

The steel single crystal has a significantly greater anisotropy parameter, with the value used in this thesis for c = -139 GPa: the errors would be expected to be larger. The errors are given in table 9.11. For steel, it is noticeable that neither method is significantly better when compared to the EBSD data.

Steel	c_{44} *% shear errors*	c_{55} *% shear errors*	c_{44} *% ODC errors*	c_{55} *% ODC errors*
DC01	9.63	6.55	0.14	9.75
DC05	5.57	0.96	12.13	0.86
Average	***7.60***	***3.78***	***6.14***	***5.31***

Table 9.11: Calculated errors associated with the predicted measurement of the elastic stiffness constants c'_{44} and c'_{55} from ultrasonic data in comparison to the EBSD prediction of the same constants for the steel samples studied.

9.3.1 - Summary

It can be concluded from these results that when measuring elastic stiffness constants of rolled sheet using ultrasound, it is important to consider the effects of crystallographic texture as it will have a significant effect on the microstructure and hence the velocity a wave propagates at. This will be more evident in samples with smaller anisotropy parameters, as the slight changes in the elasticity are difficult to detect.

9.4 – References

1. *Rose JL, Ultrasonic waves in solid media, Cambridge University Press, 1999*

2. *Bittorf C, Matthies S, Priesmeyer HG, Wagner R, Intermetallics, **7**, 1999, pp. 251-258.*

3. *Johansson S, Zeng X-H, Andersson N-E, Peng RL, Materials Science and Engineering, **A315**, 2001, pp. 129-135.*

4. *Mao SC, Han XD, Luo JF, Zhang Z, Materials Letters, **59**, 2005, pp. 3567-3571.*

5. *Kamikawa N, Tsuji N, Minamino Y, Science and Technology of Advanced Materials, **5**, 2004, pp. 163-172*

6. Essex S, Potter MDG, Dobedoe RS, Dixon S, Rev. Prog. In QNDE, 2007

7. Acknowledgement to Dr. Yichao Fan for all the advice in using PZ Flex.

8. *Ogi H, Hirao M, Honda T, J. Acoust. Soc. Am., **98(1)**, 1985, pp. 458-464*

9. *Bouda AB, Lebaili S, Benchaala A, NDT&E International, **36**, 2003, pp. 1-5*

10. *Mason WP, McSkimmin HJ, J. Appl. Phys.,* ***19****, 1948, pp. 464-473*

11. *Smith RL, Ultrasonics, 1982, pp. 211-214*

CHAPTER 10

Final Conclusions

10.1 – Conclusions of thesis

Methods to correlate data obtained using the microscopic technique EBSD to rapid non-destructive ultrasonic measurements on rolled sheet metal have been established. This body of work has been focussed on the investigation of quantifying crystallographic texture, characterizing the crystallographic grains, and determining the elasticity properties of the sample sheets studied.

A novel method that manipulates EBSD Bunge-Euler angle data has been developed to quantify crystallographic texture by way of determining the orientation distribution coefficients of interest in cubic metals such as aluminium and steel. This technique produces macrotexture information from across a number of EBSD scans, and has been directly compared to results obtained from a commercially available ultrasonic texture measurement system. The EBSD data has been used to produce predictions for the nine elastic stiffness constants defining the elasticity state of a rolled sheet, and has further been manipulated to generate estimations of the S_0 Lamb wave velocity as it varies with direction. The ODCs were then extrapolated to compare to the ultrasonic technique. Of the six sheet samples studied in detail, five have produced a strong correlation of agreement in both the velocity predictions and the ODC values determined from both techniques.

The one instance where poor correlation existed between the predicted and measured velocity profiles, through-thickness EBSD scan techniques were developed to ascertain if any inhomogeneity of texture through the bulk existed. In this 0.5 mm thick aluminium sheet, an apparent layering of <111> crystallographic orientations sub-surface was evident, in contrast

to a more random distribution of orientations in the bulk. This result has highlighted the importance of in-plane measurements, with even thin sheet metal displaying inhomogeneity of material properties.

Linearly polarized bulk SH waves were used in a pulse-echo experimental setup in an attempt to characterize grain size and shape, as well as relevant elastic stiffness constants. Grain size characterization using attenuation proved extremely difficult, with too many variables to determine without any prior knowledge of the sheet microstructure. EBSD, which can measure average grain size to sub-micron accuracy, is a more beneficial technique for making such a measurement.

The grain aspect ratio, a result of the elongation in the volume in the rolling direction, was measured ultrasonically from a relative attenuation measurement using the linearly polarized SH waves along the rolling and transverse directions. Any difference in attenuation is predominately due to a variation in scattering, with diffraction effects being similar for both. For thin sheet thicknesses (< 1 mm), problems with mode conversions influenced decay envelopes. For thicker sheet samples, with thicknesses approaching 1.5 mm, the ratio of the total attenuation coefficients along the transverse to rolling directions were in very good agreement to the EBSD-measured aspect ratio values; 1% variation in the aluminium sample, 5% in the steel sample.

The elastic stiffness constants generated from the Bunge-Euler data were then compared to ultrasonic predictions, using relationships linking the shear elastic stiffness constants c'_{44} and c'_{55} to ultrasonic velocity and also to the ODCs. In aluminium, the average error between the EBSD and the ultrasonically determined ODC values were 1.2%, and in steel the average error was at 5.72%.

10.2 – Further work

There is much scope to develop this work further. If time had allowed, more emphasis could have been placed on the attenuation experiments presented here. Methods

using more than one reception EMAT could have been developed to determine values of α for different distances x for instance.

With regards to the texture analysis work, there are still unresolved issues regarding the 0.5 mm thick aluminium sheet that displayed surface-to-bulk inhomogeneity; this is a particularly important issue to resolve. This work concentrated on quantifying texture by calculating specific ODCs of interest. A great amount of work using diffraction techniques to analyse texture determines the percentages of the differing types of rolled and recrystallising textures present in a sample. It would be interesting to investigate whether from a ultrasonic 'velocity against angle' plot such as that performed in this body of work, a method could be derived to identify the textures that are present, and extended further to determine the relative amounts of such textures. Data partitioning using EBSD would be useful for correlating the data, using simulated EBSD data for pure textures and known 'mixtures' of textures to calculate expected velocity against angle plots to compare to ultrasonic measurements.

This work has solely studied cubic-crystallising metals aluminium and steel, and can be applied to all rolled cubic metals. Work to extend to other non-cubic metals, such as zinc and titanium, would generalize the technique. For hexagonal materials, it should be noted that the measurable ODCs and the Euler angle definitions are different to the cubic case, and as such, the mathematics involved would require completely reworking.

The further use of EBSD to correlate and better understand NDT experiments should also be investigated in the future. For example, introductory work has been completed developing image registration techniques that align two EBSD IPF maps taken from the same area of a sample before and after a given experiment. From here, various properties of the two scans can be compared to / subtracted from each other to ascertain differences in the microstructure, such as the colours assigned or just specific angles. Applications of such a technique would be useful in ascertaining whether a measurement technique was infact non-destructive, or for evaluation of the evolution of microstructure with load or temperature, and correlating to different ultrasonic response too.

Appendix A

Fortran programs extrapolating the elastic stiffness constants from EBSD data

To determine the elastic stiffness constants from the EBSD Eulerian angle data, programs were coded in Fortran, based on the mathematical framework presented in chapter 6. Below are the two programs used to obtain this data. The first one, *SayersAl*, is for exclusive use for data obtained from aluminium samples. The second program *SayersSteel* is for application of the DC series steel data collected.

A.1 - Aluminium program

```
PROGRAM SayersAl

implicit none

    real(8):: phi1, phi2,

theta,a1,a2,a3,a4,a5,a6,a7,r1,r2,r3,r4,r5,r6,r7,r8,r9,C11,C22,C33,C44,C55,C66,C23,C13,C12,W400,W4
20,W440

    real(8), dimension(3,3)::g
    integer::N,u_in,ios, counter,f

    counter=0
    N=0

    N=0
    OPEN(UNIT=u_in, IOSTAT=ios, FILE='/home/resrch/ph/rbak/microscope/angledata.txt', &
STATUS='old',
    ACTION='read')

    do

      READ (u_in,*,END=100) phi1,theta,phi2,a1,a2,a3,a4,a5,a6,a7

       g(1,1)=cos(phi1)*cos(phi2)-sin(phi1)*sin(phi2)*cos(theta)
       g(2,1)=-cos(phi1)*sin(phi2)-sin(phi1)*cos(phi2)*cos(theta)
       g(3,1)=sin(phi1)*sin(theta)
       g(1,2)=sin(phi1)*cos(phi2)+cos(phi1)*sin(phi2)*cos(theta)
       g(2,2)=-sin(phi1)*sin(phi2)+cos(phi1)*cos(phi2)*cos(theta)
       g(3,2)=-cos(phi1)*sin(theta)
       g(1,3)=sin(phi2)*sin(theta)
       g(2,3)=cos(phi2)*sin(theta)
       g(3,3)=cos(theta)


            r1=r1+g(1,1)*g(1,1)*g(2,1)*g(2,1)+g(1,1)*g(1,1)*g(3,1)*g(3,1)+g(2,1)*g(2,1)*g(3,1)*g(3,1)

            r2=r2+g(1,2)*g(1,2)*g(2,2)*g(2,2)+g(1,2)*g(1,2)*g(3,2)*g(3,2)+g(2,2)*g(2,2)*g(3,2)*g(3,2)
```

```
        r3=r3+g(1,3)*g(1,3)*g(2,3)*g(2,3)+g(1,3)*g(1,3)*g(3,3)*g(3,3)+g(2,3)*g(2,3)*g(3,3)*g(3,3)

        r4=r4+g(1,2)*g(1,2)*g(1,3)*g(1,3)+g(2,2)*g(2,2)*g(2,3)*g(2,3)+g(3,2)*g(3,2)*g(3,3)*g(3,3)

        r5=r5+g(1,3)*g(1,3)*g(1,1)*g(1,1)+g(2,3)*g(2,3)*g(2,1)*g(2,1)+g(3,3)*g(3,3)*g(3,1)*g(3,1)

        r6=r6+g(1,1)*g(1,1)*g(1,2)*g(1,2)+g(2,1)*g(2,1)*g(2,2)*g(2,2)+g(3,1)*g(3,1)*g(3,2)*g(3,2)

        r7=r7+g(1,2)*g(1,2)*g(1,3)*g(1,3)+g(2,2)*g(2,2)*g(2,3)*g(2,3)+g(3,2)*g(3,2)*g(3,3)*g(3,3)

        r8=r8+g(1,1)*g(1,1)*g(1,3)*g(1,3)+g(2,1)*g(2,1)*g(2,3)*g(2,3)+g(3,1)*g(3,1)*g(3,3)*g(3,3)

        r9=r9+g(1,1)*g(1,1)*g(1,2)*g(1,2)+g(2,1)*g(2,1)*g(2,2)*g(2,2)+g(3,1)*g(3,1)*g(3,2)*g(3,2)

        N=N+1

        PRINT*, N

    end do

100 close(u_in)

        r1=r1/N
        r2=r2/N
        r3=r3/N
        r4=r4/N
        r5=r5/N
        r6=r6/N
        r7=r7/N
        r8=r8/N
        r9=r9/N

        PRINT*, 'r1=', r1
        PRINT*, 'r2=', r2
        PRINT*, 'r3=', r3
        PRINT*, 'r4=', r4
        PRINT*, 'r5=', r5
        PRINT*, 'r6=', r6
        PRINT*, 'r7=', r7
        PRINT*, 'r8=', r8
        PRINT*, 'r9=', r9

        C11=108.2+20.2*r1
        C22=108.2+20.2*r2
        C33=108.2+20.2*r3
        C44=28.5-10.1*r4
        C55=28.5-10.1*r5
        C66=28.5-10.1*r6
        C23=61.3-10.1*r7
        C13=61.3-10.1*r8
        C12=61.3-10.1*r9

        PRINT*, C11
        PRINT*, C22
        PRINT*, C33
        PRINT*, C44
        PRINT*, C55
        PRINT*, C66
        PRINT*, C23
        PRINT*, C13
        PRINT*, C12


END PROGRAM SayersAl
```

A.2 - Steel program

```
PROGRAM SayersSteel

implicit none

    real(8):: phi1, phi2,

theta,a1,a2,a3,a4,a5,a6,a7,r1,r2,r3,r4,r5,r6,r7,r8,r9,C11,C22,C33,C44,C55,C66,C23,C13,C12,W400,W4
20,W440

    real(8), dimension(3,3)::g
    integer::N,u_in,ios, counter,f

    counter=0
    N=0

    N=0
    OPEN(UNIT=u_in, IOSTAT=ios, FILE='/home/resrch/ph/rbak/microscope/angledata.txt', &
STATUS='old',
    ACTION='read')

    do

      READ (u_in,*,END=100) phi1,theta,phi2,a1,a2,a3,a4,a5,a6,a7

       g(1,1)=cos(phi1)*cos(phi2)-sin(phi1)*sin(phi2)*cos(theta)
       g(2,1)=-cos(phi1)*sin(phi2)-sin(phi1)*cos(phi2)*cos(theta)
       g(3,1)=sin(phi1)*sin(theta)
       g(1,2)=sin(phi1)*cos(phi2)+cos(phi1)*sin(phi2)*cos(theta)
       g(2,2)=-sin(phi1)*sin(phi2)+cos(phi1)*cos(phi2)*cos(theta)
       g(3,2)=-cos(phi1)*sin(theta)
       g(1,3)=sin(phi2)*sin(theta)
       g(2,3)=cos(phi2)*sin(theta)
       g(3,3)=cos(theta)


            r1=r1+g(1,1)*g(1,1)*g(2,1)*g(2,1)+g(1,1)*g(1,1)*g(3,1)*g(3,1)+g(2,1)*g(2,1)*g(3,1)*g(3,1)

            r2=r2+g(1,2)*g(1,2)*g(2,2)*g(2,2)+g(1,2)*g(1,2)*g(3,2)*g(3,2)+g(2,2)*g(2,2)*g(3,2)*g(3,2)

            r3=r3+g(1,3)*g(1,3)*g(2,3)*g(2,3)+g(1,3)*g(1,3)*g(3,3)*g(3,3)+g(2,3)*g(2,3)*g(3,3)*g(3,3)

            r4=r4+g(1,2)*g(1,2)*g(1,3)*g(1,3)+g(2,2)*g(2,2)*g(2,3)*g(2,3)+g(3,2)*g(3,2)*g(3,3)*g(3,3)

            r5=r5+g(1,3)*g(1,3)*g(1,1)*g(1,1)+g(2,3)*g(2,3)*g(2,1)*g(2,1)+g(3,3)*g(3,3)*g(3,1)*g(3,1)

            r6=r6+g(1,1)*g(1,1)*g(1,2)*g(1,2)+g(2,1)*g(2,1)*g(2,2)*g(2,2)+g(3,1)*g(3,1)*g(3,2)*g(3,2)

            r7=r7+g(1,2)*g(1,2)*g(1,3)*g(1,3)+g(2,2)*g(2,2)*g(2,3)*g(2,3)+g(3,2)*g(3,2)*g(3,3)*g(3,3)

            r8=r8+g(1,1)*g(1,1)*g(1,3)*g(1,3)+g(2,1)*g(2,1)*g(2,3)*g(2,3)+g(3,1)*g(3,1)*g(3,3)*g(3,3)

            r9=r9+g(1,1)*g(1,1)*g(1,2)*g(1,2)+g(2,1)*g(2,1)*g(2,2)*g(2,2)+g(3,1)*g(3,1)*g(3,2)*g(3,2)

            N=N+1

            PRINT*, N

    end do

100 close(u_in)

             r1=r1/N
            r2=r2/N
            r3=r3/N
```

```
r4=r4/N
r5=r5/N
r6=r6/N
r7=r7/N
r8=r8/N
r9=r9/N

PRINT*, 'r1=', r1
PRINT*, 'r2=', r2
PRINT*, 'r3=', r3
PRINT*, 'r4=', r4
PRINT*, 'r5=', r5
PRINT*, 'r6=', r6
PRINT*, 'r7=', r7
PRINT*, 'r8=', r8
PRINT*, 'r9=', r9

C11=230+278*r1
C22=230+278*r2
C33=230+278*r3
C44=117-139*r4
C55=117-139*r5
C66=117-139*r6
C23=135-139*r7
C13=135-139*r8
C12=135-139*r9

PRINT*, C11
PRINT*, C22
PRINT*, C33
PRINT*, C44
PRINT*, C55
PRINT*, C66
PRINT*, C23
PRINT*, C13
PRINT*, C12


END PROGRAM SayersSteel
```

Appendix B

Study of localized texture and the number of grains that must be sampled statistically.

It became immediately apparent during this study that analysing EBSD scans taken from a variety of points across the sheet produces a variation in the predictions of the nine elastic stiffness constants and hence the S_0 Lamb wave velocity profile predictions to correlate with the ultrasonic texture measurement data. The issue of localized texture (microtexture) has been recognised in recent literature. This appendix introduces the procedure undertaken to determine the amount of angular data that is required and how many grains need to be sampled, for the EBSD data gathered to be considered truly representative and statistically viable.

The case study presented here is the 1mm thick aluminium AL104325 sheet purchased from Advent RM. As a reminder, the ultrasonic texture measurement result is shown here in figure B.1.

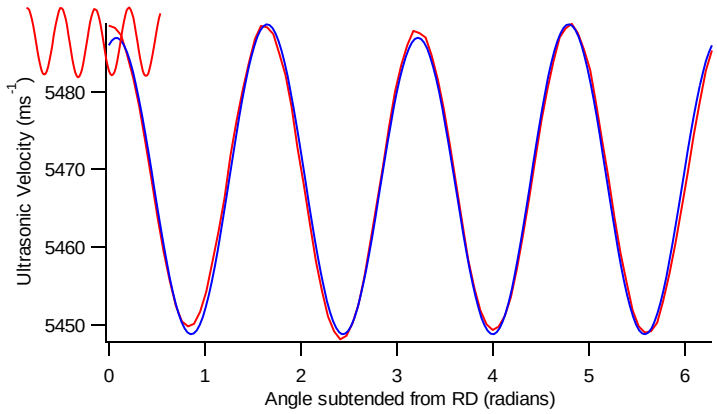

Figure B.1: Ultrasonic velocity profile for 1mm thick Aluminium sheet Al104325. The red line is the measured velocity data, the blue line is the corresponding applied fit.

The orientation distribution coefficients calculated from the mathematical fit applied to the velocity profile are given in table B.1.

Thickness (mm)	W_{400}	W_{420}	W_{440}
1	$2.95 \times 10^{-3} \pm 0.0045\%$	$1.08 \times 10^{-3} \pm 2.05\%$	$5.99 \times 10^{-3} \pm 5.79\%$

Table B.1: ODC values with % errors that have been extrapolated from the ultrasonic velocity data for the 1mm thick aluminium sheet AL104325.

Figure B.2 shows a typical EBSD surface scan IPF map taken from the sheet.

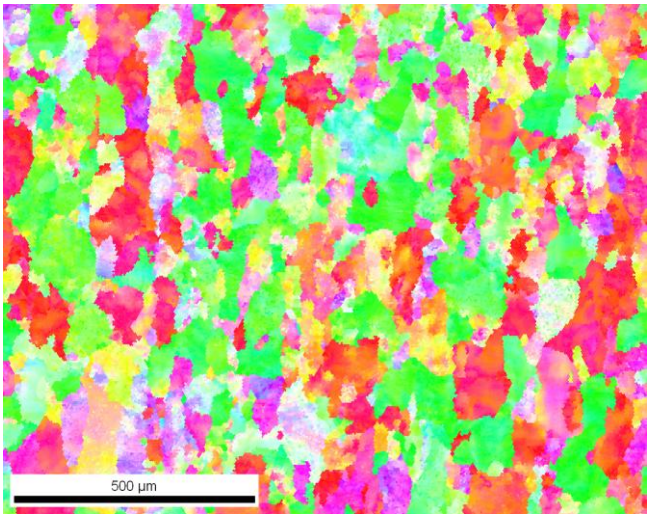

Figure B.2: EBSD Inverse Pole Figure map taken from a sample of the 1 mm thick aluminium sheet sample AL104325.

The sheet itself was split into twelve sections after the ultrasonic measurements were completed, with six scans being taken from one side of the sheet, and a further six being taken from the other side. Each scan was conducted at a suitable magnification and resolution levels, altered depending on factors such as the sample surface finish. The idea is that this will construct a large database to analyse, covering a relatively large number of grains and would indicate the existence of consistently varying localized textures or if the crystallographic orientations, the microstructure, and therefore texture, would be similar across the entire sheet.

Each scan was analysed individually to identify the elastic constants predictions and then to generate the velocity profile predictions. The data was then combined to determine the threshold where the data became statistically representative.

To give an indication of the repeatability of the texture across the sheet, presented here are the results from the first six scans taken. Figures B.3-B.8 are the generated S_0 Lamb wave velocity profile predictions produced.

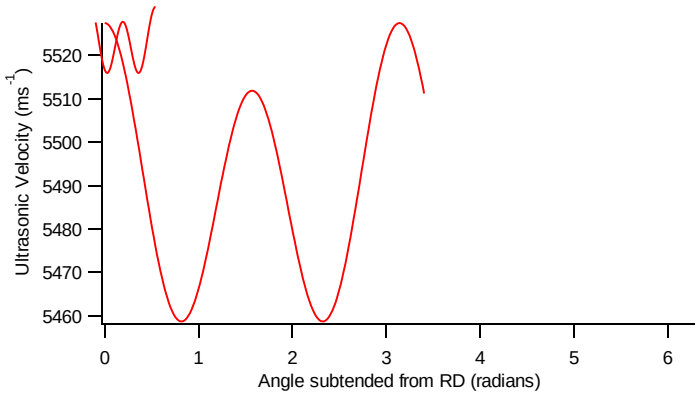

Figure B.3: S_0 mode Lamb wave velocity angular variation prediction from EBSD Eulerian angle data obtained from section 1 scan on 1 mm thick aluminium sheet AL104325.

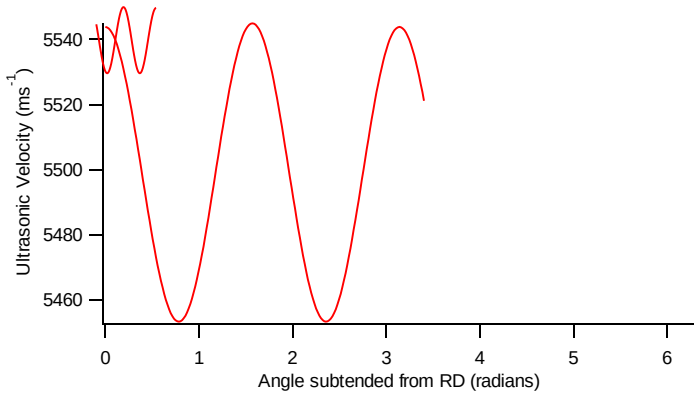

Figure B.4: S_0 mode Lamb wave velocity angular variation prediction from EBSD Eulerian angle data obtained from section 2 scan on 1 mm thick aluminium sheet AL104325.

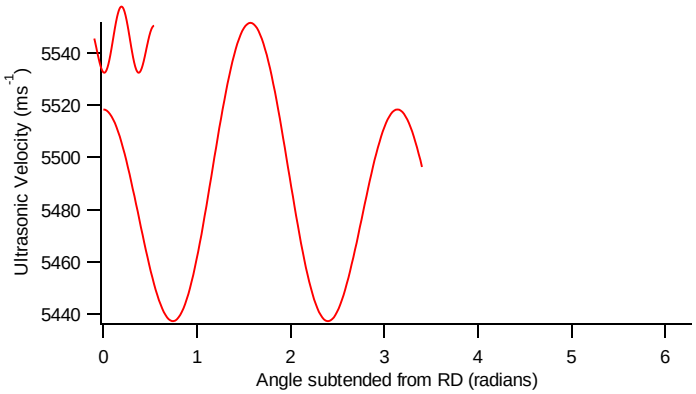

Figure B.5: S_0 mode Lamb wave velocity angular variation prediction from EBSD Eulerian angle data obtained from section 3 scan on 1 mm thick aluminium sheet AL104325.

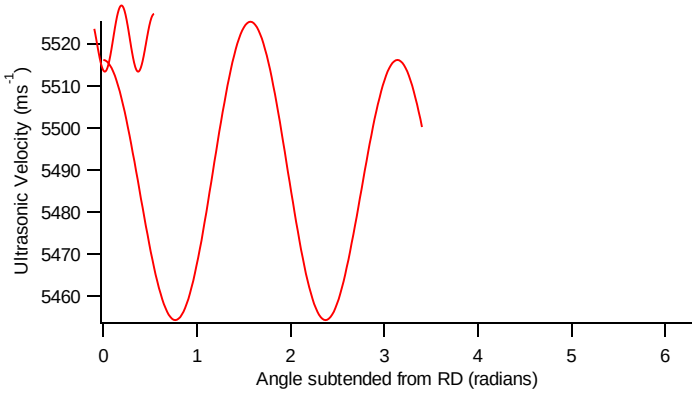

Figure B.6: S_0 mode Lamb wave velocity angular variation prediction from EBSD Eulerian angle data obtained from section 4 scan on 1 mm thick aluminium sheet AL104325.

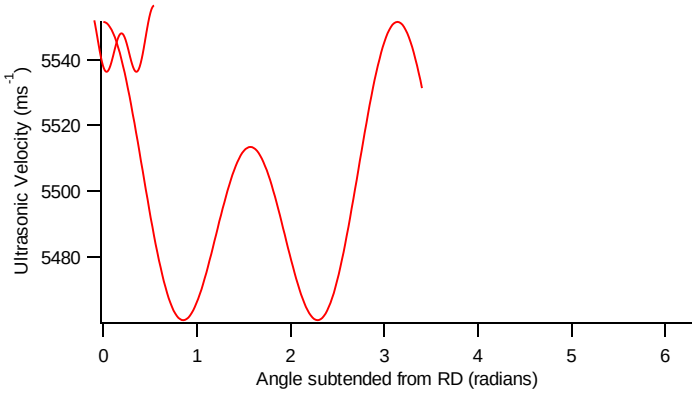

Figure B.7: S_0 mode Lamb wave velocity angular variation prediction from EBSD Eulerian angle data obtained from section 5 scan on 1 mm thick aluminium sheet AL104325.

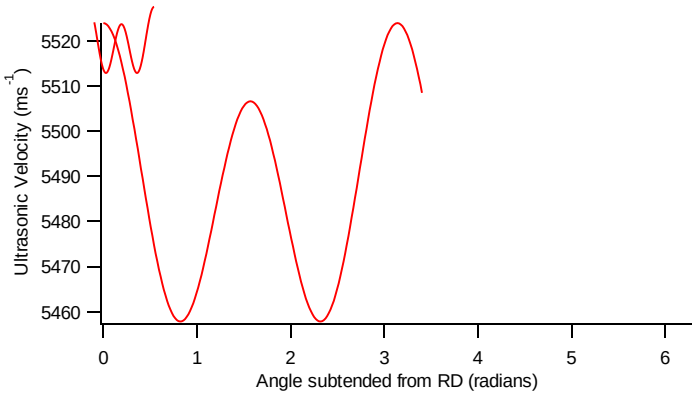

Figure B.8: S_0 mode Lamb wave velocity angular variation prediction from EBSD Eulerian angle data obtained from section 6 scan on 1 mm thick aluminium sheet AL104325.

On analysis of these six velocity profile predictions, it is evident that on each occasion the EBSD data has identified the 4-fold symmetry this sheet possesses. This equates to the W_{440} coefficient being larger than the W_{420} coefficient. It was observable from the ODCs generated that the predicted W_{440} coefficients were consistently larger in magnitude than the W_{420} values, a measure of 2-fold symmetry. Five of the remaining six scans also followed this pattern displayed above. An erroneous result was seen in sample 8. The auto IPF plot is shown in figure B.9.

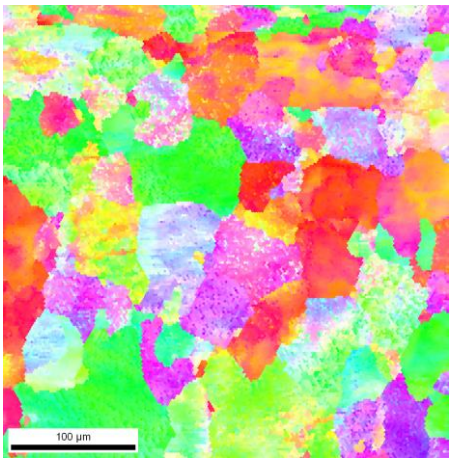

Figure B.9: EBSD Inverse Pole Figure map taken from the sample of section 8 taken from the 1 mm thick aluminium sheet sample AL104325.

There is nothing immediately worrying when observing this scan and comparing it to figure B.2. However, the predicted velocity scan behaves significantly differently to the other 11 sections. This is given in figure B.10.

Figure B.10: S_0 mode Lamb wave velocity angular variation prediction from EBSD Eulerian angle data obtained from section 8 scan on 1mm thick aluminium sheet AL104325.

Here the W_{420} coefficient was larger than the W_{440} coefficient. One possible explanation of this is that in comparison to the other scans this was a small dataset, sampling just 38504 data points, and was performed at a high magnification. With just a few grains sampled in the scan in comparison to others (112), this will have influenced the apparent elasticity of the sample and the ensuing texture measurement predictions.

Inspection of the [111] pole figure is a traditional method to investigate what texture components exist. Figure B.11 displays the [111] pole figure for section 8, with figure B.12 showing the [111] pole figure taken for section 5. With reference to chapter 5, the pole figure representing section 5 is very similar to the idealised pole figure configuration for a rolled aluminium sheet sample, which is what should be expected.

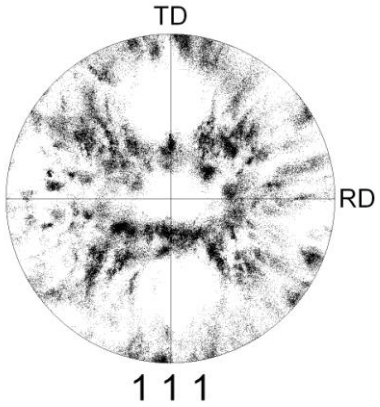

Figure B.11: [111] pole figure for section 8 sample taken from 1 mm thick aluminium sheet AL104325.

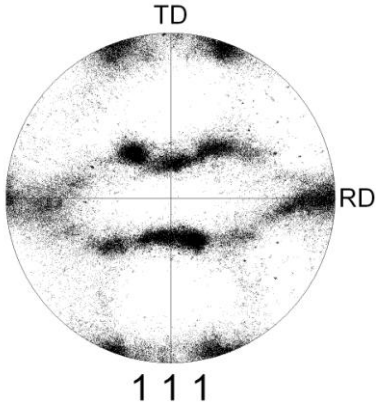

Figure B.12: [111] pole figure for the section 5 sample taken from 1 mm thick aluminium sheet AL104325.

This particular circumstance is an important indicator of the limitations of EBSD, the apparent existence of localized textures, and the need to average over a few scans.

The purpose of this small study was to investigate the size of the data set required for the EBSD elasticity and texture predictions to be consistent and statistically viable. This can be considered to hold if when averaging over a set number of scans, that regardless of which scans are included, the predicted ultrasonic behaviour will remain similar. The previous discussion has certainly indicated that using one scan is definitely not reliable for producing representative data.

Figure B.13 displays the predicted velocity profile when averaged over all 12 EBSD scans taken. The angular data has been taken from a total of 2978 grains. When comparing to the ultrasound data given in figure B.1, there is evidence of a strong correlation. There is a discrepancy in the absolute velocities, which is discussed in chapter 9, but the overall pattern in determining the fast and slow directions relative to the rolling direction indicates that the EBSD is confirming the accuracy of the ultrasonic technique at the microstructural level.

Collating and averaging data over twelve EBSD scans is extremely time consuming, so if it is possible to get similarly reliable results from a smaller number of scans this would be beneficial.

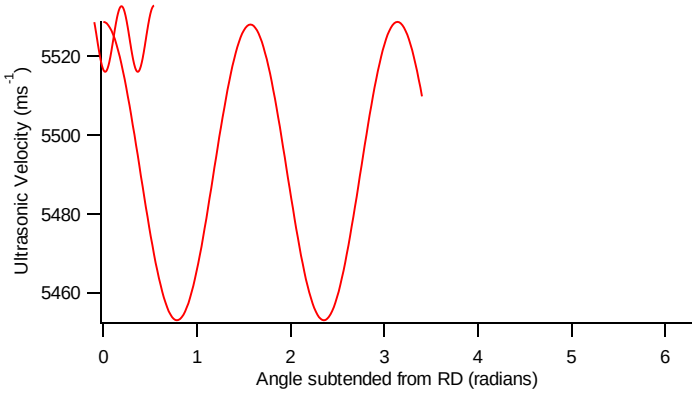

Figure B.13: S_0 mode Lamb wave velocity angular variation prediction from all twelve EBSD Eulerian angle datasets obtained from the 1mm thick aluminium sheet AL104325.

Investigations averaging over four of the scans taken indicate that this is not enough data. Figure B.14 shows the predicted velocity averaged from datasets taken from sections 1, 3, 5 and 7.

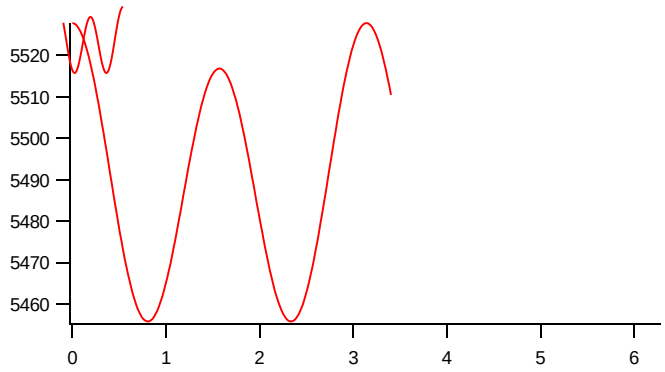

Figure B.14: S_0 mode Lamb wave velocity angular variation prediction from four EBSD Eulerian angle datasets obtained from the 1mm thick aluminium sheet AL104325, namely sections 1, 3, 5 and 7.

Figure B.15 is another example of a predicted velocity profile, this time from the datasets 4, 6, 8 and 10. It is noticeable that the peaks parallel to the rolling direction correspond to a lower velocity than those velocities parallel to the transverse direction, whereas for figure B.14 the inverse is true. Though there is not a large difference in predictions, such details manifest from significant differences in the elastic stiffness constants.

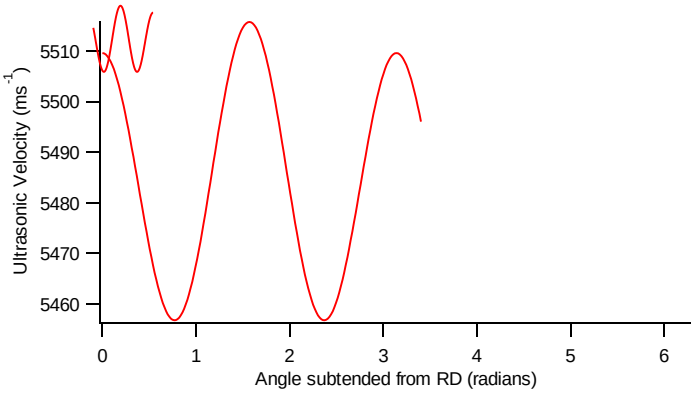

Figure B.15: S_0 mode Lamb wave velocity angular variation prediction from four EBSD Eulerian angle datasets obtained from the 1mm thick aluminium sheet AL104325, namely sections 4, 6, 8 and 10.

The next logical step was to investigate the repeatability of predictions using six different datasets. Figure B.16 displays the predicted velocity behaviour averaged from datasets 1-6.

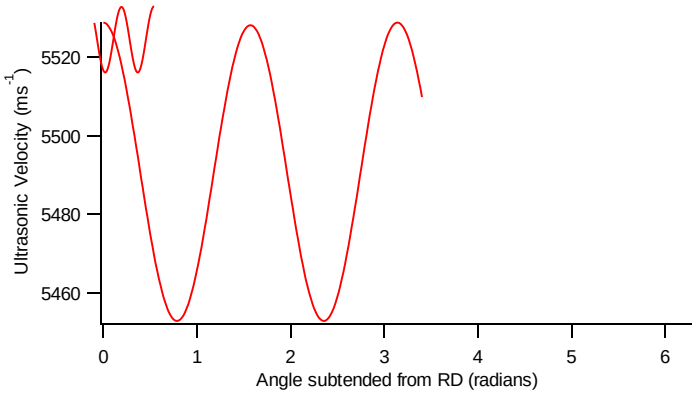

Figure B.16: S_0 mode Lamb wave velocity angular variation prediction from six EBSD Eulerian angle datasets obtained from the 1mm thick aluminium sheet AL104325, namely sections 1, 2, 3, 4, 5 and 6.

It is noticeable here that along the RD and TD, the velocities are approximately equal, which is very similar to, and within experimental error of, the results obtained ultrasonically that are given in figure B.1.

Further combinations of six datasets were studied, and all, and even those that included the dataset from section eight, produced similar ultrasonic predictions.

Based on the premise of therefore using six data sets, this equates to, in this instance, averaging over approximately 450,000 data points. The average number of grains that are sampled over six scans completed will be a minimum of 1420, and a maximum of 1924.

In conclusion, it is unreliable to use just one EBSD scan to make generic texture measurements. Localized textures exist in sheet metal, and as such a stand-alone scan cannot be considered statistically representative. At least 1400 grains from across the sheet need to be sampled to generate a more complete analysis of the microstructure and average texture in the sheet. Following on from the discussion in chapter 9 regarding the 0.5mm thick AL104232 aluminium sheet, it is also advisable to study in-plane EBSD data to confirm homogeneity of the microstructure and texture throughout the bulk of the sheet. If this does

not exist, then surface scans cannot be considered representative of the average bulk texture either.

The 1 mm thick sheet was selected as this was the sample with the biggest average grain size studied in this thesis Therefore, for the other sheets, for similar areas scanned more grains would in fact be sampled increasing the reliability of the average texture data obtained.